Title
Soil-Foundation-Structure Interaction Effects on the Cyclic Failure Potential of Silts and Clays

Author
Buenker, Jason Michael

Publication Date
2020

Peer reviewed|Thesis/dissertation

UNIVERSITY OF CALIFORNIA
Los Angeles

Soil-Foundation-Structure Interaction Effects on the Cyclic Failure Potential of Silts and Clays

A dissertation submitted in partial satisfaction of the requirements for the degree
Doctor of Philosophy in Civil Engineering

by

Jason Buenker

2020

ABSTRACT OF THE DISSERTATION

Soil-Foundation-Structure

Interaction Effects on the Cyclic Failure Potential of Silts and Clays

by

Jason Buenker

Doctor of Philosophy in Civil Engineering

University of California Los Angeles, 2020

Professor Scott J. Brandenberg, Chair

Soil-structure-interaction (SSI) plays an important role in seismically-induced ground failure; however, the contribution is poorly understood and rarely considered in geotechnical engineering practice. Semi-empirical methodologies used in practice to evaluate ground failure solely consider demand from vertically propagating shear waves in the free field. Mounting evidence suggests this approach may significantly underpredict induced demand in soils below shallow foundations by neglecting SSI-induced stress contributions. Observations made during post-earthquake reconnaissance suggest that soils below low- to mid-rise structures supported on shallow foundations may be more susceptible to ground failure than soils in the corresponding free field. Recent physical and numerical modeling studies substantiate this evidence by demonstrating that SSI-

induced stresses contribute to ground failure potential and may exacerbate the consequences of ground failure. Studies to date have centered on liquefaction-based (e.g. sand-like) ground failure; complementary studies on cyclic softening (e.g. clay-like) ground failure are not available.

This research seeks to fill that knowledge gap by evaluating the SSI-induced seismic loading increment imparted by shallow foundations on fine-grained soils within the context of cyclic softening ground failure. The research is based on an analysis framework that utilizes elastic solutions to define SSI-induced stress demands beneath shallow foundations. The framework proposes a new demand parameter called the deviatoric strength ratio to quantify incremental stress demands under complex stress paths below footings. To substantiate the framework and provide empirical case history data on cyclic softening, the author performed a geotechnical centrifuge testing program at the Center for Geotechnical Modeling at the University of California Davis. The program consisted of two dynamic centrifuge tests incorporating structures founded on strip footings and bearing on fine grained soil. The structures incorporated a range of mass and stiffness properties at approximately the same bearing pressure to evaluate the influence of structure response on cyclic softening. Analysis results indicate a strong relationship between permanent foundation settlement or rotation and indices that represent spatially averaged cyclic strains in foundation soils when subjected to deviatoric stress demands from ground response and SSI.

The dissertation of Jason Buenker is approved.

Lisa M. Star

Jonathan P. Stewart

Yousef Bozorgnia

Jian Zhang

Scott J. Brandenberg, Committee Chair

University of California Los Angeles

2020

To Clara…to Matilda…

TABLE OF CONTENTS

Abstract of the Dissertation ii
Table of Contents vi
List of Figures x
List of Tables xv
List of Symbols xvi
List of Acronyms xxi
Acknowledgements xxiii
Vita xxv
1 Introduction 1
2 Existing Research 5
2.1 SSI Observed in Post-Earthquake Reconnaissance 5
2.1.1 1999 Chi-Chi Taiwan Earthquake 6
2.1.2 1999 Kocaeli Turkey Earthquake 7
2.2 Semi-Empirical Cyclic Softening Evaluation 8
2.3 Ground Failure Evaluation Incorporating SSI 10
2.4 Centrifuge Studies Incorporating SSI-Induced Ground Failure 11
2.5 Numerical Modeling Studies Incorporating SSI-Induced Ground Failure 12

2.6 Analytical SSI-Induced Stress Evaluation 15
3 Research Framework 16
3.1 Component Stresses 19
3.1.1 SSI Component Stresses 22
3.1.2 Free Field Component Stresses 25
3.2 Deviatoric Stresses 26
3.2.1 Deviatoric Stresses in Direct Simple Shear Testing 28
3.2.2 Deviatoric Stresses in Triaxial Compression Testing 30
3.2.3 Cyclic Deviatoric Stresses as a Function of Loading Cycles 31
3.3 SSI Stress Generator Tool 33
4 Clay Strength Evaluation 46
4.1 Strength Normalization Parameters 46
4.2 Deviatoric Conversion of Laboratory Data 48
4.3 Strain-Dependent Deviatoric Strength Ratio 52
4.3.1 Original Cyclic Direct Simple Shear Data by Eslami (2017) 52
4.3.2 Adjusted Cyclic Direct Simple Shear Data by Eslami (2017) 57
4.4 Cyclic Strain Functions 62
5 Centrifuge Test JZB01 66
5.1 Instrumentation 68
5.2 Model Container 69
5.3 Pore Fluid 70
5.4 Soil 71
5.4.1 Sand 71
5.4.2 Clay 74
5.5 Structure Installation 84
5.6 T-Bar Testing 84
5.7 Centrifuge Testing 86
5.7.1 Spins 1 through 4 87
5.7.2 Spin 5 88
5.8 Model Deconstruction 91
6 Centrifuge Test JZB02 92
6.1 Model Container 94
6.2 Pore Fluid 95
6.3 Soil 95
6.3.1 Sand 96

6.3.2 Clay 98
6.4 Structure Installation 107
6.5 In Situ Testing 107
6.6 Centrifuge Testing 109
6.6.1 Spin 1 109
6.6.2 Spin 2 109
6.7 Model Deconstruction 111
7 Structural Models 112
7.1 Structure Configuration and Assembly 112
7.2 Strain Gages 124
7.2.1 Gage Installation 124
7.2.2 Strain Measurement 125
7.2.3 Gage Calibration 127
7.3 Fixed-Base Structural Frequency 134
7.4 Structural Behavior 137
7.4.1 Structure 1 Behavior 137
7.4.2 Structures 2 and 3 Behavior 140
7.5 Flexible-Base Structural Frequency 141
8 Data Processing and Presentation 145
8.1 Data Processing 146
8.1.1 Data Truncation 148
8.1.2 Baseline Correction 149
8.1.3 Tukey Window 150
8.1.4 Butterworth Filter 151
8.1.5 Processing Sequence 152
8.1.6 Processed Ground Motions 153
8.2 Input Motions 157
8.3 Empirical Trends 159
8.4 Motion Amplification or Deamplification 160
8.5 Combined Ground Motions 163
8.6 Ground Motion Intensity Measures 165
9 In Situ Clay Strength and Bearing Capacity of Structures 175
9.1 Design Basis 176
9.2 Bearing Capacity Formulation 176
9.3 Clay Undrained Shear Strength 178

9.3.1 Model JZB01 Clay Strength 178
9.3.2 Model JZB02 Clay Strength 182
9.4 Bearing Capacity Evaluation 183
9.5 Bearing Capacity Conclusions 187
10 Cyclic Softening Evaluation 188
10.1 Soil Behavior Type 188
10.2 Cyclic and Deviatoric Resistance Ratio 190
10.3 Cyclic and Deviatoric Stress Ratio 191
10.3.1 Stress Demand 192
10.3.2 Cycle Counting 197
10.4 Factor of Safety and Induced Strain 198
10.5 Strain-Based Displacement Indices 203
10.6 Limitations 207
10.6.1 Wave Propagation Effects 208
10.6.2 Structural Models 210
10.6.3 Soil Nonlinearity 210
11 Conclusions 212
12 Future Research Opportunities 214
Appendix A: Cyclic Direct Simple Shear Data Processing 217
Appendix B: Cyclic Shear Strain Below Structure Footings 267
Works Cited 282

LIST OF FIGURES

Figure 1: Soil Stress Components below a Shallow Foundation 17
Figure 2: Footing Configuration with Assumed Plane-Strain Conditions (L >> B) 19
Figure 3: Linearly Increasing Vertical Strip Load 23
Figure 4: Deviatoric Strength Ratio Graphical Derivation 28
Figure 5: Single Degree of Freedom Stress Generator Tool 35
Figure 6: Ground versus SDOF Response for a Range of Frequency Ratios 38
Figure 7: Phase Angle between Peak Ground and SDOF Response..... 39
Figure 8: Normalized Vertical Normal Stress Components from Stress Tool 40
Figure 9: Normalized Horizontal Normal Stress Components from Stress Tool 41
Figure 10: Normalized Shear Stress Components from Stress Tool 42
Figure 11: Normalized Deviatoric Stress Components from Stress Tool..... 43
Figure 12: Influence of Structure to Ground Motion Frequency on SSI Demand..... 45
Figure 13: Cyclic Stress Ratio and Cyclic Strength Ratio Curves (Eslami, 2017)..... 48
Figure 14: Deviatoric Conversion of DSS Laboratory Data..... 50
Figure 15: Deviatoric Resistance Ratio Trends from Cyclic Strength Ratio Data 51
Figure 16: SBFW Cyclic Direct Simple Shear Curve Fitting on Original Data..... 54
Figure 17: SKFW Cyclic Direct Simple Shear Curve Fitting on Original Data..... 54
Figure 18: Cyclic Clay Strength Curves for Original Eslami (2017) Data..... 56

Figure 19: SBFW Cyclic Direct Simple Shear Curve Fitting on CSR-Adjusted Data 59
Figure 20: SKFW Cyclic Direct Simple Shear Curve Fitting on CSR-Adjusted Data 60
Figure 21: Clay Strength Curves for CSR-Adjusted Eslami (2017) Data 61
Figure 22: Relationship Between Deviatoric Power Law Coefficients 64
Figure 23: Relationship Between Cyclic Shear Strain and d Coefficient 65
Figure 24: JZB01 Model Configuration 67
Figure 25: Hinged Plate Container Graphic 69
Figure 26: Hinged Plate Container Photo 70
Figure 27: JZB01 Soil Profile 71
Figure 28: Sand Pluviation 72
Figure 29: JZB01 Sand Pluviator Calibration 73
Figure 30: JZB01 Clay Atterberg Limits 76
Figure 31: JZB01 Consolidation Testing 76
Figure 32: Clay Deposition 78
Figure 33: Consolidation using Hydraulic Press 80
Figure 34: JZB01 Model Configuration during Clay Consolidation - Part 1 80
Figure 35: JZB01 Pore Pressure and Settlement during Clay Consolidation – Part 1 81
Figure 36: Hydraulic Press Failure 82
Figure 37: JZB01 Model Configuration during Clay Consolidation - Part 2 83
Figure 38: JZB01 Pore Pressure during Clay Consolidation – Part 2 83
Figure 39: JZB01 Structure Configuration 84
Figure 40: T-Bar Configuration 85
Figure 41: T-Bar Test Data from Model JZB01 Centrifuge Testing 86
Figure 42: JZB02 Model Configuration 93
Figure 43: Flexible Shear Beam Container Graphic 94
Figure 44: Flexible Shear Beam Container Photo 95
Figure 45: JZB02 Soil Profile 96
Figure 46: JZB02 Sand Pluviator Calibration 97
Figure 47: JZB02 Clay Atterberg Limits 98
Figure 48: JZB02 Consolidation Testing 99

Figure 49: JZB02 Model Configuration during Bottom Clay Consolidation 102
Figure 50: JZB02 Pore Pressure and Settlement during Bottom Clay Consolidation – Part 1 103
Figure 51: JZB02 Pore Pressure and Settlement during Bottom Clay Consolidation – Part 2 104
Figure 52: JZB02 Model Configuration during Middle Clay Consolidation 104
Figure 53: JZB02 Pore Pressure and Settlement during Middle Clay Consolidation ... 105
Figure 54: JZB02 Model Configuration during Top Clay Consolidation 105
Figure 55: JZB02 Pore Pressure and Settlement during Top Clay Consolidation 106
Figure 56: JZB02 Pore Pressure and Settlement during All Clay Consolidation 107
Figure 57: CPT-2 Tip Resistance from Model JZB02 Spin 2 108
Figure 58: Structure 1 Assembly 114
Figure 59: Structure 1 Section for Model JZB01 114
Figure 60: Structure 1 Section for Model JZB02 115
Figure 61: Structure 1 Profile for Model JZB01 116
Figure 62: Structure 1 Profile for Model JZB02 117
Figure 63: Structure 2 Assembly 118
Figure 64: Structure 2 Section 118
Figure 65: Structure 2 Profile 119
Figure 66: Structure 3 Assembly 120
Figure 67: Structure 3 Section 120
Figure 68: Structure 3 North I-beam Profile 121
Figure 69: Structure 3 South I-beam Profile 122
Figure 70: Strain Gage Configurations (National Instruments, 2018) 124
Figure 71: Structure 1 RS2 Model to Simulate Pluck Testing 128
Figure 72: Structure 2 RS2 Model to Simulate Pluck Testing 128
Figure 73: Structure 3 RS2 Model to Simulate Pluck Testing 129
Figure 74: Structure 1 RS2 Relationship between A1 Acceleration and SG1 Strain ... 130
Figure 75: Structure 3 RS2 Relationship between A12 Acceleration and SG13 Strain 130
Figure 76: Structure 1 Pluck Test Calibration for Strain Gage SG1 132
Figure 77: Structure 3 Pluck Test Calibration for Strain Gage SG13 132

Figure 78: Structure 1 Pluck Test Frequency Data 135
Figure 79: Structure 2 Pluck Test Frequency Data 135
Figure 80: Structure 3 Pluck Test Frequency Data 136
Figure 81: Structure 1 RS2 Model and Displaced Shapes from Pluck Test Modeling . 139
Figure 82: Structure 1 RS2 Model Response to Simulated Pluck Testing 139
Figure 83: Structure 1 RS2 Model Pluck Test Simulation Frequency Data 140
Figure 84: JZB01 Flexible-Base Structural Frequency Evaluation 143
Figure 85: JZB02 Flexible-Base Structural Frequency Evaluation 144
Figure 86: Acceleration Record Processing Procedure 147
Figure 87: Data Truncation for JZB 01 Motion No. 1 – SW7-333 [0.2] 148
Figure 88: Baseline Correction for JZB 01 Motion No. 1 – SW7-333 [0.2] 149
Figure 89: Tukey Window for JZB 01 Motion No. 1 – SW7-333 [0.2] 151
Figure 90: Butterworth Filter for JZB 01 Motion No. 1 – SW7-333 [0.2] 152
Figure 91: Jupyter Notebook Used to Process Motions with JZB01 Data from SW7-333 [0.2] 153
Figure 92: Base Motion Response Spectra for JZB01 and JZB02 158
Figure 93: Model JZB01 Cumulative Displacement and Rotation 159
Figure 94: Model JZB02 Cumulative Displacement and Rotation 160
Figure 95: Peak Horizontal Acceleration versus Shaking Event 161
Figure 96: Structure 1 Response Summary during JZB01 Shake TCU-078 [0.4] 162
Figure 97: Structure 2 Response Summary during JZB01 Shake TCU-078 [0.4] 162
Figure 98: Structure 3 Response Summary during JZB01 Shake TCU-078 [0.4] 163
Figure 99: Model JZB01 Data for Shake TCU-078 [0.4] 164
Figure 100: Model JZB02 Data for Shake TCU-078 [0.6] 165
Figure 101: Model JZB01 Acceleration-Based Settlement Relationships 167
Figure 102: Model JZB02 Acceleration-Based Settlement Relationships 168
Figure 103: Model JZB01 CAV-Based Settlement Relationships 169
Figure 104: Model JZB02 CAV-based Settlement Relationships 170
Figure 105: Model JZB01 CAV_{dp}-Based Settlement Relationships 171
Figure 106: Model JZB02 CAV_{dp}-Based Settlement Relationships 172

Figure 107: Model JZB01 AI-Based Settlement Relationship 173
Figure 108: Model JZB02 AI-Based Settlement Relationship 174
Figure 109: Structure 1 Configuration for Bearing Capacity Evaluation..... 177
Figure 110: JZB01 Spin 5 Excess Pore Water Pressure below Structure 1 179
Figure 111: Clay Undrained Shear Strength from T-Bar Testing 181
Figure 112: JZB02 Structure 2 OCR and Undrained Shear Strength Profile 183
Figure 113: Structure 1 Settlement 185
Figure 114: Peak Horizontal Accelerations for Structure 1 185
Figure 115: Structure 1 Seismic FS Against Bearing Capacity Failure 186
Figure 116: Cyclic Soil Behavior and Susceptibility Criteria..... 190
Figure 117: Pseudo-Static Structure Behavioral Models 193
Figure 118: Static Stress and Dynamic Deviatoric Stress at Maximum Structure Response for JZB01 Structure 1 during TCU-078 [0.4] 195
Figure 119: Demand Time Histories for JZB01 Structure 1 during TCU-078 [0.4]..... 196
Figure 120: DSR Time series for JZB01 Structure 1 during TCU-078 [0.4] 197
Figure 121: CSR Time Series for JZB01 Structure 1 during TCU-078 [0.4] 198
Figure 122: Deviatoric Factor of Safety Against Cyclic Softening..... 199
Figure 123: CSR-Based Factor of Safety Against Cyclic Softening..... 200
Figure 124: Deviatoric Factor of Safety at Multiple Strain Levels 202
Figure 125: Strain Contours below JZB01 Structure 1 for TCU-078 [0.4]..... 204
Figure 126: Displacement Index 1 Normalized Relationship 206
Figure 127: Displacement Index 2 Normalized Relationship 206
Figure 128: Displacement Index 3 Normalized Relationship 207
Figure 129: Displacement Index 4 Normalized Relationship 207
Figure 130: Normalized Frequency Content of Top Structure Horizontal Motions..... 209

LIST OF TABLES

Table 1: Cyclic Clay Strength Coefficients for Original Eslami (2017) Data 56
Table 2: Cyclic Clay Strength Coefficients for CSR-Adjusted Eslami (2017) Data 62
Table 3: JZB01 Clay Properties 77
Table 4: JZB01 Spin Summary 87
Table 5: Input Earthquake Ground Motions 90
Table 6: JZB01 Shaking Event Sequence 90
Table 7: JZB02 Shaking Event Sequence 110
Table 8: Structural Bearing Pressure Summary 123
Table 9: Strain Gage Calibration Factors and Sensitivities 133
Table 10: Structure Frequencies 136
Table 11: JZB01 Applied Data Processing Parameters 155
Table 12: JZB02 Applied Data Processing Parameters 156
Table 13: Bearing Capacity Summary 184

LIST OF SYMBOLS

LATIN SYMBOLS

a	Power law coefficient used to express CRR
a_h	Horizontal acceleration
a_{max}	Maximum horizontal acceleration
b	Power law coefficient used to express CRR
B	Footing half-width
B_f	Bottom structural flange width
c	Power law coefficient used to express DRR
C_{2D}	Correction for two-dimensional versus one-dimensional cyclic loading
C_c	Compression index
C_k	Permeability index
C_r	Recompression index
C_{SG}	Strain gage calibration factor
c_v	Coefficient of vertical consolidation
c_w	Structure web thickness
$C_{\epsilon a}$	Strain gage calibration constant
CAV	Cumulative absolute velocity
CAV_5	Cumulative absolute velocity with a 5 cm/s^2 threshold
CAV_{dp}	Standardized cumulative absolute velocity
CRR	Cyclic resistance ratio
CRR_m	Magnitude corrected cyclic resistance ratio
CSR	Cyclic stress ratio
CSR_{base}	Cyclic stress ratio during initial loops of direct simple shear testing

CSR_{peak}	Peak cyclic stress ratio
CSR_M	Magnitude corrected cyclic stress ratio
d	Power law coefficient used to express DRR
D_{5-95}	Significant duration
D_f	Footing embedment depth
DRR	Deviatoric resistance ratio
DRR_M	Magnitude corrected deviatoric resistance ratio
DSR	Deviatoric strength ratio
DSR_M	Magnitude corrected deviatoric strength ratio
DSR_{max}	Maximum deviatoric strength ratio
DSR_{pk}	Local peak of deviatoric strength ratio
e	Void ratio
E	Young's modulus
e_c	Eccentricity
e_{max}	Maximum void ratio
e_{min}	Miniumum void ratio
f_{LM}	Frequency
f_n	Fixed-base natural frequency
f_o	Flexible-base natural frequency
FS	Factor of safety
FS_{DSR}	Factor of safety against cyclic softening, deviatoric stress framework
g	Acceleration of gravity
G	Soil shear modulus
G_s	Ratio of water mass density to soil mass density
GF	Gage factor
h	Single degree-of-freedom structure height
I	Moment of inertia
I_a	Arias intensity
i_c	Load inclination factor
k	Permeability
K_o	Soil at-rest earth pressure coefficient
K_{OCR}	Overconsolidation ratio correction factor
k_w	Wave number
K_{ssi}	Soil-structure-interaction correction factor
K_α	Static shear stress ratio correction factor
K_σ	Confining pressure correction factor
L_f	Bottom structural flange length
m	structure mass
M_b	Base moment

M_s	Mass of solids
M_{SG}	Bending moment at strain gage
M_w	Earthquake moment magnitude
MSF	Magnitude scaling factor
N	Number of uniform stress cycles
N_{eq}	Number of equivalent uniform stress cycles
N_g	Induced gravity during centrifuge testing
n_H	High pass filter order
n_L	Low pass filter order
N_{pk}	Length of array of local peaks of deviatoric strength ratio
OCR	Overconsolidation ratio
p	Bearing pressure
P	Axial load
p_a	Atmospheric pressure
P_o	Static component of axial load
PGA	Peak ground acceleration
PGA_{Base}	Base peak ground acceleration
PGV	Peak ground velocity
$PSA_{Base}[T_{So}]$	Base pseudo-spectral acceleration at the site's fundamental period
q	Deviatoric stress
q_a	Allowable foundation stress
q_{cyc}	Cyclic deviatoric stress
q_f	Deviatoric stress invariant at monotonic failure
q_o	Initial deviatoric stress invariant
q_{ult}	Ultimate bearing capacity
q_σ	Overburden pressure at the footing level
r_d	Depth-dependent stress reduction coefficient
r_e	Stress reduction coefficient
R_1	Geometric parameter defined in Figure 1
R_2	Geometric parameter defined in Figure 1
S_a	Pseudo-spectral acceleration
S_{a1}	Pseudo-spectral acceleration at a period of 1 second
S_{aT}	Pseudo-spectral acceleration at the period of the structure
s_u	Undrained shear strength
$s_{u,DSS}$	Undrained shear strength from direct simple shear test
$s_{u,TXC}$	Undrained shear strength from triaxial compression test
$Sens_{final}$	Final strain gage sensitivity
SIR	Shake intensity rate
t	Time

T_m	Mean period
u	Relative displacement of structure
u_g	Ground displacement
u_{go}	Ground motion displacement amplitude
u_o	Static porewater pressure
u_w	Porewater pressure
$\ddot{u}_{b,pk}$	Peak base acceleration
$\ddot{u}_{go}$	Ground motion acceleration amplitude
u_{max}	Maximum relative displacement of structure
u_t^t	Total structure displacement
V_b	Base shear
V_S	Soil shear wave velocity
V_{sand}	Volume of solids
V_T	Total volume
V_V	Volume of voids
x	Horizontal distance from the center of the footing
z	Depth or depth below footing
z_w	Groundwater depth below footing

GREEK SYMBOLS

α	Geometric parameter defined in Figure 1
δ	Geometric parameter defined in Figure 1
γ_{cyc}	Cyclic shear strain
γ_{xz}	Shear strain from vertically propagating shear waves
ΔM	Dynamic base moment increment
ΔP	Dynamic axial loading increment
Δu	Excess porewater pressure
ΔV	Dynamic base shear increment
$\Delta\sigma$	Change in stress
$\Delta\sigma_{ff}$	Change in free field stress due to ground shaking
$\Delta\sigma_{ssi}$	Change in foundation stress due to soil-structure interaction
ε	Strain
ϵ_a	Axial strain
ϵ_b	Bending strain
θ_1	Geometric parameter defined in Figure 1

θ_2	Geometric parameter defined in Figure 1
ν	Soil Poisson's ratio
ξ	Structure damping
ρ	soil mass density
ρ_s	Mass density of solids
ρ_w	Mass density of water
σ	Stress
$\sigma_{o,ff}$	Initial free field stress
$\sigma_{o,ssi}$	Initial foundation stress
σ_p	Maximum past consolidation pressure
σ_{vc}	Vertical confining stress
σ_{xx}	horizontal normal stress
σ_{xz}	in-plane shear stresses
σ_{yy}	out-of-plane normal stress
σ_{zz}	vertical normal stress
$\sigma_1, \sigma_2, \sigma_3$	Principal stresses
σ'_{vc}	Effective vertical confining stress
τ_{cyc}	Cyclic shear stress
τ_f	Cyclic shear stress at soil failure
τ_{peak}	Peak induced shear stress during earthquake shaking
τ_{xz}	Shear stress from vertically propagating shear waves
∅	Phase angle
ω	Ground motion frequency
ω_{HC}	High pass corner frequency
ω_{LC}	Low pass corner frequency
ω_n	Fixed-base structure frequency

LIST OF ACRONYMS

AI	Arias Intensity
CAV	Cumulative Absolute Velocity
CGM	Center for Geotechnical Modeling
CPT	Cone Penetration Test
CRR	Cyclic Resistance Ratio
CSR	Cyclic Stress Ratio
DRR	Deviatoric Resistance Ratio
DSR	Deviatoric Strength Ratio
DSS	Direct Simple Shear
FFT	Fast Fourier Transforms
FSB	Flexible Shear Beam Container
GF	Gage Factor
HPC	Hinged Plate Container
ICP	Integrated Circuit Piezoelectric
LL	Liquid Limit
LP	Linear Potentiometer
MEMS	Micro-Electromechanical System
OCR	Overconsolidation Ratio
PBA	Peak Base Acceleration
PEER	Pacific Earthquake Engineering Research Center
PGA	Peak Ground Acceleration
PHA	Peak Horizontal Acceleration
PL	Plastic Limit
PI	Plasticity Index

PPT	Pore Pressure Transducer
SDOF	Single Degree of Freedom
SSI	Soil Structure Interaction
TXC	Triaxial Compression
VMG	Vishay Measurements Group

ACKNOWLEDGEMENTS

A PhD takes a village. I would not be here without abundant help from so many. I owe thanks to many people, but there are a few that deserve special gratitude…

To my advisor, Scott Brandenberg, thank you for nearly all the good ideas in this dissertation and more than a little patience while I worked them out. Special thanks for the opportunity to do research at UCLA in the first place and then teaching me the skills needed to put that research in motion. Extra special thanks for replying to that e-mail four years ago regarding late applications to the department.

To my unofficial co-advisor, Jon Stewart, thank you for consistent clarity regarding how others might actually use these results. You were an invaluable check on this work and helped ensure progress moved consistently in a meaningful direction. And thanks for the coffee on multiple occasions.

Thanks also to my other committee members, Yousef Bozorgnia, Jian Zhang, and Lisa Star. Your feedback was on point and made this dissertation significantly better. I promise we'll have virtual donuts and coffee over our next VC!

To Paolo Zimmaro, thanks for the many inspirations during these four years. You're a true colleague and a brilliant engineer, and it was my good fortune to work and teach with you.

To Mandro Eslami, I owe you multiple beers. Thanks for such critical help at UC Davis when things looked bleak. Thanks especially for the levity, camaraderie, and for figuring out how to say 'good morning' in Russian. I look forward to retelling these stories for a long time.

To Umma and Appa, I owe you perhaps the most critical thanks. Concluding a PhD in a pandemic comes with special challenges and it simply would not have happened without your help. You gave us a roof, childcare, meals, and seemingly endless support. The MVP of this work is Umma, who watched Matilda while I wrote the vast majority of these pages. I owe you a very long vacation.

To Matilda, the intent was always to finish this work before you arrived. But babies grow faster than academics make progress, and now you're over a year old as I finish. Thanks for being an inspiration during both high and low times. I can't wait to spend more time watching you grow.

Finally, all previous thanks pale beside the gratitude I owe my wife, Clara. It takes a special love to let your husband leave a good job and return to school at age 30. It takes even more to tolerate two long sojourns to UC Davis (one with Matilda on the way) and then carry the team through a cross-country move as I slowly made progress. You've gone above and beyond to make this possible. I owe you so much. Thank you.

VITA

Education

Master of Science in Civil Eng., Dec. 2009, University of Illinois Urbana-Champaign

Bachelor of Science in Civil Eng., May 2008, University of Illinois Urbana-Champaign

Professional Experience

Graduate Student Researcher, UCLA, Sep. 2016 to Present, Soil-Foundation-Structure Interaction Effects on the Cyclic Failure Potential of Silts and Clays, Advisor: Scott J. Brandenberg

Senior/Staff Engineer, Shannon & Wilson, Jan. 2010 to Present, Seattle, Washington and Glendale, California

Teaching Assistant, UCLA, Spring 2018 and Spring 2019 Quarters, CEE 123 – Advanced Geotechnical Design, Instructor: Scott J. Brandenberg

Selected Publications

Buenker, J.M. et al., 2019. Centrifuge Testing on Bentonite Clay - Test UCLA JZB01 in Soil-Foundation-Structure Interaction Effects on the Cyclic Failure Potential of Silts and Clays. Centrifuge Data Report. DesignSafe-CI.

Buenker, J.M., Brandenberg, S.J. & Stewart, J.P., 2020a. Centrifuge Testing on Kaolinite Clay - Test UCLA JZB02 in Soil-Foundation-Structure Interaction Effects on the Cyclic Failure Potential of Silts and Clays. Centrifuge Data Report. DesignSafe-CI.

Buenker, J.M., Brandenberg, S.J. & Stewart, J.P., 2020b. Centrifuge Modeling of Cyclic Softening in Low Plasticity Clays Partially Induced by Seismic Soil-Structure-Interaction. In Hambleton, J.P., Makhnenko, R. & Budge, A.S., eds. Geo-Congress 2020: Geotechnical Earthquake Engineering and Special Topics (GSP 318). Minneapolis, 2020b. American Society of Civil Engineers.

Buenker, J.M., Brandenberg, S.J. & Stewart, J.P., 2020c. Centrifuge Testing of Soil-Foundation-Structure Interaction Effects on Cyclic Failure Potential of Fine-Grained Soil. Earthquake Spectra, p.(Publication Pending).

1 INTRODUCTION

Cyclic ground failure is a staggering source of economic loss and potential life safety risk during earthquakes. Most such loss and risk are generated by ground failure impacts to structures. Structures experience settlement, rotation, reduced bearing capacity, increased load, and other deleterious impacts due to the loss of soil shear strength induced by ground failure. Mounting evidence suggests that cyclic ground failure triggering and its consequences are significantly influenced by SSI-induced stress demands (e.g. demands on the underlying soil generated by structure response). However, the SSI contribution to ground failure is poorly understood and rarely considered in geotechnical engineering practice. State-of-the-practice semi-empirical methodologies used to evaluate ground failure potential solely consider stress demand from vertically propagating shear waves in the free field. The methods neglect SSI-induced stresses. This approach may underpredict (or overpredict) ground failure potential depending on characteristics of the ground motion, structure, and soil deposit.

Recent research has sought to improve this approach. Physical centrifuge modeling and numerical modeling studies have demonstrated that SSI-induced stresses contribute to

cyclic failure potential and that SSI demand may exacerbate the consequences of failure. These efforts largely center on liquefaction-based (e.g. sand-like) ground failure; complimentary studies on cyclic softening (e.g. clay-like) ground failure are not available. Further, no clear framework exists to integrate findings from these studies into existing semi-empirical methodologies. There is a clear research need to develop procedures for evaluating cyclic failure potential of fine-grained soils in a manner that includes SSI effects.

My research seeks to fill that knowledge gap by presenting an SSI-based framework for the evaluation of cyclic softening ground failure potential. The framework utilizes elastic solutions to define SSI-induced stress demands beneath shallow foundations and proposes a new demand parameter, called the deviatoric strength ratio (DSR), to quantify incremental stress demands from complex stress paths below footings. The framework uses DSR as a basis to evaluate factor of safety against cyclic softening ground failure and induced strain below the foundation from cyclic softening.

The framework is substantiated and validated using data from a geotechnical centrifuge modeling program that I performed at the Center for Geotechnical Modeling (CGM) at the University of California Davis. The centrifuge modeling program consisted of two dynamic centrifuge models (designated JZB01 and JZB02) performed using a 9-meter-radius geotechnical centrifuge. The models incorporated three structures with a range of mass and stiffness properties founded on clay-like soil susceptible to cyclic softening. JZB01 incorporated a single bentonite-based clay layer and JZB02 incorporated three kaolinite-based clay layers interlayered with sand lenses. I tested the models at an induced gravity due to centrifugal acceleration (N_g) of 40g for JZB01 and 57g for JZB02. I shook each model with a suite of ground motions during spinning. Using data collected during model shaking, I evaluated cyclic softening potential below model structures using the proposed new framework. Induced SSI demand was evaluated using instrumentation monitored

during centrifuge testing. Clay strength was evaluated using direct simple shear testing data by others that I reprocessed within the deviatoric stress framework. I present cylic softening evaluation results as deviatoric factor of safety against ground failure and as a series of strain-based indices calculated by integrating strain over various ranges dependent on footing width.

This dissertation summarizes the total output of my research effort. Chapter 2 reviews existing research to date on the SSI contribution to cyclic ground failure. Chapter 3 proposed the new framework for evaluation of cyclic ground failure potential and presents a tool to evaluate SSI-induced soil stresses for a single degree of freedom (SDOF) system using the new framework. Chapter 4 presents laboratory strength data expressed in terms of the new framework. The basis for this chapter is a journal paper that is currently in progress for the Journal of Geotechnical and Geoenvironmental Engineering. I anticipate submitting this paper for review in summer 2020 and publication in 2021. Chapters 5 through 7 provide details on the centrifuge modeling program used to test and substantiate the new framework. The basis for this chapter is two data reports (Buenker et al., 2019; Buenker et al., 2020a) published on DesignSafe-CI, which is a collaborative multi-disciplinary cyber infrastructure hosted by the National Hazards Engineering Research Center through the University of Texas at Austin. Chapter 8 presents selected portions of the centrifuge data applicable to ground failure analyses and data that demonstrates potential SSI effects. The partial basis for this chapter is a data paper submitted for publication in Earthquake Spectra (Buenker et al., 2020c). This paper is currently in review and I anticipate publication in late 2020. Chapter 9 presents a pseudo-static bearing capacity evaluation for centrifuge model JZB01 and JZB02 Structure 1 during each test. The basis for this chapter is a conference paper (Buenker et al., 2020b) published at GeoCongress 2020. Chapter 10 presents a cyclic softening evaluation for the centrifuge

model JZB01 and JZB02 structures to demonstrate the new framework, including various strain indices to demonstrate results. The basis for this chapter is a journal paper that is currently in progress for the Journal of Geotechnical and Geoenvironmental Engineering. I anticipate submitting this paper for review in summer 2020 and publication in 2021. Chapter 11 summarizes conclusions and recommendations resulting from the research effort. Chapter 12 presents recommendations for future work.

The intent of this research was always to take an incremental step forward in the integration of SSI effects with ground failure evaluation. The framework proposed here, and the centrifuge testing performed to validate the framework, represent a small, but significant step towards this goal.

2 EXISTING RESEARCH

This research resides at the intersection of existing semi-empirical methods used to evaluate ground failure potential and dynamic stress demands associated with SSI-based loading from shallow foundations. Critical to this research are observations of SSI-induced ground failure from post-earthquake reconnaissance and recent work to evaluate SSI influence on structure performance during earthquakes. I review each component here to formulate a basis for the SSI-inclusive cyclic softening ground failure framework developed in subsequent chapters.

2.1 SSI OBSERVED IN POST-EARTHQUAKE RECONNAISSANCE

Documented impacts to civil infrastructure from ground failure date to at least the 1964 Niigata, Japan and 1964 Prince William Sound, Alaska Earthquakes. Modern post-earthquake reconnaissance observations note an abundance of case histories potentially driven by SSI effects. The body of evidence from recent earthquakes regarding SSI influence on ground failure includes:

- 2011 Tohoku, Japan Earthquake – Low-rise residential buildings (~3 stories) on shallow foundations tended to settle more than the surrounding free field (Ashford et al., 2011).
- 2011 Christchurch, New Zealand Earthquake – Numerous low-rise buildings performed more poorly than surrounding free field soils due to ground failure impacts (Cubrinovski et al., 2011).
- 1999 Chi-Chi Earthquake, Taiwan – SSI-induced cyclic softening was at least partially responsible for ground failure below 3- to 6-story apartment buildings supported on mat foundations (Chu et al., 2008; Chu et al., 2004).
- 1999 Kocaeli, Turkey Earthquake – Extensive liquefaction generated heavy damages below a large number of 3 to 5 story buildings founded on shallow mats, with the more severe examples of liquefaction adjacent to and under buildings. Free field manifestations of liquefaction were infrequent, suggesting a significant SSI component to ground failure (Bray et al., 2004; Sancio et al., 2002).

Critically to this research, Chu et al. (2008) and Bray et al. (2004) observed SSI-influenced cyclic softening during the 1999 Chi-Chi Earthquake in Taiwan and the 1999 Kocaeli Earthquake in Turkey, respectively. In each case, these authors observed evidence of cyclic softening below structures founded on shallow foundations, but without corresponding cyclic softening in the free field. This is strong evidence that SSI plays an important role in cyclic softening ground failure. These case histories are reviewed further here.

2.1.1 1999 Chi-Chi Taiwan Earthquake

The Chi-Chi Earthquake (M_w = 7.6) occurred on September 21, 1999 in west-central Taiwan. The city of Wufeng, which is situated on an alluvial plain crossed by several rivers descending from Taiwan's central mountains, was particularly impacted by the

earthquake. The TCU-065 ground motion station in southeast Wufeng recorded a peak ground acceleration (PGA) equal to 0.8g, with about 40 seconds of strong ground shaking. The earthquake generated ground failure throughout Wufeng, consisting of liquefaction, cyclic softening, lateral spreading, and seismically-induced settlement (Chu et al., 2004). A site in near the TCU-065 ground motion station, designated Wufeng Site A, included several mid-rise structures (three to six stories) that experienced bearing- or punching-type failures of spread footing foundations during the earthquake. The reinforced concrete structures were underlain by low plasticity clayey soils. The structures settled 10 to 30 centimeters and typically experienced column failure at the first-floor level. No evidence of cyclic softening ground failure was observed in the adjacent free-field or below single-story residential structures adjacent to the site.

Chu et al. (2008) performed pseudo-static bearing capacity calculations on the mid-rise structures at Wufeng Site A. They found that incorporating a reduced clay strength generated from cyclic softening was necessary to explain the observed structure performance (e.g. to generate a bearing capacity factor of safety less than one). They also performed a cyclic softening evaluation for the on-site clay and found that free field clay had a factor of safety greater than one against cyclic softening, therefore implying that SSI-induced demand from the structures must be at least partially responsible for clay behavior below the structures.

2.1.2 1999 Kocaeli Turkey Earthquake

The Kocaeli Earthquake (M_w = 7.4) occurred on August 17, 1999 in northwestern Turkey. The earthquake damaged approximately one quarter of building stock in the town of Adapazari, which resides on a fluvial plain bounded by two rivers. A significant number of buildings consisted of modern reinforced concrete buildings ranging from three to five stories tall that were founded on shallow mats and experienced liquefaction or cyclic

softening (Sancio et al., 2002). The relative infrequency of ground failure observations in the open field and the "working of buildings into softened fine-grained subgrade soils" (Bray et al., 2004) suggests a significant SSI component to the ground failure mechanism. Martin et al. (2004) estimated the PGA in Adapazari to be about 0.24g. The majority of published literature on this case history is centered around the distinction between liquefiable versus non-liquefiable material, as existing ground failure evaluation methodologies at the time of the earthquake still relied on the Chinese Criteria to discern liquefaction susceptibility. However, the case history is perhaps more notable for the extent of observed SSI-induced cyclic softening and potential SSI-induced building damages. Boulanger and Idriss (2007) even use the Carrefour Shopping Center site from this case history to demonstrate their semi-empirical cyclic softening evaluation procedure, which is presented in the next section.

2.2 SEMI-EMPIRICAL CYCLIC SOFTENING EVALUATION

Boulanger and Idriss (2007) propose a semi-empirical procedure to evaluate cyclic softening in clay-like fine-grained silts and clays during earthquakes. This procedure forms the backbone of the deviatoric stress-based framework proposed later in this document.

The semi-empirical cyclic softening evaluation procedure is based on existing semi-empirical procedures for liquefaction triggering evaluation, which consists of a comparison between cyclic stress imparted by ground shaking and cyclic resistance mobilized against ground failure. Cyclic stress ratio (CSR) is used in liquefaction trigging or cyclic softening evaluation to quantify induced seismic shear stress. The magnitude-corrected CSR is calculated as:

$$CSR_M = r_e \frac{\tau_{peak}}{\sigma'_{vc}} = 0.65 \left(\frac{\sigma_{vc} a_{max} r_d}{\sigma'_{vc}} \right) \quad \textbf{(2-1)}$$

a_{max} is the maximum horizontal acceleration at the ground surface in g, σ_{vc} and σ'_{vc} are the total and effective vertical confining stress at depth z, respectively, and r_d is a stress reduction coefficient that accounts for the flexibility of the soil. The factor 0.65 is used to convert peak cyclic stress, τ_{peak} to a representative cyclic stress mobilized over the earthquake duration (Idriss & Boulanger, 2006).

Cyclic resistance ratio (CRR) is used to quantify cyclic soil resistance to ground failure. The magnitude-corrected CRR is calculated as:

$$CRR_M = C_{2D} \left(\frac{\tau_{cyc}}{s_u} \right)_{M=7.5} \frac{s_u}{\sigma'_{vc}} MSF \; K_\alpha \quad \textbf{(2-2)}$$

C_{2D} is a correction for two-dimensional versus one-dimensional cyclic loading, $\left(\frac{\tau_{cyc}}{s_u} \right)_{M=7.5}$ is the ratio of cyclic stress to undrained soil strength, s_u for the equivalent number of uniform stress cycles in a magnitude, $M_w = 7.5$ earthquake, MSF is the magnitude scaling factor, and K_α is the static shear stress ratio correction factor to account for sloping ground or initial shear stress (Boulanger & Idriss, 2007). The procedure presents methods to estimate $\left(\frac{\tau_{cyc}}{s_u} \right)_{M=7.5}$ based on in situ tests, laboratory tests, and empirical correlations.

The original intent of this research was to incorporate SSI-induced stresses into the existing simplified procedure by Boulanger and Idriss (2007). One proposed approach was to add a correction term to the CSR equation (i.e. K_{ssi}) and modify the K_α term to account for SSI-induced stresses. The deviatoric stress framework proposed here grew from the difficulties in implementing that approach and molding the exiting framework to include SSI-induced stresses. The incorporation of the deviatoric stress framework into a

simplified procedure or working the framework into existing simplified procedures constitutes the majority of remaining and future work associated with this research.

2.3 GROUND FAILURE EVALUATION INCORPORATING SSI

Prior to the body of recent work, Rollins & Seed (1990) provided among the first studies regarding the influence of SSI on ground failure. Their conclusions were based on field case histories, model tests, and simplified analyses. Their proposed framework to evaluate SSI impacts was based on existing simplified procedures to evaluate liquefaction. Case histories cited in their review include large-diameter oil tanks that apparently increased sand liquefaction resistance during the 1964 Niigata and 1978 Miyagi-ken-Oki Earthquakes in Japan and buildings that seemingly generated greater liquefaction than observed in the surrounding free-field during the 1976 Tangshan, China Earthquake (Liu & Qiao, 1984). Model tests include shake table and centrifuge test models that yielded mixed results. Critically to this research, Rollins & Seed (1990) indicate that buildings with a fundamental period between 0.1s and 0.5s may generate SSI effects that are more likely to cause liquefaction below the building than in the free field, which dovetails closely with the recent observations presented above.

SSI may influence both the capacity and demand side of ground failure evaluation. Seed (1983) first introduced the K_α correction factor to represent the effects of initial static shear stress using laboratory testing. Rollins & Seed (1990) expanded this approach into a framework to account for (1) initial static shear stress correction, K_α; (2) higher confining pressure correction, K_σ; (3) higher overconsolidation ratio correction, K_{OCR}; (4) change in vertical effective stress, $\Delta\sigma$; and (5) the influence of response interaction between the structure and soil induced by the building load, S_a/a_{max}. Some of this work is incorporated in practice today, as state-of-the-practice semi-empirical liquefaction triggering

procedures incorporate K_α and K_{OCR} correction factors to account for sloping ground and overburden, respectively. However, typical equations used to evaluate the factors are not extended to incorporate induced stress from foundations and are mostly intended to facilitate liquefaction evaluation for dams (Youd et al., 2001; Cetin et al., 2004; Boulanger & Idriss, 2012). Idriss and Boulanger (2010) even dropped the K_α factor from the liquefaction case history database that forms the basis for development of semi-empirical liquefaction trigging procedures, because the case histories are dominated by level or nearly-level ground conditions. Rollins & Seed (1990) represents the last real effort to incorporate SSI effects into procedures used to evaluate ground failure potential.

A recurring theme in the available evidence is that SSI effects from low-rise structures tend to amplify ground failure potential. These structures likely have fundamental periods in the range identified by Rollins & Seed (1990) and are supported on shallow foundations over soil that provides suitable static bearing, but is loose or soft enough to be susceptible to cyclic ground failure during an earthquake. Ground motions with frequency contents that correspond to near the structure periods are likely to generate heavy, amplifying SSI effects from these structures that may be detrimental to ground failure potential. Failure to capture these effects is likely to generate unconservative seismic design for these critical buildings, many of which may be residential structures. The research summarized here is intended to build upon the framework by Rollins & Seed (1990) for SSI-induced cyclic softening ground failure.

2.4 CENTRIFUGE STUDIES INCORPORATING SSI-INDUCED GROUND FAILURE

A recent centrifuge testing program has sought to further study liquefaction trigging mechanisms and induced settlement below shallow foundations (Dashti et al., 2010a; Dashti et al., 2010b; Allmond & L., 2012; Zupan et al., 2013; da Silva Marques et al., 2014;

Hayden et al., 2015). The program incorporated 9 centrifuge tests with structures founded on potentially liquefiable sand or silt and a free field to evaluate response without SSI effects (Allmond et al., 2015). The centrifuge tests differed in the thickness, depth, and relative density, of the potentially liquefiable sand or silt to evaluate the impact of these factors on structural performance. Dashti et al. (2010a) and incorporated a prototype scale 3-meter-thick sand, a 3-meter-thick silt, and a 6-meter-thick sand. Allmond and Kutter (2012) incorporated a prototype scale 3.9-meter-thick sand and 2.5-meter-thick sand. Zupan et al. (2013) incorporated a 4.5-meter-thick sand. Da Silva Marques et al. (2014) incorporated a 2.3-meter-thick sand. Hayden et al. (2015) incorporated a 4.6-meter-thick sand. Key liquefaction-induced building settlement mechanisms identified in these studies include: (1) volumetric mechanisms, such as rapid localized drainage, sedimentation, and consolidation, and (2) shear mechanisms, such as partial bearing capacity loss and SSI-induced building ratcheting (Dashti et al., 2010a; Dashti et al., 2010b). All tests reported building settlements that were larger than corresponding settlements in the free field, which indicates the importance of SSI-based effects on liquefaction triggering and settlement.

Test data from these centrifuge studies have formed the basis for numerical models and empirical relationships proposed to express SSI-induced ground failure settlement as a function of footing width, liquefiable layer thickness, structure properties, etc. (Dashti et al., 2010a; Dashti et al., 2010b; Hayden et al., 2015). However, these findings have not been incorporated into the existing ground failure evaluation framework.

2.5 NUMERICAL MODELING STUDIES INCORPORATING SSI-INDUCED GROUND FAILURE

Recent numerical modeling studies have built upon the above centrifuge testing by demonstrating and quantifying the role that SSI plays in liquefaction triggering and

settlement below shallow foundations. Numerical models typically involve large-scale parametric studies run with a suite of ground motions over hundreds to thousands of total analyses. Macedo and Bray (2018) ran parametric studies over 1300 numerical analyses with 36 applied earthquake ground motions to study key indicators of shear-induced building settlement due to liquefaction. They concluded that relative density, thickness, and depth of the liquefiable layer, along with building contact pressure and width are the best predictors of shear-induced building settlement. They also reviewed several intensity measures, including peak ground acceleration, PGA (g), peak ground velocity PGV (cm/s), Arias intensity (AI), I_a (m/s), standardized cumulative absolute velocity (CAV), CAV_{dp} (g-s), significant duration, D_{5-95} (s), shake intensity rate, SIR (m/s), mean period, T_m (s), spectral acceleration at a period of 1 second with 5 percent damping, S_{a1} (g), spectral acceleration at the period of the structure with 5 percent damping, S_{aT} (g). The CAV_{dp} definition (Campbell & Bozorgnia, 2011) is:

$$CAV_{dp} = \sum_{i=1}^{N} \left(H[PGA_i - 0.025] \int_{i-1}^{i} |a(t)| dt \right) \quad \textbf{(2-3)}$$

N is the number of discrete 1 second time intervals, PGA_i is the PGA in time interval i (inclusive of the first and last points), and $H(x)$ is the Heaviside step function with $H(x) = 0$ for $x < 0$ and $H(x) = 1$ for $x \geq 0$. CAV_{dp} is set to zero if $CAV_{dp} < 0.16g \cdot s$ or the 5 percent damped spectral acceleration from 0.1 to 0.5 seconds does not exceed 0.2g. CAV_{dp} is a modified version of the original definition for CAV, shown in Equation (2-4).

$$CAV = \int |a(t)| dt \quad \textbf{(2-4)}$$

Macedo and Bray (2018) indicate the intensity measures that correlate best with shear-induced building settlement are CAV_{dp}, I_a, and S_{a1}. They indicate measures that describe the intensity, frequency content, and duration of shaking is a preferred predictor of settlement. In their study, CAV_{dp} was the best settlement predictor. This conclusion dovetails with Kramer and Mitchell (2006), who suggest an alternative form of cumulative absolute velocity, CAV, designated CAV_5, as the most predictive single intensity measure from 300 candidate intensity measures. Their conclusion was based on numerical analysis of 450 ground motion records from 22 earthquakes input into a series of soil profiles.

$$CAV_5 = \int_0^\infty \langle \chi \rangle |a(t)| dt \qquad \textbf{(2-5)}$$

$\langle \chi \rangle = 0$ where $|a(t)| < 5\ {}^{cm}/_{s^2}$ and $\langle \chi \rangle = 1$ where $|a(t)| \geq 5\ {}^{cm}/_{s^2}$.

Researchers Dashti and Karimi performed a comparable numerical study to Macedo and Bray (2018), but with a review of 28 intensity measures to evaluate the predictive capacity of each measure to estimating the liquefaction hazard in terms of peak excess pore pressure ratio and structure performance (Karimi & Dashti, 2017; Dashti & Karimi, 2017). Karimi and Dashti (2016) validated the numerical model used in the study based on previous centrifuge testing (Dashti et al., 2010a; Dashti et al., 2010b). Among intensity measures at the base rock, far-field soil surface, and foundation level with the best predictive power were base pseudo-spectral acceleration at the site's fundamental period, $PSA_{Base}[T_{So}]$ for predicting far-field pore pressure ratio and base peak ground acceleration, PGA_{Base} and I_a for predicting pore pressures below the foundation. Among intensity measures at the base rock, far-field soil surface, and foundation level with the best predictive power for structure performance in terms of settlement were base rock CAV

and CAV_5. Interestingly, Dashti and Karimi conclude the base rock intensity measures were more predictive of the liquefaction hazard in the far field and at the foundation level than intensity measures of ground motions at those locations.

2.6 ANALYTICAL SSI-INDUCED STRESS EVALUATION

Dynamic stress below a footing is a combination of ground motion-induced stress from vertically propagating shear waves (e.g. site response) and SSI-based stresses from corresponding structural shaking. Each source transmits waves dependent on the frequency of respective motions, with site response waves influenced by ground motion frequency and the natural frequency of the soil deposit and SSI-based waves influenced by the structure natural frequency. This problem is comparable to placing well-known static stress distribution solutions by Boussinesq or Westergaard in dynamic motion and summing the total contributions over time. Heidarzadeh et al. (2015) and Heidarzadeh et al. (2018) proposed solutions to the SSI-based stress component for point loads and line loads on the surface of an elastic half-space. Their solutions use dimensionless parameters to provide the dynamic stresses. The Heidarzadeh et al. (2015) solution is a dynamic analysis of the classical Boussinesq and Cerruti problems (Boussinesq, 1885; Cerruti, 1882). The Heidarzadeh et al. (2018) solution is a dynamic analysis of the classical Flamant problem (Flamant, 1892). The solutions are presented in terms of stress amplitude bulbs plotted in radial form with dimensionless frequencies. Heidarzadeh et al. (2015) also includes solutions for phase shift between stresses and the vertical or horizontal point loads; however, phase is not included in the Heidarzadeh et al. (2018) solutions. Some information regarding phase exists in Heidarzadeh (2016). The Heidarzadeh solutions are used to evaluate potential error from phase shift of induced stresses in the deviatoric stress framework presented later in this document.

3 RESEARCH FRAMEWORK

This research proposes an SSI-based framework for the evaluation of ground failure potential. The framework is intended to quantify SSI-based stress demands from shallow foundations during earthquake shaking. Although applicable to cyclic ground failure in general, the framework is stated in terms of cyclic softening-based ground failure to facilitate later analysis of dynamic centrifuge modeling data that incorporates clay susceptible to cyclic softening.

The stress condition acting on a soil element beneath a strip footing during earthquake shaking is illustrated in Figure 1. The stress condition can be conceptualized as a summation of the four components in Equation (3-1), where $\boldsymbol{\sigma_{o,ff}}$ is the initial stress condition in the free-field (i.e., the stress condition that would exist in the absence of structural loads), $\boldsymbol{\sigma_{o,ssi}}$ is the initial condition due to surface stresses arising from foundation pressures due to SSI, $\boldsymbol{\Delta\sigma_{ff}}$ is the change in stress in the free-field due to ground shaking, and $\boldsymbol{\Delta\sigma_{ssi}}$ is the change in stress imposed by the foundation due to SSI.

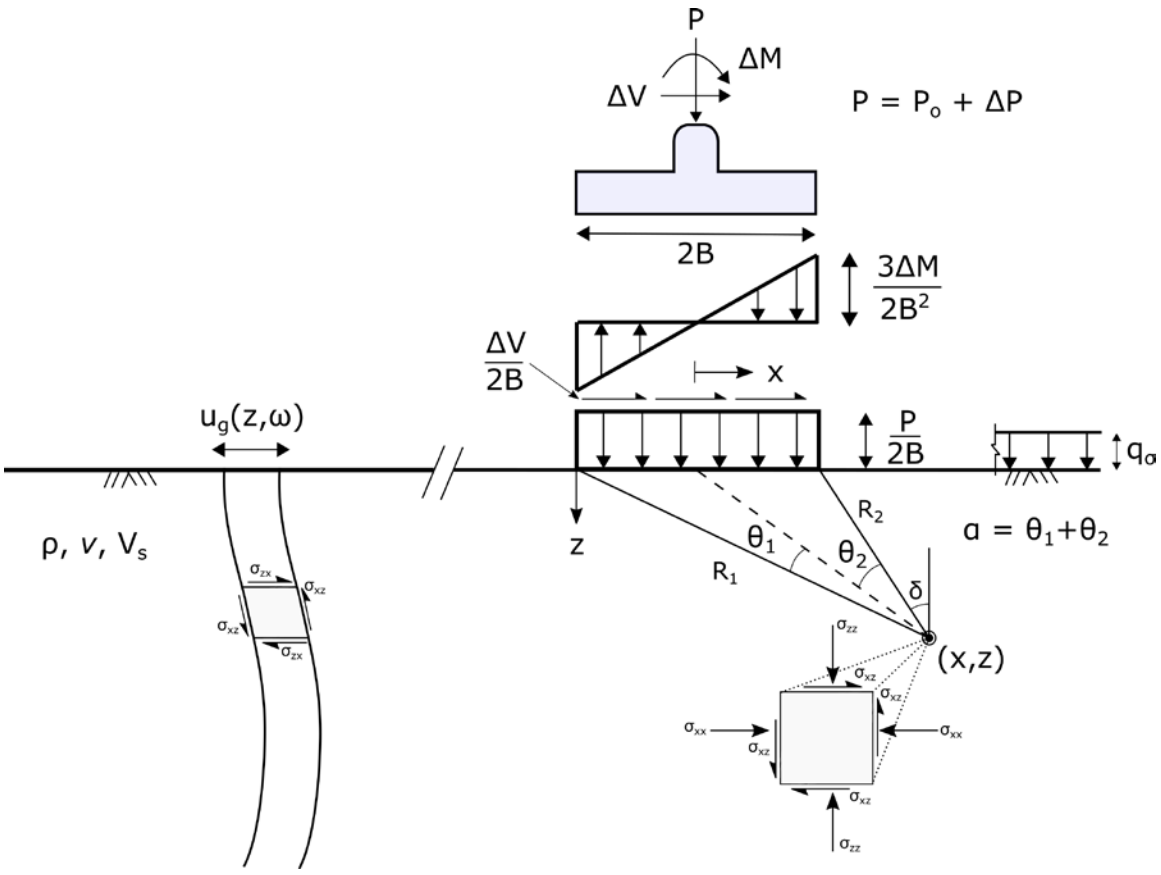

Figure 1: Soil Stress Components below a Shallow Foundation

$$\boldsymbol{\sigma} = \boldsymbol{\sigma}_{o,ff} + \boldsymbol{\sigma}_{o,ssi} + \boldsymbol{\Delta\sigma}_{ff} + \boldsymbol{\Delta\sigma}_{ssi} \qquad \textbf{(3-1)}$$

Each component of Equation (3-1) is a 3x3 Cauchy stress tensor of the form in Equation (3-2), where σ_{zz} is vertical normal stress, σ_{xx} is horizontal normal stress, σ_{yy} is out-of-plane normal stress, σ_{xz} and σ_{zx} are in-plane shear stresses, and σ_{xy}, σ_{yx}, σ_{zy}, and σ_{yz} are out-of-plane shear stresses.

$$\boldsymbol{\sigma} = \begin{bmatrix} \sigma_{xx} & \sigma_{xy} & \sigma_{xz} \\ \sigma_{yx} & \sigma_{yy} & \sigma_{yz} \\ \sigma_{zx} & \sigma_{zy} & \sigma_{zz} \end{bmatrix} \qquad \textbf{(3-2)}$$

Plane-strain conditions approximate the footing configuration in Figure 2, where the in-plane footing width, $2B$ is much greater than the out-of-plane footing length, $2L$. This configuration matches that of structures used in centrifuge modeling that provided case history data for the verification of this framework. For plane-strain conditions the out-of-plane shear stress terms are zero, $\sigma_{xy} = \sigma_{yx} = \sigma_{zy} = \sigma_{yz} = 0$, and the equation reduces to Equation (3-3).

$$\boldsymbol{\sigma} = \begin{bmatrix} \sigma_{xx} & 0 & \sigma_{xz} \\ 0 & \sigma_{yy} & 0 \\ \sigma_{xz} & 0 & \sigma_{zz} \end{bmatrix} \qquad \textbf{(3-3)}$$

The framework could conceivably be applied to the non-plane-strain conditions with square or rectangular footings where one footing dimension is not considerably greater than the other. This configuration would create non-zero σ_{xy} terms that must be evaluated at the zero term positions in Equation (3-3). The σ_{xy} terms would require component elastic solutions that are not included in this dissertation.

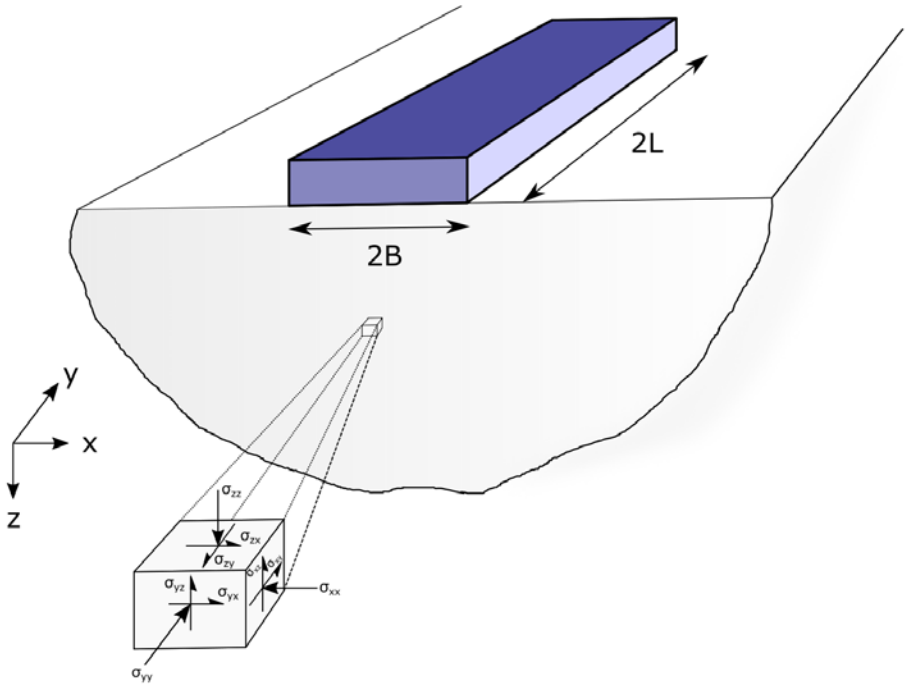

Figure 2: Footing Configuration with Assumed Plane-Strain Conditions (L >> B)

Superposition of stresses implied by Equation (3-3) is not mechanically rigorous when soil behavior is nonlinear, and cases of ground failure invariably involve soil nonlinearity. However, seismic loads are often computed as elastic demands, and the demands are subsequently compared with soil strength to compute a factor of safety. I adopt the elastic demand approach here, in which case the superposition implied by Equation (3-3) is appropriate in the context of this analysis approach.

3.1 COMPONENT STRESSES

Elastic stress solutions for σ_{zz}, σ_{xx}, and σ_{xz} are expressed in Equations (3-4) through (3-15), where z is depth, x is horizontal distance from the center of the footing, g is the acceleration of gravity, ν is the soil Poisson's ratio, ρ is the soil mass density, V_S is soil shear wave velocity, q_σ is overburden pressure at the footing level, ω is the ground motion frequency, u_{go} is the ground motion amplitude, P is axial load, P_o is the static component

of axial load, ΔP is the dynamic axial loading increment, ΔV is dynamic base shear, ΔM is dynamic base moment, $2B$ is footing width, and α, δ, θ_1, θ_2, R_1, and R_2 are geometric parameters defined in Figure 1.

Stress solutions for σ_{zz}:

$$\sigma_{zzo,ff} = \rho g z + q_\sigma \tag{3-4}$$

$$\sigma_{zzo,ssi} = \frac{P_o}{2B\pi}[\alpha + sin\,\alpha\, cos(\alpha + 2\delta)] \tag{3-5}$$

$$\Delta\sigma_{zz,ff} = 0 \tag{3-6}$$

$$\begin{aligned}\Delta\sigma_{zz,ssi} = \frac{\Delta P}{2B\pi}[\alpha + sin\,\alpha\, cos(\alpha + 2\delta)] + \frac{\Delta V}{2B\pi}[sin\,\alpha\, sin(\alpha + 2\delta)] \\ + \frac{3\Delta M}{4B^2\pi}\left[\frac{2x}{B}\alpha - sin2\delta - sin(2\alpha + 2\delta)\right]\end{aligned} \tag{3-7}$$

Stress solutions for σ_{xx}:

$$\sigma_{xxo,ff} = \rho g z\left(\frac{\nu}{1-\nu}\right) \tag{3-8}$$

$$\sigma_{xxo,ssi} = \frac{P_o}{2B\pi}[\alpha - sin\,\alpha\, cos(\alpha + 2\delta)] \tag{3-9}$$

$$\Delta\sigma_{xx,ff} = 0 \tag{3-10}$$

$$\Delta\sigma_{xx,ssi} = \frac{\Delta P}{2B\pi}[\alpha - \sin\alpha\cos(\alpha + 2\delta)] + \frac{\Delta V}{2B\pi}[ln(R_1^2/R_2^2) - \sin\alpha\sin(\alpha + 2\delta)] + \frac{3\Delta M}{4B^2\pi}\left[\frac{2x}{B}\alpha + \frac{2z}{B}(ln[R_2^2] - ln[R_1^2]) + \sin 2\delta + \sin(2\alpha + 2\delta)\right] \quad \textbf{(3-11)}$$

Stress solutions for σ_{xz}:

$$\sigma_{xzo,ff} = 0 \quad \textbf{(3-12)}$$

$$\sigma_{xzo,ssi} = \frac{P_o}{2B\pi}[\sin\alpha\sin(\alpha + 2\delta)] \quad \textbf{(3-13)}$$

$$\Delta\sigma_{xz,ff} = -u_{go}\rho V_s\omega\sin\left(\frac{\omega z}{V_s}\right) \quad \textbf{(3-14)}$$

$$\Delta\sigma_{xz,ssi} = \frac{\Delta P}{2B\pi}[\sin\alpha\sin(\alpha + 2\delta)] + \frac{\Delta V}{2B\pi}[\alpha - \sin\alpha\cos(\alpha + 2\delta)] + \frac{3\Delta M}{4B^2\pi}\left[\cos 2\delta - \cos(2\alpha + 2\delta) + \frac{2z}{B}(\theta_1 - \theta_2)\right] \quad \textbf{(3-15)}$$

Each equation in the suite of stress solutions that incorporates SSI was derived from static elastic flexible foundation solutions for uniform vertical strip loading by Jurgenson (1934), uniform horizontal strip loading solution by Scott (1963), and linearly increasing vertical strip loading solution by Scott (1963). Stress solutions for vertically propagating shear waves by Kramer (1996) are used to evaluate free field shear stresses from site response.

Note that $\Delta\sigma_{xz,ff}$ includes a frequency term. Application of this equation over a broadband ground motion recording is therefore most efficient in the frequency domain.

In addition to the above equations, σ_{yy} is also required to populate the Cauchy stress tensor. Stress solutions for σ_{yy} are not readily available in the literature. Based on elasticity principals, σ_{yy} can instead be stated in terms of σ_{zz}, σ_{xx}, and ν in Equation (3-16).

$$\sigma_{yy} = \nu(\sigma_{zz} + \sigma_{xx}) \qquad \textbf{(3-16)}$$

The above solutions have limitations. Flexible foundation solutions create stress conditions that differ from those for foundations with finite or infinite stiffness. These differences are large immediately beneath the foundation and decrease with distance from the foundation. Further, static stress solutions defined in the $\Delta\sigma_{ssi}$ terms above do not account for wave propagation effects imposed by a vibrating structure. Heidarzadeh et al. (2015) used the boundary element method to address this problem by developing dynamic solutions for a harmonically oscillating vertical point load, which is the Boussinesq (1885) problem and horizontal point load, which is the Cerruti (1882) problem. Heidarzadeh et al. (2018) developed corresponding dynamic solutions for harmonically oscillating vertical and horizontal line loads, which are the Flamant (1892) problem. The solutions could conceivably be integrated over a finite footing width to obtain solutions for loaded areas. However, this framework adopts static elastic solutions herein, and subsequently utilize dynamic solutions to assess potential errors due to wave propagation effects.

3.1.1 SSI Component Stresses

The SSI stress components of Equations (3-5), (3-7), (3-9), (3-11), (3-13), and (3-15) derive from elastic solutions available through Poulos & Davis (1974). Elastic stresses

induced by uniform vertical load on a strip footing were evaluated by Jurgenson (1934). Elastic stresses induced by uniform shear load on a strip footing were evaluated by Scott (1963). The footing configuration, coordinate system, and geometry for each of those solutions match that of Figure 1; therefore, the solutions may be applied directly to form the equations presented in the previous section without modification.

Elastic stresses induced by applied base moment on a strip footing is more complex than each of the uniform loading solutions; therefore, a brief derivation is presented here. Stresses induced by an applied base moment on a strip footing may be modeled as a linearly increasing vertical load on the footing. Elastic stresses for a linearly increasing vertical load on a strip footing were evaluated by Scott (1963). Figure 3 below presents the configuration of the Scott solution and Equations (3-17), (3-18), and (3-19) present the applicable expressions. The term $3\Delta M/2B^2$ is based on the expression for moment applied to an eccentric footing, $P/2B \cdot 6e_c/2B$ where eccentricity, $e_c = \Delta M/P$.

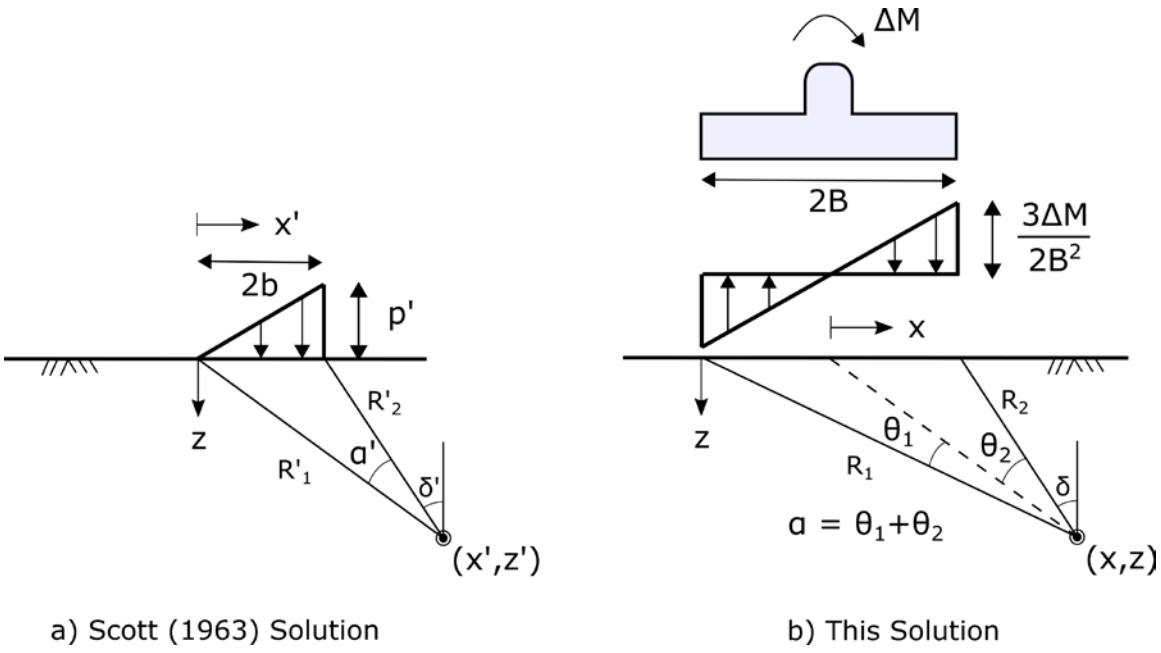

Figure 3: Linearly Increasing Vertical Strip Load

$$\sigma_{zM} = \frac{p'}{2\pi}\left[\frac{x'}{b}\alpha' - sin(2\delta')\right] \quad \textbf{(3-17)}$$

$$\sigma_{xM} = \frac{p'}{2\pi}\left[\frac{x'}{b}\alpha' - \frac{z}{b}ln\left(\frac{R'^2_1}{R'^2_2}\right) + sin(2\delta')\right] \quad \textbf{(3-18)}$$

$$\sigma_{xzM} = \frac{p'}{2\pi}\left[1 + cos(2\delta') - \frac{z\alpha'}{b}\right] \quad \textbf{(3-19)}$$

Note the differences in the Scott (1963) solution versus the Figure 1 solution. In the Scott (1963) solution, the loading stress is applied over half the footing width used in Figure 1. The Scott (1963) solution must also be applied twice to evaluate the positive stress increment on the Figure 1 footing right half and negative stress increment on the Figure 1 footing left half. For clarity, the Scott (1963) input parameters and equivalent Figure 1 input parameters are summarized:

Scott (1963) Parameter	Figure 1 Positive Increment Parameter	Figure 1 Negative Increment Parameter
$2b$	B	B
R'_1	R_o	R_o
R'_2	R_2	R_1
α'	θ_1	θ_2
δ'	δ	$-\delta - \alpha$
x'	x	$-x$
z	z	z
p'	$3\Delta M/2B^2$	$-3\Delta M/2B^2$

Expressions for the Figure 1 positive and negative pressure increments were combined and simplified to produce the component stress solutions presented above for the ΔM terms in the SSI solutions.

3.1.2 Free Field Component Stresses

Dynamic free field stresses are generated by vertically propagating shear waves. Based on Kramer (1996), the equation for horizontal displacement, u_g from vertically propagating shear waves as a function of depth, z, and time, t is indicated in Equation (3-20), where u_{go} is the ground motion amplitude at $z = 0$ and $t = 0$, ω is the wave frequency, and k_n is the wave number.

$$u_g(z,t) = u_{go}\, cos(\omega t - k_n z) \qquad \textbf{(3-20)}$$

Shear strain from vertically propagating shear waves may be expressed as the derivative of the wave equation with respect to depth, z:

$$\gamma_{xz} = \frac{du(z,t)}{dz} = u_{go} k_n\, sin(\omega t - k_n z) \qquad \textbf{(3-21)}$$

Shear stress, τ_{xz} is a function of shear strain and the shear modulus, G:

$$\tau_{xz} = G\gamma_{xz} = u_{go} G k\, sin(\omega t - k_n z) \qquad \textbf{(3-22)}$$

The k_n term is defined in terms of ω and shear wave velocity, V_s, as $k_n = \omega / V_s$. The G term is expressed using soil density ρ and V_s as $G = \rho V_s^2$. Using these expressions, Equation (3-22) simplifies to:

$$\tau_{xz} = u_{go} \rho V_s \omega\, sin\left(\omega\left[t - \frac{z}{V_s}\right]\right) \qquad \textbf{(3-23)}$$

The pseudo-spectral acceleration for an SDOF dynamic system is expressed as $\ddot{u}_{go} = \omega^2 u_{go}$. Equation (3-23) can therefore be stated in terms of acceleration as:

$$\tau_{xz} = \frac{\ddot{u}_{go}\rho_s V_s}{\omega} sin\left(\omega\left[t - \frac{z}{V_s}\right]\right) \quad \textbf{(3-24)}$$

Subsequent calculations typically employ a time invariant solution to perform calculations in the frequency domain. The final form of the equation is therefore:

$$\tau_{xz} = \frac{-\ddot{u}_{go}\rho_s V_s}{\omega} sin\left(\frac{\omega z}{V_s}\right) \quad \textbf{(3-25)}$$

Alternatively, the equation can be expressed in displacement terms as:

$$\tau_{xz} = -u_{go}\rho_s V_s \omega \, sin\left(\frac{\omega z}{V_s}\right) \quad \textbf{(3-26)}$$

Equation (3-26) is used for the free field dynamic stress term $\Delta\sigma_{xz,ff}$ above.

3.2 DEVIATORIC STRESSES

Conventional ground failure analysis is performed in terms of shear stresses, as a comparison between demand-based cyclic stress ratio, CSR, and capacity-based cyclic resistance ratio, CRR. A more fundamental means of expressing stress quantities that include SSI components is deviatoric stress, which is based on principal stresses σ_1, σ_2, and σ_3. The principal stresses are equal to the eigenvalues of $\boldsymbol{\sigma}$, as shown in Equation (3-27).

$$\begin{bmatrix}\sigma_1 \\ \sigma_2 \\ \sigma_3\end{bmatrix} = eig(\boldsymbol{\sigma}) \quad \textbf{(3-27)}$$

The deviatoric stress invariant, q, is defined in Equation (3-28) in terms of principal stresses σ_1, σ_2, and σ_3. The deviatoric stress invariant is analogous to the diameter of the

Mohr's circle of stress but includes all three principal stress components rather than just the major and minor principal stress components, σ_1 and σ_3, that are used to define Mohr's circle.

$$q = \sqrt{\frac{1}{2}[(\sigma_1 - \sigma_2)^2 + (\sigma_2 - \sigma_3)^2 + (\sigma_1 - \sigma_3)^2]} \quad \textbf{(3-28)}$$

The incremental deviatoric stress invariant imposed by shaking can be computed as $\Delta q = q - q_o$, where q_o is the initial deviatoric stress invariant computed for the condition where $\Delta\sigma_{ff} = \Delta\sigma_{ssi} = 0$. A useful metric for the evaluation of ground failure potential in the context of deviatoric stress is the ratio of the incremental deviatoric stress imposed by shaking to the stress increment required to fail the soil. This ratio can be termed the deviatoric strength ratio, DSR, defined using the expression in Equation (3-29), where q_f is the value of the deviatoric stress invariant at monotonic failure.

$$DSR = \frac{q - q_o}{q_f - q_o} \quad \textbf{(3-29)}$$

This ratio is consistent with conventional interpretations of factor of safety against cyclic ground failure from vertically propagating shear waves, expressed $FS = \tau_f/\tau_{cyc}$, where the term τ_f is shear stress at soil failure and τ_{cyc} is induced cyclic shear stress. Figure 4 presents this relationship graphically using Mohr's circle. The figure is based on a simple shear loading condition, where σ_{ho} is initial horizontal stress on the soil, σ_{vo} is initial vertical stress on the soil, τ_{max} is the maximum induced shear stress in the soil, and s_u is the soil undrained shear strength. This conventional interpretation is limited by the use of shear stresses in a two dimensional configuration that does not account for the existing state of stress in the soil. DSR overcomes these limitations by incorporating deviatoric stress and

the q_o term, respectively. Worth noting is that another limitation of the conventional interpretation is that $\tau_f \sim s_u$ and $\tau_{max} \sim \tau_{cyc}$, neither of which are strictly true. The DSR framework eliminates these issues.

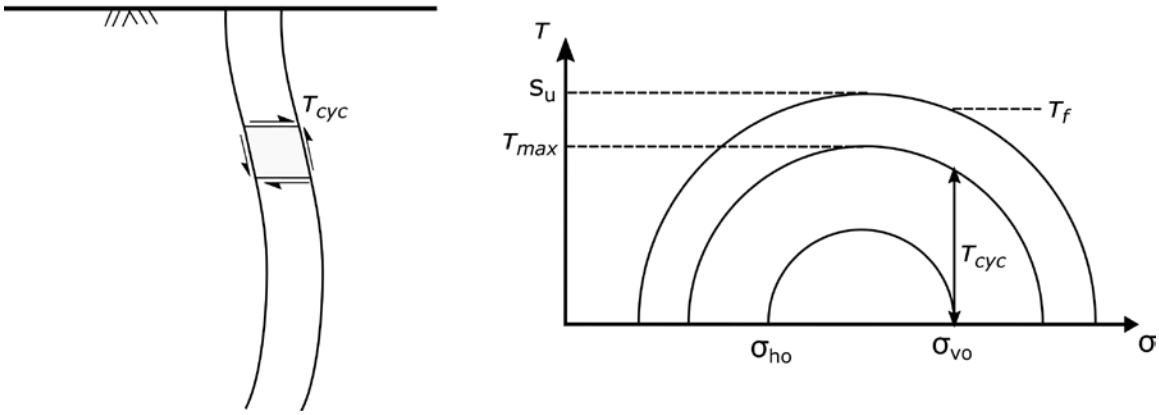

Figure 4: Deviatoric Strength Ratio Graphical Derivation

The q_f term in the DSR equation is based on monotonic undrained shear strength. Undrained shear strength is typically measured using a direct simple shear (DSS) or triaxial compression (TXC) testing. For consistency with the DSR equation, the DSS or TXC undrained shear strength must be restated in deviatoric terms to evaluate q_f. The following sections therefore derive the associated deviatoric expressions for the DSS and TXC stress paths. Equivalent expressions for an equivalent cyclic deviatoric stress term, q_{cyc} follows, with corresponding expressions for DSR as a function of the equivalent number of loading cycles and the resulting factor of safety expression.

3.2.1 Deviatoric Stresses in Direct Simple Shear Testing

A K_o consolidated DSS stress path is characterized by the Cauchy stress tensor in Equation (3-30), where K_o is the at-rest earth pressure coefficient, σ_{vc} is the vertical

consolidation stress (assume that consolidation total stresses and effective stresses are the same for the DSS laboratory specimen), and $s_{u,DSS}$ is the shear stress on horizontal and vertical planes at failure.

$$\boldsymbol{\sigma}_{\mathbf{f,DSS}} = \overbrace{\begin{bmatrix} K_o\sigma_{vc} & 0 & 0 \\ 0 & K_o\sigma_{vc} & 0 \\ 0 & 0 & \sigma_{vc} \end{bmatrix}}^{\boldsymbol{\sigma_o}} + \overbrace{\begin{bmatrix} 0 & 0 & s_{u,DSS} \\ 0 & 0 & 0 \\ s_{u,DSS} & 0 & 0 \end{bmatrix}}^{\boldsymbol{\Delta\sigma}} \qquad \textbf{(3-30)}$$

Note that $s_{u,DSS}$ is not equal to the radius of the Mohr circle at failure for anisotropically consolidated conditions. However, undrained shear strength is usually interpreted this way because elastic demands for vertically propagating shear waves involve an increase in shear stress that can be compared directly with $s_{u,DSS}$. Furthermore, K_o is generally not measured in a DSS test, and the initial shear condition therefore cannot be incorporated into the definition of shear strength. The evaluation of deviatoric stress terms (i.e. q_f, q_{cyc}, etc.) from DSS data therefore necessarily requires the assumption of K_o.

Substituting σ_o and $\sigma_{f,DSS}$ from Equation (3-30) into Equation (3-29). results in expressions for q_o and q_f in Equations (3-31) and (3-32) for a DSS stress path.

$$q_o = \sigma_{vc}(1 - K_o) \qquad \textbf{(3-31)}$$

$$q_f = \sqrt{q_o^2 + 3s_{u,DSS}^2} \qquad \textbf{(3-32)}$$

The term q_f is based on restating monotonic laboratory data in deviatoric stress terms. Similar restatement of cyclic laboratory data into deviatoric stress terms is useful for

developing a relationship between DSR and the number of loading cycles. For cyclic DSS testing, this relationship is conventionally stated as CSR versus the number of loading cycles, where $CSR = \tau_{cyc}/\sigma'_{vc}$, τ_{cyc} is the induced cyclic shear stress, and σ'_{vc} is the effective vertical confining stress. The τ_{cyc} term can be converted to an equivalent deviatoric stress term, q_{cyc} using the generalized form of the equations developed above to express q_f, expressed in Equation (3-33). Note that similarly to the q_f derivation above, calculation of q_{cyc} from cyclic DSS data requires the assumption of K_o to compute the q_o term.

$$q_{cyc} = \sqrt{q_o^2 + 3\tau_{cyc}^2} \qquad \textbf{(3-33)}$$

Using $q = q_{cyc}$, the DSR curve for DSS laboratory data is then computed using Equation (3-29).

3.2.2 Deviatoric Stresses in Triaxial Compression Testing

A TXC stress path is characterized by the Cauchy stress tensor in Equation (3-34). The initial consolidation condition is equal to σ_o from Equation (3-30) and triaxial compression tests are most commonly isotropically consolidated such that $K_o = 1$ and $q_o = 0$, though anisotropic consolidations may be used.

$$\boldsymbol{\sigma}_{\mathbf{f,TXC}} = \overbrace{\begin{bmatrix} K_o\sigma_{vc} & 0 & 0 \\ 0 & K_o\sigma_{vc} & 0 \\ 0 & 0 & \sigma_{vc} \end{bmatrix}}^{\boldsymbol{\sigma}_{\mathbf{o}}} + \overbrace{\begin{bmatrix} 2s_{u,TXC} & 0 & 0 \\ 0 & 0 & 0 \\ 0 & 0 & 0 \end{bmatrix}}^{\boldsymbol{\Delta\sigma}} \qquad \textbf{(3-34)}$$

Substituting σ_o and $\sigma_{f,TXC}$ from Equation (3-34) into Equation (3-29). results in expressions for q_o and q_f in Equations (3-31) and (3-35) for a TXC stress path, where undrained shear strength for a TXC stress path, $s_{u,TXC}$, is typically interpreted as half of the deviator stress at failure, as indicated by Equation (3-35).

$$q_f = 2s_{u,TXC} \quad \textbf{(3-35)}$$

Critically, consolidation stress is measured during TXC testing and a K_o value can be calculated, meaning no assumptions are required to perform the deviatoric stress conversion.

The laboratory data used to evaluate deviatoric-based ground failure under this framework are based on DSS; TXC testing is provide here for informational purposes only and to provide context for the DSS equations listed above.

3.2.3 Cyclic Deviatoric Stresses as a Function of Loading Cycles

Inputting $q = q_{cyc}$ into Equation (3-29) yields a curve representing DSR imposed on a soil specimen judged to have reached a failure condition in a uniform number of loading cycles. This relationship is analogous to CRR, which is often represented as a function of number of loading cycles according to the equation $CRR = aN^{-b}$, where a is the value of CRR required to cause failure in one loading cycle, and b is an exponent that controls the rate at which CRR decreases with N. The value of DRR can be represented as a function of number of uniform loading cycles according to Equation (3-36). For cases where $q_o = 0$, $b = d$. In cases where $q_o > 0$, there is no scalar relationship between b and d, and I suggest that the value of d should be regressed from laboratory test data after performing appropriate conversion to plot DRR versus N.

$$DRR = cN^{-d} \quad \textbf{(3-36)}$$

The DRR curve is now compared with DSR mobilized during an earthquake to evaluate ground failure. Idriss and Boulanger (2008) describe a cycle counting procedure in which a broadband acceleration time series can be converted to a magnitude-corrected cyclic strength ratio, $CSR_M = r_e \cdot CSR_{peak}$, at an equivalent number of uniform loading cycles, N_{eq}, where $r_e = 0.65$ is a reference scalar value. The factor of safety is then computed as $FS = CRR_M/CSR_M$. I adopt a similar procedure here for DSR.

For a broadband DSR time series defined by Equation (3-29), I identify all of the local maxima and minima that cross $\pm 0.1 \cdot DSR_{max}$ and define these values as an array, DSR_{pk}, of length N_{pk}. Further, I define $DSR_M = 0.65 \cdot DSR_{max}$. I then assume that each DSR_{pk} value is associated with half of a loading cycle, and compute the equivalent number of cycles at DSR_M for each value of DSR_{pk}, and sum over the time series based on Equation (3-37).

$$N_{eq} = 0.5 \sum_{j=1}^{N_{pk}} \left(\frac{\left| DSR_{pk,j} \right|}{DSR_M} \right)^{1/d} \quad \textbf{(3-37)}$$

The selection of $\pm 0.1 \cdot DSR_{max}$ as the peak threshold is somewhat arbitrary, but is consistent with other researchers (Idriss & Boulanger, 2008; Boulanger & Idriss, 2007) and intended to capture demand from larger half-cycles without extensive influence from low amplitude half-cycles. Regardless of the selected threshold, the low amplitude half-cycles make little difference in the evaluation due to the power law relationship in Equation (3-36).

The applicable DRR to calculate factor of safety is $DRR_M = DRR(N_{eq})$. The factor of safety against ground failure is then computed according to Equation (3-38).

$$FS_{DSR} = \frac{DRR_M}{DSR_M} \quad \textbf{(3-38)}$$

I use data from the centrifuge modeling program detailed in the next section to demonstrate the efficacy of DSR as a predictive parameter for ground failure. The DSR factor of safety is compared to consequences of ground failure, including structure settlement, rotation, or other evidence of bearing capacity failure. Lower factors of safety consistently correlate with more severe consequences of ground failure.

3.3 SSI STRESS GENERATOR TOOL

The structural demand input parameters for the SSI-based framework detailed in Section 3.1 are axial, shear, and bending moment loading. These inputs can be evaluated using several approaches.

- SSI-based axial, shear, and moment demands could be evaluated from code-based design procedures and input into the framework to evaluate induced stresses.
- Nonlinear or equivalent linear structural models could be performed to capture a range of structural responses, with SSI-based axial, shear, and moment outputs.
- Centrifuge testing detailed later in this dissertation allowed for the direct measurement of axial, shear, and moment SSI components from integrated circuit piezoelectric (ICP) accelerometers and strain gages.

However, geotechnical problems rarely afford advanced knowledge of structural parameters. Most geotechnical work is performed prior to structural modeling when only

preliminary structural parameters may be available for design. To facilitate use of the framework in a practical geotechnical setting, I developed an SSI stress generator tool capable of evaluating stresses for an SDOF system subject to a sinusoidal ground motion. The tool is implemented in a Jupyter notebook. Figure 5 presents the stress generator tool with default inputs.

The stress generator tool requires the inputs foundation width, $2B$ (meters), SDOF structure mass, m (kilograms), SDOF structure height, h (meters), SDOF structure frequency, ω_n (radians per second), SDOF structure damping ξ (%), soil Poisson's Ratio, ν, soil mass density, ρ (kilograms per cubic meter), soil shear wave velocity, V_s (meters per second), groundwater depth, z_w (meters), soil overburden pressure at the footing bottom, q_σ, (kPa), ground motion frequency, ω (radians per second), and peak ground acceleration, PGA (g). The parameter PGA is equal to the $\ddot{u}_{go}$ used in the previous section. The applied ground motion is sinusoidal according to the equation:

$$u_g(t) = \ddot{u}_{go}/\omega^2 \cdot sin(\omega t) = u_{go} \cdot sin(\omega t) \qquad \textbf{(3-39)}$$

Note that the inputs include the parameter z_w to evaluate effective static soil stress that is omitted from the framework in the previous section.

Stress Generator Inputs and Figure:

SDOF Structure Inputs

Base Width, $2B$:	4	meters
Mass, m:	32	Mg/m
Height, h:	6	m
Frequency, ω_n:	7	rad/s
Damping, ξ:	5	%

Soil Inputs

Poisson's Ratio, ν:	0.45	
Density, ρ:	1850	kg/m3
Shear Wave Velocity, V_s:	200	m/s
Groundwater Depth, z_w:	0	m
Overburden, q_σ:	20	kPa

Dynamic Inputs

Ground Motion Frequency, ω:	10	rad/s
Peak Ground Acceleration, $\ddot{u}_{go}$:	0.1	g

Stress Sources

- ☑ Static Free Field Stress
- ☑ Dynamic Free Field Stress
- ☑ Static Foundation Stress
- ☑ Dynamic Foundation Stress

Value Displayed in Figure 1:
- ◉ σ_{zz}
- ○ σ_{xx}
- ○ σ_{yy}
- ○ σ_{xz}
- ○ q

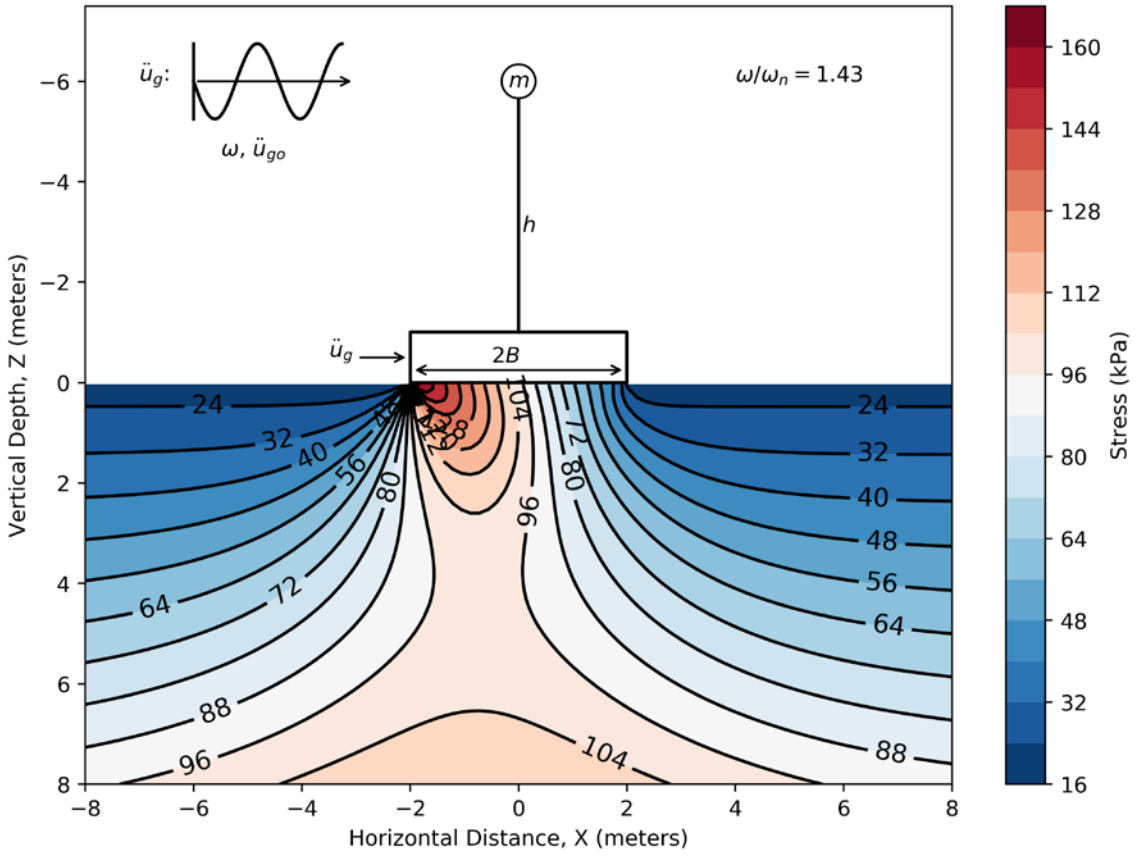

Figure 5: Single Degree of Freedom Stress Generator Tool

Component stress sources within the tool may be toggled on and off to facilitate evaluation of impacts from the various stress sources. The component stress sources match sources outlined in the framework and expressed in Equation (3-1), which include initial static stress in the free-field, initial static stress due foundation pressures, dynamic stress in the free-field due to ground shaking, and SSI-based dynamic stress imposed by the foundation.

SSI-based demands from a SDOF structure are a function of base shear, V_b and base moment, M_b. These demand parameters are evaluated in the tool using the following equations, where u_{max} the maximum relative displacement of the SDOF mass:

$$V_b = \omega_n^2 \cdot u_{max} \cdot m \quad \textbf{(3-40)}$$

$$M_b = \omega_n^2 \cdot u_{max} \cdot m \cdot h \quad \textbf{(3-41)}$$

The value u_{max} may be evaluated from the transfer function and phase equations below (Chopra, 2012):

$$u(t) = \ddot{u}_{go}/\omega_n^2 \cdot \sqrt{C^2 + D^2} \cdot sin(\omega t - \emptyset) \quad \textbf{(3-42)}$$

$$\emptyset = tan^{-1}(-D/C) \quad \textbf{(3-43)}$$

$$C = \frac{1 - (\omega/\omega_n)^2}{[1 - (\omega/\omega_n)^2]^2 + [2\xi(\omega/\omega_n)]^2} \quad \textbf{(3-44)}$$

$$D = \frac{-2\xi(\omega/\omega_n)}{[1 - (\omega/\omega_n)^2]^2 + [2\xi(\omega/\omega_n)]^2} \quad \textbf{(3-45)}$$

where u_{max} is the maximum value of $u(t)$. The parameter $\emptyset$ is the phase difference between u_{go} and u_{max}, which is a function of the frequency ratio ω/ω_n, as shown in Figure 6. The values u_{go} and u_{max} occur simultaneously at $\emptyset = 0°$ and $\emptyset = 180°$, and otherwise occur out of phase at the angle $\emptyset$. At $0 \leq \emptyset < 90$, u_{go} and u_{max} are in phase and at $90 < \emptyset \leq 180$ the two are out of phase. The tool only incorporates the sign of $\emptyset$ and otherwise assumes u_{go} and u_{max} occur simultaneously (i.e. the tool does not consider phase lag). This assumption leads to smaller errors in the solution at low ξ and progressively larger errors at higher ξ. For higher values of ξ, the error in the solution is most pronounced near $\omega/\omega_n = 1$. To demonstrate the effect, Figure 7 presents $\emptyset$ as a function of ω/ω_n and ξ.

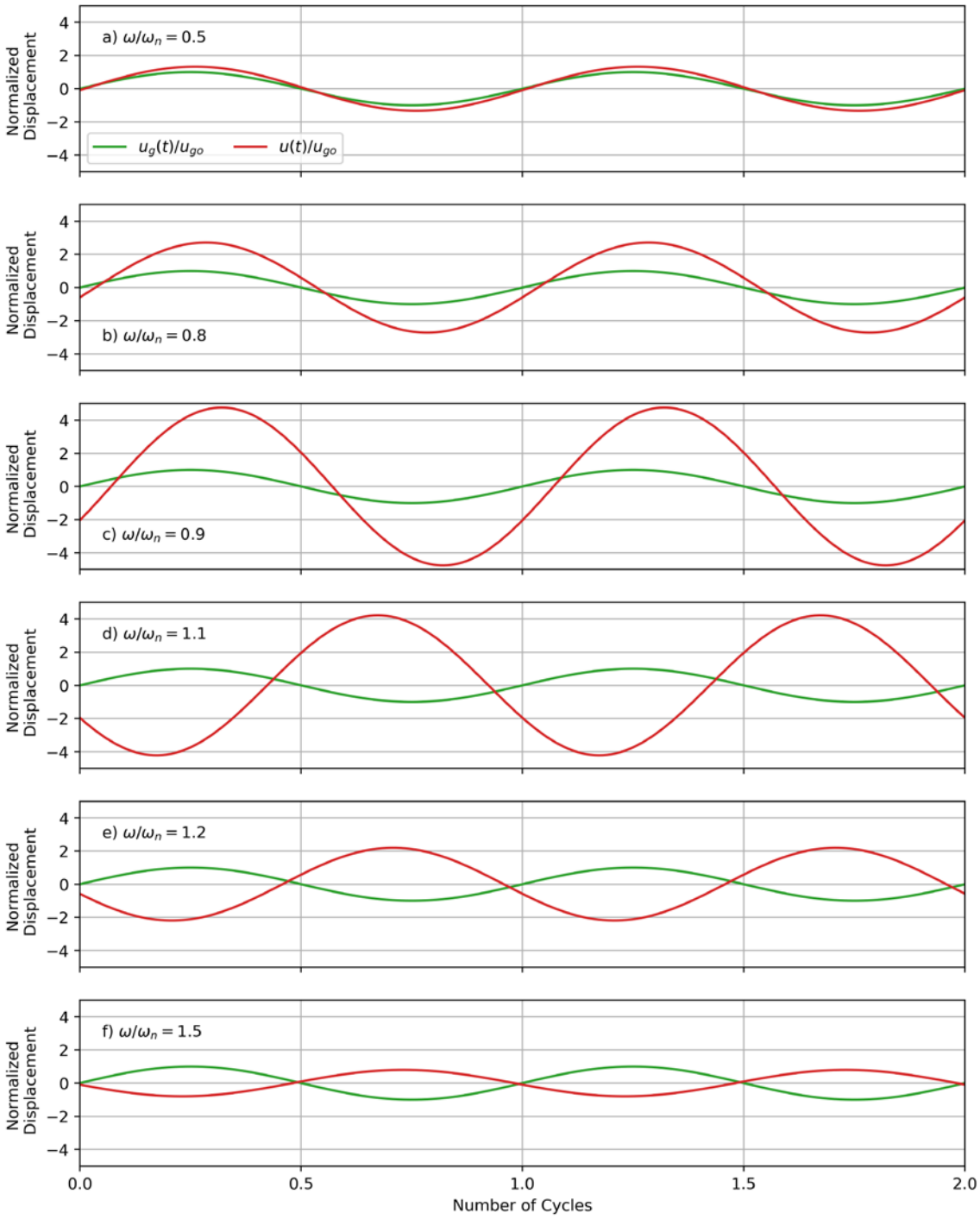

Figure 6: Ground versus SDOF Response for a Range of Frequency Ratios

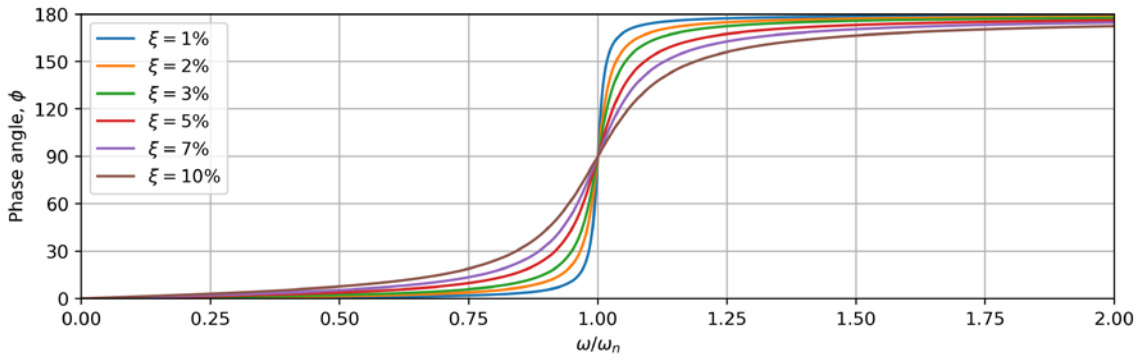

Figure 7: Phase Angle between Peak Ground and SDOF Response

Stress parameters calculated by the tool include the stress parameters required for the framework solution (e.g. vertical normal stress, σ_{zz}, horizontal normal stress, σ_{xx}, out-of-plane normal stress, σ_{yy}, in-plane shear stress, σ_{xz}, and deviatoric stress q). Figure 8 through Figure 11 present normalized σ_{zz}, σ_{xx}, σ_{xz}, q from the stress tool for the input parameters in Figure 5. The stress components are normalized by the footing contact pressure, $p = m \cdot g/2B$.

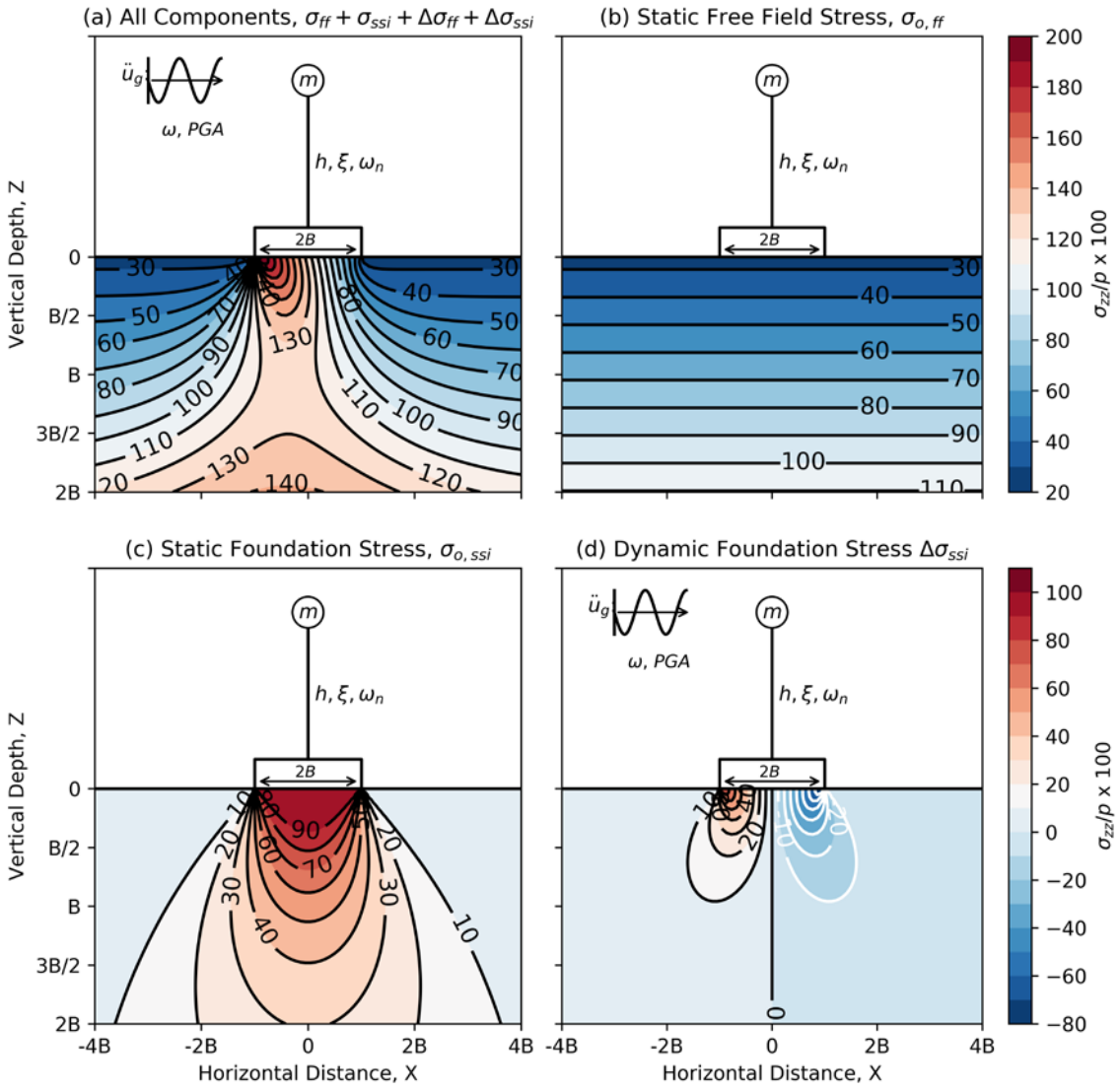

Figure 8: Normalized Vertical Normal Stress Components from Stress Tool

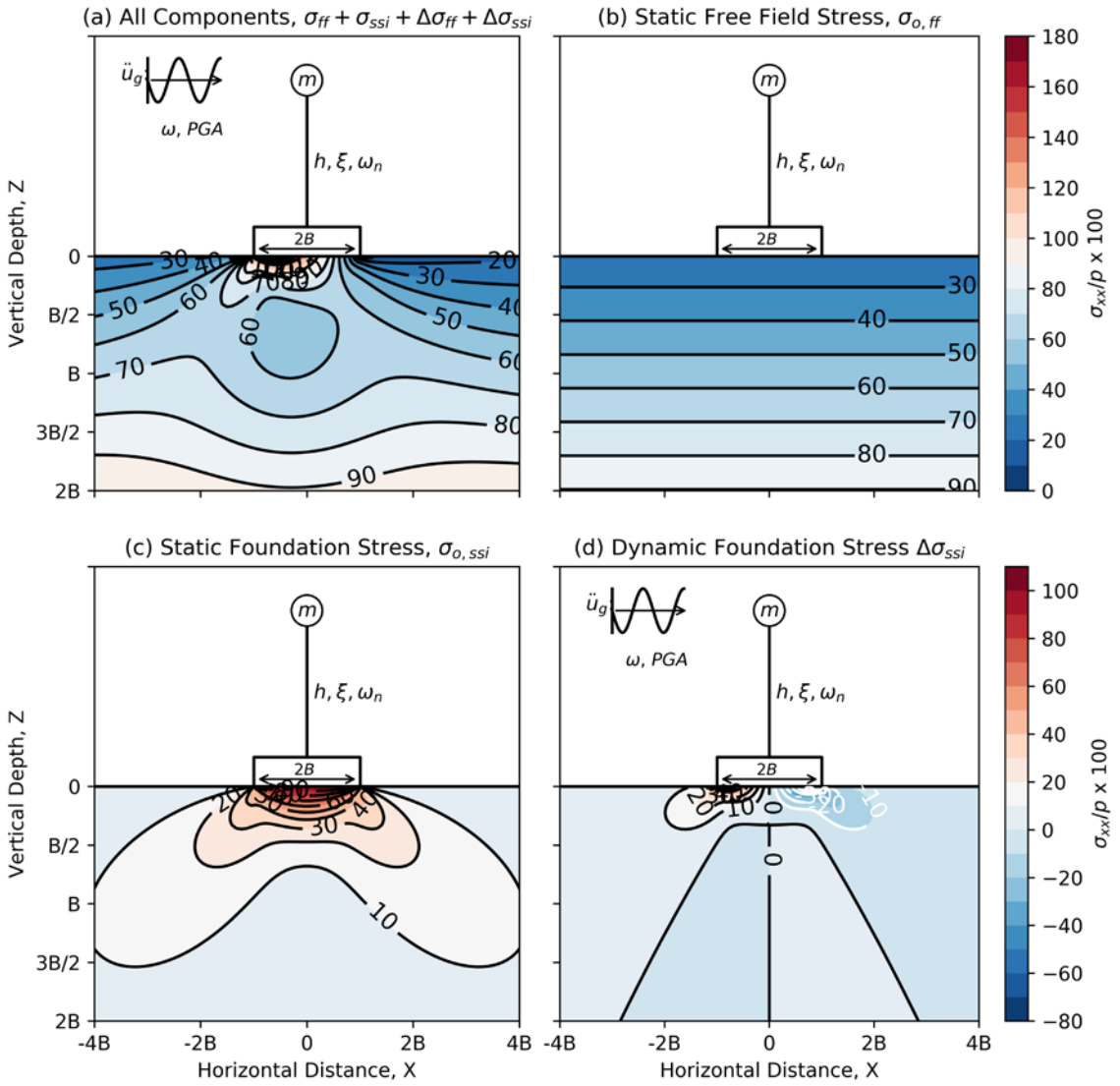

Figure 9: Normalized Horizontal Normal Stress Components from Stress Tool

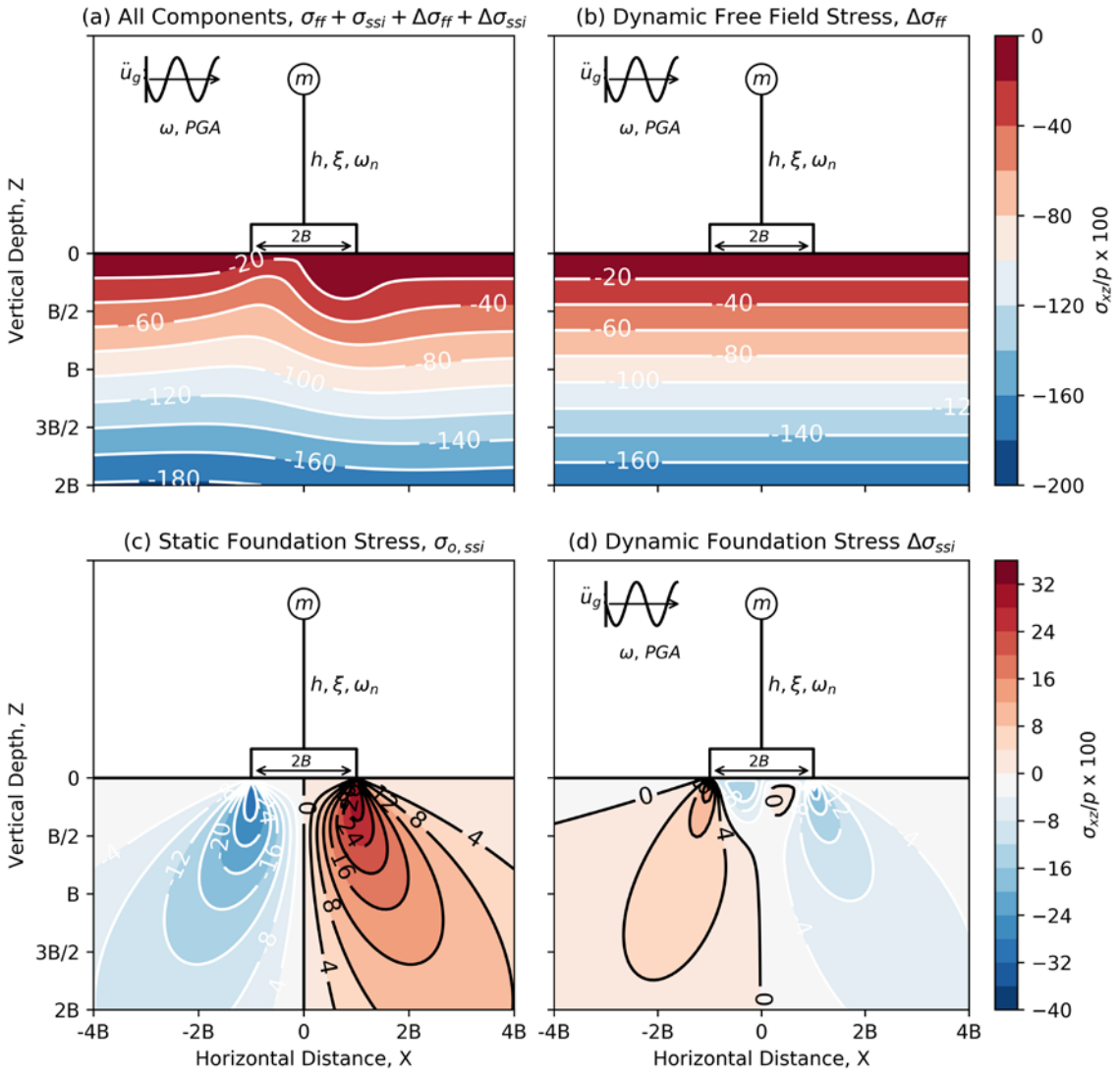

Figure 10: Normalized Shear Stress Components from Stress Tool

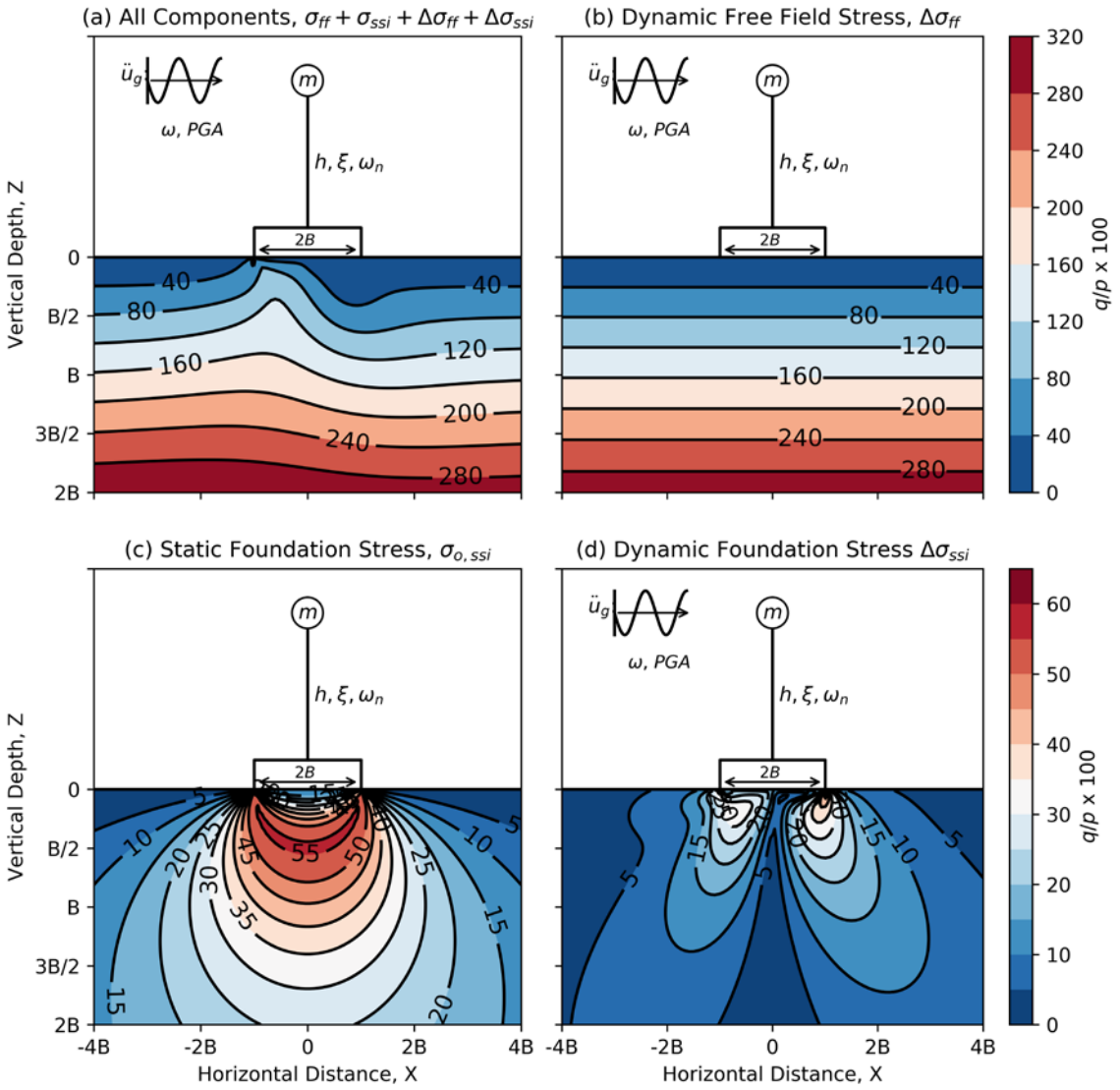

Figure 11: Normalized Deviatoric Stress Components from Stress Tool

The tool can be used to demonstrate the influence of structure and ground motion frequency on the SSI-based demand of the SDOF structure through a parametric study. I parameterized the study by expressing frequency as the ratio ground motion frequency to the natural frequency of the structure, ω/ω_n. I evaluated this frequency ratio over a range of values both less than and greater than unity. At $\omega/\omega_n = 1$, the structure is at resonance and SSI-based demand peaks. I omitted this case from the study because of the large

induced structural demand that dwarfs demand at other frequency ratios. Figure 12 presents the parametric study using σ_{zz} as the demand parameter. Note the large jump in demand near $\omega/\omega_n = 1$ and the phase shift when ω/ω_n transitions from less than one to greater than one. This figure has significant implications to ground failure evaluation, including:

- Long-period structures are unlikely to induce significant additional demand and may actually improve cyclic soil behavior through increased confining pressure. This conclusion dovetails well with observations by Rollins and Seed (1990) that the presence of oil tanks mitigated the development of liquefaction in a sand deposited that would have otherwise liquefied during two earthquakes, as discussed in Section 2.3. Note also that long-period structures are typically large and/or tall and applied confining pressures from these structures would likely dwarf additional demand, consistent with the parametric study.
- Short-period structures or structures with periods near the ground motion period may exert significant additional demand on the soil, particularly below the edges of footings where induced moment may have the highest impact. This conclusion dovetails well with existing observations of low-rise residential structures adversely impacting ground failure potential during earthquakes, as discussed in Section 2.

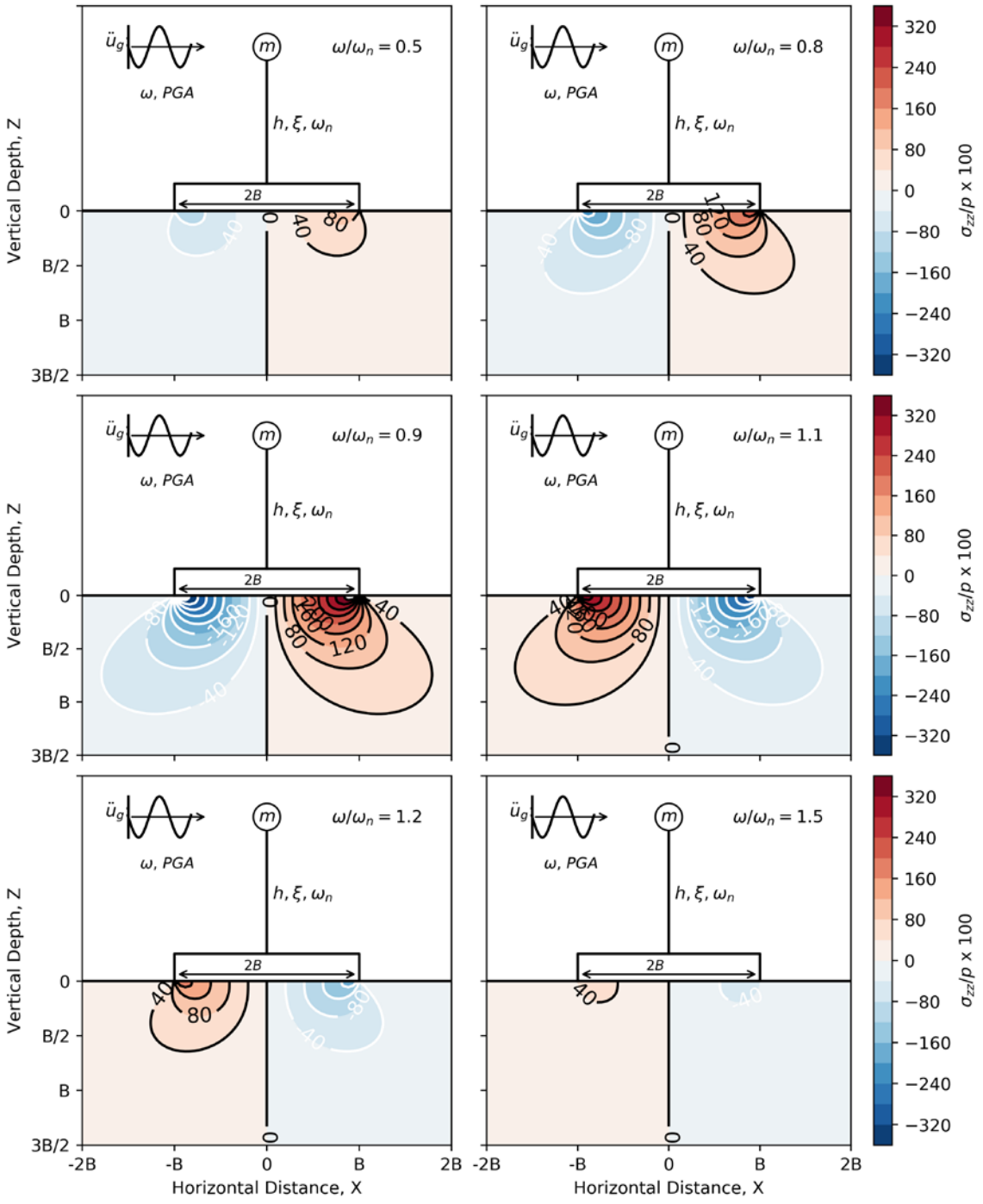

Figure 12: Influence of Structure to Ground Motion Frequency on SSI Demand

4 CLAY STRENGTH EVALUATION

The centrifuge modeling program detailed later in this dissertation incorporated two fine-grained soils modeled after clay blends developed by Eslami (2017). Fine-grained soil used in model JZB01 was based on Eslami blend SBFW; fine-grained soil in model JZB02 was based on Eslami blend SKFW. Eslami (2017) performed extensive laboratory testing to characterize the strength of these blends, consisting of constant-height monotonic and cyclic DSS testing. The centrifuge model soils are not identical to the target blends (particularly for JZB01); however, because the clay minerology and base material are the same, the test results remain applicable for use in the analysis of ground failure potential. These laboratory tests provide the basis to evaluate capacity-side parameters in the deviatoric cyclic softening evaluation framework detailed in Chapter 3. I present applicable components of the laboratory test data here and convert cyclic strength data to deviatoric stress terms.

4.1 STRENGTH NORMALIZATION PARAMETERS

Eslami (2017) conducted monotonic DSS testing on SBFW and SKFW specimens over a range of over-consolidation ratios (OCRs). Testing was performed at a rate of 1 percent

shear strain per minute to a shear strain of 20 percent. Shear strength was evaluated as shear stress corresponding to the peak undrained shear strength ratio. Test data generally displayed strength normalization consistent with the form proposed by Ladd (1991), suggesting clay-like soil behavior. The Ladd (1991) expression is presented in Equation (4-1), where S is the normalized undrained shear strength ratio for a normally consolidated soil and m is the slope of s_u/σ'_{vc} versus OCR in a log-log plot.

$$\frac{s_u}{\sigma'_{vc}} = S \cdot OCR^m \qquad \textbf{(4-1)}$$

Eslami (2017) fit the form of this expression to the monotonic DSS data. He reported $S = 0.213$, $m = 0.718$ for the SBFW blend and $S = 0.198$, $m = 0.594$ for the SKFW blend.

The Ladd (1991) expression is dependent on clay-like critical state behavior, where the critical state line parallels the normal consolidation line. The SBFW blend supports this behavior, however, the SKFW blend is not fully clay-like. An alternative expression of monotonic undrained shear strength is Equation (4-2):

$$\frac{s_u}{p_a} = S \cdot \left(\frac{\sigma'_{vc}}{p_a}\right)^n \cdot OCR^m \qquad \textbf{(4-2)}$$

The value p_a is atmospheric pressure. Eslami et al. (202X) fit this alternative expression to the monotonic DSS data. Based on the curve fitting results, they reported $S = 0.21$, $n = 0.97$, $m = 0.78$ for the SBFW blend and $S = 0.19$, $n = 0.92$, $m = 0.62$ for the SKFW blend. The n coefficient is near unity for the SBFW blend, implying the coherence of Equation (4-1) to the data. Note the use of the variable m in this section solely denotes normalized undrained shear strength ratio for a normally consolidated soil and does not denote structure mass, as used otherwise in this dissertation.

4.2 DEVIATORIC CONVERSION OF LABORATORY DATA

Eslami (2017) conducted cyclic DSS testing on SBFW and SKFW specimens to characterize clay cyclic shear strength as a function of the number of uniform loading cycles, N. CSR and cyclic strength ratio curves by Eslami (2017) for the SBFW and SKFW blends are presented in Figure 13. The shear strength used to normalize the data, $s_{u,DSS}$, is the monotonic shear strength calculated using Equation (4-1).

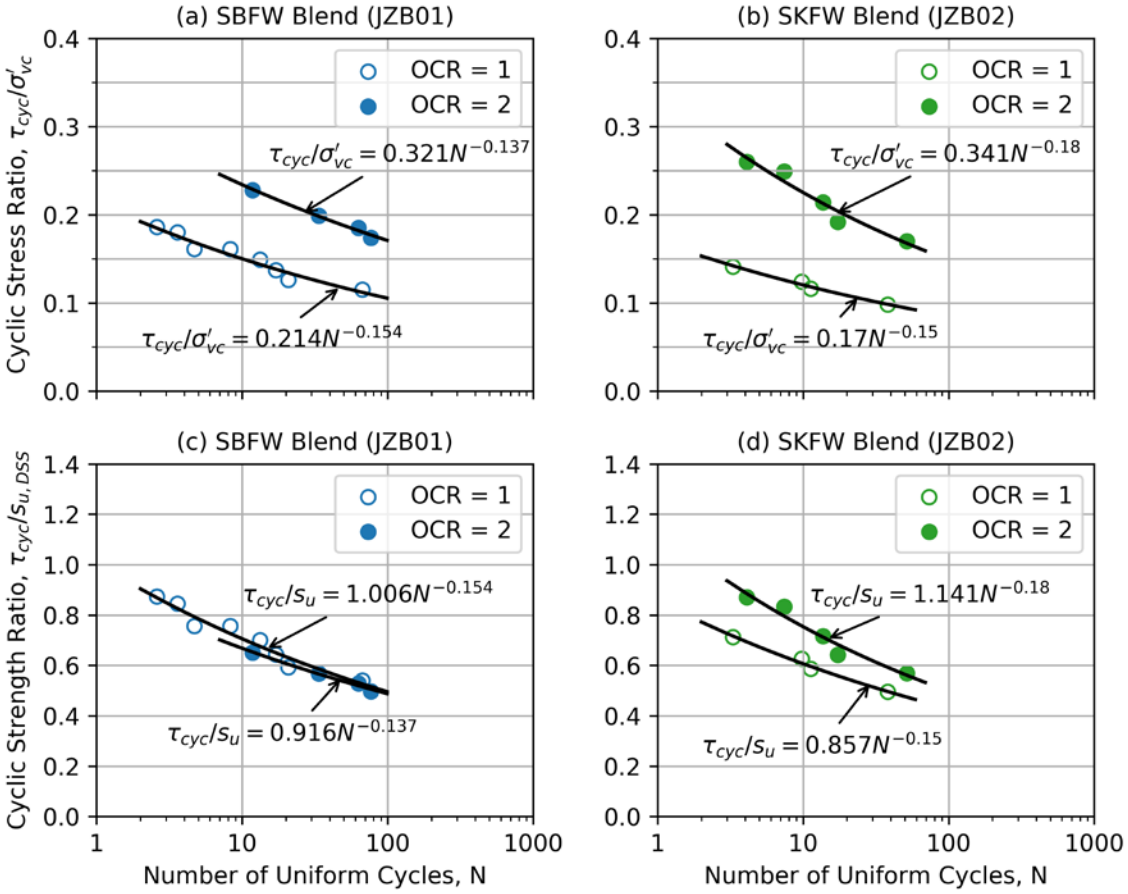

Figure 13: Cyclic Stress Ratio and Cyclic Strength Ratio Curves (Eslami, 2017)

Eslami (2017) performed cyclic DSS testing under uniform sinusoidal stress controlled conditions at a frequency of 0.1 Hz under a consolidation stress of 50 kPa. He judged specimens to reach cyclic failure at a peak shear strain of 3 percent.

Data used to develop the CSR and cyclic strength ratio curves may be restated in deviatoric strength terms as DSR using the conversion procedure summarized in Section 3.2. The conversion requires the assumption of K_o because this value was not measured during DSS testing. Because K_o is an effective stress parameter and DSR is calculated in total stress terms here, the conversion instead uses Poisson's ratio, ν as an input and calculates K_o using the expression $K_o = \nu/(1-\nu)$. This expression for K_o is only valid if the soil behaves elastically and is loaded vertically with zero horizontal strain, which may not be realistic here. The conversion therefore assumes a range of ν values to demonstrate the relative insensitivity of calculated DSR to the underlying K_o or ν assumption. Here K_o and ν correspond to the consolidated stress state before cyclic loading, meaning soil behavior is unlikely to be undrained (e.g. $\nu < 0.5$). Undrained soil behavior (e.g. $\nu \sim 0.5$) is likely to occur during cyclic loading, but only the consolidated stress condition and soil behavior is applicable to the lab data conversion presented here because $\Delta\sigma_{xx} = \Delta\sigma_{yy} = 0$.

To convert the DSS data, I first calculated q_o in accordance with Equation (3-31). Then I evaluated the monotonic term q_f from $s_{u,DSS}$ using Equation (3-32) and the cyclic term q_{cyc} from τ_{cyc} using Equation (3-33). Finally, I calculated DSR using Equation (3-29) with $q = q_{cyc}$. Cyclic strength is conventionally expressed as a function of the number of loading cycles using a CRR curve, which is expressed as a power law function of the form aN^{-b} that is fit to the CSR data. Deviatoric strength may analogously be expressed as DRR based on Equation (3-36), which is a function of the form cN^{-d} that is fit to DSR data. Because of the q_o term in the DSR equation, the aN^{-b} function cannot easily be converted directly into a deviatoric expression. I instead performed curve fitting that re-regress the power law relationship directly to the DSR data using a non-linear least squares regression. Figure 14 presents the regressed DRR curves for a range of ν values for data

from Figure 13. Only data for the SBFW blend at $OCR = 1$ and the SKFW blend at $OCR = 2$ is presented in the figure because these OCRs are closest to the JZB01 and JZB02 OCRs during centrifuge testing.

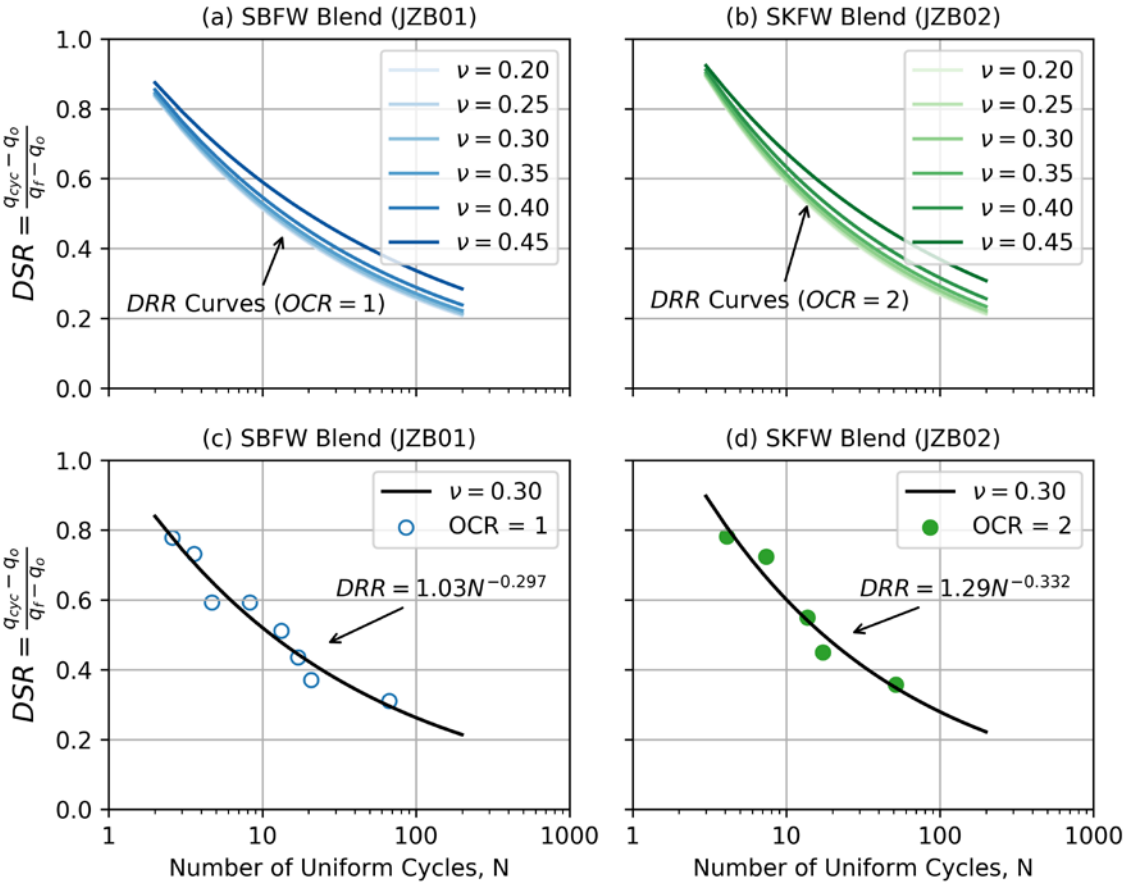

Figure 14: Deviatoric Conversion of DSS Laboratory Data

Note the relative insensitivity of the DRR curves to ν for a given OCR, with the exception of the nearly undrained behavior associated with $\nu = 0.45$ that is distinct from the body of curves. As previously indicated, the specimen stress state is unlikely to be undrained during the phase of DSS testing that requires the ν assumption, which is during initial consolidation to facilitate the calculation of q_o. The ν value at the end of the DSS consolidation phase is likely to correspond to ν of 0.2 to 0.4. This indicates the ν assumption is unlikely to significantly impact analysis results.

Based on these results, I selected $\nu = 0.3$ and developed DRR curves for each blend at each corresponding OCR. Figure 14 presents DRR curves for the SBFW blend at $OCR = 1$ and the SKFW blend at $OCR = 2$. Figure 15 presents DRR curves for both blends at both OCR levels, as well as the original cyclic strength ratio data from Eslami (2017) presented in Figure 13. The DRR curves display the same general trends as the cyclic strength ratio data.

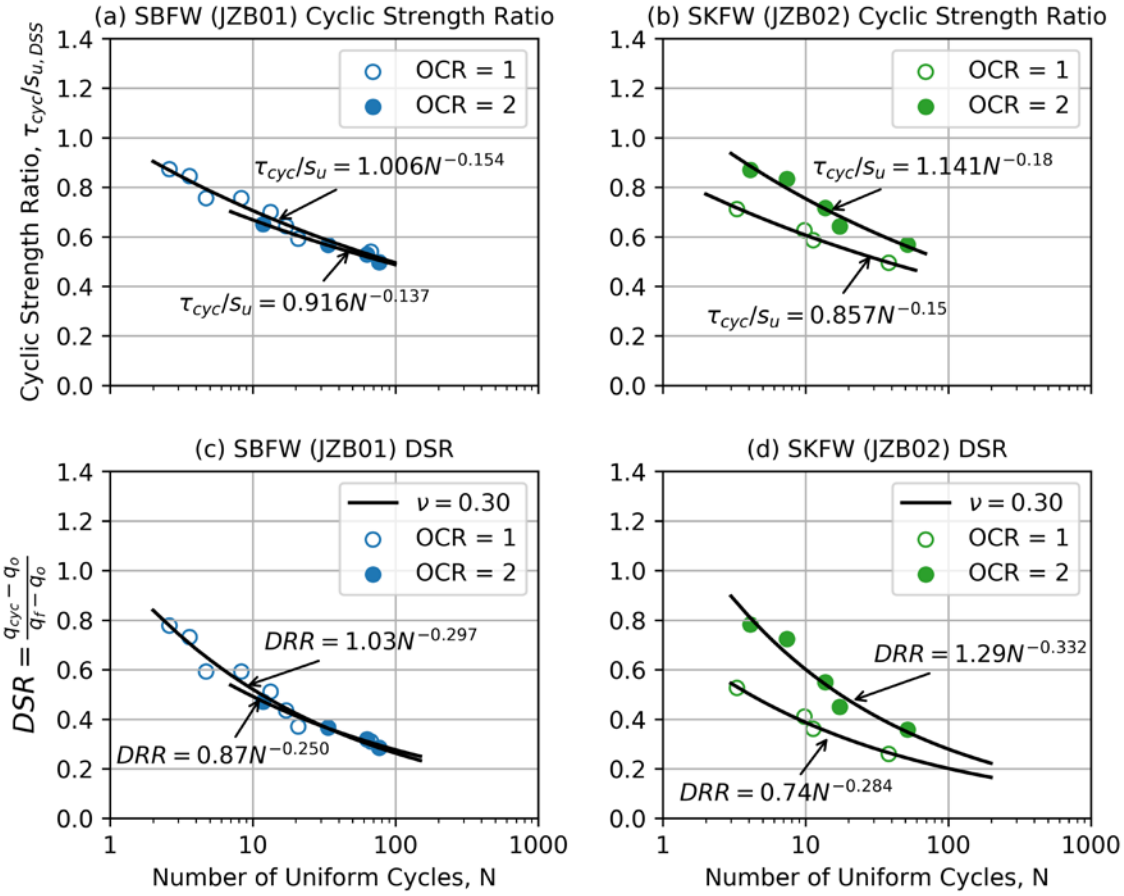

Figure 15: Deviatoric Resistance Ratio Trends from Cyclic Strength Ratio Data

4.3 STRAIN-DEPENDENT DEVIATORIC STRENGTH RATIO

CSR and cyclic strength ratio values reported by Eslami (2017) correspond to a cyclic shear strain, γ_{cyc} of 3 percent. DRR curves calculated from that data therefore also correspond to $\gamma_{cyc} = 3\%$. DRR curves can be developed for alternative strain levels by reprocessing the data as DSR in terms of the desired strains. The motivation for developing DRR at alternative strain levels is to facilitate evaluation of strain from induced stress demand. Evaluated strain can then be used to form an index that provides a proxy of structure performance defined as induced displacement or rotation. Chapter 10 presents procedures for calculating cyclic shear strain from the proposed deviatoric stress framework and strain-based displacement indices developed for the purpose of evaluating structure performance.

4.3.1 Original Cyclic Direct Simple Shear Data by Eslami (2017)

Figure 16 and Figure 17 present data from the cyclic DSS tests for the SBFW and SKFW blends, respectively, by Eslami (2017). Data presented in the figures is the original, unmodified data from the DSS testing published by Eslami (2017). The data consists of stress-strain loops presented as CSR plotted versus γ_{cyc} and strain response over time presented as γ_{cyc} plotted versus N. The full dataset for the SBFW and SKFW blends is presented in Appendix A. The CSR versus γ_{cyc} plot indicates CSR is not constant for a given test. Rather, the CSR versus γ_{cyc} plot indicates a decrease in CSR at high strains. Even at low strains, the CSR is rarely constant, as positive and negative stress loops typically peak at different CSR values. The lack of a consistent CSR is likely due to difficulties associated with the DSS equipment maintaining stress control during testing. The γ_{cyc} versus N plot indicates an increase in strain with number of cycles for both clays,

but a markedly shaper increase for the SKFW blend. This effect is indicative of behavior of the respective clay blends and is discussed at the end of this section.

I developed the following procedure to streamline reprocessing DSS data over a range of strains:

1. Identify local maxima or minima in the CSR versus γ_{cyc} data along with corresponding points in the γ_{cyc} versus N dataset. These points are identified as "Peaks" in Figure 16 and Figure 17. Although the term "peak" is typically a time domain designation, the term is used here to identify local maxima or minima in the datasets for simplicity. Note that the corresponding γ_{cyc} versus N points are often near the local peak γ_{cyc}, but rarely correspond to actual peak γ_{cyc}. The largest differences in peak CSR and peak γ_{cyc} occur at high strains.
2. Fit a 6th-order polynomial curve to the γ_{cyc} versus N peaks and a 2nd-order polynomial curve to the CSR versus γ_{cyc} peaks using least squares regression. Fit curves to both positive peaks and negative peaks. See the lines designated "Fit" in Figure 16 and Figure 17.
3. Calculate CSR and N at the desired strain levels using the polynomial functions.
4. Plot calculated CSR versus N. Regress CRR curves by fitting $CRR = aN^{-b}$ functions to the CSR versus N datapoints. See Figure 18.
5. Convert CSR to DSR in accordance with the procedure outlined in Section 4.2.
6. Plot DSR versus N. Regress DRR curves by fitting $DRR = cN^{-d}$ functions to the DSR versus N datapoints. See Figure 18.

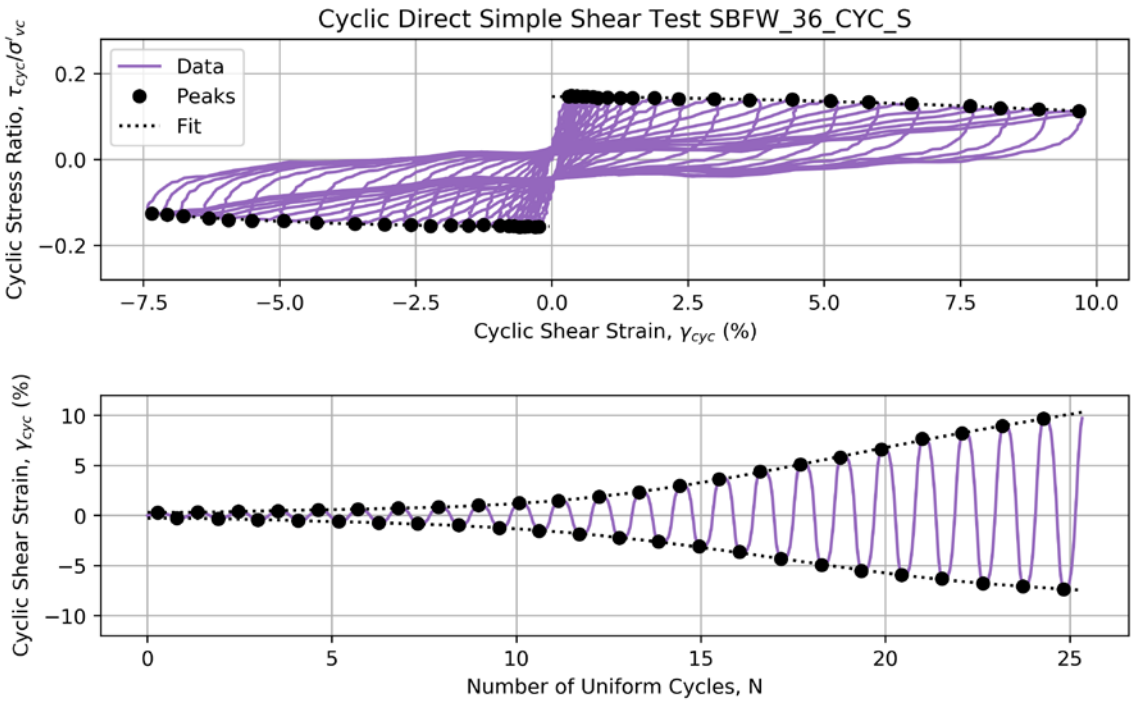

Figure 16: SBFW Cyclic Direct Simple Shear Curve Fitting on Original Data

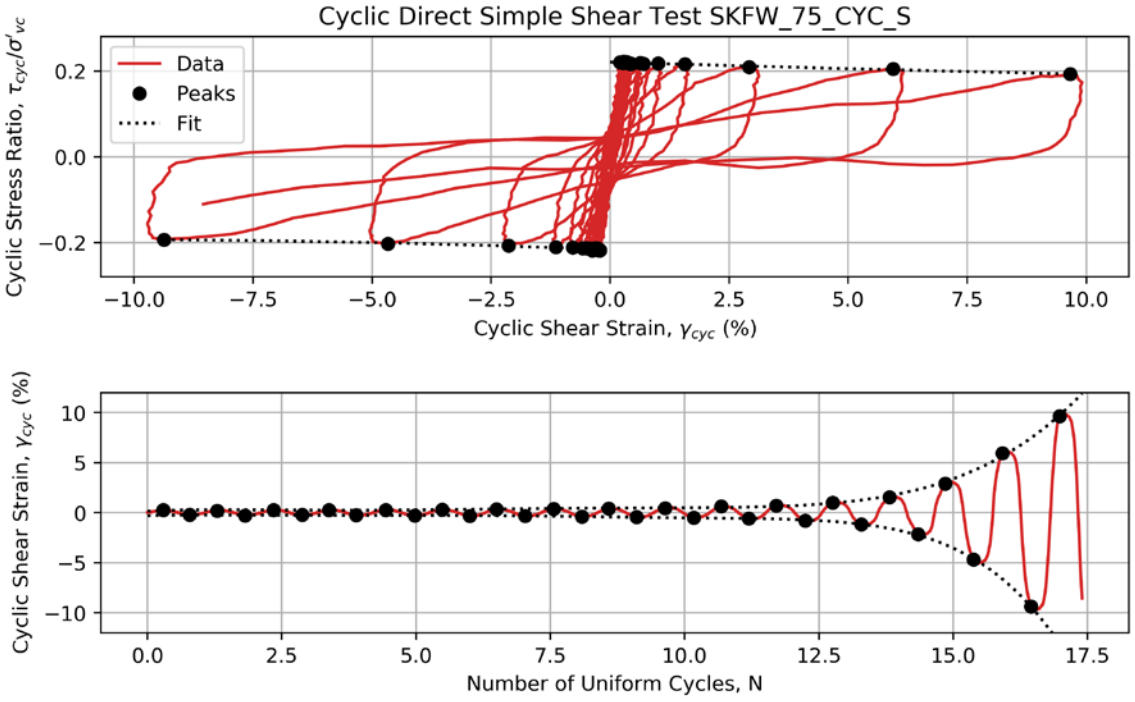

Figure 17: SKFW Cyclic Direct Simple Shear Curve Fitting on Original Data

This procedure was performed twice on the Eslami (2017) DSS dataset. Initial data reprocessing was performed on the original, unmodified version of the Eslami (2017) data, as presented in the figures in this section. Consistency issues during the fitting of strain-dependent CRR curves to the data prompted me to adjusted the CSR values for each test to a consistent value and then reprocess the data again, as presented in figures in the following section.

Figure 18 presents the datapoints and regressions that resulted from data reprocessing on the unmodified, original Eslami (2017) data. Table 1 summarizes the CRR and DRR regression coefficients. Note that data is only presented here for the $OCR = 1$ specimens for the SBFW blend and the $OCR = 2$ specimens for the SKFW blend because these OCRs most closely match OCRs in clay during centrifuge testing detailed later in this dissertation.

The regression coefficients developed here for $\gamma_{cyc} = 3\%$ are not a perfect match to the Eslami (2017) coefficients. Differences likely originate from the curve-fitting procedures used to develop CSR and N datapoints for each DSS test.

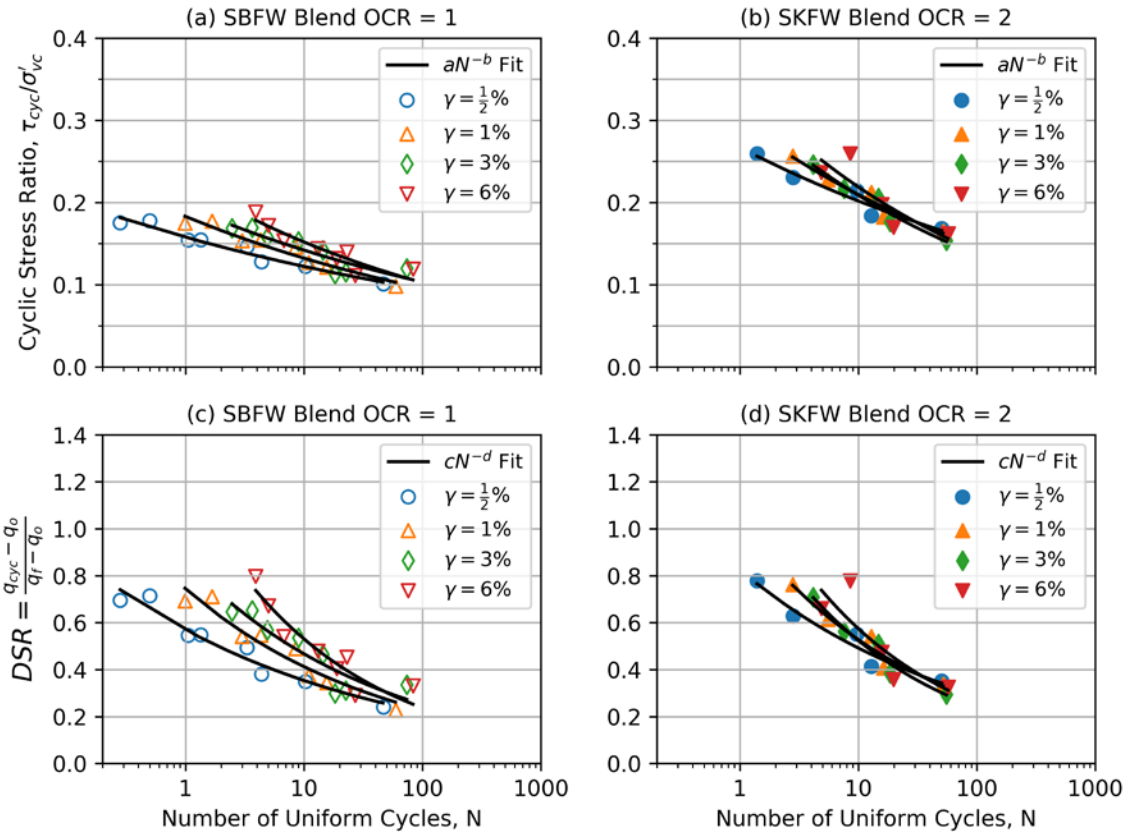

Figure 18: Cyclic Clay Strength Curves for Original Eslami (2017) Data

Table 1: Cyclic Clay Strength Coefficients for Original Eslami (2017) Data

Blend	*OCR*	*Strain*	*CRR Fit Parameters*		*DRR Fit Parameters*	
			a	***b***	***c***	***d***
SBFW	1	½	0.158	0.111	0.569	0.207
SBFW	1	1	0.183	0.141	0.745	0.256
SBFW	1	3	0.195	0.138	0.866	0.268
SBFW	1	6	0.225	0.171	1.189	0.35
SKFW	2	½	0.267	0.121	0.825	0.225
SKFW	2	1	0.299	0.154	1.017	0.285
SKFW	2	3	0.319	0.184	1.149	0.341
SKFW	2	6	0.342	0.194	1.285	0.35

The strain-based derivation of cyclic strength provides insight into behavior of the SBFW and SKFW blends. Note that CRR and DRR curves for various strains in Figure 18 are distinct for the SBFW blend, but tightly bunched and less distinguishable for the SKFW blend. This configuration implies gradual strain accumulation in the SBFW blend, but rapid strain accumulation in the SKFW blend. Gradual strain accumulation is indicative of clay-like soil behavior that is likely to be susceptible to cyclic softening ground failure. Rapid strain accumulation is more sand-like, with cyclic behavior that more closely resembles liquefaction triggering. The SKFW blend should not be interpreted as a sand-like material, but rather as more sand-like than the SBFW blend. Further, the SKFW behavior, although fundamentally clay-like, is likely to experience a triggering-type mechanism during cyclic softening that follows the onset of rapid strain.

4.3.2 Adjusted Cyclic Direct Simple Shear Data by Eslami (2017)

The variable CSR in the high-strain DSS data leads to systemic error in the derivation of CRR and DRR curves. To mitigate this error, I corrected the DSS data by adjusting data peaks to a test-specific base CSR, designated CSR_{base}, and an equivalent number of uniform cycles, N_{eq}. This data correction process is analogous to the conversion of a broadband ground motion time series into the equivalent number of uniform stress cycles at a consistent stress amplitude. This conversion process is detailed in Section 3.2.3 for the deviatoric stress framework proposed in this dissertation.

To perform the data correction, I took CSR_{base} as equal to the average CSR amplitude over the first 10 peaks of the CSR versus γ_{cyc} data. I then calculated N_{eq} for each peak in the CSR data, designated CSR_{pk}, using the N value corresponding to that peak, N_{pk}, as shown in Equation (4-3):

$$N_{eq} = N_{pk}\left(\frac{CSR_{pk}}{CSR_{base}}\right)^{1/b} \quad \textbf{(4-3)}$$

The corrected data peaks have a test-specific constant CSR amplitude equal to CSR_{base}, revised N values equal to N_{eq}, and unchanged γ_{cyc} corresponding to the original data. Equation (4-3) requires an input b parameter. I initially assumed $b = 0.135$ in accordance with Boulanger and Idriss (2007). I then checked the assumption by fitting aN^{-b} curves to the resulting CSR_{base} versus N_{eq} datapoints for the suite of DSS tests. I found that the output b from the fitted power law curves was dependent on both the blend and the strain level; however, output b was not sensitive to the assumed input b. To demonstrate the insensitivity, I varied assumed input b over the full range of output b, which caused the output b to change by only +/-0.002. I therefore assumed input $b = 0.135$ for the remainder of the data processing.

I then implemented the data processing procedure detailed in the previous section. Step 1 consisted of identifying peaks in the CSR_{base} versus cyclic shear strain, γ_{cyc} data along with corresponding points in the γ_{cyc} versus N_{eq} data. Step 2 consisted of fitting a 6th-order polynomial curve to the γ_{cyc} versus N_{eq} peaks using least squares regression. Note that no regression was necessary for the CSR_{base} versus N_{eq} data, because CSR_{base} is a constant for a given DSS test. Figure 19 and Figure 20 present data peaks and curve fits for the CSR-adjusted data for SBFW and SKFW blends, respectively, from Eslami (2017). The figures also indicate points on the γ_{cyc} versus N plot for the desired values of γ_{cyc} based on the polynomial curve fits.

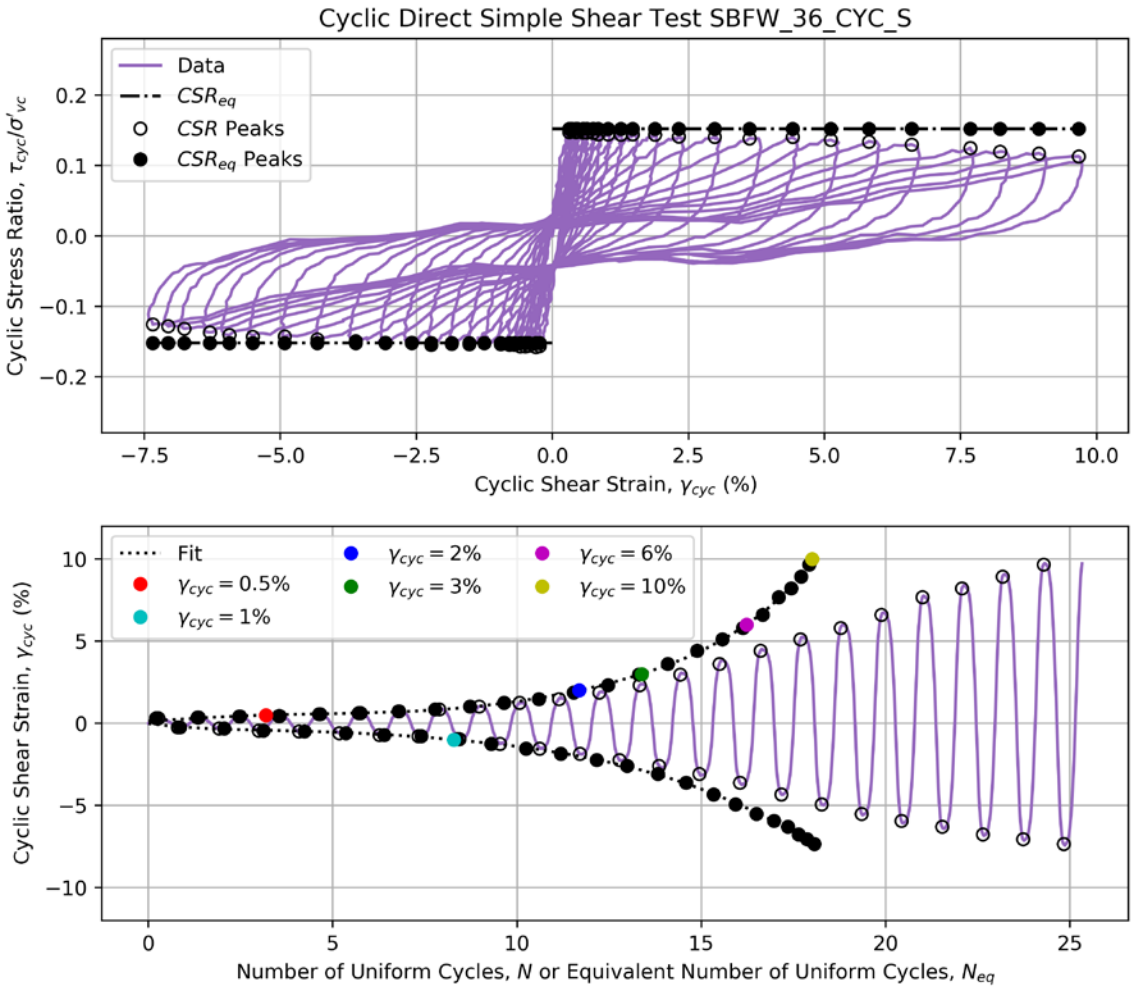

Figure 19: SBFW Cyclic Direct Simple Shear Curve Fitting on CSR-Adjusted Data

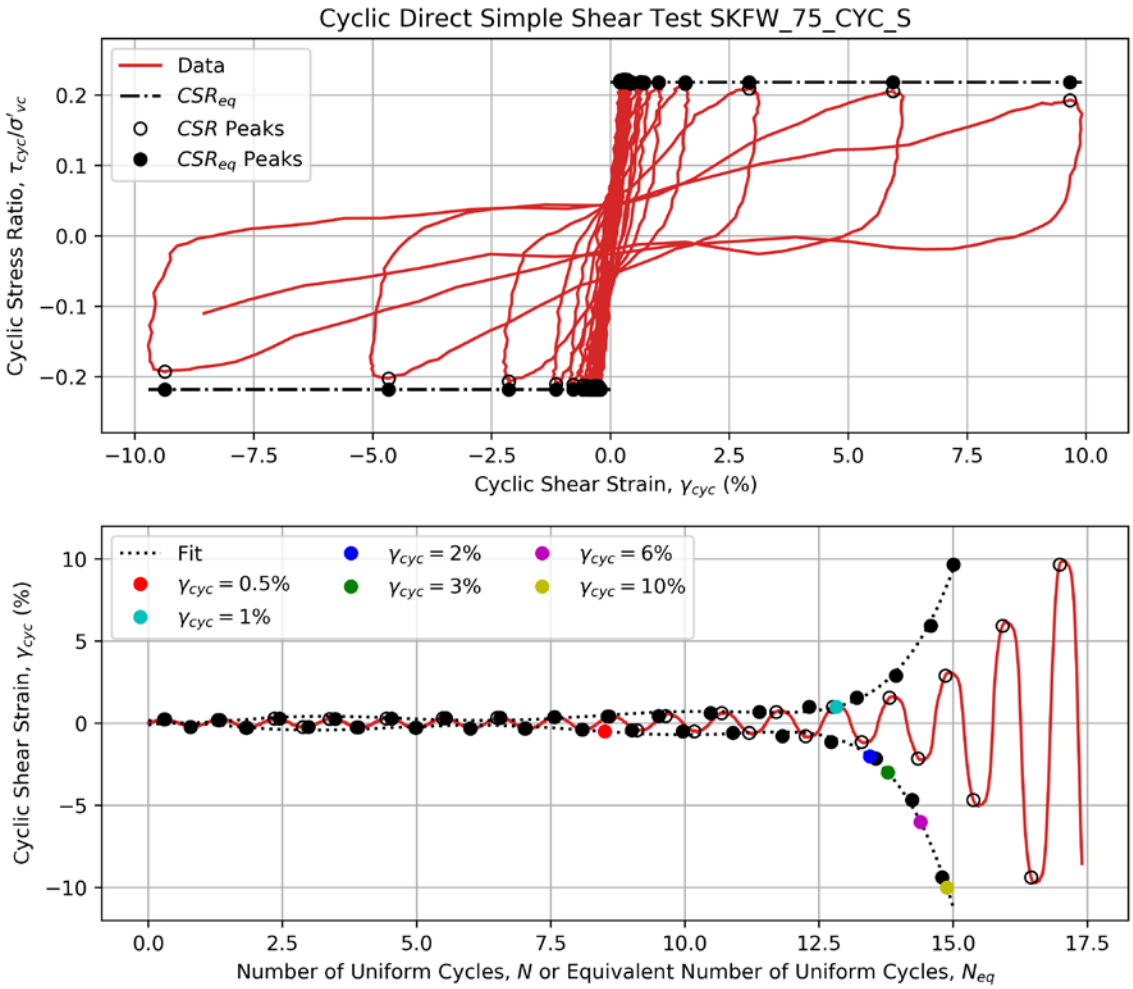

Figure 20: SKFW Cyclic Direct Simple Shear Curve Fitting on CSR-Adjusted Data

I processed data for the remaining cyclic DSS tests in a similar fashion to the above to populate the CSR and DSR datapoints. I then regressed CRR and DRR curves to the data for each strain level. Figure 21 presents the datapoints and regressions. Table 2 summarizes the CRR and DRR regression coefficients. Note that the curves and coefficients are similar, but not identical, to the curves and coefficients developed for the original Eslami (2017) data. Therefore, I used the curves and coefficients in Table 2 for the remainder of the cyclic softening analyses presented in this dissertation.

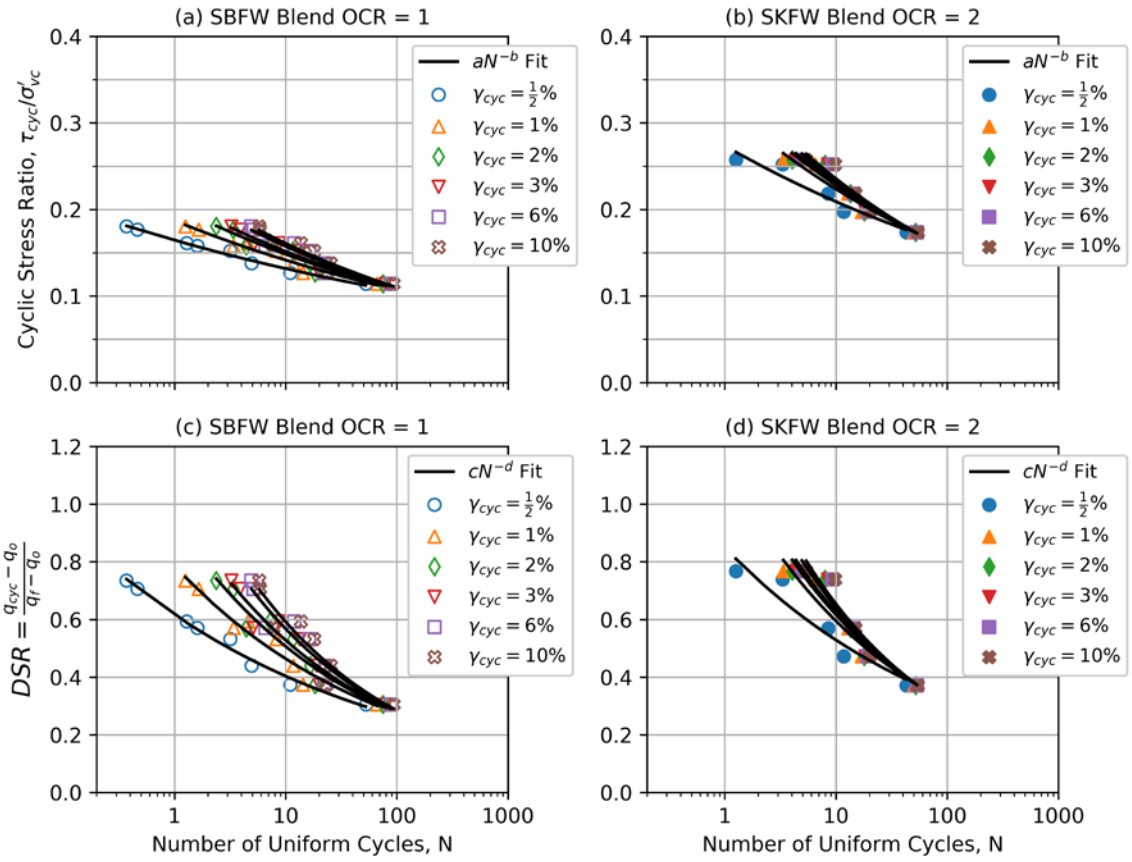

Figure 21: Clay Strength Curves for CSR-Adjusted Eslami (2017) Data

Table 2: Cyclic Clay Strength Coefficients for CSR-Adjusted Eslami (2017) Data

Blend	*OCR*	*Strain*	*CRR Fit Parameters*		*DRR Fit Parameters*	
			a	*b*	*c*	*d*
SBFW	1	½	0.165	0.097	0.616	0.184
SBFW	1	1	0.187	0.121	0.786	0.229
SBFW	1	2	0.204	0.139	0.933	0.265
SBFW	1	3	0.212	0.147	1.008	0.281
SBFW	1	6	0.227	0.160	1.151	0.307
SBFW	1	10	0.235	0.165	1.232	0.319
SKFW	2	½	0.273	0.117	0.849	0.206
SKFW	2	1	0.320	0.156	1.128	0.278
SKFW	2	2	0.334	0.166	1.221	0.297
SKFW	2	3	0.341	0.171	1.266	0.307
SKFW	2	6	0.352	0.179	1.345	0.322
SKFW	2	10	0.361	0.185	1.41	0.334

4.4 CYCLIC STRAIN FUNCTIONS

A key application of the strain-variable DRR curves presented in Figure 21 is to enable evaluation of strain as a function of DRR and N. Direct calculation of strain from given inputs facilitates rapid analysis of the cyclic softening evaluation. Analyses can be run repeatedly to develop strain contour plots below structures to analyze ground failure potential. Strain could conceivably be integrated over a given interval to evaluate displacement or develop index parameters that provide a proxy of displacement. The computational demand required to develop strain contour plots is high. Thousands of grid points are required to generate plots of sufficient density to enable contouring. It is therefore critical that the strain function be expressed simply and be easily evaluated without the aid of a solver. I developed strain functions here for the curves in Figure 21.

The c and d coefficients from the expression $DRR = cN^{-d}$ are interdependent, as shown in Figure 22 below. It is mathematically convenient to state the relationship between d and c in the form $10^{x_1+x_2 d}$, which allows for simplification of the expression for d in the power law relationship. See the derivation below:

$$\begin{aligned} log_{10}\left(cN^{-d}\right) &= log_{10} c - d\, log_{10} N \\ &= log_{10}\left(10^{x_1+x_2 d}\right) - d\, log_{10} N \\ &= x_1 + x_2 d - d\, log_{10} N = x_1 + d(x_2 - log_{10} N) \end{aligned} \qquad \textbf{(4-4)}$$

This expression results in the following equation for d:

$$d = \frac{log_{10} DRR - x_1}{x_2 - log_{10} N} > 0 \qquad \textbf{(4-5)}$$

Note that the range limitation stating that $d > 0$ is used to limit applicability of the expression to the usable range of the data. Figure 22 presents the x_1 and x_2 coefficients developed from a non-linear least squares regression to the c and d coefficients for the selected function.

The relationship between c and d allows γ_{cyc} to be expressed as a single parameter. I elected to express γ_{cyc} as a function of d for ease of implementation with the relationship between c and d. Figure 23 presents the γ_{cyc} and d datapoints. The functional form of the relationship is open to interpretation; however, I selected a power law relationship, such that the relationship yields visually reasonable results beyond the range of the given dataset. The relationship is expressed as:

$$\gamma_{cyc}(\%) = 0.25\% < x_3 + x_4 d^{x_5} < 10\% \qquad \textbf{(4-6)}$$

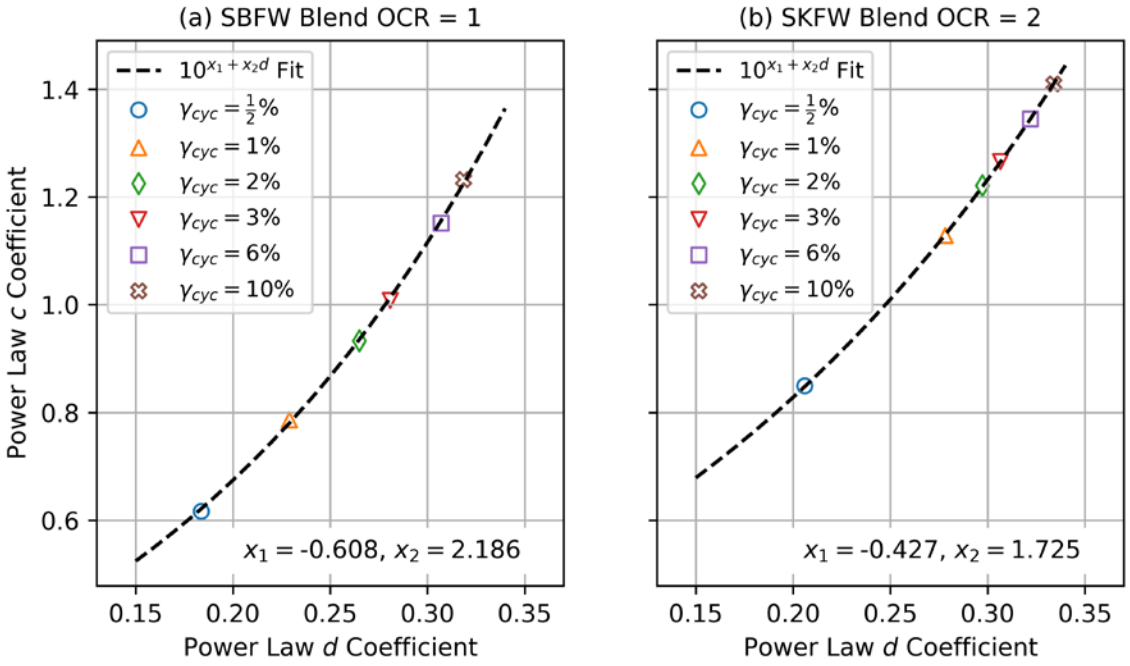

Figure 22: Relationship Between Deviatoric Power Law Coefficients

Figure 23 presents the x_3, x_4, and x_5 coefficients developed from a non-linear least squares regression. Strain is limited to a maximum value of 10%, which is consistent with the maximum strain data typically available from DSS testing. Strain is limited to a minimum value of 0.25% due to limitations in the DSS data, which would otherwise yield γ_{cyc} that does not converge to zero as d nears zero. Coupled with the expression for d above in (4-5), this limitation has the consequence of non-zero strain for the full range of input DRR and N values. Non-zero strain for even very low DRR and N suggests that the expression implies there will never be a point of zero strain for any inputs. This physical impossibility is an unfortunate trade-off for the computational efficiency gained in expressing γ_{cyc} in terms of c and d and using simple functional forms for each curve fitting. Forcing the functional forms used above to converge on $\gamma_{cyc} = 0$ results in poor curve fits that are not representative of the data trends, particularly at low strains. More complex

expressions that relate γ_{cyc} directly to DRR and N were developed to overcome this limitation; however, the forms required a solver to evaluate γ_{cyc}, making the expressions computationally prohibitive. Further, the Eslami (2017) DSS test data is relatively sparse at $\gamma_{cyc} < 0.5\%$. Of the 21 total tests, nine have initial strain peaks that are greater than 0.25%, meaning data would have to be extrapolated to calculate N or N_{eq} at low strains and these values would consistently be less than one. The twelve tests with initial strain peaks that are less than 0.25% are generally low CSR tests, meaning data would not exist for higher CSR values at $\gamma_{cyc} < 0.25\%$ without extrapolation, casting doubt on the viability of strain relationships derived from this data. For practical purposes here, subsequent cyclic softening evaluations assume $\gamma_{cyc} < 0.25\%$ as effectively zero.

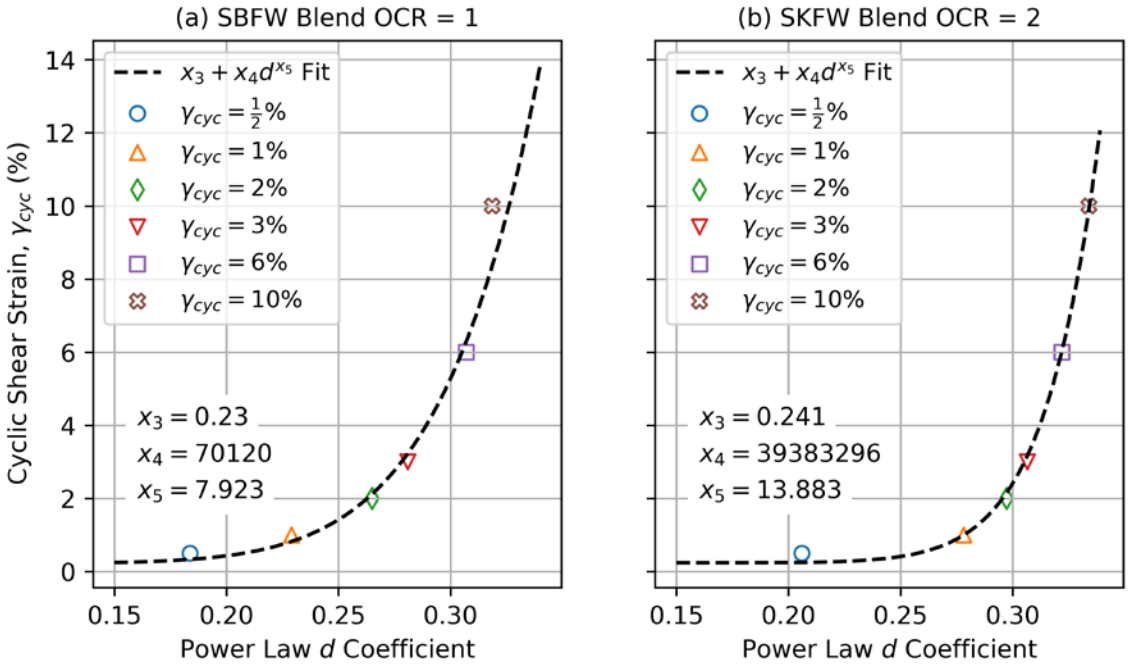

Figure 23: Relationship Between Cyclic Shear Strain and d Coefficient

5 CENTRIFUGE TEST JZB01

I performed centrifuge test JZB01 at the CGM from July 17, 2017 to February 12, 2018. The JZB01 model consisted of sand underlying a bentonite-based surficial clay with the three structures described in Chapter 7 founded on the clay deposit. I collected data during testing using 113 instruments installed in soil layers, mounted on structures, and mounted on the exterior of the model container. Figure 24 presents the JZB01 model profile configuration and instrumentation.

This chapter summarizes the JZB01 model construction, testing, and data collection; however, details are omitted for brevity. The JZB01 data report (Buenker et al., 2019) provides additional information on the test program, including details omitted here. The report is available through DesignSafe-CI, which is a collaborative multi-disciplinary cyber infrastructure hosted by the National Hazards Engineering Research Center through the University of Texas at Austin.

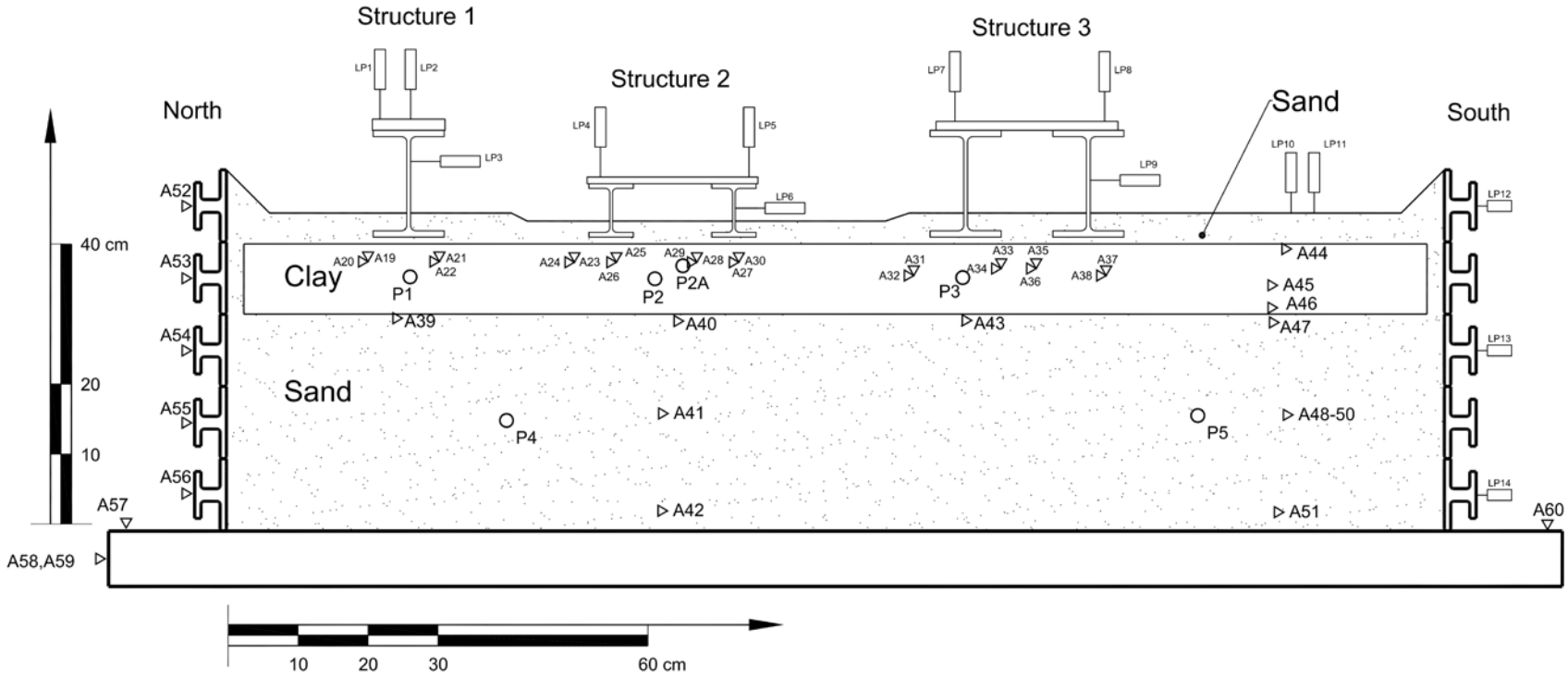

Figure 24: JZB01 Model Configuration

5.1 INSTRUMENTATION

Instrumentation installed to measure the model response included ICP accelerometers, MEMS accelerometers, linear potentiometers (LPs), pore pressure transducers (PPTs), and strain gauges. Strain gauges were affixed to the model structures and are discussed in more detail later. ICP accelerometers are designated with a prefix “A-”, MEMS accelerometers with a prefix “M-”, LPs with a prefix “LP-“, and PPTs with a prefix “P-“ followed by a sensor number in the model profile figure.

ICP accelerometers consisted of Model 352 accelerometers by PCB Piezotronics, which were oriented to measure acceleration about the long axis of the accelerometer. ICPs were coated with waterproofing and embedded in the soil profiles, while uncoated ICPs were also affixed to the exterior of the model containers. MEMS accelerometers were mounted to the structures in addition to ICPs. The ICPs are bandwidth-limited, and cannot directly measure static tilt, whereas the MEMS accelerometers can be used as tilt sensors in addition to measuring dynamic response during shaking.

LPs consisted of 600 Series Linear Position Sensors by BEI Sensors. I installed LPs to measure horizontal and vertical displacements of structures, vertical displacements of the ground surface in the far field, and horizontal displacements of HPC model container rings. LP stroke ranged from 1 to 6 inches depending on the application. Because the ICPs are bandwidth limited, LPs were co-located with ICPs to quantify the low frequency portion of the model response.

PPTs consisted of 2Mie transducers by Keller. I installed PPTs to measure pore water pressure in sand and clay layers. I removed porous stones from PPTs prior to use and cleaned both the transducer housing and porous stones with alcohol. I then installed porous stones in the PPTs under vacuum and kept the assembled transducer submerged

in water until calibration. I calibrated PPTs against the master high-resolution PPT at the CGM. I then kept PPTs submerged in water until installation in the model.

5.2 MODEL CONTAINER

I constructed the model in the CGM's hinged-plate container (HPC). The HPC consists of a solid base with rigid side walls along the long axis and annular ring assemblies that form the short axis walls. The base, side walls, and annular rings are aluminum. The container derives its name from the hinged annular rings, which are positioned on runners mounted to grooves in the rigid walls. The rings exhibit low shear stiffness and may be deformed by hand when empty. The container includes a water-tight rubber liner installed in the container interior. The liner consists of 1/8-inch thick rubber that CGM staff bolted and sealed to the bottom of the container. I used clamps to fit the liner taught against the container sides prior to soil deposition. The container also includes shear rods installed at the long ends of the container to reduce boundary effects. Figure 25 presents a graphic of the container. Figure 26 presents a photo of the container.

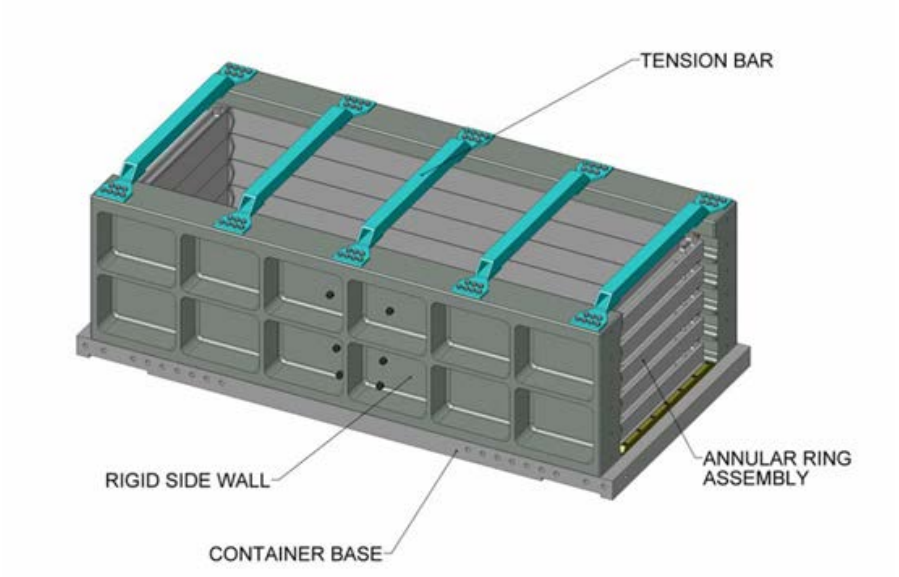

Figure 25: Hinged Plate Container Graphic

Figure 26: Hinged Plate Container Photo

5.3 PORE FLUID

All pore fluid used to construct model JZB01 consisted of deionized water. Water was selected as the pore fluid over methylcellulose or other viscosity-scalable fluid, because the object of this centrifuge study is to evaluate cyclic clay behavior that is likely to be undrained during ground shaking. Because viscosity is scalable during centrifuge testing, material behavior dependent on pore fluid flow (e.g. liquefaction) may not be captured by this model. Model sand behavior during dynamic shaking is likely to be unrealistic due to rapid drainage caused by the absence of a viscosity-scalable pore fluid.

Water was maintained at the model surface following saturation of the base sand and throughout deposition of the clay. Water was then maintained at the approximately bottom of footing level following the placement of surficial sand.

5.4 SOIL

The JZB01 model soil profile consisted of bentonite-based clay overlying sand, as shown in Figure 27. I deposited sand at greater than 90% relative density to prevent liquefaction. I intended the sand to provide drainage at the bottom of the clay during consolidation. I selected the clay layer thickness such that Prandtl-based failure wedges generated by potential bearing capacity failure mechanisms would occur solely within the clay zone. I also placed a thin (~1cm) layer of hand-deposited sand at the clay surface, such that our structures did not create suction by resting directly on the clay. I deposited the surficial sand by hand and the sand was not placed with density control. Sand was also used to form vertical sand drains along the north and south ends of the clay layer. The sections below summarize soil properties and depositional methodology associated with each soil type.

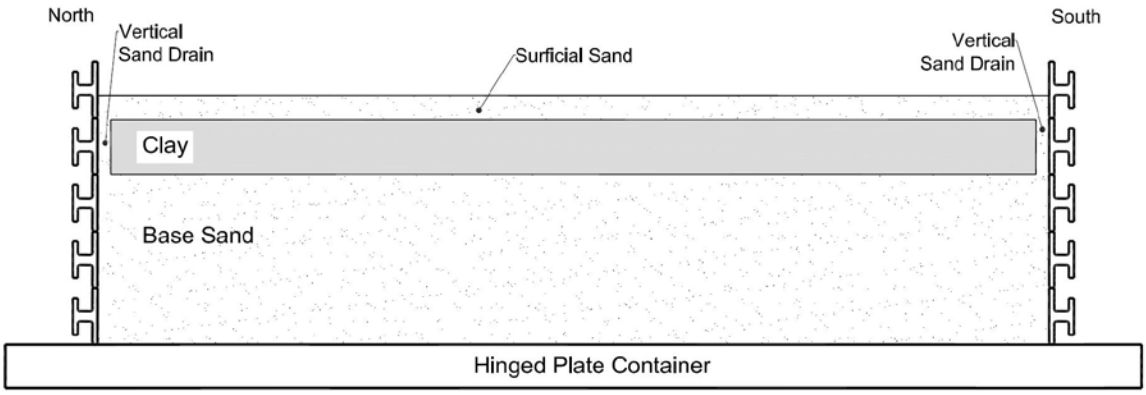

Figure 27: JZB01 Soil Profile

5.4.1 Sand

Sand consisted of F-65 Ottawa sand, which is a uniformly graded quartz sand composed of naturally grounded grains. The CGM developed standardized properties of F-65 Ottawa Sand based on a series of laboratory tests (Bastidas, 2016). The standardized properties

include values for maximum void ratio, e_{max}, minimum void ratio, e_{min}, and specific gravity of solids, G_s:

I deposited sand below the clay using a variable speed pluviator. Depositional density of the sand depends on pluviator speed, drop height, and drum grooving pattern. I calibrated the pluviator to select pluviator speed and drop height needed to generate high depositional sand density. Sand above the clay and to the sides of the clay was placed by hand without using the pluviator.

5.4.1.1 Pluviator Calibration

I calibrated the pluviator by evaluating sand density deposited by the pluviator at various speeds and drop heights. I performed the calibration by depositing sand in a small steel mold of known volume (13,680 mL), as shown in Figure 28.

Figure 28: Sand Pluviation

I measured the mass of sand, M_s deposited in the steel mold. I calculated the volume of sand, V_{sand} deposited in the mold as:

$$V_{sand} = \frac{M_s}{\rho_s} = \frac{M_s}{G_s \rho_w} \quad \textbf{(5-1)}$$

The unit density of water, $\rho_w = 998\frac{kg}{m^3}$. I then calculated void ratio, e of the deposited sand:

$$e = \frac{V_V}{V_s} = \frac{V_T - V_{sand}}{V_{sand}} \quad \textbf{(5-2)}$$

V_T equals the volume of the steel mold indicated above. I then calculated sand relative density, RD:

$$RD = \frac{e_{max} - e_s}{e_{max} - e_{min}} \quad \textbf{(5-3)}$$

I used e_{max} and e_{min} values consistent with Bastida (2016). I first calibrated the pluviator for a drop height of 40 inches at all available pluviation speeds. I then repeated the calibration for a drop height of 28 inches, until I determined that the 28-inch drop height yielded consistently lower relative density than the 40-inch drop height. Figure 29 presents our calibration data.

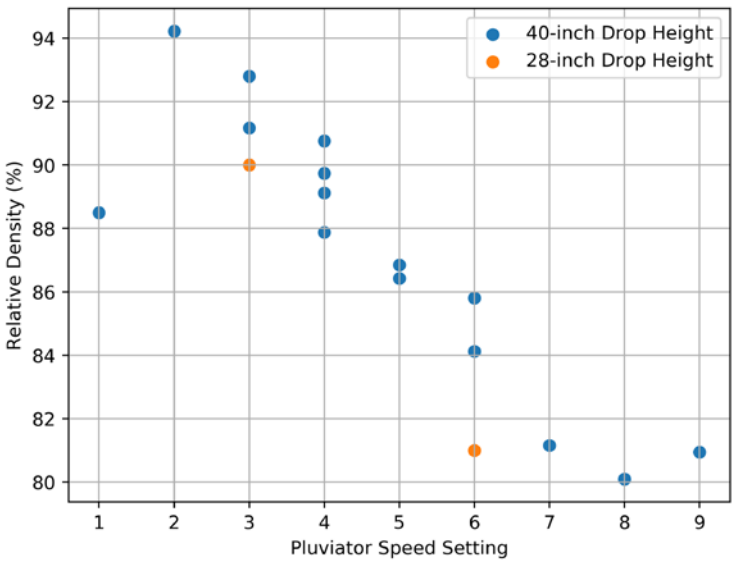

Figure 29: JZB01 Sand Pluviator Calibration

5.4.1.2 Deposition

I deposited sand in our model at pluviation speed Setting 3 with a 40-inch drop height to achieve approximately 92 percent relative density, in accordance with Figure 29. I deposited sand in lifts, with a maximum lift height of 5 cm. Following each lift, I removed surface inundations or mounding using a shop vacuum to create a flat sand surface for subsequent lifts.

I saturated the sand by adding 112 liters of deionized water over three days. I added water using a hose that dripped water onto a sponge that was situated on the sand surface. The intent of the sponge was to seep water into the sand without disturbing the sand surface. I regulated water flow such that the sponge remained moist, without allowing water to accumulate and flow from the sponge across the sand surface. I maintained a level container during saturation. I terminated saturation when I observed standing water on the sand surface.

5.4.2 Clay

Clay consisted of a synthetic soil blend composed of 5 percent bentonite and 95 percent SIL-CO-SIL #45 ground silica. The original intent was for clay in model JZB01 to match the SBFW soil blend developed by Eslami (2017); however, laboratory testing on the clay performed after the JZB01 centrifuge testing indicated the JZB01 clay differed significantly from the target blend. The difference existed because of use of an alternative bentonite source from the UCLA lab.

5.4.2.1 Laboratory Testing

I performed Atterberg limits and consolidation laboratory tests to characterize properties and behavior of the JZB01 clay and compare them to the Eslami SBFW blend. Figure 30 presents Atterberg limits test results. Figure 31 presents consolidation test results.

Permeability, k and coefficient of verical consolidation, c_v in Figure 31 are only plotted in the compression range. Table 3 summarizes laboratory test results for each clay blend, with compression, recompression, and permeability indices, $C_c, C_r,$ and C_k, respectively, selected using the data in Figure 31.

The laboratory testing indicates the JZB01 clay is more plastic then the Eslami SBFW clay, with slower consolidation times by an order of magnitude. Clay compressibility is similar. These laboratory test results match our observations during consolidation of the JZB01 clay, as summarized in Section 5.4.2.3, which indicated very slow consolidation times for the JZB01 clay.

A limiting feature of the clay not previously identified before centrifuge testing was that the clay tended to swell when submerged in water, if not under continuous overburden pressure. Swelling tended to negate the effects of consolidation stress history and drastically reduced strength developed as a result of consolidation. Figure 31 Subplot (d) presents consolidation results demonstrating the effect of clay swell. The JZB01-3 (Initial Test) consolidation curve consists of a load-unload-reload sequence. Following this sequence, all consolidation load was removed from the sample and the sample was allowed to remain submerged in water in the consolidation press for about 48 hours. Following the soak, consolidation load was then added to the press. The JZB01-3 (Post-Soak) curve is the sequence following the reapplication of load. As indicated, the clay exhibits a normally-consolidated behavior that is not indicative of the stress history previously applied during the consolidation test. The consolidation stress applied during Stage 10 was 23 kPa, meaning the maximum past pressure, σ_p experienced by the clay post-swell must be less than this value. The swelling behavior was not identified until after centrifuge testing.

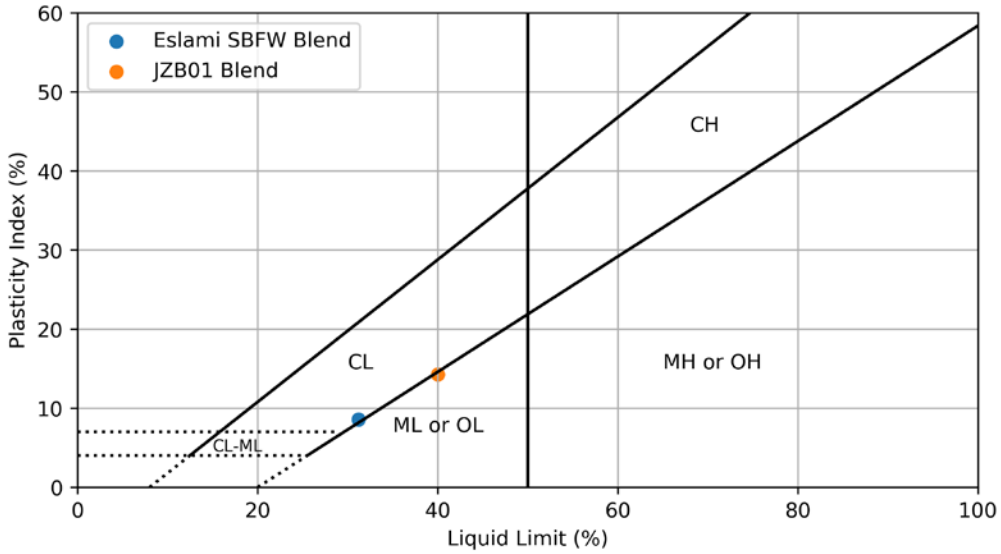

Figure 30: JZB01 Clay Atterberg Limits

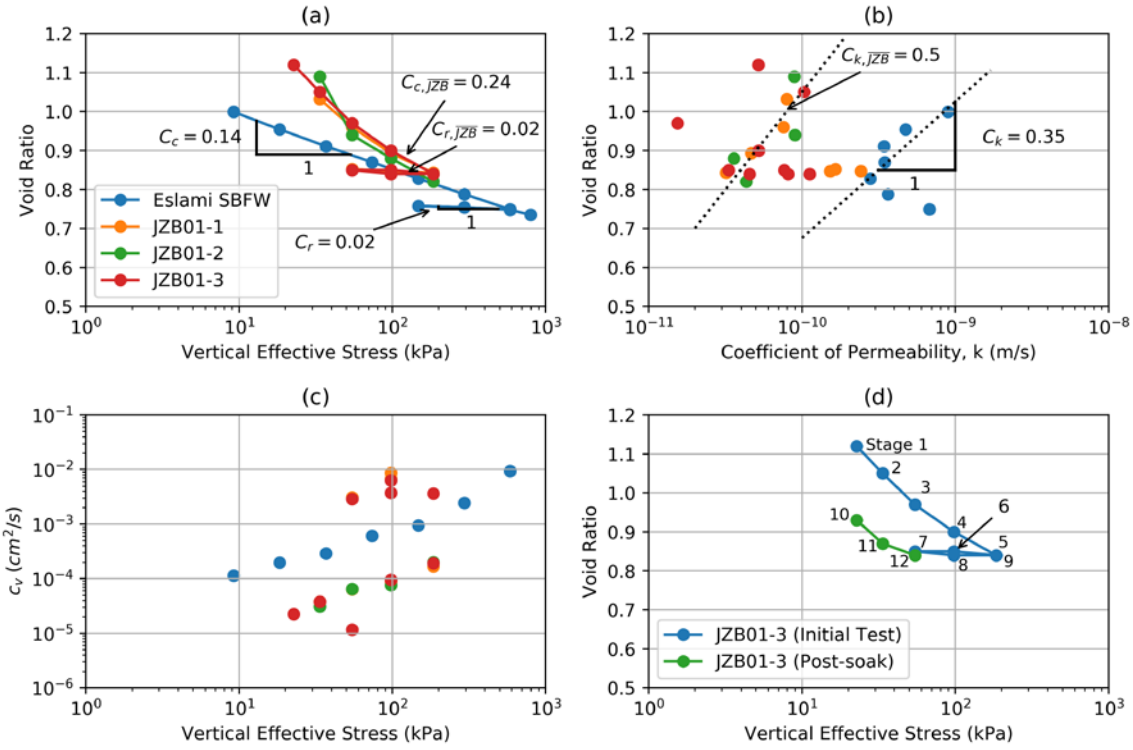

Figure 31: JZB01 Consolidation Testing

Table 3: JZB01 Clay Properties

Clay	Liquid Limit, LL	Plastic Limit, PL	Plasticity Index, PI	Compression Index, C_C	Re-compression Index, C_r	Permeability Index, C_k
JZB01 Blend	40	26	14	0.16	0.01	0.37
Eslami SBFW Blend	31	23	9	0.14	0.01	0.09

5.4.2.2 Mixing and Deposition

I mixed clay in the CGM's industrial-strength mixer. I performed mixing by first adding SIL-CO-SIL #45 ground silica to the mixer with enough water to bring the material to the liquid limit of the full clay blend. I then added bentonite in small doses to avoid clumping in the mixture. I blended clay in the mixer for 10 hours. I then deposited clay in the model container in a single lift. I used a pneumatic pump to transfer the clay from the mixer to the model container. Prior to depositing the clay, I placed aluminum sheets at each end of the model container and backfilled the sheets with sand to create vertical drainage paths. I maintained these aluminum sheets in the container through clay deposition and consolidation to prevent migration of clay into the vertical drains. Figure 32 presents the clay deposition.

Figure 32: Clay Deposition

5.4.2.3 Consolidation Part 1

I consolidated the clay to create stress history and build strength in the clay deposit. The clay slurry is weak and prone to squeezing immediately after mixing and deposition; therefore, I performed preliminary consolidation using dead weight from overburden sand. I placed overburden sand by building sideboards around the top of the model container and filling enclosed space with sand. I added sand to the model equivalent to 5.6 kPa overburden pressure at the clay surface. I allowed pore pressure dissipation under the sand overburden for 3 days. I then removed the sand and placed a layer of geosynthetic and filter paper over the clay.

I performed subsequent consolidation using the hydraulic press. The hydraulic press consists of two hydraulic actuators connected to a steel plate, as shown in Figure 33. Each actuator is independently controlled and operated. The actuators are connected to a

feedback system that maintains a target pressure in the actuator that is controlled by an operator.

I evaluated degree of consolidation in the clay by monitoring pore water pressure using PPTs and settlement using LPs. I installed PPTs in the clay at the locations shown in Figure 34 and LPs over the steel press plate. Figure 35 presents pore pressure, settlement, and target loads during consolidation beginning October 26, 2018. The target load is approximate, as the feedback system used to control pressure applied by the press may vary by +/- 2kPa or greater. The figure indicates an instance when clay material ejected from the model due to excessive overburden pressure applied by the press. I rapidly lowered overburden pressure after observing the material ejection.

I continued consolidation on the hydraulic press until November 4, 2017, when power failure at the CGM caused the hydraulic press to lose pressure in the actuators. When power returned, the press feedback system sought to rapidly equalize the target actuator pressure. The south actuator responded to the feedback system more quickly than the north actuator, which caused the steel plate connected to the actuators to plunge into the north side of the model, see Figure 36. The plunging plate caused the large-scale bearing capacity failure in the clay. Overburden pressure applied by the hydraulic press immediately prior to the power failure was about 80 kPa.

I repaired damage to the clay caused by the hydraulic press failure by cutting away chunks of intact clay using a steel trawl from the bearing failure wedge and placing them in the cavity generated by the bearing failure. I the smoothed and evened the surface of the clay with leftover clay from the original mix and water.

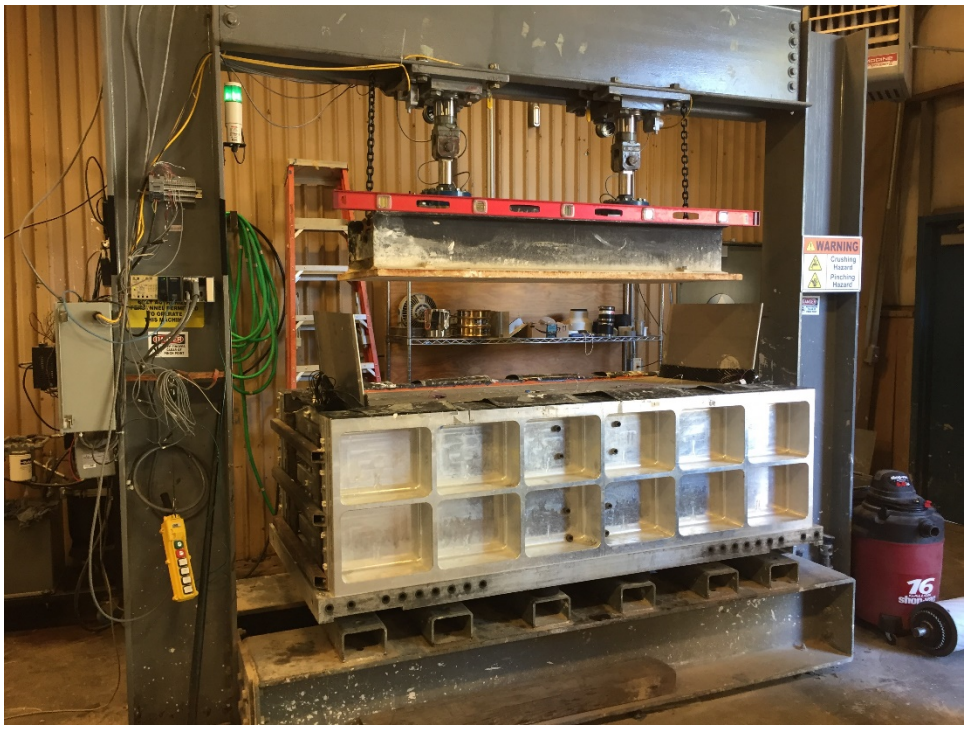

Figure 33: Consolidation using Hydraulic Press

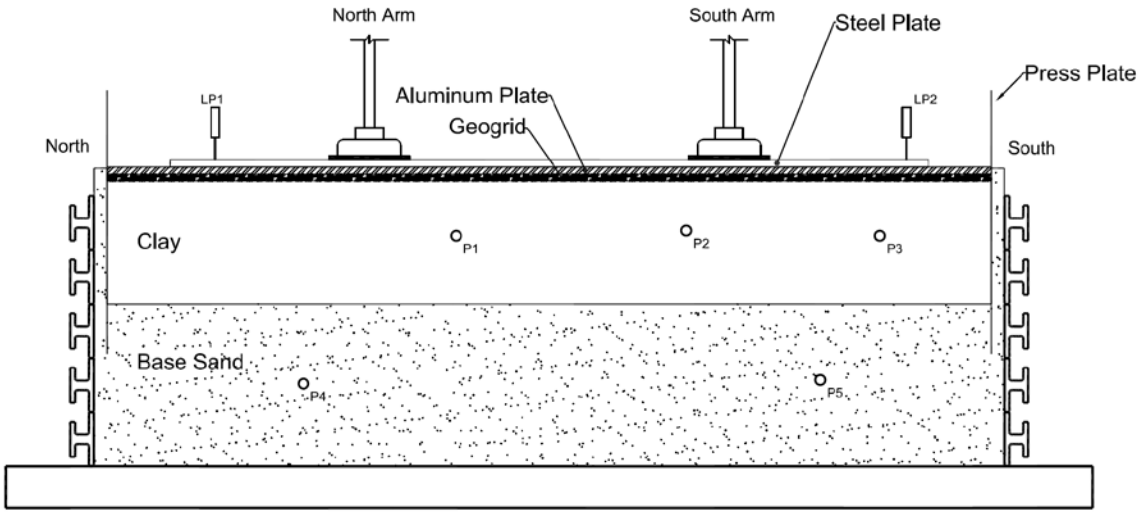

Figure 34: JZB01 Model Configuration during Clay Consolidation - Part 1

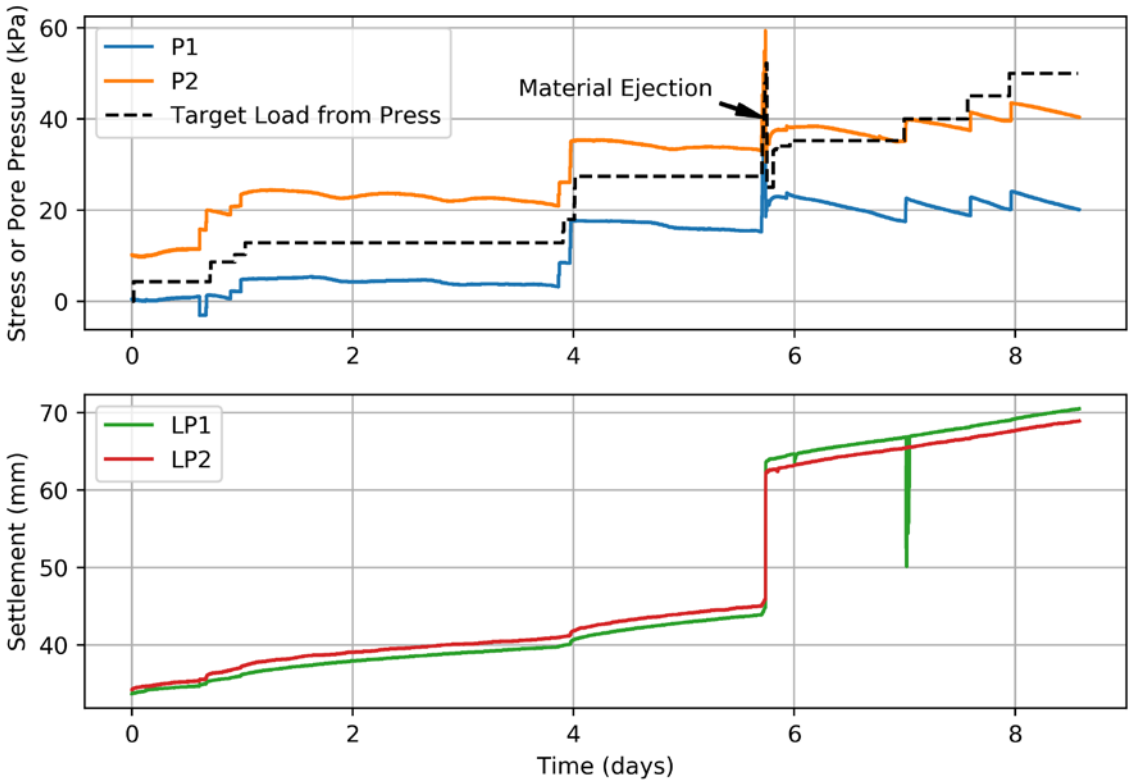

Figure 35: JZB01 Pore Pressure and Settlement during Clay Consolidation – Part 1

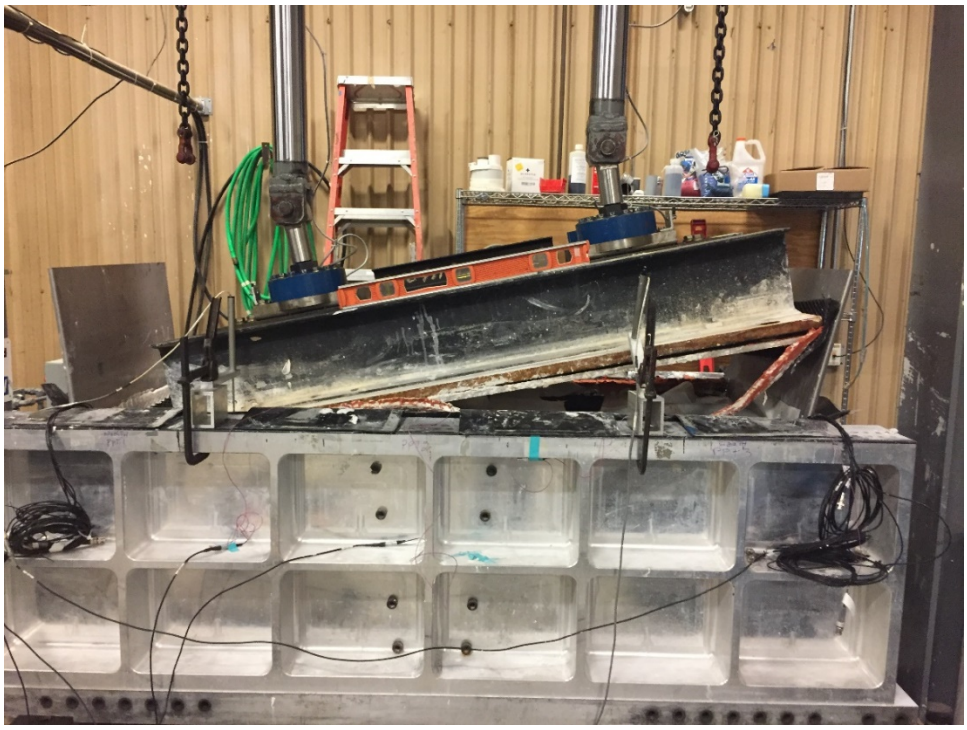

Figure 36: Hydraulic Press Failure

5.4.2.4 Consolidation Part 2

I returned the model container to the hydraulic press and finished consolidation to a final applied pressure of 200 kPa. Figure 37 present the model configuration and instrument positions during this phase of consolidation. Figure 38 presents pore pressures and target loads for consolidation beginning November 17, 2017. This plot terminates on November 26, 2017 due to failure of the computer terminal used to run the PPT data acquisition system. I restarted the data acquisition system on November 29, 2017 and collected data until consolidation was approximately 95% complete at 200 kPa. Note that this figure includes an instance of press instability when the press loads rapidly varied by +/- 100 kPa.

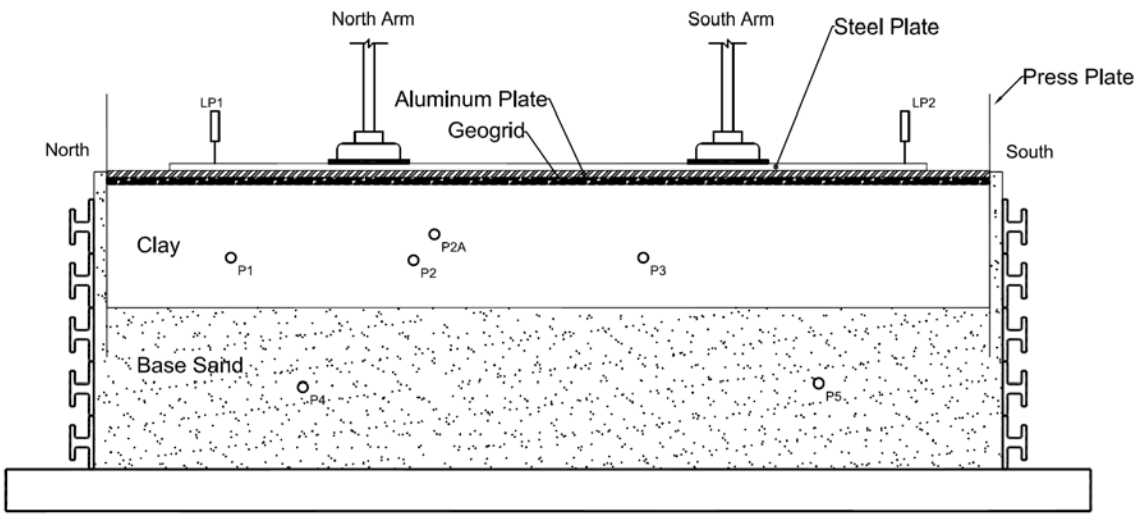

Figure 37: JZB01 Model Configuration during Clay Consolidation - Part 2

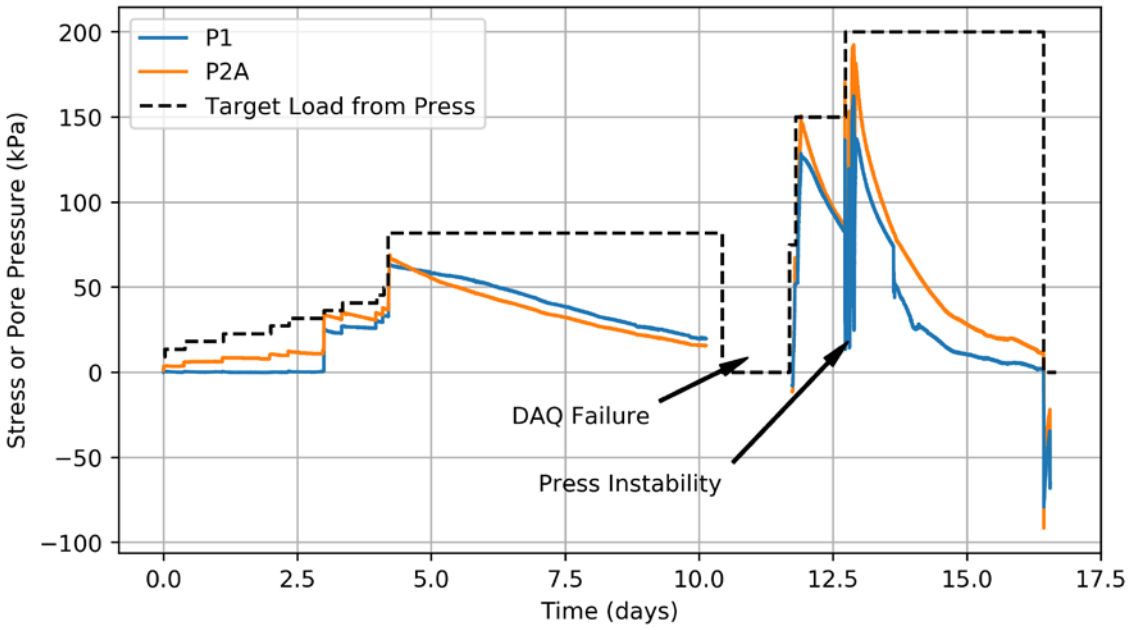

Figure 38: JZB01 Pore Pressure during Clay Consolidation – Part 2

5.5 STRUCTURE INSTALLATION

I installed structures in the model following clay consolidation on the hydraulic press and placement of the thin (~1cm) surficial sand layer over the clay. I oriented structures such that the longitudinal structure axis was perpendicular to the direction of shaking (the long axis of the model container). I positioned structures to avoid the HPC cross-bracing tension bars and such that Prandtl-based bearing failure wedges of adjacent structures would not overlap or pass through the vertical sand drains at the ends of the container. Figure 39 presents the final structure configuration in the model container.

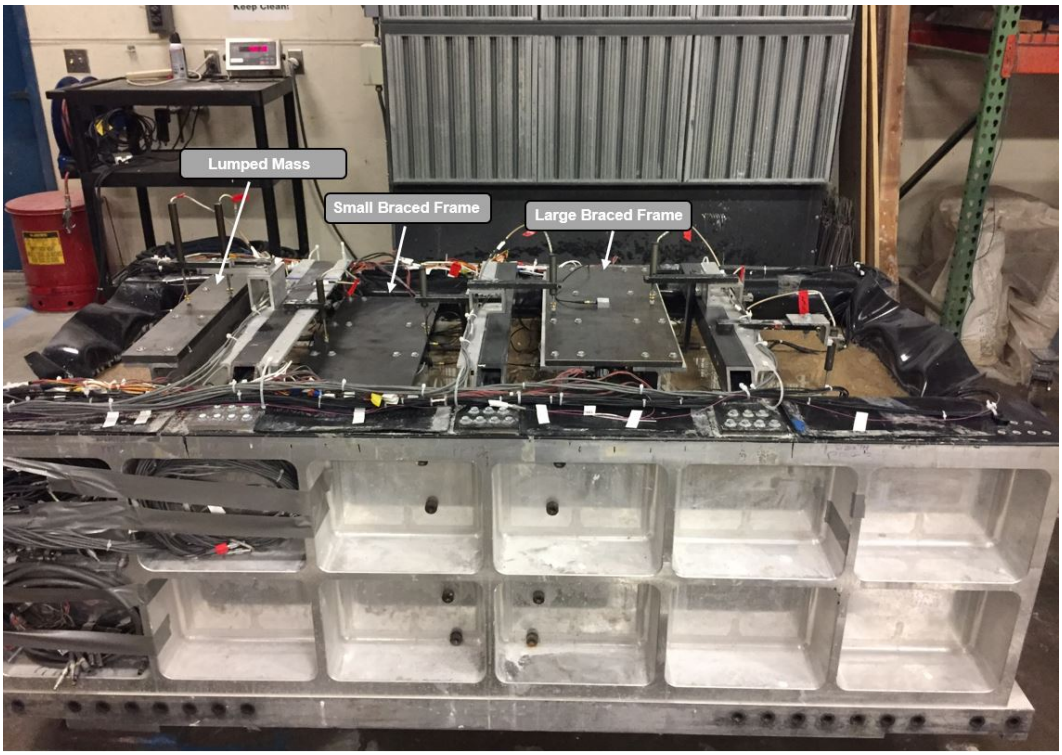

Figure 39: JZB01 Structure Configuration

5.6 T-BAR TESTING

I performed T-Bar testing to characterize clay undrained shear strength. The T-Bar is a full-flow penetrometer similar to the cone penetration test (CPT) that records resistance to

penetration. The T-Bar is advanced by a hydraulic ram at a rate of 0.5 cm/s. Figure 40 presents a graphic of the T-Bar. Although the conventional T-Bar includes load cells at the tip and the top of the shaft; only the shaft load cell was functional on the T-Bar used in this test.

I performed a series of T-Bar tests with the model at rest ($N_g = 1g$) and one T-Bar test during centrifuge testing. The T-Bar tests at rest were intended as a check on clay strengths immediately prior to centrifuge testing and are omitted here for brevity. The T-Bar test performed during centrifuge testing, designated TB-7, was intended to characterized clay strength in flight. Figure 41 presents the TB-7 test data.

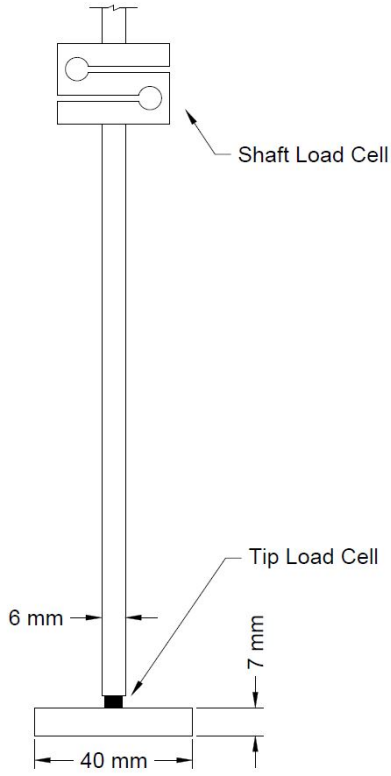

Figure 40: T-Bar Configuration

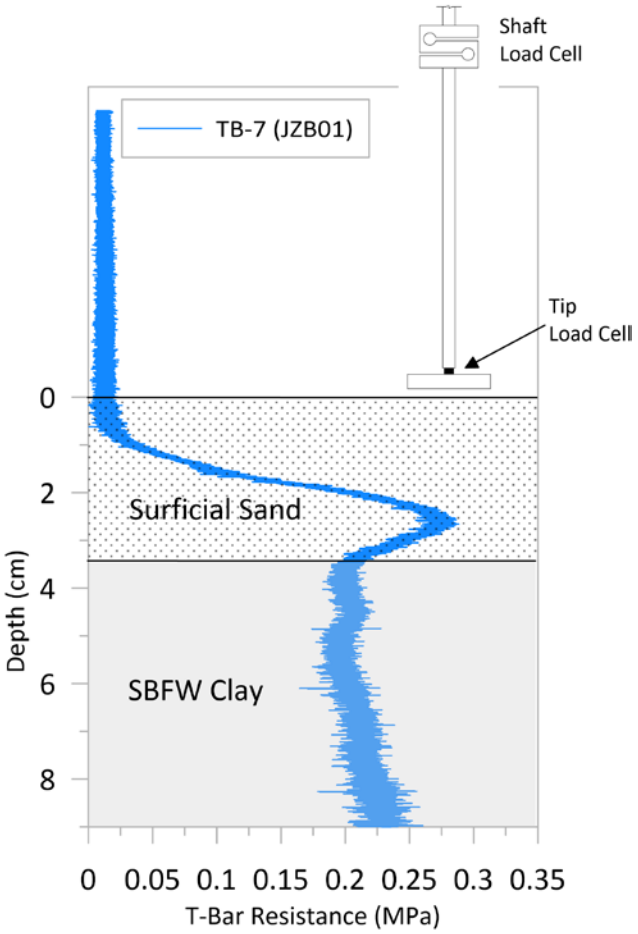

Figure 41: T-Bar Test Data from Model JZB01 Centrifuge Testing

5.7 CENTRIFUGE TESTING

I conducted centrifuge testing of the model beginning January 2018 and performed five total tests (e.g. spins). Spins 1-4 were performed without applying dynamic ground motions to the model due to issues during model spin-up. Spin 5 is the only test that included dynamic ground motions. Table 4 summarizes spins for model JZB01. I collected instrumentation measurement data at 1 Hz frequency during centrifuge testing. The CGM refers to data collected at this interval as slow data, which is collected throughout operation of the centrifuge including during spin-up, application of ground motions, spinning between ground motions, and spin-down. I collected instrumentation measurement data at 5,000 Hz frequency during the application of ground motions. The

CGM refers to data collected at this interval as fast data, which is only collected at user-controlled intervals.

Table 4: JZB01 Spin Summary

Spin	Date	Maximum *N*	Shaking (Y/N)
1	2018 Jan. 11	30	N
2	2018 Jan. 17	30	N
3	2018 Jan. 29	57	N
4	2018 Jan. 31	26	N
5	2018 Feb. 7	40	Y

5.7.1 Spins 1 through 4

Spins 1 and 2 were terminated during centrifuge spin-up after observing bearing capacity failures in Structure 1. After each spin, I repaired damage to the clay below and adjacent to Structure 1 by removing disturbed clay and reinstalling the structure.

Following Spin 2, I collected four samples below each structure and in the far field. I measured water content of each sample and used these values to calculate void ratio. Measured water contents were 0.37, 0.39, 0.36, and 0.35; calculated void ratios were 0.973, 1.021, 0.937, and 0.921. At the time of centrifuge testing, I compared calcuated to expected void ratios using the SBFW blend consolidation curve by Eslami (2017) in Figure 31. The maximum past consolidation pressure in the clay corresponding to the measured void ratios was significantly less than the 200 kPa achieved after consolidation on the hydraulic press. Later, using consolidation curves developed from testing on samples of unused JZB01 clay slurry, I determined that the measured void ratios corresponded to maximum past consolidation pressure of about 40 to 80 kPa. See Figure 31. I concluded that the clay lost stress history prior to testing, which resulted in lower clay strength that likely generated the bearing capacity failure. The lost stress history was likely caused by

disturbance and swelling. Disturbance may have occurred when the structures were placed on the clay surface, and subsequently removed from the model during instrumentation installation. Swelling likely occurred due to the presence of bentonite in the clay. Based on these observations, I concluded that the model required additional consolidation to maintain stable structures during spin-up.

Spin 3 was performed to reconsolidate the clay and increase clay strength. Prior to the spin, I removed structures and about half the clay thickness from the model, such that the final clay thickness was about 10 centimeters. I then added overburden on the clay that would generate about 200 kPa of overburden on the clay at $N_g = 57g$. The overburden included about 5 ½ cm sand, a 1-inch aluminum plate, and a 1-inch steel plate. I performed the spin until excess pore water pressures in the center of the clay dissipated to an average of 75 percent, yielding an average maximum past pressure of 150 kPa in the clay. I monitored the pore pressure in the clay using piezometers and displacement of the overburden using LPs. Following the consolidation spin, I reinstalled structures in the model and reattached all instrumentation.

Spin 4 was terminated after repeated power failures in the centrifuge safety systems prompted the GCM staff to terminate the test during spin-up. Following Spin 4, I removed structures to facilitate centrifuge diagnostics and repair by the CGM staff. I reinstalled the structures once the CGM staff completed troubleshooting the centrifuge.

5.7.2 Spin 5

Spin 5 was finally performed with success and shaking was applied to the model during spinning. Bearing capacity failure did not occur in the structure during spin-up; however, based on PPT and LP behavior, I anticipate that the clay again lost stress history due to swelling during the interval between the Spin 3 consolidation and Spin 5.

Fourteen ground motions were applied to the JZB01 model during Spin 5. Ground motions at the CGM are applied by servo-hydraulic shakers about the long axis of the model container, which corresponds to a direction parallel to the short axis of the structures. Ground motions were based on five root motions applied at various scale factors, designated Step, SW7-333, TCU-078, Kobe-PI(83), and Exponential Sine Sweep. The Step ground motion is a short interval pulse motion intended to evaluate model response in the linear behavior range. The Sine Sweep and Exponential Sine Sweep ground motions are synthetic motions developed by Seylabi et al. (2019). The Kobe-PI(83) and TCU-078 ground motions are based recorded earthquake ground motions available through the Pacific Earthquake Engineering Research Center (PEER) as part of NGA-West2 (Ancheta et al., 2013). Table 5 summarizes the earthquake ground motions. Table 6 summarizes the sequence of ground motions applied to JZB01, including the peak base acceleration, $\ddot{u}_{b,pk}$ observed in ICP A42. Note that because ground motions at the CGM used displacement based input from hydraulic shakers, the motions are approximate representations of the target ground motion records and do not consist of input of the actual recorded ground motion.

Structure 1 experienced bearing capacity failure during ground motion No. 7. I did not observe bearing capacity failure in either of the frame structures; however, the frames experienced significant settlement and rotation that I observed using LPs.

Table 5: Input Earthquake Ground Motions

Ground Motion Record	Earthquake	Year	Magnitude	Station	Horizontal Component	PEER Record Number
Kobe – PI(83)	Kobe, Japan	1995	6.90	Port Island (83 m)	90	3763
TCU-078	Chi-Chi, Taiwan	1999	7.62	TCU078	90	1512

Table 6: JZB01 Shaking Event Sequence

Shake No.	Event Name	Scale Factor	Model Scale PBA (g)	Prototype Scale PBA (g)	Fast Data File Name
0	Step	1	0.47	0.01	02072018@092140@112100@64.4rpm.txt
1	SW7-333	0.2	2.39	0.04	02072018@092140@114054@64.5rpm.txt
2	TCU-078	0.2	2.52	0.04	02072018@092140@115751@64.4rpm.txt
3	SW7-333	0.4	6.94	0.12	02072018@092140@120948@64.4rpm.txt
4	TCU-078	0.4	7.20	0.13	02072018@092140@121555@64.5rpm.txt
5	SW7-333	0.6	10.53	0.18	02072018@092140@122742@64.5rpm.txt
6	TCU-078	0.6	11.48	0.20	02072018@092140@123426@64.5rpm.txt
7	SW7-333	0.8	14.36	0.25	02072018@092140@124112@64.4rpm.txt
8	TCU-078	0.8	14.00	0.25	02072018@092140@124649@64.4rpm.txt
9	SW7-333	1	18.95	0.33	02072018@092140@125316@64.5rpm.txt
10	TCU-078	1	16.42	0.29	02072018@092140@125830@64.5rpm.txt
11	Kobe-PI(83)	1	4.18	0.07	02072018@092140@130339@64.4rpm.txt
12	Kobe-PI(83)	3	14.08	0.25	02072018@092140@130950@64.4rpm.txt
13	Exp. Sine Sweep	1	5.02	0.09	02072018@092140@131634@64.4rpm.txt

5.8 MODEL DECONSTRUCTION

Ground motions applied during Spin 5 generated bearing capacity failure in Structure 1 and caused significant rotation in the braced frame structures. I documented the shaking-induced structure deformations by surveying the clay during model deconstruction. The clay showed clear deformation about one half to one footing width below the structure. Deformation occurred as squeezing of the clay around the footing; a conventional wedge-shaped bearing failure was not obvious during deconstruction. Although Structures 2 and 3 did not experience bearing capacity failure, I observed similar deformation below structure footings during deconstruction. Deformation zones for each structure were effectively independent. I did not observe overlap or interaction in the deformation zones.

6 CENTRIFUGE TEST JZB02

I performed centrifuge test JZB02 at the CGM from October 24, 2018 to January 26, 2019. The JZB02 model consisted of sand underlying a layered kaolinite-based surficial clay with the three structures described in Chapter 7 founded on the clay deposit. I collected data during testing using 136 instruments installed in soil layers, mounted on structures, and mounted on the exterior of the model container. The instruments consisted of the same ICP, MEMS, LP, and PPT models used in JZB01. Figure 42 presents the JZB02 model profile configuration and instrumentation.

This chapter summarizes the JZB02 model construction, testing, and data collection; however, details are omitted for brevity. The JZB02 data report (Buenker et al., 2020a) provides additional information on the test program, including details omitted here. The report is available through DesignSafe-CI, like the JZB01 data report.

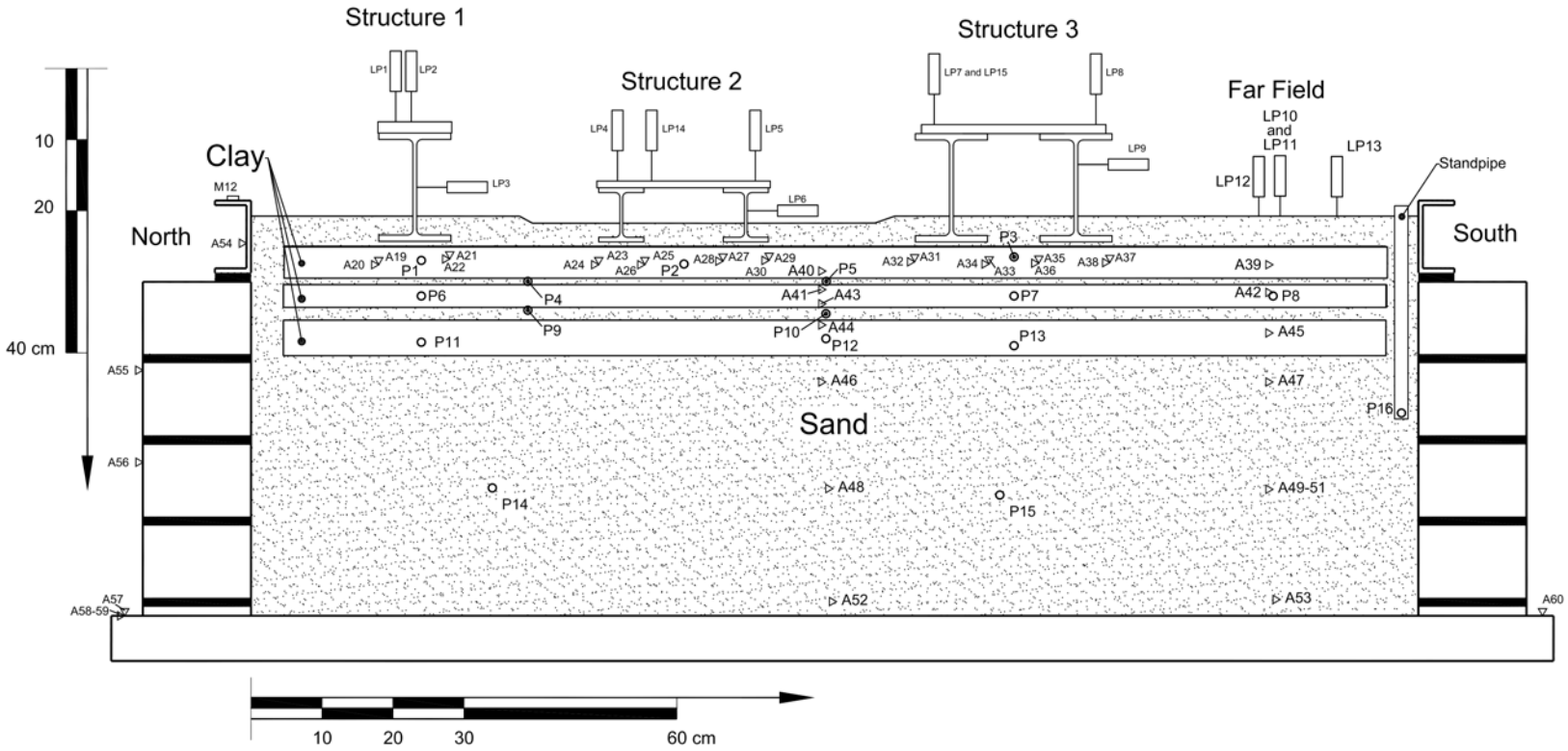

Figure 42: JZB02 Model Configuration

6.1 MODEL CONTAINER

I constructed the model in the CGM's flexible shear beam container (FSB) 2.1. The FSB 2.1 consists of a solid aluminum base with semi-rigid side walls composed of stacked aluminum rings. The 10-centimeter tall aluminum rings are separated by layers of Neoprene rubber. Although deformable during dynamic shaking on the centrifuge, the rings are not deformable by hand and maintain a semi-rigid shape during model construction. The container is water-tight, with three drains covered by filter fabric in the model floor. Figure 43 presents a graphic of the container. The container also includes shear rods installed at the long ends of the container to reduce boundary effects. Figure 44 presents a photo of the container.

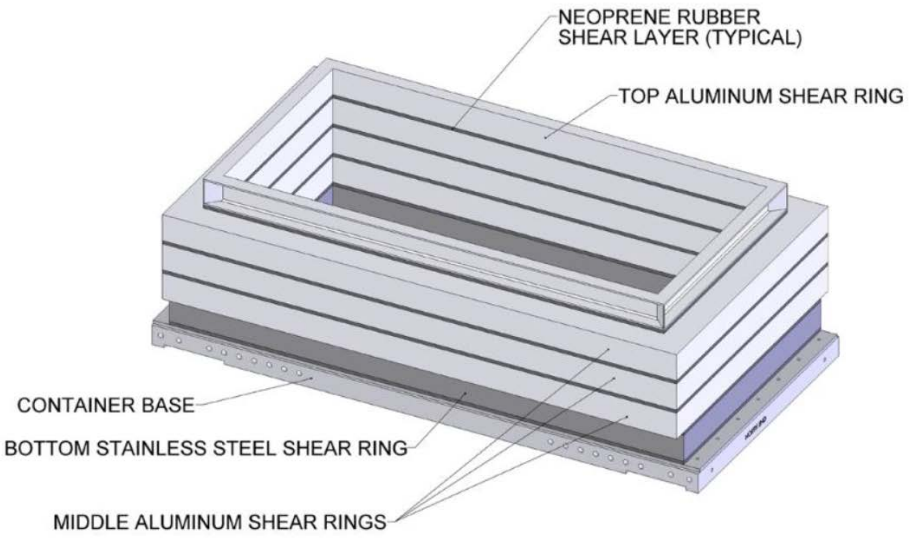

Figure 43: Flexible Shear Beam Container Graphic

Figure 44: Flexible Shear Beam Container Photo

6.2 PORE FLUID

Similar to the JZB01 model, all pore fluid used to construct model JZB02 consisted of deionized water. Water was selected as the pore fluid over methylcellulose or other viscosity-scalable fluid, because the object of this centrifuge study is to evaluate cyclic clay behavior that is likely to be undrained during ground shaking. Because viscosity is scalable during centrifuge testing, material behavior dependent on pore fluid flow (e.g. liquefaction) may not be captured by this model. Model sand behavior during dynamic shaking is likely to be unrealistic due to rapid drainage caused by the absence of a viscosity-scalable pore fluid.

6.3 SOIL

The JZB02 model soil profile consisted of layered kaolinite-based clay with intermediate sand lenses overlying dense base sand. The clay was subdivided into three approximately 4-cm-thick layers separated by thin lenses of sand. The bottom sand lens was 2 cm thick

and the top sand lens was 1 cm thick. I deposited sand at greater than 90% relative density to prevent liquefaction. I intended the sand to provide drainage for clay during consolidation. I also placed a thin (~1cm) layer of hand-deposited sand at the clay surface, such that our structures did not create suction by resting directly on the clay. I also placed hand-deposited vertical sand drains at the ends of the container to facilitate vertical drainage around the clay layers. The sections below summarize soil properties and depositional methodology associated with each soil type. Figure 45 presents the JZB02 soil profile.

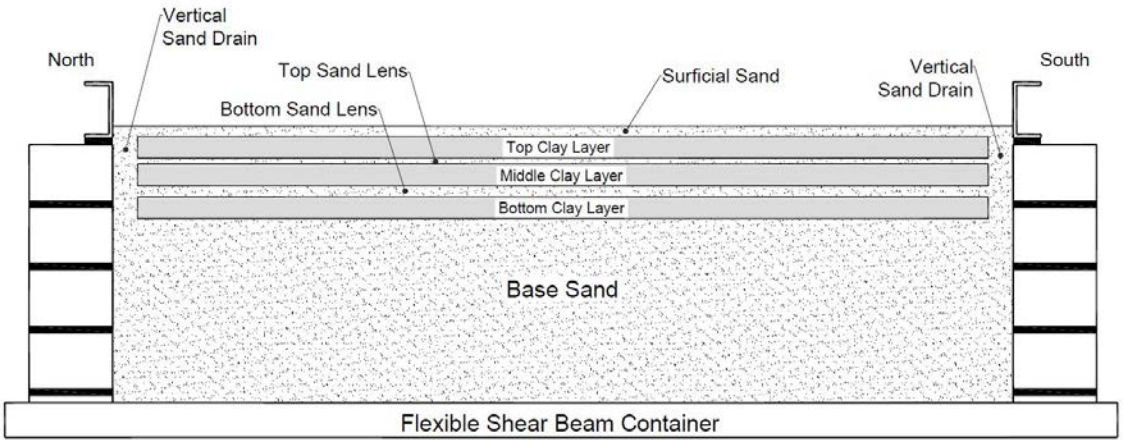

Figure 45: JZB02 Soil Profile

6.3.1 Sand

Sand consisted of F-65 Ottawa sand, which is the same sand used in model JZB01. I deposited sand below the clay and in between the clay layers using a variable speed pluviator. I calibrated the pluviator using the approach described in Section 5.4.1.1. Figure 46 presents our calibration curve. Sand above the clay and to the sides of the clay was placed by hand without using the pluviator.

I deposited sand below the clay and between the bottom and middle clay layers at pluviation speed Setting 3 with a 100 cm drop height to achieve approximately 92 percent

relative density. I deposited sand between the middle and top clay layers at pluviation speed Setting 2 with a 75 cm drop height to achieve approximately 92 percent relative density. I deposited sand below the clay in lifts, with a maximum lift height of 5 cm. Following each lift, I removed surface inundations or mounding using a shop vacuum to create a flat sand surface for subsequent lifts.

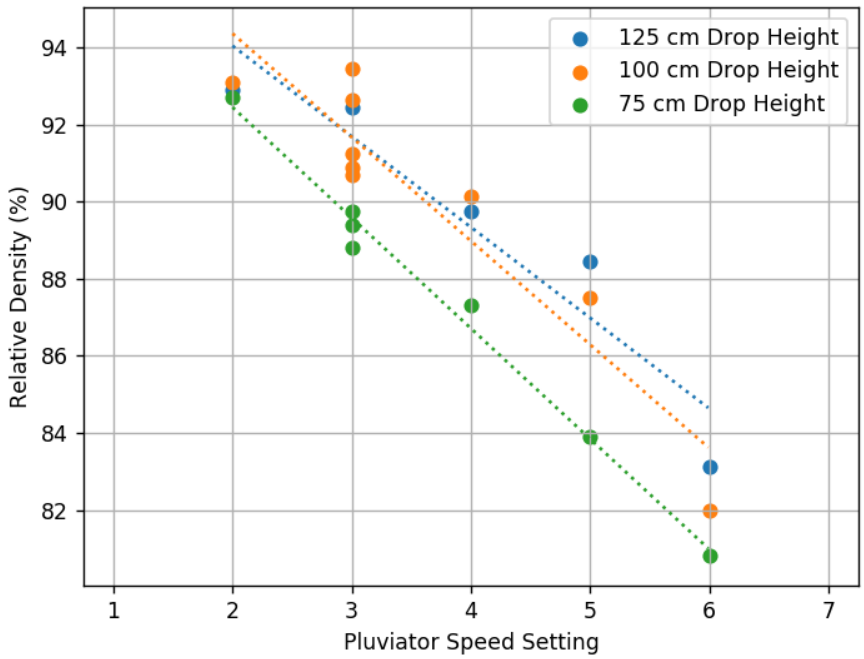

Figure 46: JZB02 Sand Pluviator Calibration

I saturated the sand with deionized water. I added water using a hose that dripped water onto a sponge that was situated on the sand surface. The intent of the sponge was to seep water into the sand without disturbing the sand surface. I regulated water flow such that the sponge remained moist, without allowing water to accumulate and flow from the sponge across the sand surface. I maintained a level container during saturation. I terminated saturation when I observed standing water on the sand surface. Saturation of sand below clay layers was performed over two days. Saturation of sand between clay layers was performed in two to three hours.

6.3.2 Clay

Clay consisted of a synthetic soil blend composed of 22 percent EPK Clay kaolinite sourced from Edgar Minerals and 78 percent SIL-CO-SIL #45 ground silica sourced from JNS SmithChem. This blend was designed to match the SKFW soil blend developed by Eslami (2017).

6.3.2.1 Laboratory Testing

I performed Atterberg limits and consolidation laboratory tests to characterize properties and behavior of the JZB02 clay and compare them to the Eslami SKFW blend. Figure 47 presents Atterberg limits test results. Figure 48 presents consolidation test results. Permeability, k and coefficient of vertical consolidation, c_v from the consolidation tests are only plotted in the compression range. As shown from the laboratory testing, the JZB02 clay properties and behavior closely match the Eslami SKFW blend.

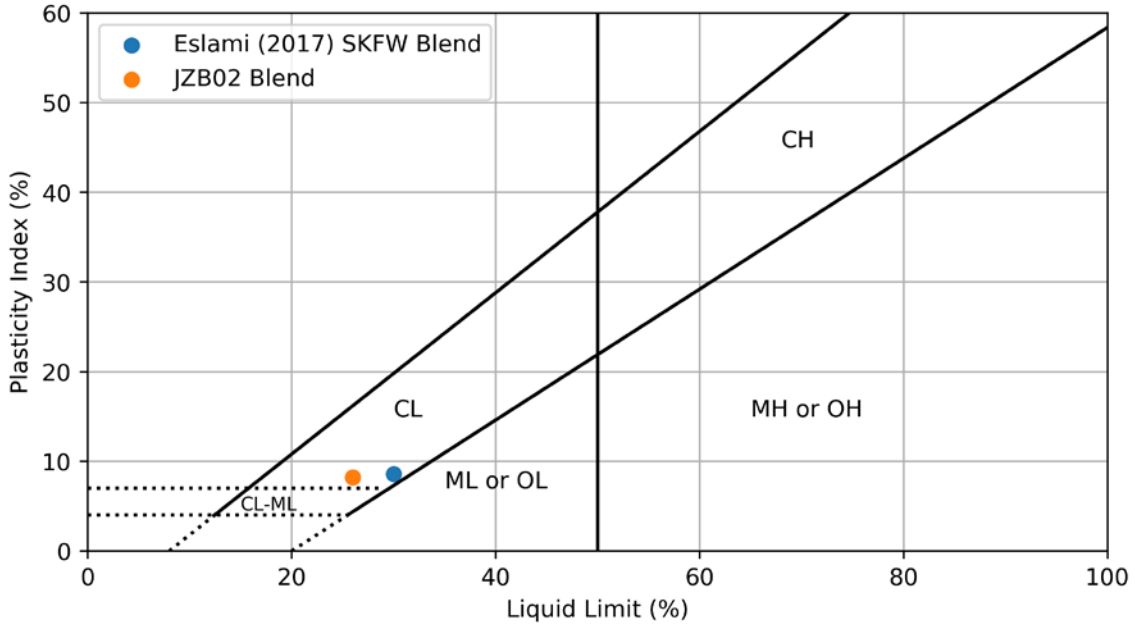

Figure 47: JZB02 Clay Atterberg Limits

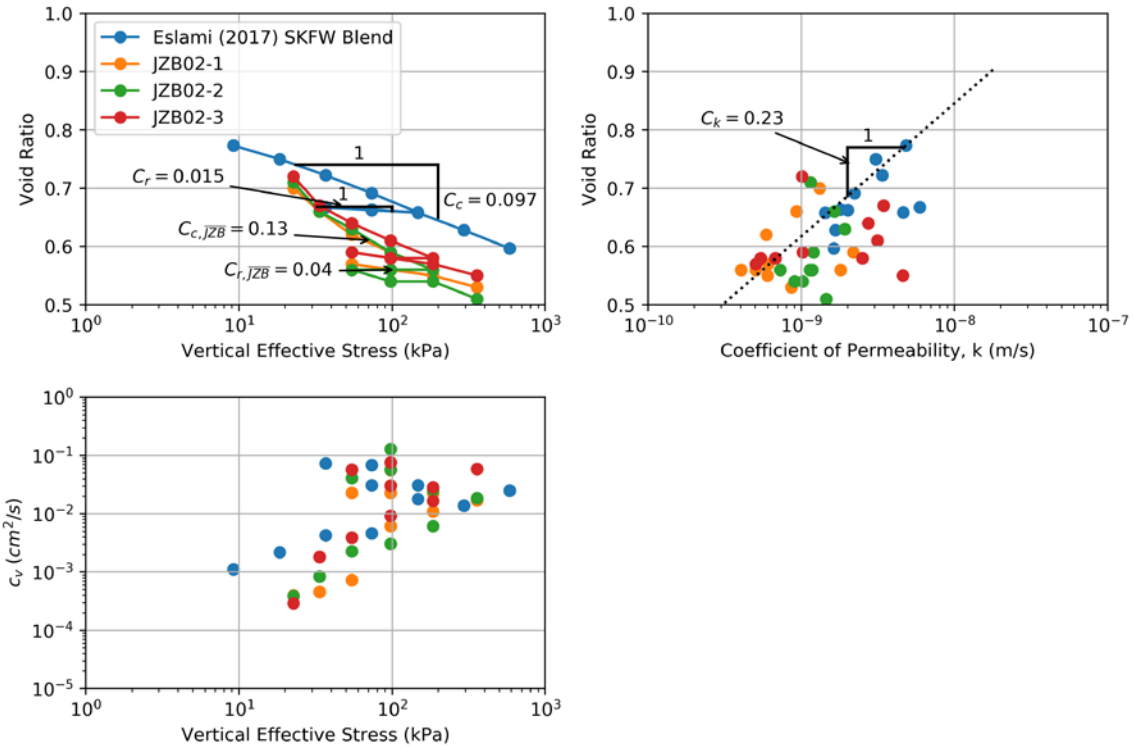

Figure 48: JZB02 Consolidation Testing

6.3.2.2 Mixing and Deposition

I mixed clay in the CGM's industrial-strength mixer. I performed mixing by first adding SIL-CO-SIL #45 ground silica to the mixer with enough water to bring the material to the liquid limit of the full clay blend. I then added kaolinite in small doses to avoid clumping in the mixture. I blended clay in the mixer overnight. I used a pneumatic pump to transfer the clay from the mixer to the model container. Prior to depositing the clay, I placed aluminum sheets at each end of the model container and backfilled the sheets with sand to create vertical drainage paths. I maintained these aluminum sheets in the container through clay deposition and consolidation to prevent migration of clay into the vertical drains.

I deposited each clay layer in a single lift and consolidated each layer prior to placing additional sand or clay. I kept the blended clay in the CGM's mixer while I consolidated clay deposited in the model container. Because several days typically elapsed between

deposition of clay lifts due to consolidation and other factors, I re-blended clay in the mixer overnight prior to placing subsequent lifts.

6.3.2.3 Consolidation

I consolidated the clay to create stress history and build strength in the clay deposit. I consolidated each clay layer prior to placing additional sand or clay. I consolidated the bottom clay layer to a maximum past pressure of 200 kPa, the middle clay layer to a maximum past pressure of 180 kPa, and the bottom clay layer to a maximum past pressure of 150 kPa.

The clay slurry is weak and prone to squeezing immediately after mixing and deposition; therefore, I performed preliminary consolidation using dead weight from overburden sand and steel weights, like the procedure outlined in Section 5.4.2.3. I added a mass of dead weight that equated to about to 5 kPa overburden pressure at the clay surface. I allowed pore pressure dissipation under the dead weight overnight. I then removed the sand and placed a layer of geosynthetic and filter paper over the clay.

I performed subsequent consolidation using the hydraulic press discussed in Section 5.4.2.3. I evaluated degree of consolidation in the clay while on the press by monitoring pore water pressure using PPTs and settlement using LPs.

I performed consolidation on the hydraulic press in the following sequence:

- ***Bottom Clay Consolidation – Part 1*** - I consolidated the bottom clay layer beginning November 27, 2018. Figure 49 presents the model configuration during consolidation and Figure 50 presents pore pressure, settlement, and target press loads during consolidation. I performed consolidation to about 120 kPa. Then, like the narrative in Section 5.4.2.3, the CGM again experienced power failure overnight which caused the press to become unstable and plunge the steel press

plate into the north side of the model. The plunging plate squeezed clay from the model but did not generate the type of large-scale bearing capacity failure observed in JZB01. I repaired damage to the clay layer caused by the press failure by adding clay slurry.

- ***Bottom Clay Consolidation – Part 2*** - I consolidated the bottom clay layer again beginning November 29, 2018. The model configuration during consolidation matched the bottom clay consolidation Part 1. Figure 51 presents pore pressure, settlement, and target press loads during consolidation. Final consolidation pressure was 200 kPa. As show in the figure, I observed press instability during the unloading phase, where applied pressure in the actuators rapidly varied by several thousand pounds. I quickly dropped pressure in the actuators to relieve the press instability. The applied loads were not sustained, and I do not anticipate consolidation occurred in the clay during press instability.
- ***Middle Clay Consolidation*** - I consolidated the middle clay layer beginning December 5, 2018. Figure 52 presents the model configuration during consolidation. Figure 53 presents pore pressure, settlement, and target press loads during consolidation. I consolidated the clay to 180 kPa applied pressure. I again observed press instability during the unloading phase, where applied pressure in the actuators rapidly varied by several thousand pounds. I quickly dropped pressure in the actuators to relieve the press instability. Again, the applied loads were not sustained, and I do not anticipate consolidation occurred in the clay during press instability.
- ***Top Clay Consolidation*** - I consolidated the top clay layer beginning December 7, 2018. Figure 54 presents the model configuration during consolidation. Figure 55 presents pore pressure, settlement, and target press loads during consolidation. I consolidated the clay to 130 kPa applied pressure.

- ***All Clay Reconsolidation*** - I reconsolidated all clay layers beginning January 4, 2019. The model configuration during consolidation matched the model configuration during the top clay consolidation. Figure 56 presents pore pressure, settlement, and target press loads during consolidation. I consolidated the clay to 140 kPa applied pressure, which was 10 kPa higher than the previous maximum applied pressure.

Note that the model configuration figures omit ICP accelerometers installed in the sand and clay, because those instruments were not monitored during consolidation.

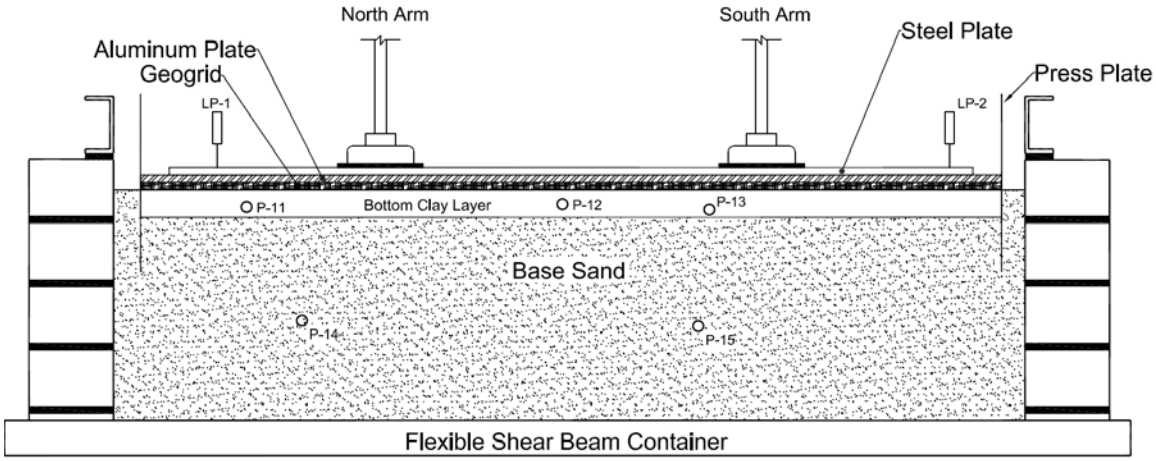

Figure 49: JZB02 Model Configuration during Bottom Clay Consolidation

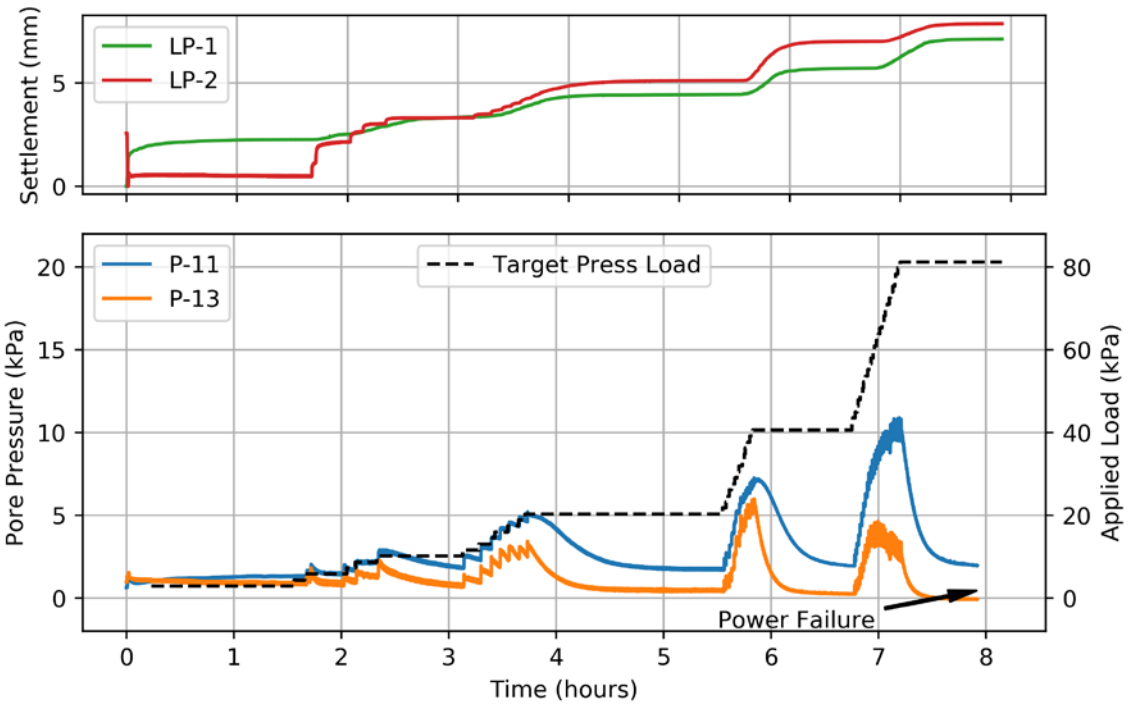

Figure 50: JZB02 Pore Pressure and Settlement during Bottom Clay Consolidation – Part 1

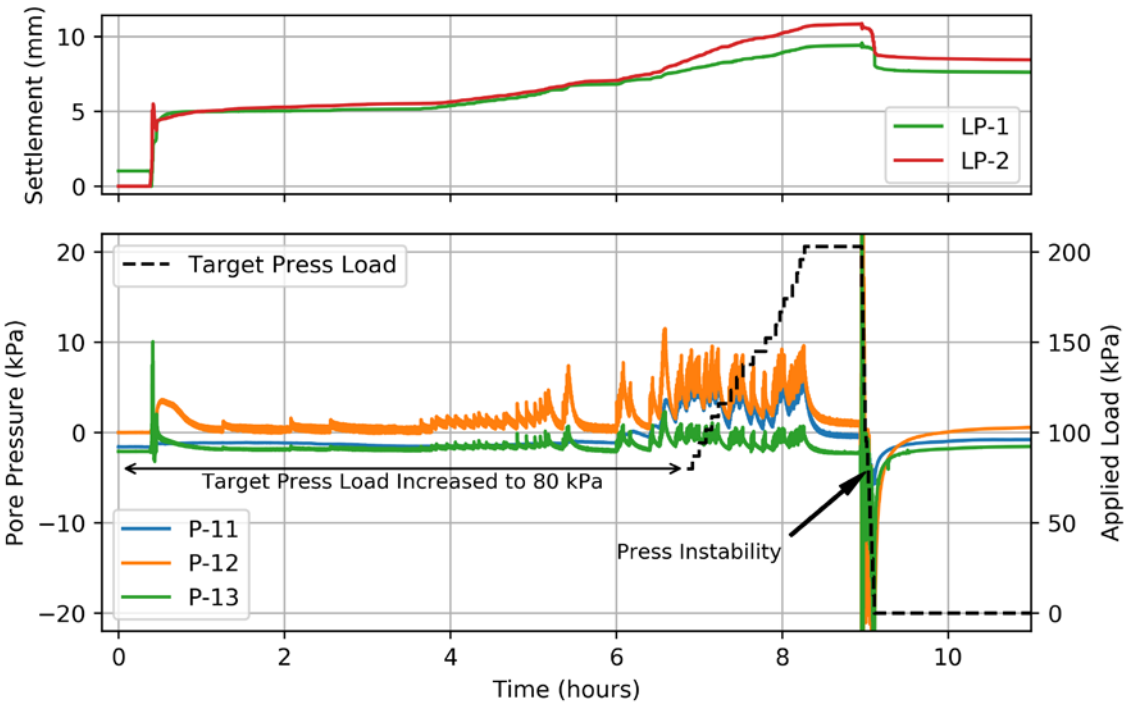

Figure 51: JZB02 Pore Pressure and Settlement during Bottom Clay Consolidation – Part 2

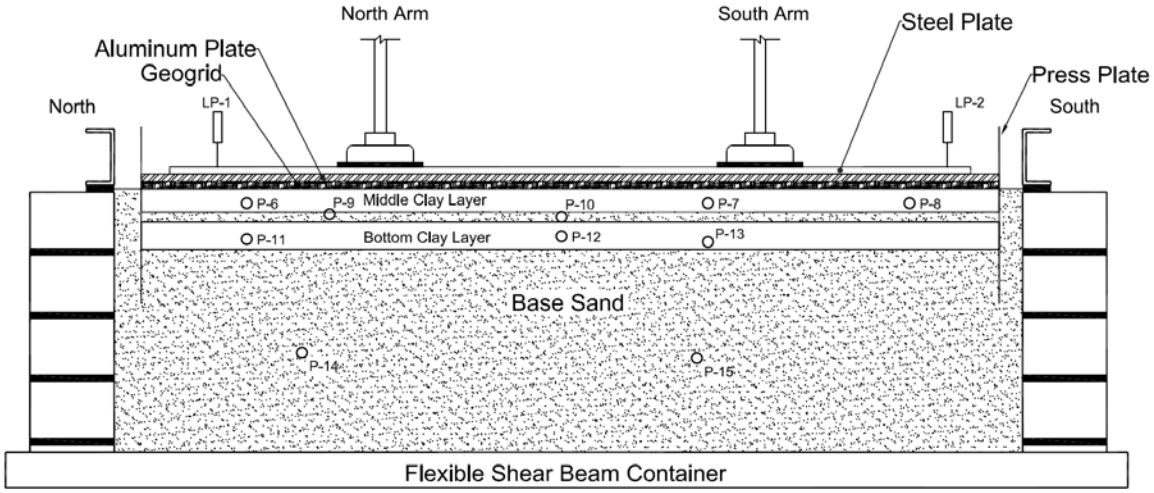

Figure 52: JZB02 Model Configuration during Middle Clay Consolidation

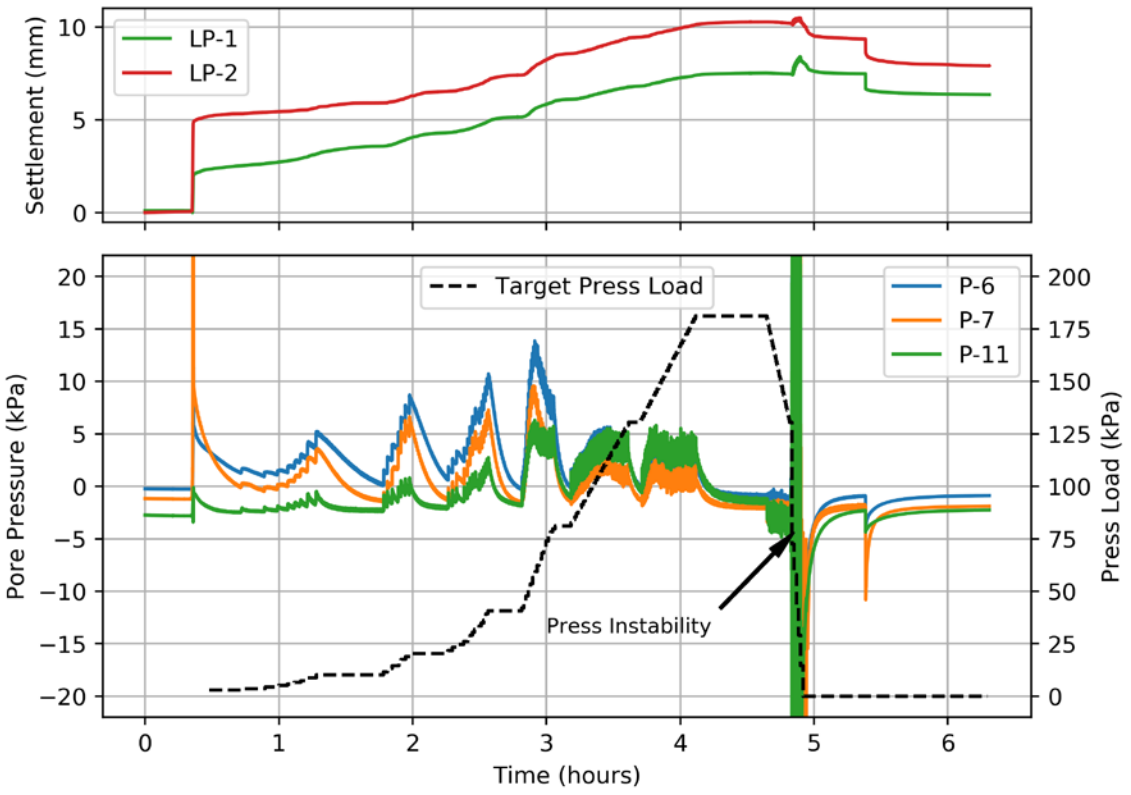

Figure 53: JZB02 Pore Pressure and Settlement during Middle Clay Consolidation

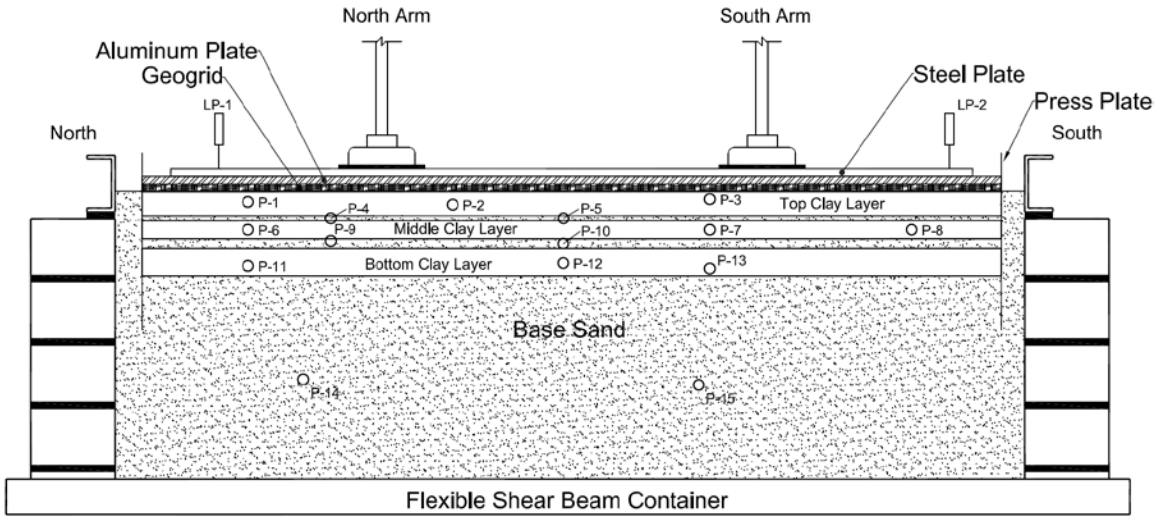

Figure 54: JZB02 Model Configuration during Top Clay Consolidation

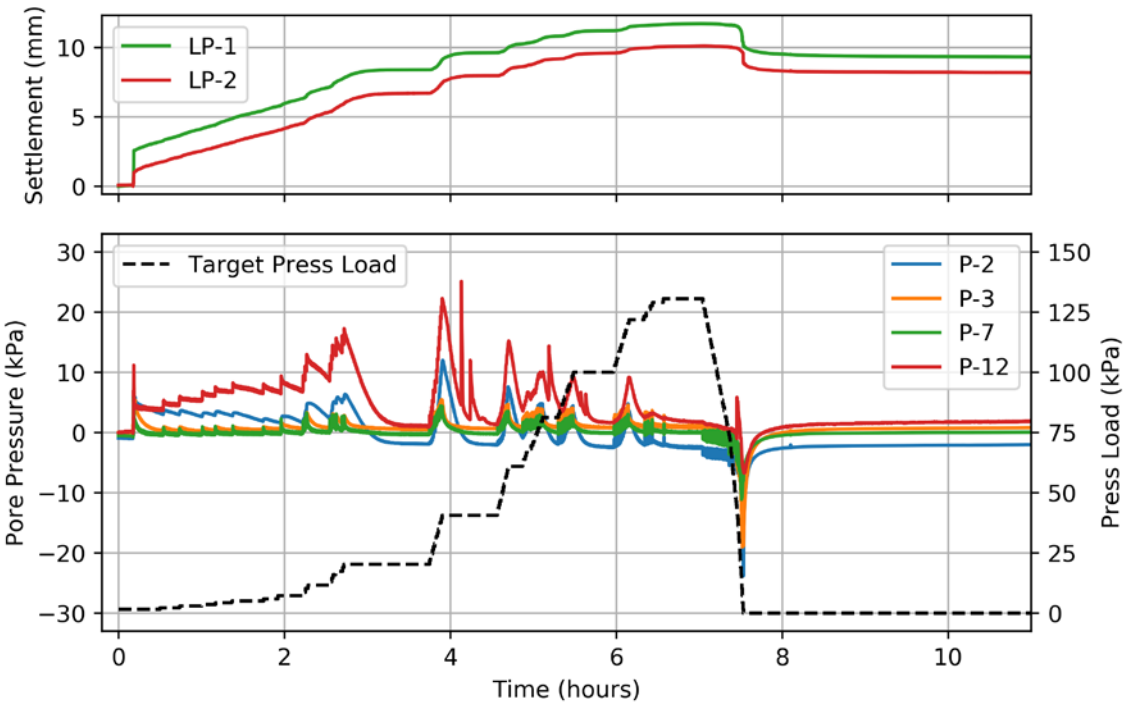

Figure 55: JZB02 Pore Pressure and Settlement during Top Clay Consolidation

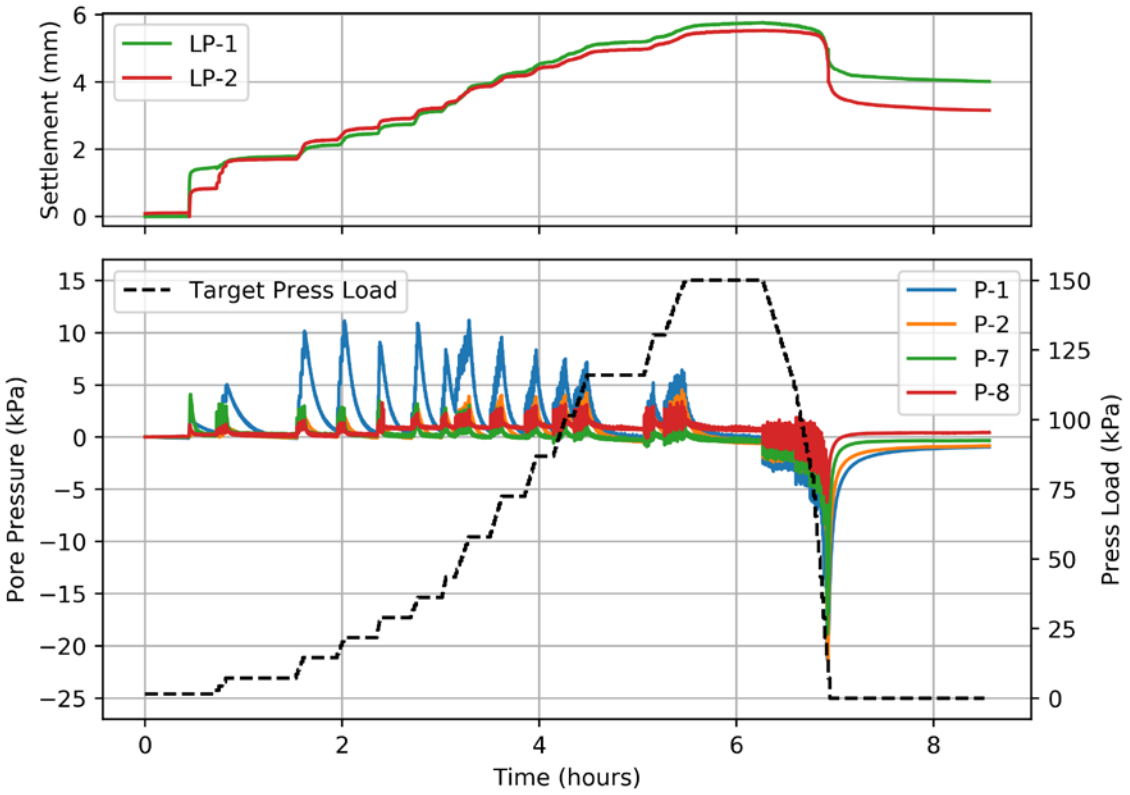

Figure 56: JZB02 Pore Pressure and Settlement during All Clay Consolidation

6.4 STRUCTURE INSTALLATION

I installed structures in the model following clay consolidation on the hydraulic press and placement of the thin (~1cm) surficial sand layer over the clay. I oriented structures such that the longitudinal structure axis was perpendicular to the direction of shaking (the long axis of the model container). I positioned structures to mirror the layout of JZB01. Once installed, I placed approximately 1 cm of sand over the footings of each structure.

6.5 IN SITU TESTING

I performed in situ testing consisting of T-Bar tests and CPTs to quantify the strength of the clay layers. The T-Bar is described in Section 5.6. The T-Bar and CPT were each advanced by a hydraulic ram at a rate of 0.5 cm/s. Each instrument included a load cell

on the instrument shaft and another on the instrument tip. I performed T-Bar tests at rest ($N_g = 1g$) and CPTs during spinning ($N_g = 57g$) for JZB02. T-Bar tests performed at rest were intended as a check on clay strengths immediately prior to centrifuge testing and are omitted here for brevity. The CPTs performed during spinning were intended to characterize soil stratigraphy and demonstrate the effect of layering on clay and sand strength. I performed one CPT during each spin of JZB02, designated CPT-1 and CPT-2. Figure 57 presents CPT tip resistance data from CPT-2, which was performed during JZB02 Spin 2.

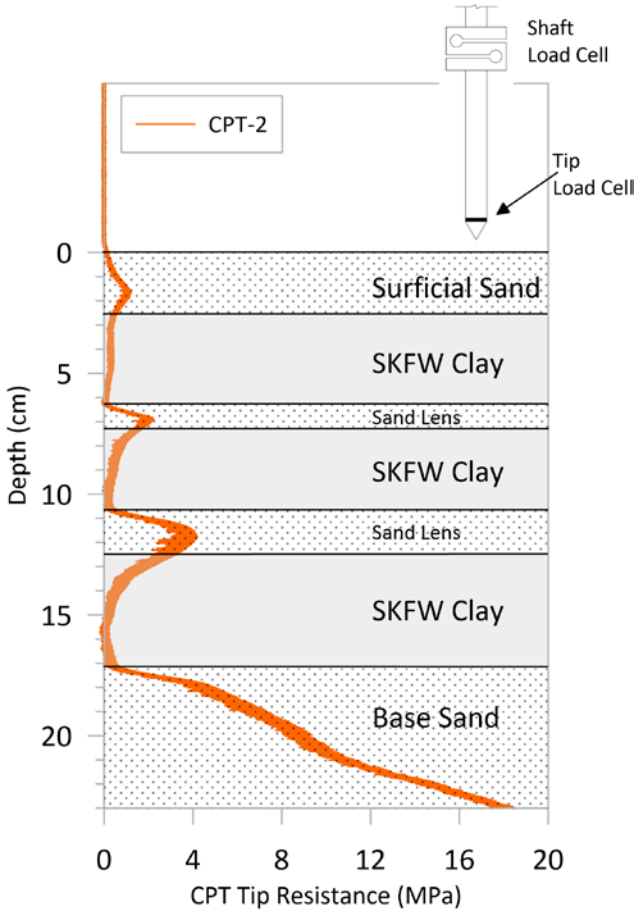

Figure 57: CPT-2 Tip Resistance from Model JZB02 Spin 2

6.6 CENTRIFUGE TESTING

I conducted JZB02 centrifuge testing in January 2018 and performed two total centrifuge tests (spins). Spin 1 was performed without applying dynamic ground motions to the model due to groundwater issues during model spin-up. Spin 2 included dynamic ground motions. I collected slow and fast data in the same manner as centrifuge testing for model JZB01, which is detailed in Section 5.6.

6.6.1 Spin 1

I performed Spin 1 on January 14, 2019. I terminated the spin after spin-up to $N_g = 57g$ because I observed a significant decrease in pressure readings shown in the PPTs. I determined that the decrease in pressure was evidence of the redistribution of water from the clay to the sand layers due to a drop in the model water table. Although the hydrostatic water table was maintained at footing level prior to testing, during spin-up the water table dropped to the approximate midpoint of the bottom clay layer. I anticipate that the water table dropped due the release of trapped air in the sand layers that only migrated out of the sand once hydrostatic water pressure increased during model spin-up. To mitigate this issue, I added a water supply line to the model that allowed us to add water during spinning. I also installed an additional PPT (P16) in an existing standpipe monitoring well following Spin 1 to monitor the location of the groundwater table during subsequent spinning.

6.6.2 Spin 2

I performed Spin 2 on January 16, 2019 at $N_g = 57g$. I added water progressively during spin-up and did not observe a drop in PPT pressure or other erratic behavior that might indicate the type of pore water redistribution observed during Spin 1. The hydrostatic pressure distribution after spin-up matched our expected pressure distribution.

Fourteen ground motions were applied to the JZB02 model during Spin 2. Ground motions were based on same five root motions as ground motions applied model JZB01, with motions applied at various scale factors. See Section 5.7.2 for additional information regarding the base ground motions. Table 7 summarizes the sequence of ground motions applied to JZB01, including the peak base acceleration, $\ddot{u}_{b,pk}$ observed in ICP A52.

Table 7: JZB02 Shaking Event Sequence

Shake No.	*Event Name*	*Scale Factor*	*Model Scale* $\ddot{u}_{b,pk}$ *(g)*	*Prototype Scale* $\ddot{u}_{b,pk}$ *(g)*	*Fast Data File Name*
0	Step	2	1.56	0.03	01162019@082639@110817@77.0rpm
1	SW7-333	0.2	1.81	0.03	01162019@082639@112208@77.0rpm
2	TCU-078	0.2	1.72	0.03	01162019@082639@113803@76.8rpm
3	SW7-333	0.4	5.76	0.10	01162019@082639@115034@76.9rpm
4	TCU-078	0.4	5.65	0.10	01162019@082639@122026@77.0rpm
5	SW7-333	0.2	2.52	0.04	01162019@082639@125704@77.0rpm
6	TCU-078	0.6	10.92	0.19	01162019@082639@131406@77.0rpm
7	SW7-333	0.2	2.51	0.04	01162019@082639@132829@76.8rpm
8	TCU-078	0.8	15.38	0.27	01162019@082639@134249@76.8rpm
9	SW7-333	0.2	2.51	0.04	01162019@082639@135801@76.8rpm
10	TCU-078	1	16.73	0.29	01162019@082639@141320@76.9rpm
11	Kobe-PI(83)	1	24.88	0.44	01162019@082639@142754@76.9rpm
12	SW7-333	0.2	2.51	0.04	01162019@082639@144705@76.9rpm
13	SW7-333	1	24.49	0.43	01162019@082639@151344@76.8rpm

Structure 1 experienced bearing capacity failure during ground motion No. 13, which was a Sweep motion applied at an amplitude factor of 1. I did not observe bearing capacity failure in either of the frame structures; however, the frames experienced significant settlement and rotation that I observed using LPs.

6.7 MODEL DECONSTRUCTION

Ground motions applied during Spin 2 generated bearing capacity failure in Structure 1 and caused significant rotation in the braced frame structures. I documented the shaking-induced structure deformations by surveying the clay during model deconstruction. The clay showed clear deformation in the top clay layer and smaller deformations in the middle clay layer. Deformation occurred as squeezing of the clay below the footing; a conventional wedge-shaped bearing failure was not obvious during deconstruction. Although Structures 2 and 3 did not experience bearing capacity failure, I observed similar deformation below structure footings during deconstruction. Deformation zones for each structure were effectively independent. I did not observe overlap or interaction in the deformation zones.

7 STRUCTURAL MODELS

The centrifuge testing program that forms the basis for this research incorporated three structures designed to capture a range of SFSI effects. The three structures were incorporated into both centrifuge models JZB01 and JZB02. Structure 1 consisted of a single I-beam with a steel plate bolted to the top. Structures 2 and 3 consisted of single-bay portal frames with either two short I-beams (Structure 2) or two tall I-beams (Structure 3) connected by a steel plate diaphragm bolted to the top flanges. The prototype-scale size, bearing pressure, and stiffness loosely approximate structures in the Wufeng Site A case history detailed in Chu et al. (2008). I designed Structure 1 to have a natural period longer than the small-strain period of the soil, Structure 2 to have a shorter natural period than the soil, and Structure 3 to have a natural period near the fundamental period of the soil deposit.

7.1 STRUCTURE CONFIGURATION AND ASSEMBLY

Structures were built from steel plates mounted to the top flanges of aluminum I-beams. I constructed each structure using 24-inch-long (61-centimeter-long) A36 steel plates and 6061 – T6 Aluminum Association standard I-beams. I connected steel plates to the

aluminum I-beams by installing steel bolts in ¼-inch holes drilled through the plates and I-beam top flanges. I instrumented the structures with ICP accelerometers by PCB Piezotronics, Model 2012-100 micro-electromechanical system (MEMS) accelerometers by Silicon Designs, and the strain gages discussed in the next section. Section 5.1 presents additional discussion regarding ICP and MEMS accelerometers. ICP accelerometers are designated “A-x”, MEMS accelerometers are designated “M-x”, and strain gages are designated “SG-x” in the following section and profile figures, where “x” is the instrument position number.

Figure 58 presents the Structure 1 assembly. Figure 59 and Figure 60 present the Structure 1 section for models JZB01 and JZB02, respectively. Figure 61 and Figure 62 present the Structure 1 profile for models JZB01 and JZB02, respectively. Note the differences in the Structure 1 models used for centrifuge models JZB01 and JZB02 consists solely the position and configuration of instrumentation. Figure 63, Figure 64, and Figure 65 present the Structure 2 assembly, section, and profile, respectively. There were no differences in the version of Structure 2 used for models JZB01 and JZB02. Figure 66, Figure 67, Figure 68, Figure 69 present the Structure 3 assembly, section, north I-beam profile, and south I-beam profile, respectively. The only difference in the version of Structure 3 used for models JZB01 and JZB02 are the addition of bending configuration strain gages, which are noted in the profile figures.

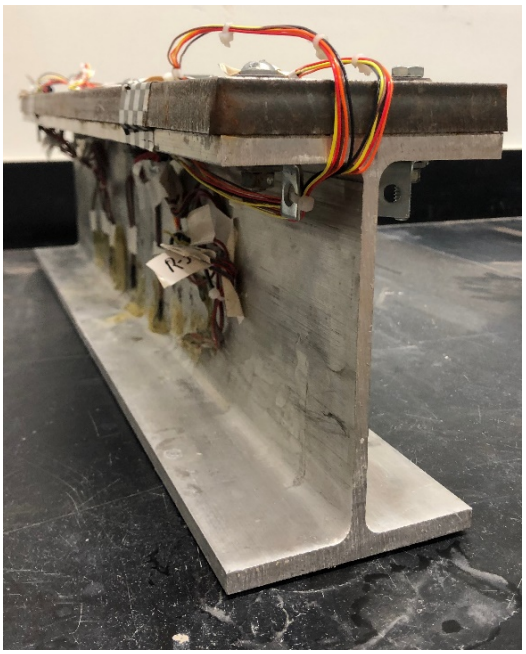

Figure 58: Structure 1 Assembly

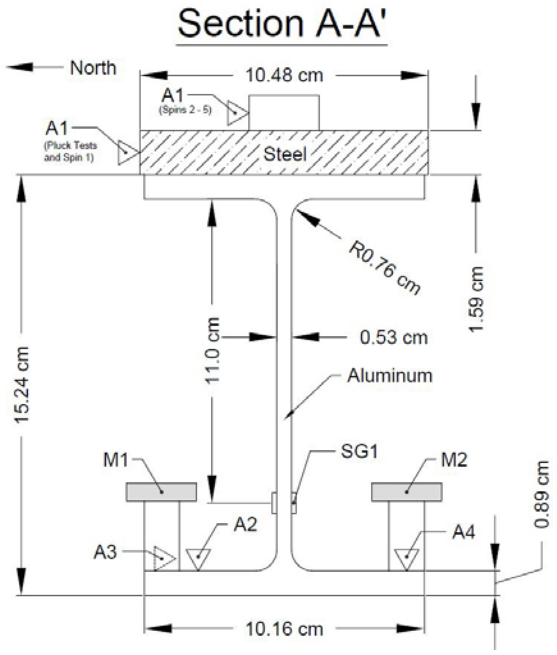

Figure 59: Structure 1 Section for Model JZB01

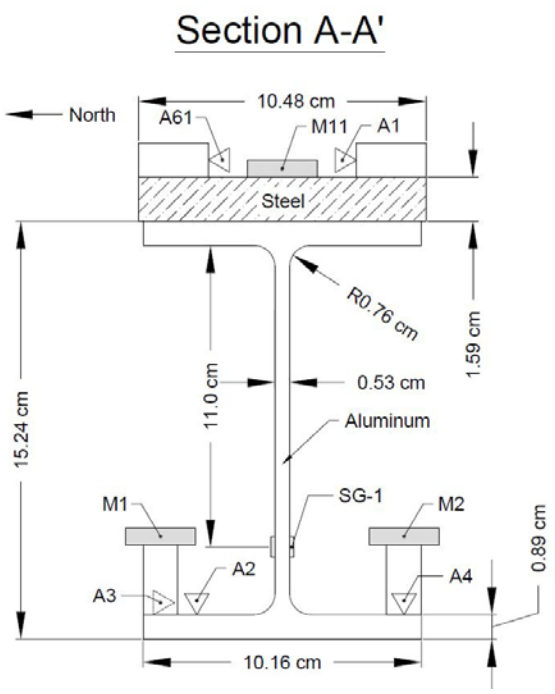

Figure 60: Structure 1 Section for Model JZB02

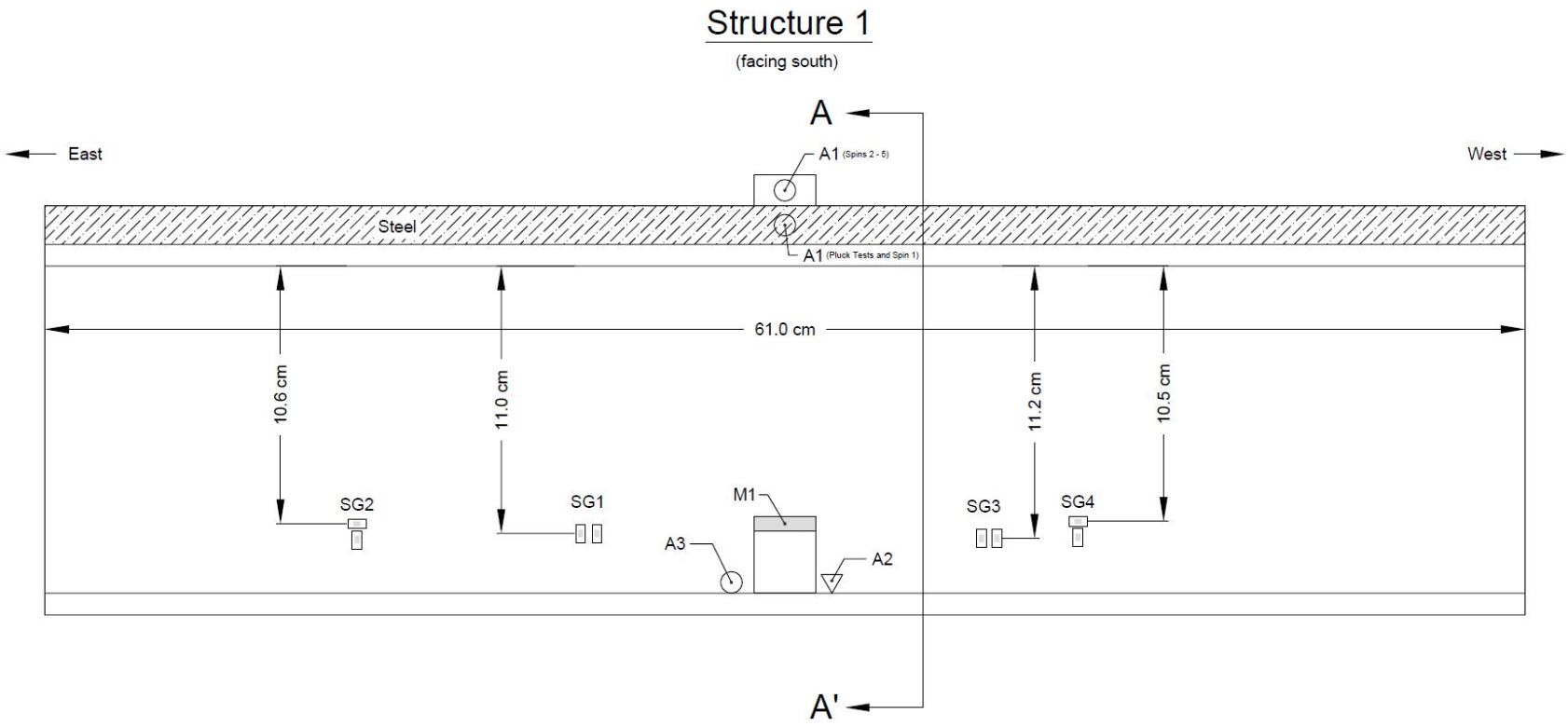

Figure 61: Structure 1 Profile for Model JZB01

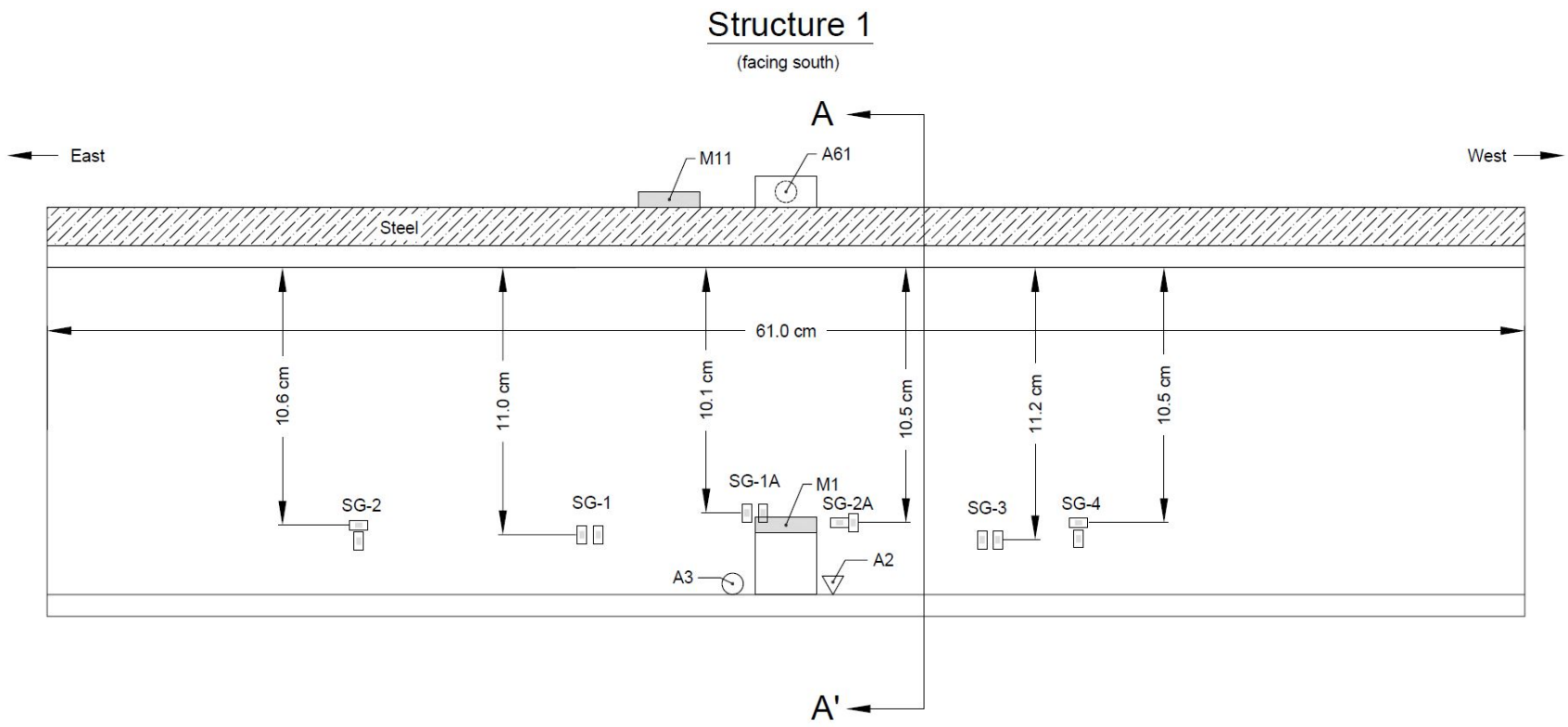

Figure 62: Structure 1 Profile for Model JZB02

Figure 63: Structure 2 Assembly

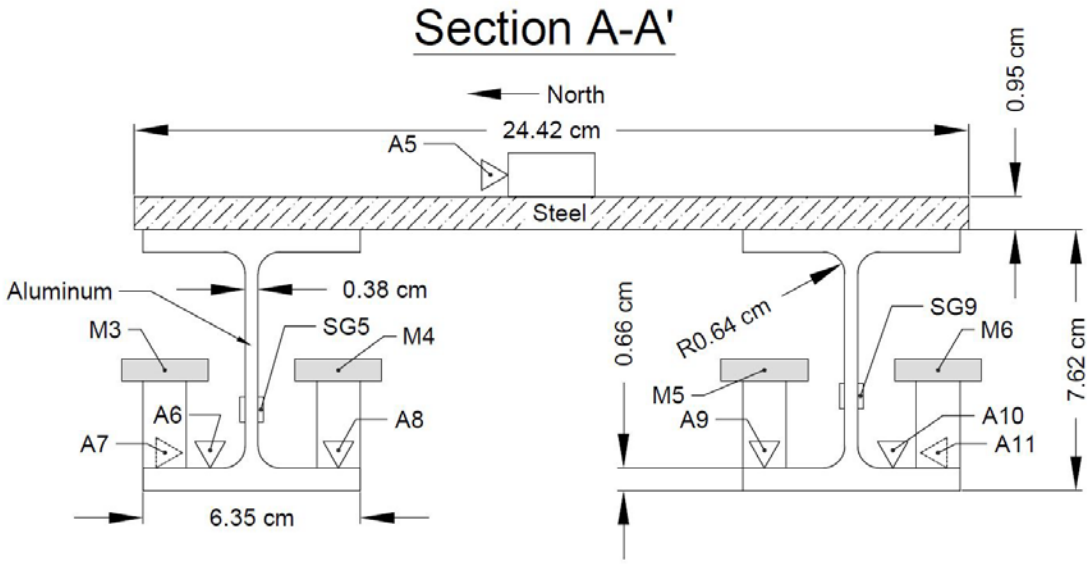

Figure 64: Structure 2 Section

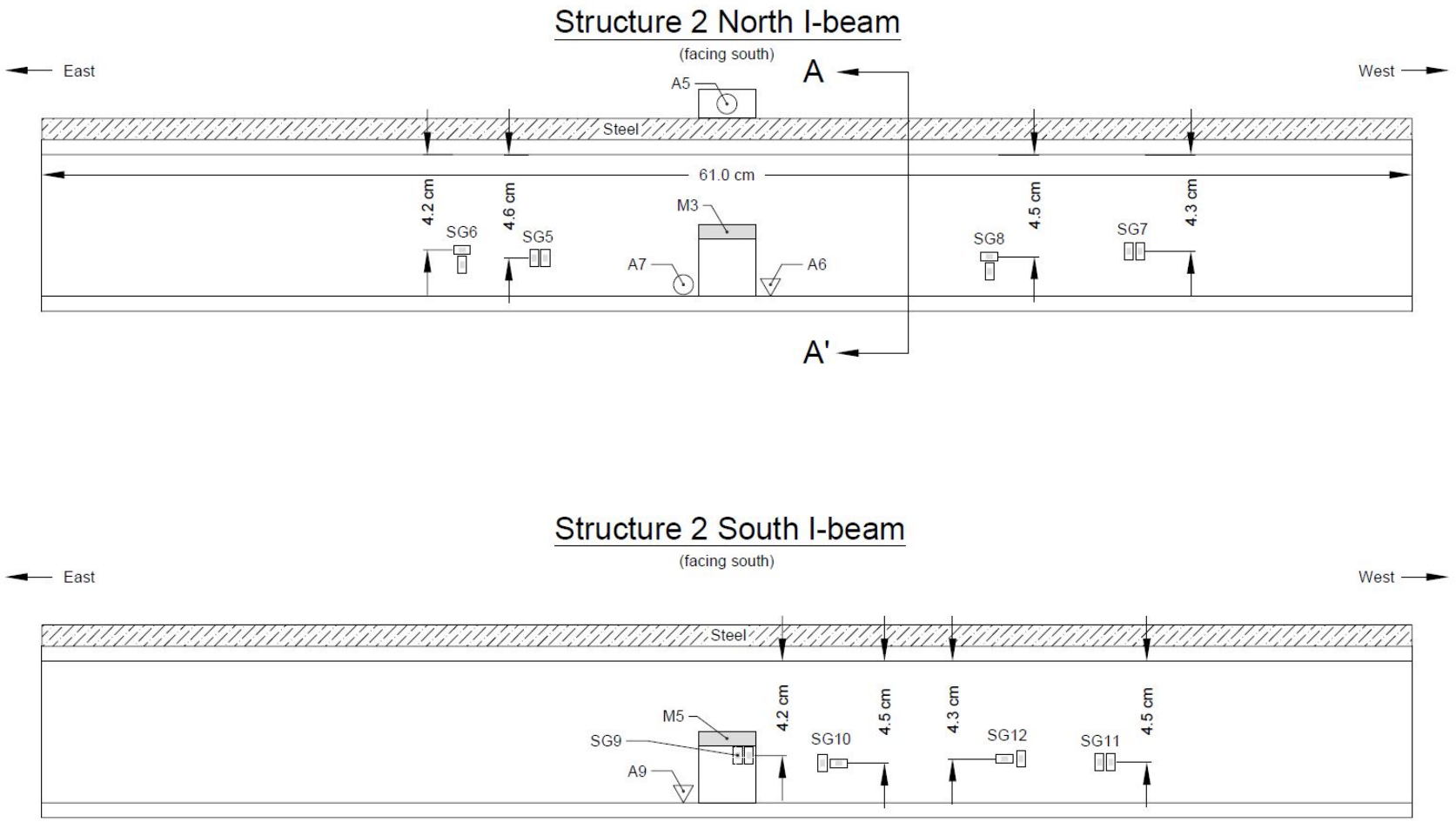

Figure 65: Structure 2 Profile

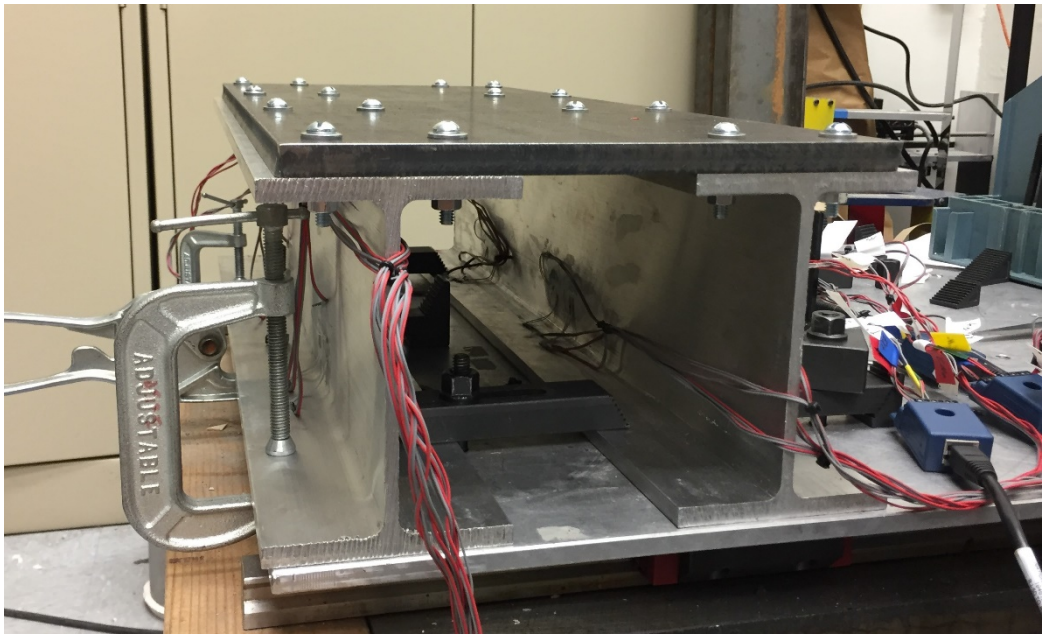

Figure 66: Structure 3 Assembly

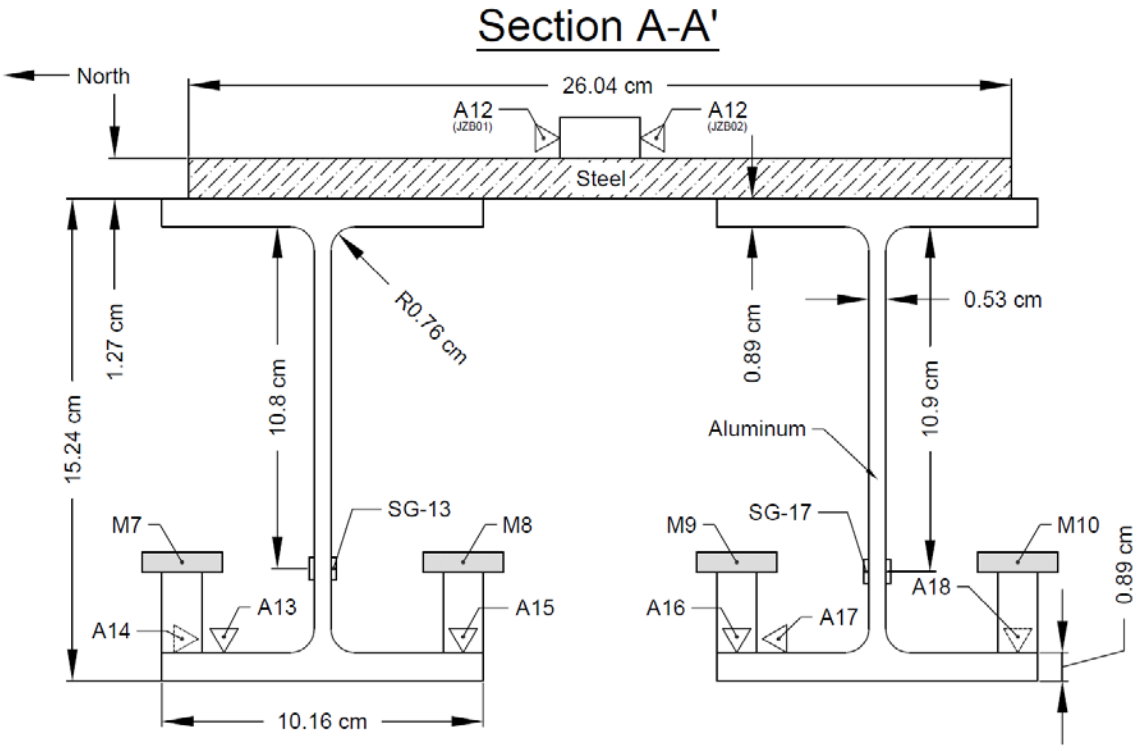

Figure 67: Structure 3 Section

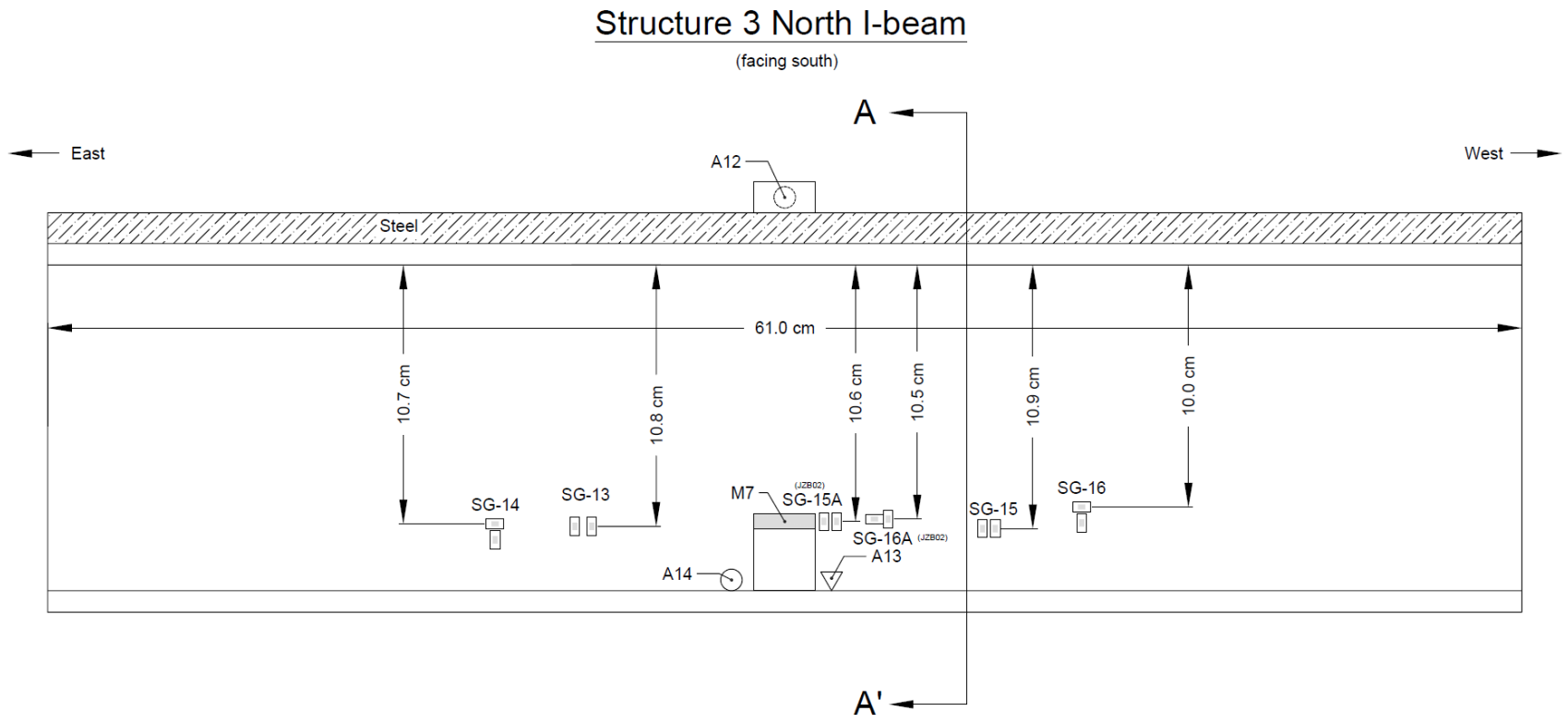

Figure 68: Structure 3 North I-beam Profile

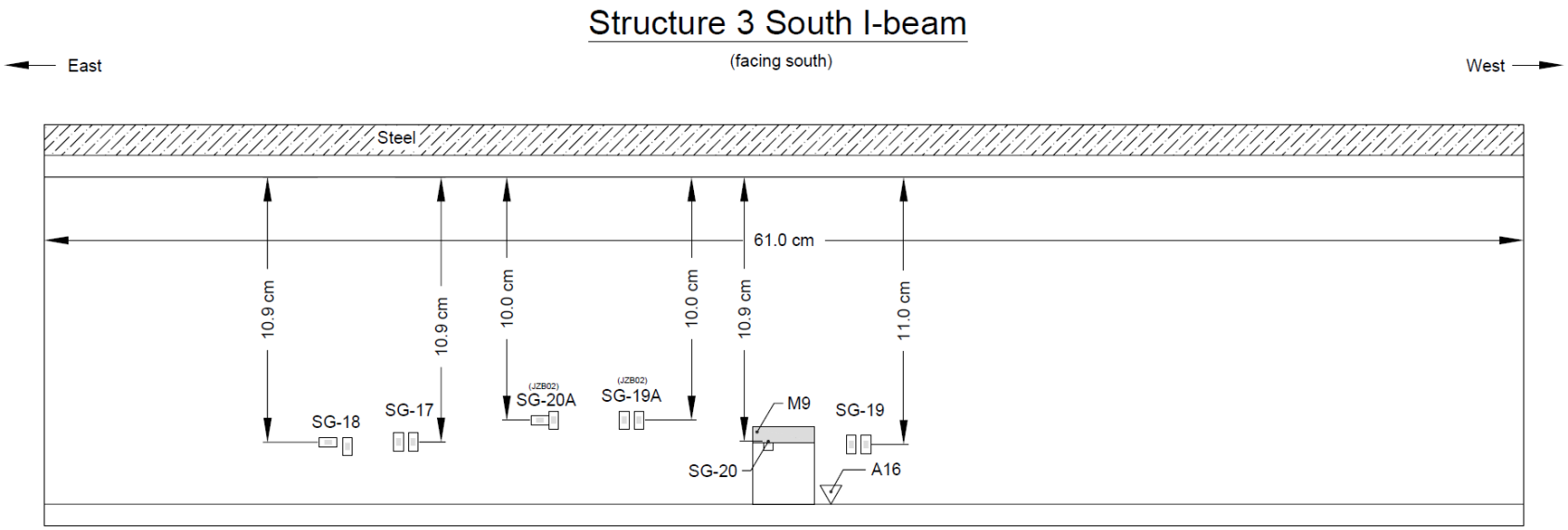

Figure 69: Structure 3 South I-beam Profile

I measured structure masses to evaluate bearing pressure applied by the structures during centrifuge testing. The applied bearing pressure, p is:

$$p = \frac{mN_g g}{B_f L_f} \quad \textbf{(7-1)}$$

Where m is the structure mass, L_f is the length of the bottom structure flange (e.g. the footing) equal to 61 cm, B_f is the bottom structural flange width, N_g is the induced gravity due to centrifugal acceleration in g, and g is the acceleration of gravity. Table 8 below summarizes the p for each structure. The scaling factor for stress between model and prototype scale is unity; therefore, the total bearing pressure applies in both model and prototype scale.

Table 8: Structural Bearing Pressure Summary

Structure	***Total Mass, m (kg)***	***Footing Width, B_f (cm)***	***JZB01 p $N_g = 40g$ (kPa)***	***JZB02 p $N_g = 57g$ (kPa)***
1	12.45	10.2	78.5	111.9
2	14.95	6.4	75.1	107.1
3	24.25	10.4	75.0	106.9

7.2 STRAIN GAGES

I instrumented structures by mounting strain gages to the webs of aluminum I-beams. Strain gages consisted of Omega KFH series 120-ohm gages, with 1-meter-long, pre-soldered leads. Gages were linear pattern gages with a 3-millimeter grid (Omega model no. KFH-3-120-C1-11L1M2R), planar x-y pattern gages with a 3-millimeter grid (KFH-3-120-D16-11L1M2S), and linear pattern gages with a 0.3-millimeter grid (Omega model no. KFH-03-120-C1-11L1M2R). I installed strain gages in Wheatstone full bridges oriented in bending and axial configurations, as shown in Figure 70. I installed gages in the lower half of I-beam webs, as shown in the structure section and profile figures presented in the previous section, with a minimum of two bending and two axial strain gage configurations per I-beam.

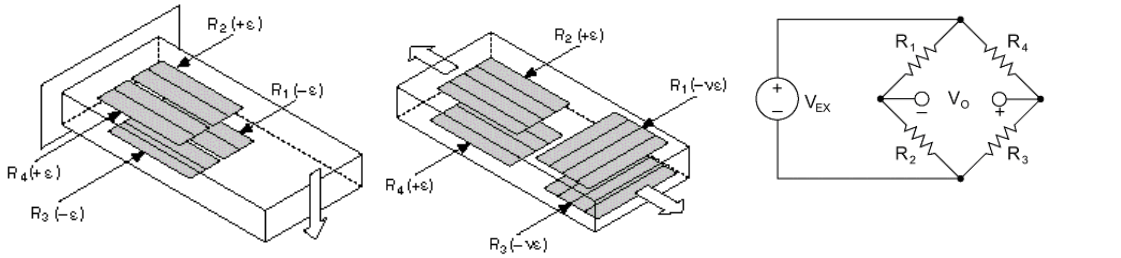

a) Bending Strain b) Axial Strain c) Wheatstone Full Bridge

Figure 70: Strain Gage Configurations (National Instruments, 2018)

7.2.1 Gage Installation

I installed strain gages in general accordance with recommended procedures by Vishay Measurements Group (VMG). Our installation procedure consisted of sanding the target application surface with fine grit sandpaper, cleaning the surface using isopropyl alcohol, applying adhesive compounds to the application surface, and then gluing the gage. Adhesive compounds consisted of a catalyst (M-Bond 200 Catalyst-C by VMG), a solvent

(M-Line Rosin Solvent by VMG), and Loctite 496 super glue. I glued each gage by fixing the gage in the desired position using mylar tape, applying hand pressure until the glue set, and then removing the mylar tape.

I protected the installed gages using Loctite epoxy. I applied epoxy to both the gage ribbons and the gage leads. To facilitate a high-quality bond between the epoxy and aluminum application surface, I sanded the application surface with fine grit sandpaper around the gages and cleaned the surface with isopropyl alcohol prior to applying epoxy.

7.2.2 Strain Measurement

Strain gages oriented in Wheatstone full-bridge configurations measure strain as change in electrical resistance. Strain gage output is expressed as millivolts per volt input (mV/V). The Wheatstone full-bridge expression for strain measurement is:

$$\frac{V_o}{V_{EX}} = \frac{1}{4}\left(-\frac{\Delta R_1}{R_1} + \frac{\Delta R_2}{R_2} - \frac{\Delta R_3}{R_3} + \frac{\Delta R_4}{R_4}\right) \qquad \textbf{(7-2)}$$

This expression may be simplified by defining the gage factor (GF) as:

$$GF = \frac{\Delta R/R}{\varepsilon} \qquad \textbf{(7-3)}$$

Strain measured by bending configuration full bridges in Figure 70 (a) is equal to $-\epsilon_b$ at the R1 and R3 positions and ϵ_b at the R2 and R4 positions. Strain measured by axial configuration full bridges in Figure 70 (b) is equal to ϵ_a at the R2 and R4 positions and $-v\epsilon_a$ at the R1 and R3 positions, where v is Poisson's ratio.

Assuming equal magnitude strain in each gage ($|\varepsilon_{b1}| = |\varepsilon_{b2}| = |\varepsilon_{b3}| = |\varepsilon_{b4}|$), Wheatstone full-bridge sensitivity in the bending configuration is evaluated as:

$$\frac{V_o}{V_{EX}} = \frac{GF}{4}(\varepsilon_{b1} + \varepsilon_{b2} + \varepsilon_{b3} + \varepsilon_{b4}) = GF\varepsilon_b \qquad \textbf{(7-4)}$$

Correspondingly, Wheatstone full-bridge sensitivity in the axial configuration is evaluated as:

$$\frac{V_o}{V_{EX}} = \frac{GF}{4}(\nu\varepsilon_{a1} + \varepsilon_{a2} + \nu\varepsilon_{a3} + \varepsilon_{a4}) = GF\left(\frac{1+\nu}{2}\right)\varepsilon_a \qquad \textbf{(7-5)}$$

The data acquisition system used at the CGM measures strain gage output in a differential module configuration according to the following expression:

$$\varepsilon = \left[\frac{1}{Sensitivity}\right] V_{measured} \qquad \textbf{(7-6)}$$

with $V_{measured}$ equal to V_o/V_{EX}, based on the differential module configuration.

This expression may be reconfigured for consistency with the Wheatstone full-bridge sensitivity equations according to the following:

$$\frac{V_o}{V_{EX}} = \varepsilon_{b,a}[Sensitivity] \qquad \textbf{(7-7)}$$

Bending configuration sensitivity may therefore be expressed as $Sensitivity$=GF and axial configuration sensitivity as $Sensitivity$=GF(1+ν2). The calibrated GF reported by the strain gage manufacturer was 2.01 +/- 1.0% for linear pattern gages with a 3-millimeter grid, 2.01 +/- 1.0% for planar x-y pattern gages with a 3-millimeter grid, and 1.51 +/- 1.5% for linear pattern gages with a 0.3-millimeter grid. The Poisson's ratio, v, of 6061 - T6 aluminum is 0.331. Based on Equation (7-4) for bending configuration sensitivity and Equation (7-5) for axial configuration sensitivity, these values yield:

- $Sensitivity$=2.01mv/V (bending configuration, 3-millimeter grid)
- $Sensitivity$=1.51mv/V (bending configuration, 0.3-millimeter grid)
- $Sensitivity$=1.34mv/V (axial configuration, 3-millimeter grid)
- $Sensitivity$=1.00mv/V (axial configuration, 0.3-millimeter grid)

I considered these sensitivity factors as factory-based sensitivities. While the factory-based sensitivities are likely sufficient for axial configuration strain, bending configuration strain may require further calibration to account for installation effects. I therefore adjusted the sensitivity factors by strain gage calibration factors derived in the next section.

7.2.3 Gage Calibration

I used data collected during pluck testing performed on the structures to calibrate bending configuration strain gages. Pluck testing consisted of clamping the base of each structure to a fixed surface and striking the top of each structure with a rubber mallet. I performed gage calibration by comparing structural response evaluated using an ICP accelerometer to measured strain values. The measured strain values incorporated the Wheatstone full-bridge sensitivity factors derived above.

An understanding of structural response is required to use pluck testing results for strain gage calibration. Structures used in this testing are not readily idealized as simple lumped mass or frame structures due to distributed masses, filleted joints, composite stiffness, and other factors. I consequently evaluated structural response by developing finite element models of the structures using the software RS2 9 Modeler v. 9.029 (Rocscience, Inc., 2018). I simulated structural pluck testing in RS2 using multi-stage dynamic loading that laterally displaced the model and then instantaneously released the displacement. Figure 71, Figure 72, and Figure 73 present the Structures 1, 2, and 3 RS2 models.

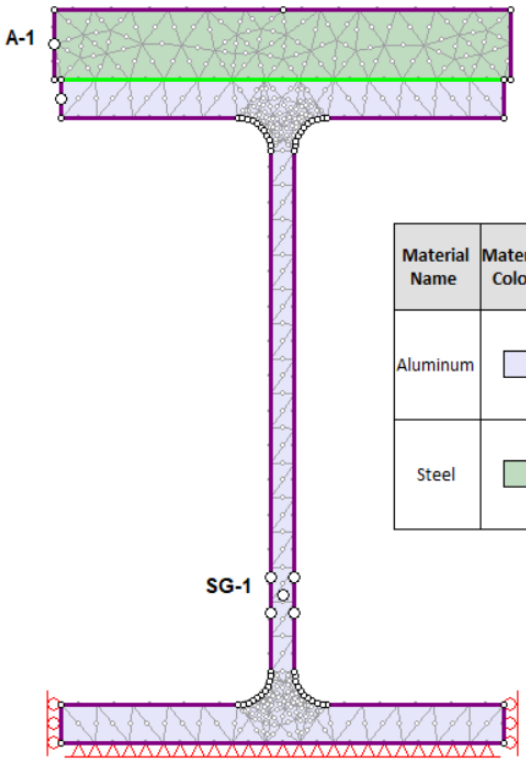

Material Name	Material Color	Initial Element Loading	Unit Weight (kN/m3)	Elastic Type	Poisson's Ratio	Young's Modulus (kPa)	Material Type
Aluminum		Field Stress and Body Force	27	Isotropic	0.33	6.9e+07	Elastic
Steel		Field Stress and Body Force	78.5	Isotropic	0.3	2.5e+08	Elastic

Figure 71: Structure 1 RS2 Model to Simulate Pluck Testing

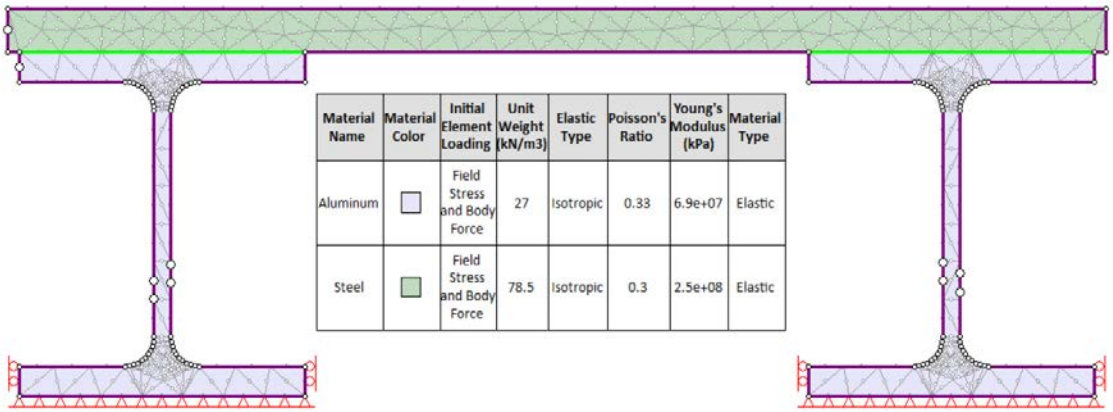

Material Name	Material Color	Initial Element Loading	Unit Weight (kN/m3)	Elastic Type	Poisson's Ratio	Young's Modulus (kPa)	Material Type
Aluminum		Field Stress and Body Force	27	Isotropic	0.33	6.9e+07	Elastic
Steel		Field Stress and Body Force	78.5	Isotropic	0.3	2.5e+08	Elastic

Figure 72: Structure 2 RS2 Model to Simulate Pluck Testing

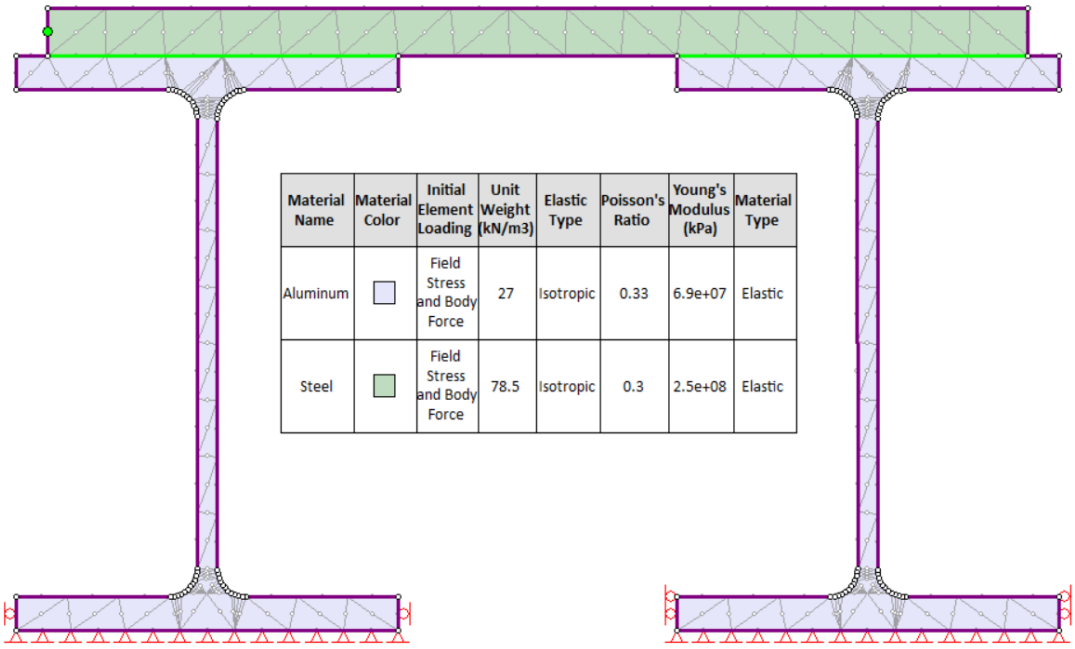

Figure 73: Structure 3 RS2 Model to Simulate Pluck Testing

I evaluated structure response by comparing the relationship between acceleration at a given horizontal accelerometer, a_h (e.g. A1) and strain a given bending-configuration strain gage, ϵ_b (e.g. SG1). Figure 74 presents this comparison and the resulting relationship between accelerometer A1 and for strain gage SG1 on Structure 1. The relationship is linear, which is intuitive because, given first-mode dominant structural response, bending strain is linearly dependent on moment and moment is linearly dependent on the mass acceleration at the top of the structure, along with other constant values. Expressed mathematically:

$$\epsilon_b(t) = \frac{c_w M_{SG}(t)}{EI} = \frac{c_w M_{SG}[\sum a_h(t), m, h]}{EI} \qquad \textbf{(7-8)}$$

E, I, c_w, m, and h are constants specific to the structural system representing Young's modulus, moment of inertia, web thickness, mass, and height, respectively. M_{SG} is moment at the strain gage and $a_h(t)$ is acceleration at the accelerometer position.

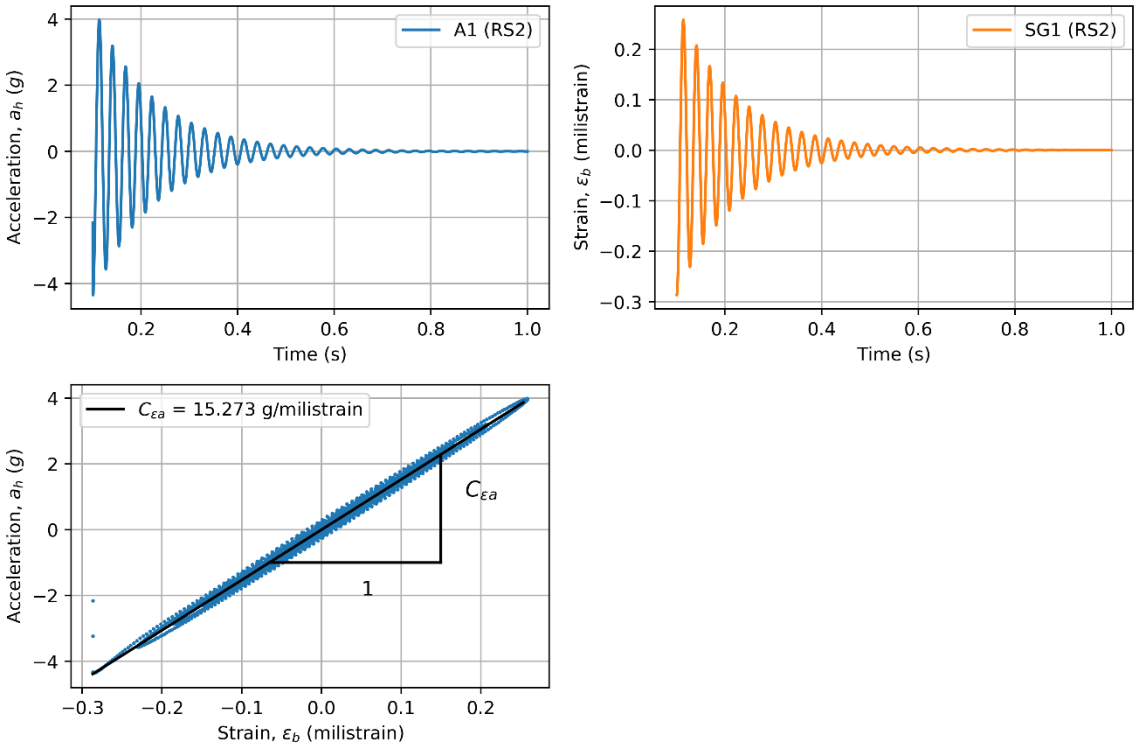

Figure 74: Structure 1 RS2 Relationship between A1 Acceleration and SG1 Strain

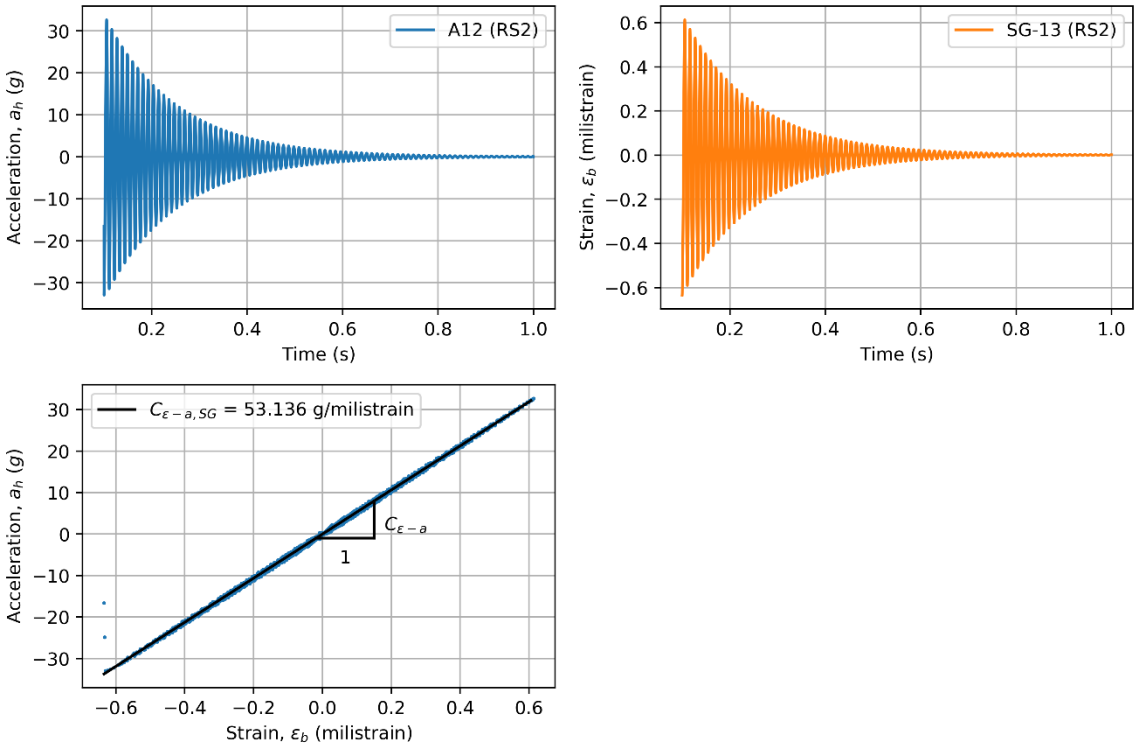

Figure 75: Structure 3 RS2 Relationship between A12 Acceleration and SG13 Strain

The structural system constants may be combined into a singular value for convenience, as:

$$\epsilon_b(t) = \frac{a_h(t)}{C_{\epsilon a}} \qquad \textbf{(7-9)}$$

The $C_{\epsilon a}$ constant is highly dependent on gage position; therefore, I used RS2 to derive this constant for each actual bending configuration gage position on each structure.

I then applied the $C_{\epsilon a}$ constant to calculate bending strain from accelerometer data recorded during pluck testing, $\epsilon_{b,ICP}$ (e.g. from A1). I compared this calculated, analytically-based bending strain with measured strain from the gages during pluck testing, $\epsilon_{b,SG}$ (e.g. from SG1). Figure 76 presents this comparison for strain gage SG1 on Structure 1. Figure 77 presents this comparison for strain gage SG13 on Structure 3. Note the differences in strain response between the structures. For Structure 1, the calculated strain, $\epsilon_{b,ICP}$ is significantly higher than measured strain, $\epsilon_{b,SG}$ immediately after the mallet strike that initiates the pluck test, but then damps to values that are close to measured strain over time. This effect leads to significant scatter in the calculated versus measured strain subplot. This scatter is likely due to contributions from higher mode response in Structure 1 early in the pluck test that damps over time. Subplots (a) and (c) in Figure 76 present the full record, including the higher mode response. Subplots (b) and (d) in the figure present the part of the record that most closely corresponds to single-mode frequency response, with a relatively constant, linear relationship between calculated and measured strain values. Subplot (d) clearly indicates the linear relationship between calculated and measured strain when the record is isolated to single-mode structure response. Structure 3 does not show the effect of higher modes in strain response. Subplots (a) and (b) in Figure 77 demonstrate consistently linear behavior between calculated and measured strain and little scatter exists in the data. This difference likely exists because Structure 1

is a pseudo-lumped mass with less stiffness, whereas Structure 3 is a frame with greater stiffness.

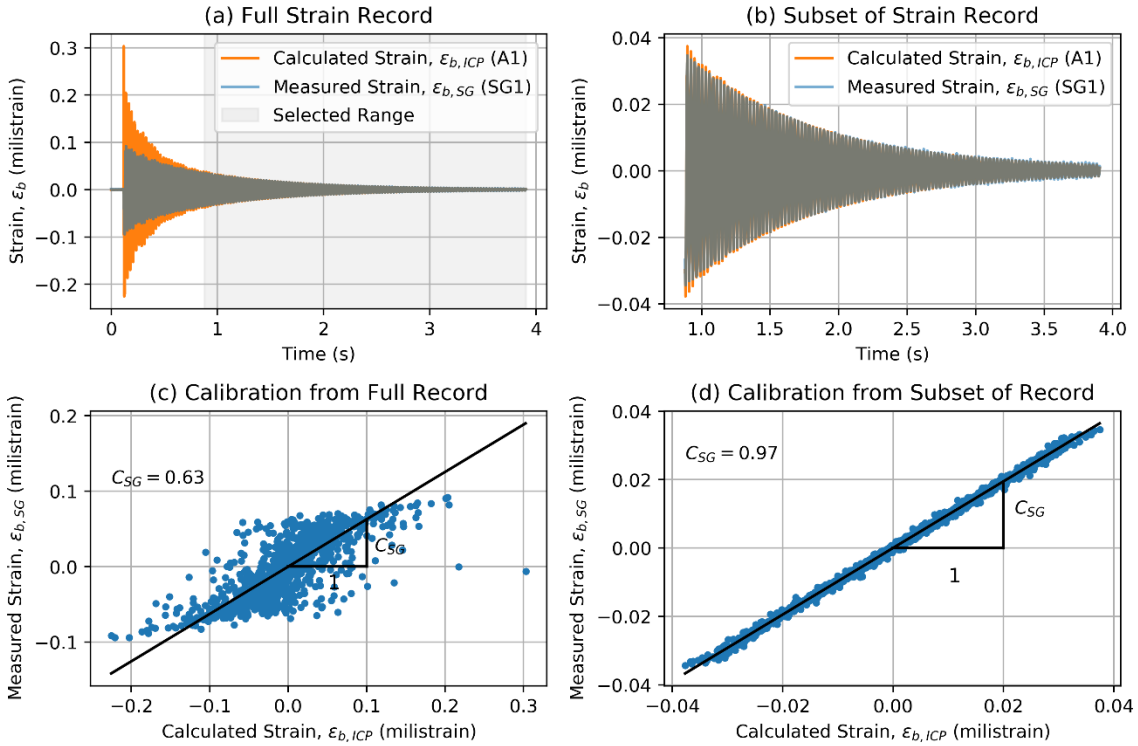

Figure 76: Structure 1 Pluck Test Calibration for Strain Gage SG1

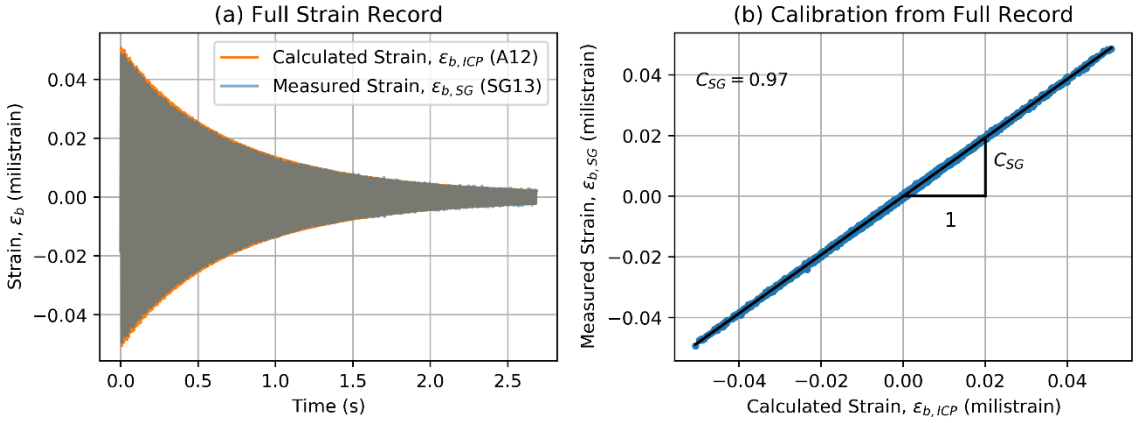

Figure 77: Structure 3 Pluck Test Calibration for Strain Gage SG13

I derived a calibration factor C_{SG} for each bending-configuration strain gage on the structures. I multiplied these calibration factors to the gage sensitivities derived in the previous section to calculate total applied sensitivity factors for each gage. The final bending-configuration strain gage sensitivity is therefore $Sens_{final} = Sensitivity \cdot C_{SG}\ (mv/V)$. Table 9 presents the $C_{\epsilon a}$ constant, calibration factor C_{SG}, and $Sens_{final}$ for each bending-configuration strain gage.

Table 9: Strain Gage Calibration Factors and Sensitivities

Gage	Model JZB01 Gages			Model JZB02 Gages		
	$C_{\epsilon a}$	C_{SG}	$Sens_{final}$	$C_{\epsilon a}$	C_{SG}	$Sens_{final}$
SG-1	15.3	0.97	1.95	20	0.97	1.95
SG-3	15	0.87	1.75	19.7	0.96	1.93
SG-1A	-	-	-	21.3	1.01	2.03
SG-5	123.3	0.95	1.91	123.2	1*	2.01
SG-7	149.5	0.94	1.89	149.4	1*	1.51
SG-9	151.9	1.2	2.41	151.9	1*	2.01
SG-11	130.8	1.08	2.17	130.7	1*	1.76
SG-13	53.1	0.96	1.93	53.1	0.62	1.25
SG-15	54.2	0.94	1.89	54.2	1	2.01
SG-15A	-	-	-	56.5	0.92	1.85
SG-17	54.9	0.89	1.79	54.9	0.89	1.79
SG-19	51.8	0.88	1.77	51.8	0.88	1.77
SG-19A	-	-	-	55.4	1	2.01

7.3 FIXED-BASE STRUCTURAL FREQUENCY

I performed pluck testing to evaluate the fixed-base natural frequency of each structure. I performed pluck testing by clamping the base of each structure to a rigid surface and striking the top of the structure with a rubber mallet. I recorded structure response using strain gages and ICP accelerometers. I evaluated the natural frequency by computing the fast Fourier transform (FFT) of the structural response time histories.

Figure 78, Figure 79, and Figure 80 present the FFTs for the Structure 1, Structure 2, and Structure 3 pluck test response time histories, respectively. This series of pluck tests were performed prior to centrifuge testing for model JZB01. The plots indicate the following:

- **Structure 1** – A peak FFT amplitude at 37 Hertz (Hz), which corresponds to the fixed-base natural frequency, and a smaller FFT amplitude spike at ~85 Hz, which is likely a second mode frequency.
- **Structure 2** – A peak FFT amplitude at 205 Hz, which corresponds to the fixed-base natural frequency, and a smaller FFT amplitude spike at ~440 Hz, which is likely a second mode frequency.
- **Structure 3** - A peak FFT amplitude at 92 Hz, which corresponds to the fixed-base natural frequency, and a smaller FFT amplitude spike at ~180 Hz, which is likely a second mode frequency.

These natural frequencies differ from theoretical frequencies calculated assuming lumped mass or braced frame behavior, as discussed in the section below. The differences reinforce the need to rely on actual measured response of the structures for analysis, as opposed to theoretical response.

I performed similar pluck testing on structures prior to centrifuge testing for model JZB02. I processed the pluck testing data in a manner similar to the JZB01 procedure above. Table 10 indicates fixed-based structural frequencies derived from pluck testing.

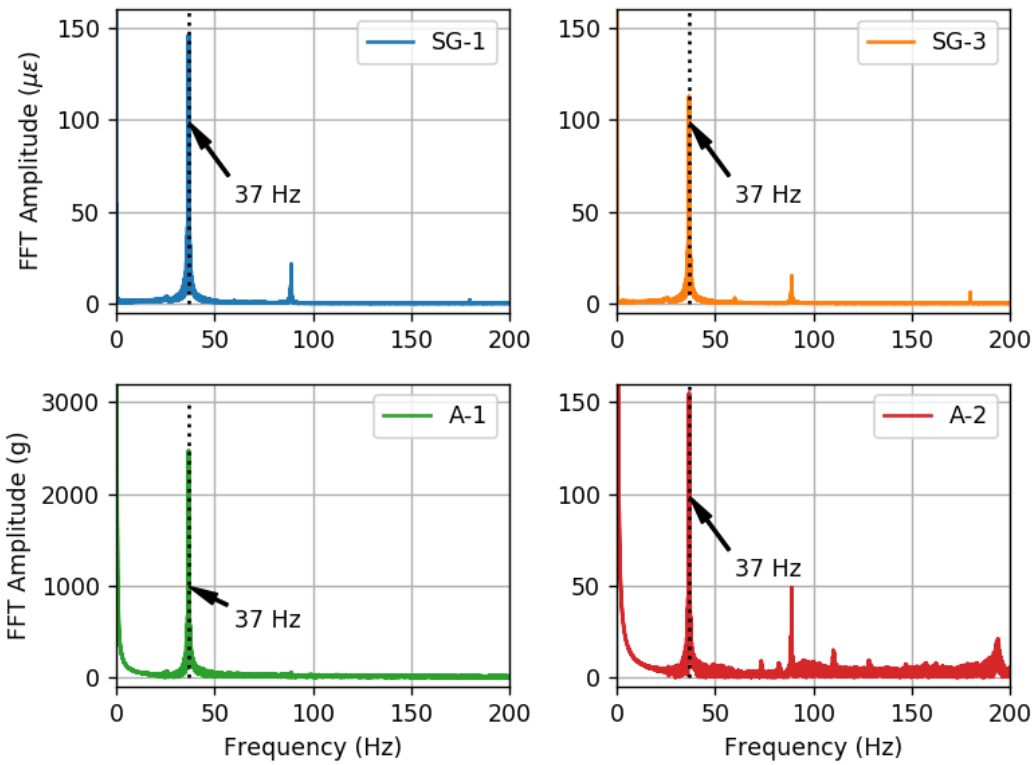

Figure 78: Structure 1 Pluck Test Frequency Data

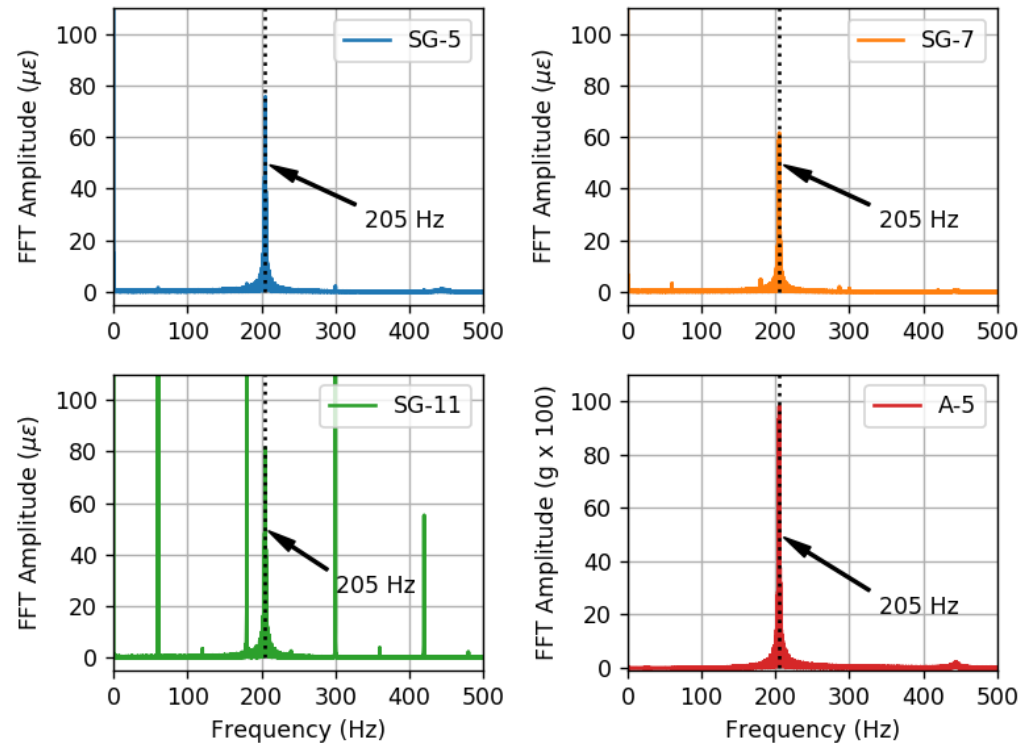

Figure 79: Structure 2 Pluck Test Frequency Data

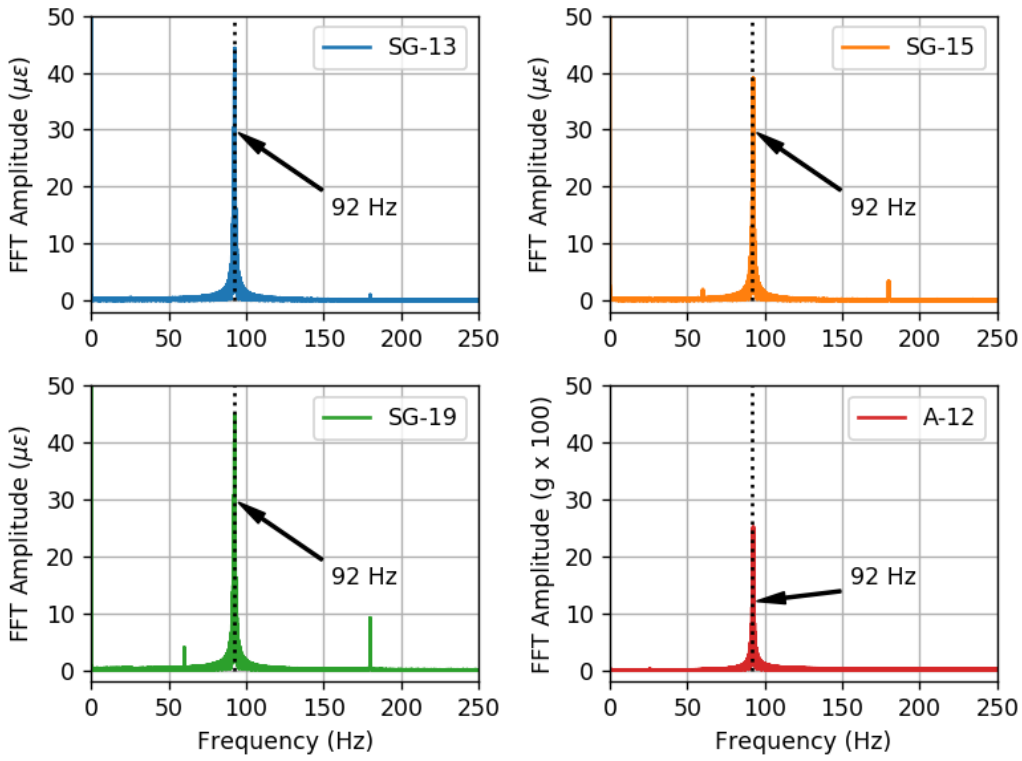

Figure 80: Structure 3 Pluck Test Frequency Data

Table 10: Structure Frequencies

Structure	Model JZB01				Model JZB02			
	Fixed Base, f_n (Hz)		Flexible Base, f_o (Hz)		Fixed Base, f_n (Hz)		Flexible Base, f_o (Hz)	
	Model	Prototype	Model	Prototype	Model	Prototype	Model	Prototype
Structure 1	37	0.93	34	0.85	38	0.67	35	0.61
Structure 2	205	5.13	92	2.30	191	3.35	123	2.16
Structure 3	92	2.30	59	1.47	93	1.63	77	1.33

7.4 STRUCTURAL BEHAVIOR

Structure 1 was previously referred to as a “lumped mass” and Structures 2 and 3 were previously referred to as “frames”. These monikers are not indictive of actual behavior, which differed from these idealizations. This is likely because (1) the structures have distributed mass rather than lumped masses as assumed in the simplified theory, and (2) the fillets that connect the web to flanges complicate selection of a representative length for the stiffness calculation. I consequently the RS2 model detailed above to understand the structural behavior. The following sections summarize structural behavior based on the RS2 models.

7.4.1 Structure 1 Behavior

During structure design, I approximated Structure 1 as a single-mode lumped mass system. The natural frequency of a single-mode lumped mass is expressed:

$$f_{LM} = \frac{1}{2\pi}\sqrt{\frac{k}{m}} = \frac{1}{2\pi}\sqrt{\frac{\frac{3EI}{h^3}}{m}} \qquad \textbf{(7-10)}$$

where k is lateral stiffness, m is the mass, E is Youngs modulus of 6061 T6 aluminum ($E = 68.9\ GPa$), I is the I-beam moment of inertia, and h is the height of the structure. The I-beam moment of inertia, I can be expressed:

$$I = \frac{t^3 L}{12} \qquad \textbf{(7-11)}$$

where t is the thickness of the I-beam web ($t = 0.53cm$) and L is the I-beam length ($L = 60.96cm$).

I assumed structural mass equal to the mass of steel and top aluminum I-beam flange. I assumed structural height equal to the distance from the bottom aluminum I-beam flange

to the center-of-mass of the combined lumped masses. These assumptions yield the following for Structure 1:

$$f_{S1} = \frac{1}{2\pi}\sqrt{\frac{\frac{3EI}{h^3}}{m}} = \frac{1}{2\pi}\sqrt{\frac{\frac{3(68.9GPa)\left[(0.53cm)^3(60.96cm)/_{12}\right]}{(14.95cm)^3}}{9.7kg}} = 35.3Hz \qquad \textbf{(7-12)}$$

This theoretical natural frequency value is lower than the value of 37 or 38 Hz observed during pluck testing (summarized in Section 7.2), which indicates the actual system is stiffer. A stiffer system suggests that differences in geometry between the actual and idealized I-beam (specifically fillets between the I-beam web and flange) may impact the structural response. To evaluate the actual structural behavior, I modeled Structure 1 in RS2, as shown in Figure 81. The figure presents our RS2 model configuration and characteristic deformation shapes at the maximum left and right displacement when subject to simulated pluck testing. The model includes Rayleigh damping with $\alpha = 0.15$ and $\beta = 0.0003$. The damping is not intended to be accurate, but rather to facilitate observation of model response in RS2 and is not critical to our interpretation of structural behavior here. I simulated pluck testing using multi-stage dynamic loading that laterally displaced the model and then instantaneously released the displacement. Figure 82 presents the model displacement response to simulated pluck testing. The figure presents lateral displacement values at query points positioned as shown in Figure 81. Figure 83 presents the FFT of the top query point displacement (QP-1). The figure indicates a peak FFT amplitude at 36.7 Hz, which agrees well with the observed value of 37 or 38 Hz during pluck testing and is near the theoretical value of 35.3 Hz.

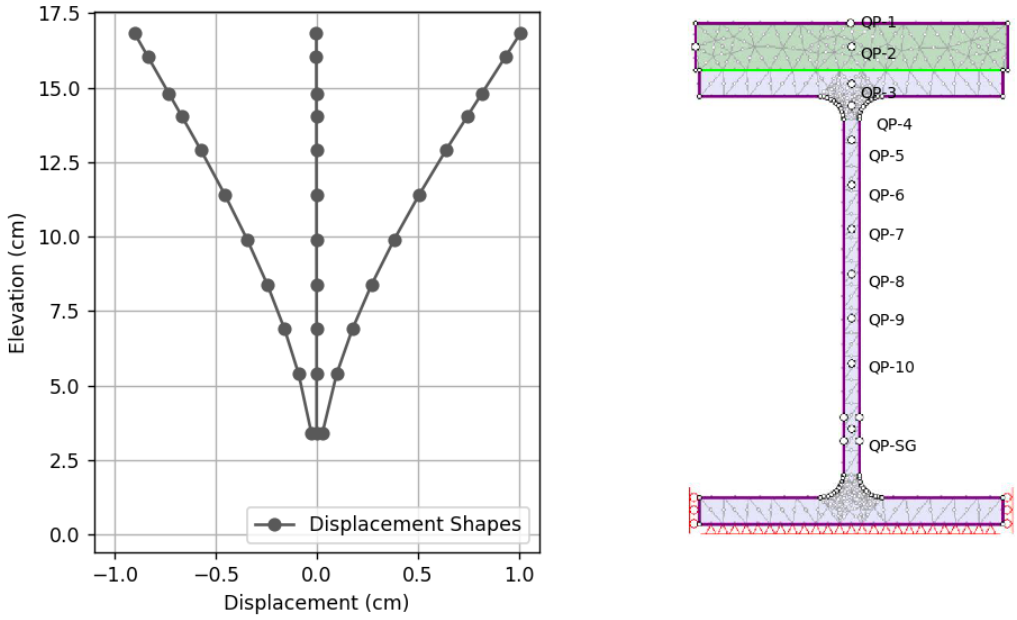

Figure 81: Structure 1 RS2 Model and Displaced Shapes from Pluck Test Modeling

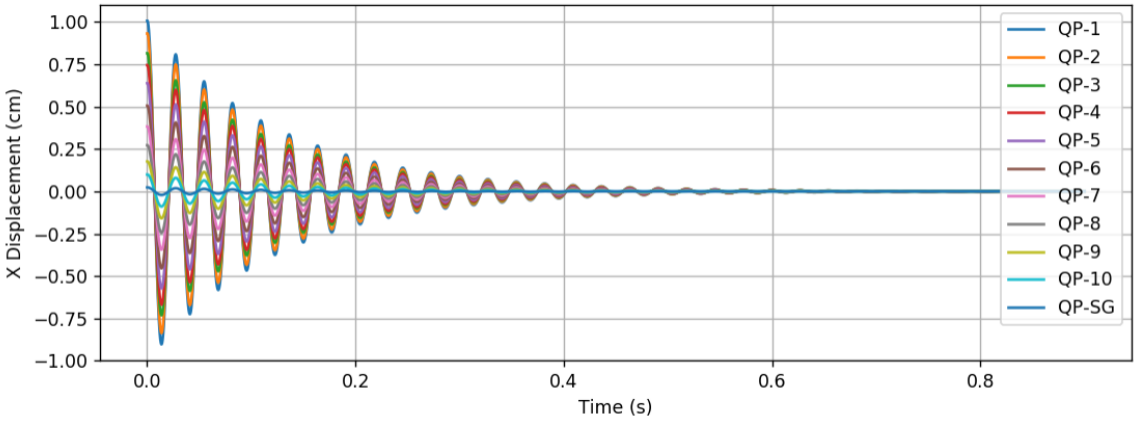

Figure 82: Structure 1 RS2 Model Response to Simulated Pluck Testing

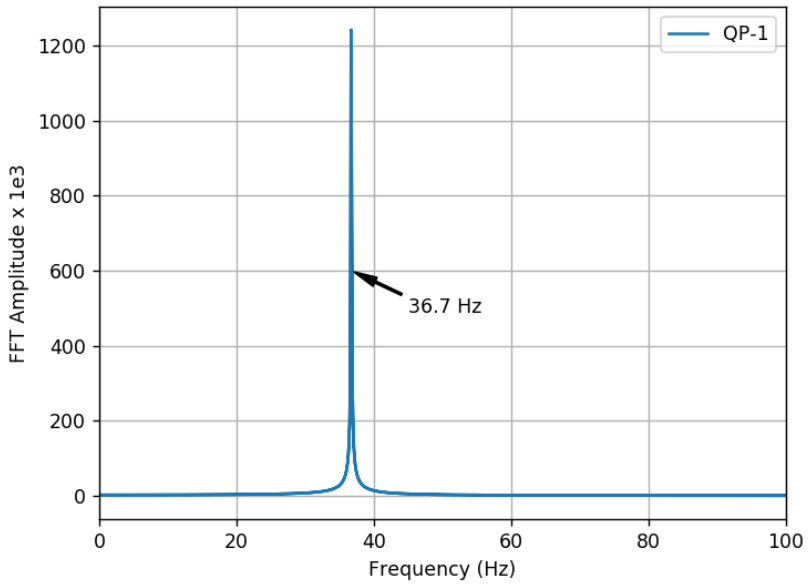

Figure 83: Structure 1 RS2 Model Pluck Test Simulation Frequency Data

7.4.2 Structures 2 and 3 Behavior

During structural design, I approximated Structures 2 and 3 as a single-mode frame system, with a rigid top mass. The natural frequency of a single-mode rigid frame is expressed:

$$f_F = \frac{1}{2\pi}\sqrt{\frac{k}{m}} = \frac{1}{2\pi}\sqrt{\frac{\frac{24EI}{h^3}}{m}} \qquad \textbf{(7-13)}$$

Variables are defined in the previous section. I assumed structural mass equal to the mass of steel and top aluminum I-beam flanges. I assumed structural height equal to the distance from the bottom aluminum I-beam flange to the top I-beam flange. The thickness of the I-beam web is $t = 0.38cm$ for Structure 2 and $t = 0.53cm$ for Structure 3.

These assumptions yield the following for Structure 2:

$$f_{S2} = \frac{1}{2\pi}\sqrt{\frac{\frac{24EI}{h^3}}{m}} = \frac{1}{2\pi}\sqrt{\frac{\frac{24(68.9GPa)\left[(0.38cm)^3(60.96cm)/_{12}\right]}{(6.30cm)^3}}{12.8kg}} = 192.1Hz \qquad \textbf{(7-14)}$$

These assumptions yield the following for Structure 3:

$$f_{S2} = \frac{1}{2\pi}\sqrt{\frac{\frac{24EI}{h^3}}{m}} = \frac{1}{2\pi}\sqrt{\frac{\frac{24(68.9GPa)\left[(0.53cm)^3(60.96cm)/_{12}\right]}{(13.46cm)^3}}{18.5kg}} = 84.8Hz \qquad \textbf{(7-15)}$$

Like Structure 1, these theoretical natural frequencies differ from the values observed during pluck testing. Structure 2 natural frequencies from pluck testing were 205 Hz for JZB01 and 191 Hz for JZB02, which suggest stiffer response for the JZB01 model and similar response for the JZB02 model. Structure 3 natural frequencies from pluck testing were 92 Hz and 93 Hz for JZB01 and JZB02, respectively, which indicates the actual system is stiffer. Actual model behavior is consistently stiffer than the theoretical response, with the exception of the Structure 2 pluck test for JZB02. These results underscore the need to use measured response for these structures during analysis, as opposed to a theoretical structure response.

7.5 FLEXIBLE-BASE STRUCTURAL FREQUENCY

I evaluated the flexible-base natural frequency of each structure during centrifuge testing. I performed the evaluation using a low amplitude step motion administered to the model during spinning. Information regarding ground motions and model spinning is presented in Chapters 5 and 6. These chapters also present instrumentation configurations, channel lists, and model sketches in plan and profile. I used the post-processed step motion generated from the procedure in Chapter 8 to evaluate flexible-base natural frequency.

The post-process step motion file is 02072018@092140@112100@64.4rpm.txt for JZB01 and 01162019@082639@110817@77.0rpm.txt for JZB02.

I evaluated the flexible-base natural frequency of each structure by calculating coherence and computing transfer functions between accelerometer response at the roof of each structure and corresponding accelerometer response in the far field. I then filtered transfer function data for frequencies where signal coherence was greater than 0.95 for Structures 1 and 3 on model JZB01 and all structures for model JZB02. The signal for Structure 2 on model JZB01 was less coherent, so I used a threshold coherence of 0.85 for the filter. I finally fit a theoretical transfer function curve from Chopra (2012) for a single degree of freedom system with 5 percent damping to the filtered transfer function datapoints. I used the best fit curve for Structures 1 and 3 on model JZB01 and all structures for model JZB02 from a nonlinear curve fitting procedure that varied natural frequency and damping. I selected a fitted curve for Structure 2 on model JZB01 due to the poor quality of curve fitting from the nonlinear procedure. I assumed the peak of the fitted transfer function curve to correspond to the flexible-base natural frequency of the structure. Figure 84 presents this evaluation for the model JZB01 structures and Figure 85 presents this evaluation for the JZB02 structures. Table 10 above summarizes the flexible-base natural frequencies for each structure respective of each model.

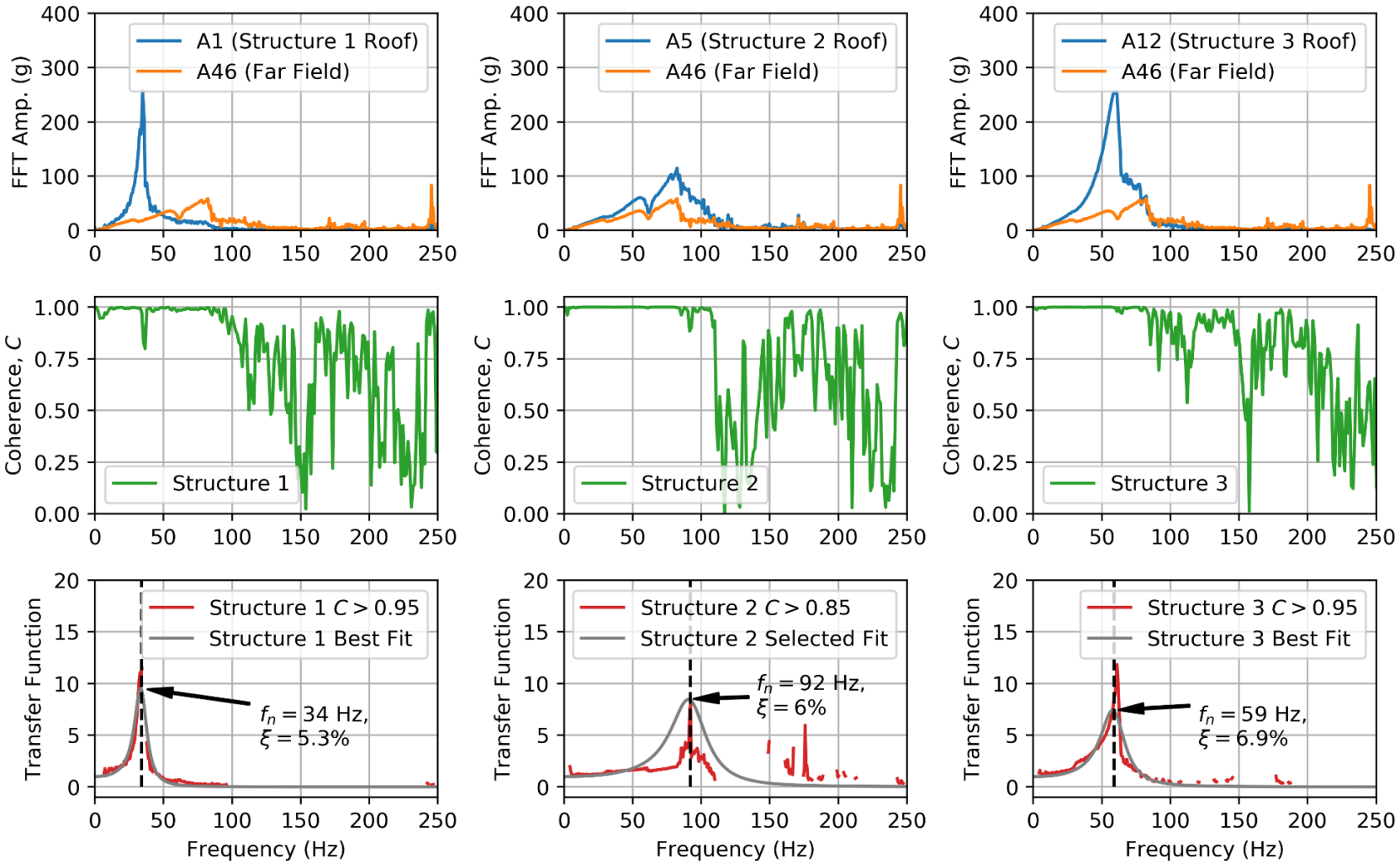

Figure 84: JZB01 Flexible-Base Structural Frequency Evaluation

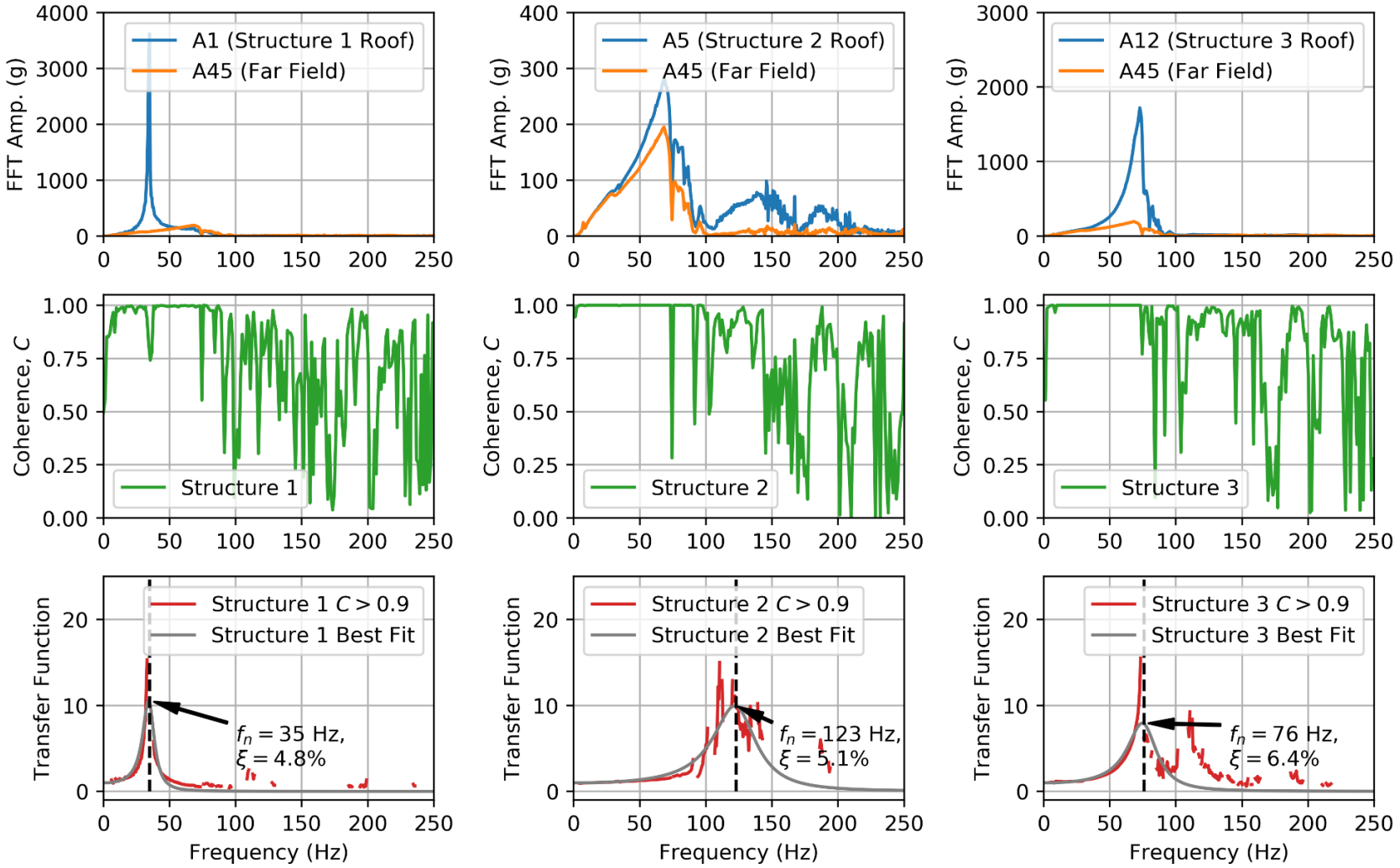

Figure 85: JZB02 Flexible-Base Structural Frequency Evaluation

8 DATA PROCESSING AND PRESENTATION

The shaking event sequence applied to centrifuge models JZB01 and JZB02 yielded a rich source of data to evaluate soil and structure response. Selected portions of the data are presented here to demonstrate various soil or structural performance parameters and give the reader a sense of the available data. Full presentation of the data is not possible in this dissertation due to the large number of instrument recordings collected during applied ground motions (e.g. 113 instruments over 14 ground motions in model JZB01 and 136 instruments over 14 ground motions in model JZB02). For a presentation of the full suite of instrument recordings, see the interactive data reports for model JZB01 (Buenker et al., 2019) and model JZB02 (Buenker et al., 2020a) published on the platform DesignSafe-CI. The data reports are published as Jupyter notebooks, which allow the user to interactively view, select, and export data.

8.1 DATA PROCESSING

Data output from instrument recordings for models JZB01 and JZB02 requires processing. I processed accelerometer data by applying truncation, baseline correction, a Tukey window, and high and low pass Butterworth filters. This data processing procedure is in general accordance with the procedure utilized in NGA-West2 (Ancheta et al., 2013) with some variations. Figure 86 presents the procedure. I processed strain gage and LP data by applying truncation and subtracting the initial value of the data recording from the data set. I processed PPT data by applying truncation.

All ground motion records presented in this chapter are in model-scale units unless otherwise noted. Conversion to from model-scale to prototype-scale units of acceleration can be performed by dividing values by N_g. Conversion to from model-scale to prototype-scale units of time and distance can be performed by multiplying values by N_g. Model-scale and prototype-scale units of velocity are equal and need not be modified by N_g.

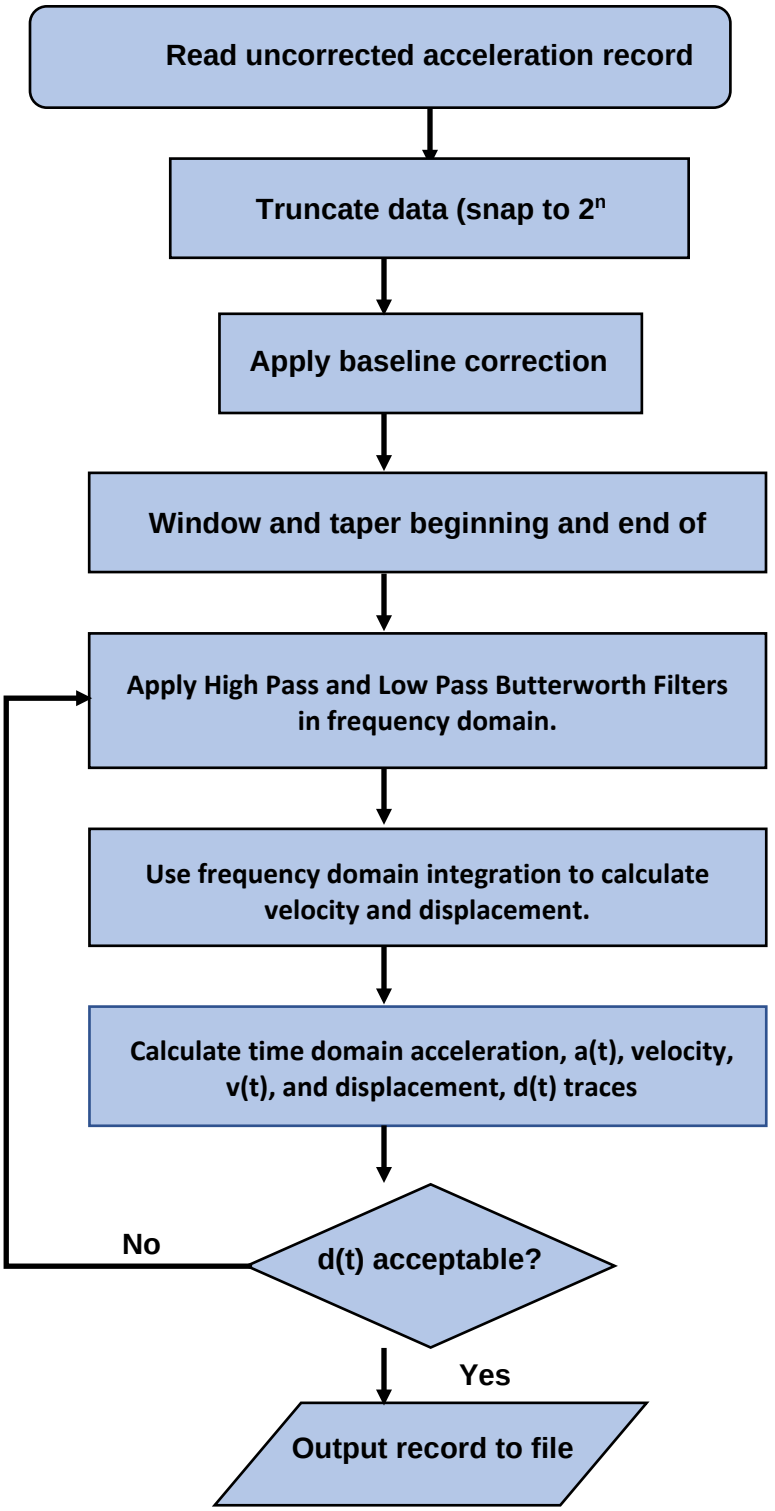

Figure 86: Acceleration Record Processing Procedure

8.1.1 Data Truncation

Ground motion data generated from models JZB01 and JZB02 was collected at user-controlled intervals at 5000 Hz sampling frequency. Centrifuge operators begin data collection several seconds prior to administering the ground motion and terminate data collection several seconds after ground motion is complete. This procedure creates long ground motion records that require truncation to isolate the predominant motion.

I truncated each ground motion record by selecting the range of each recording that represents the predominant ground motion. I typically selected ranges such that ½- to 1-seconds of the record exist before and after the predominant motion. I snapped truncation to the nearest 2^n data points to facilitate efficient calculation of Fast Fourier Transforms (FFTs) of the data. Figure 87 presents an example ground motion truncation.

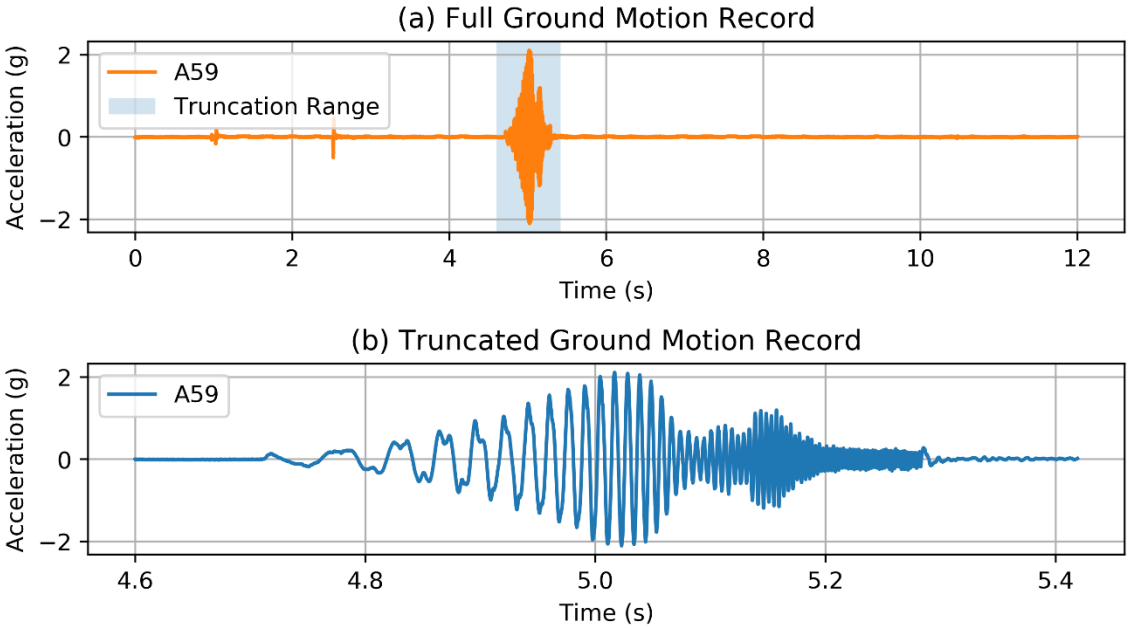

Figure 87: Data Truncation for JZB 01 Motion No. 1 – SW7-333 [0.2]

8.1.2 Baseline Correction

Baseline correction or detrending consists of subtracting a fitted curve from the accelerometer ground motion data to eliminate baseline creep or trending effects that occur during shaking. I performed baseline correction by subtracting the mean acceleration from the acceleration time series. Figure 88 presents an example baseline correction. Note that processing is not complete yet for the record shown in the figure and unwanted effects remain in the velocity and displacement traces. These effects are removed by subsequent data processing steps.

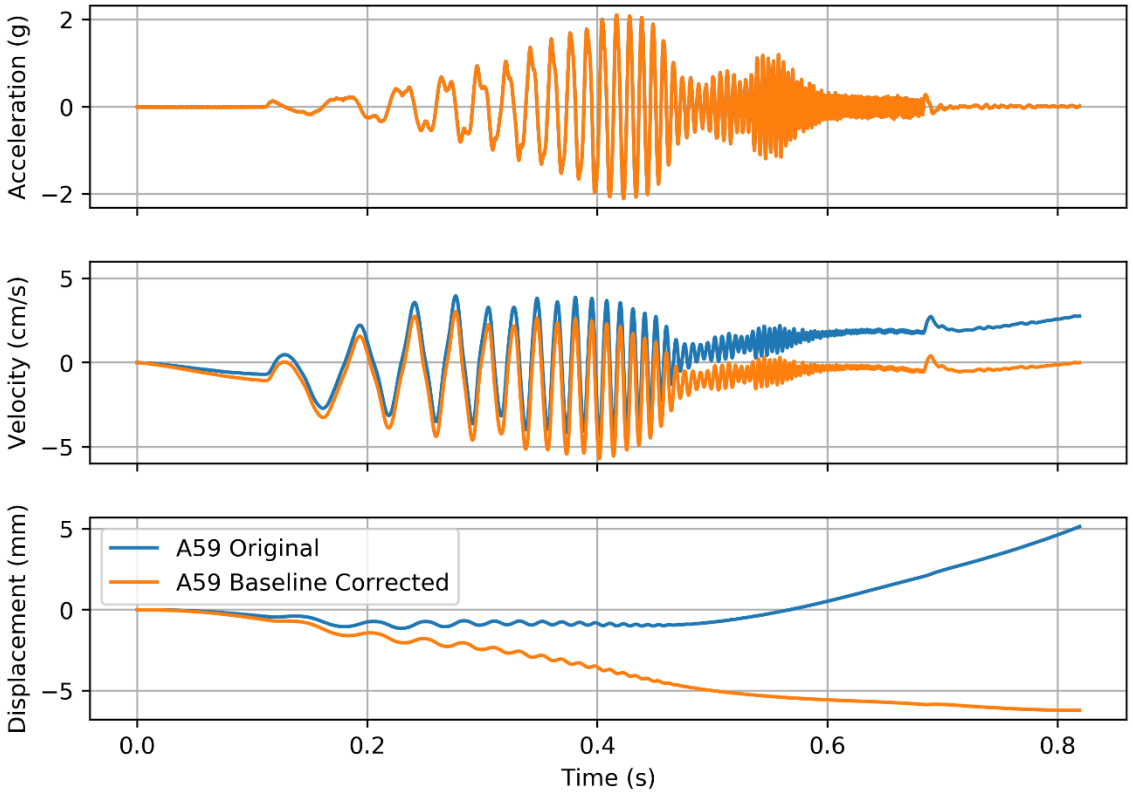

Figure 88: Baseline Correction for JZB 01 Motion No. 1 – SW7-333 [0.2]

This baseline correction procedure differs from the NGA-West2 procedure (Ancheta et al., 2013), which consists of subtracting the mean from the acceleration time series prior to other data processing (e.g. windowing and filtering) and then fitting a 6th-order polynomial

to the displacement trace after processing. The second derivative of the fitted polynomial is then subtracted from the acceleration time series. Although our procedures differ, the procedural intent and result are similar, which is elimination or reduction of velocity and displacement creep in the final time series.

8.1.3 Tukey Window

The Tukey or tapered cosine window applies a weighing function to the ground motion recording to generate zero or near-zero acceleration at the beginning and end of the record, while preserving acceleration in the zone of the predominant motion. Windowing reduces spectral leakage in the FFT, which assumes an infinitely harmonic input motion and is subject to spectral leakage if motions near the end of the recording are non-zero. The Tukey window is expressed using a time-domain shape parameter, α representing the fraction of the window inside the cosine tapered region. The Tukey window expression is:

$$w(n) = \begin{cases} \frac{1}{2}\left(1+\cos\left[\pi\left(\frac{2n}{\alpha[N-1]}-1\right)\right]\right), & 0 \le n < \frac{\alpha(N-1)}{2} \\ 1, & \frac{\alpha(N-1)}{2} \le n < (N-1)\left(1-\frac{\alpha}{2}\right) \\ \frac{1}{2}\left(1+\cos\left[\pi\left(\frac{2n}{\alpha[N-1]}+1-\frac{2}{\alpha}\right)\right]\right), & (N-1)\left(1-\frac{\alpha}{2}\right) \le n \le (N-1) \end{cases} \quad \textbf{(8-1)}$$

Here N represents the total number of time series points and n represents the index of individual time series points. I applied Tukey windows with α ranging from 0.25 to 1, depending on the ground motion. Figure 89 presents a Tukey window and an example application of the windowing function. This figure indicates little change in the ground motion due to the Tukey window, because acceleration values were already near-zero at the beginning and end of the original motion.

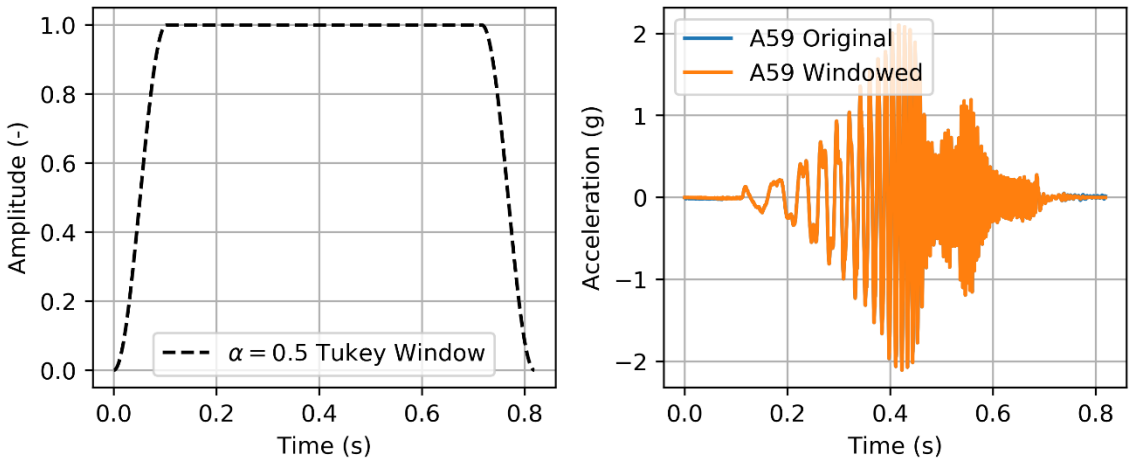

Figure 89: Tukey Window for JZB 01 Motion No. 1 – SW7-333 [0.2]

8.1.4 Butterworth Filter

Ground motion data collected during shaking routinely contains unwanted motions that are not part of the predominant shaking. These unwanted motions appear as background noise in the ground motion recording and may be generated by machinery, hydraulics, instrument base instability or other sources of motion that may impact the accelerometer recording. Centrifuge testing involves significant background noise due to the size and scale of machine components involved relative to the input ground motions.

I filtered unwanted motions and background noise from ground motion recordings using high and low pass Butterworth filters. To apply filters, I calculated FFTs of each ground motion recording and multiplied the FFT amplitudes by the following Butterworth filter frequency amplitudes:

$$High\ Pass: \qquad H(\omega)_{HP} = \frac{1}{\sqrt{1 + \left(\frac{\omega_{HC}}{\omega}\right)^{2n_H}}} \tag{8-2}$$

$$Low\ Pass: \qquad H(\omega)_{LP} = \frac{1}{\sqrt{1 + \left(\frac{\omega}{\omega_{LC}}\right)^{2n_L}}} \tag{8-3}$$

Each filter is defined by respective corner frequencies, ω_{CH} and ω_{LC} and filter orders, n_H and n_L. Figure 90 presents a Butterworth filter and example application of the filter function.

I applied filters by reviewing ground motion recordings for both predominant ground motion frequencies and errant frequencies that did not fit the ground motion. I then selected filter corner frequencies that reduced errant frequencies while preserving the predominant ground motion. I used filter order of $n_H = n_L = 2$ high and low pass filters.

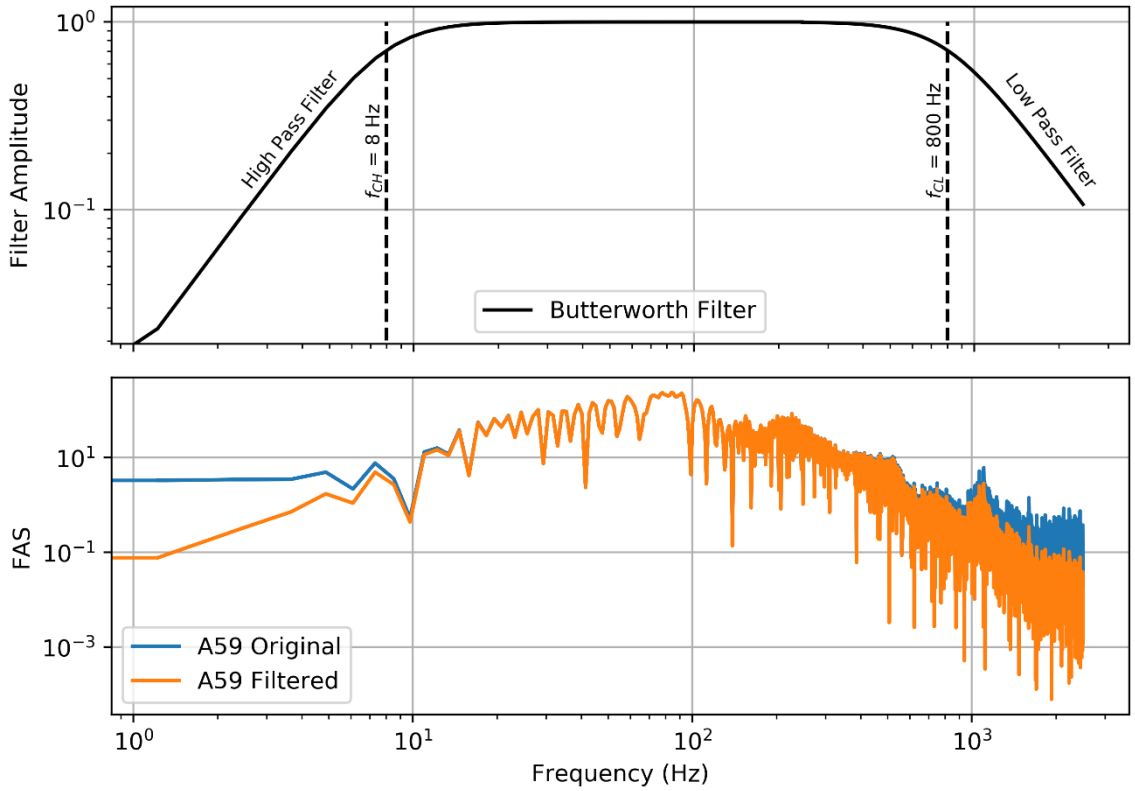

Figure 90: Butterworth Filter for JZB 01 Motion No. 1 – SW7-333 [0.2]

8.1.5 Processing Sequence

I performed the data processing sequence using an interactive Jupyter notebook. The notebook applies data truncation to all accelerometer recordings in the ground motion, while individually applying baseline correction, Tukey windowing, and filtering. The

notebook therefore enables the user to select different baseline corrections, Tukey windows and filters for different accelerometers in the same ground motion recording. Figure 91 presents a view of the Jupyter notebook used to process these ground motions.

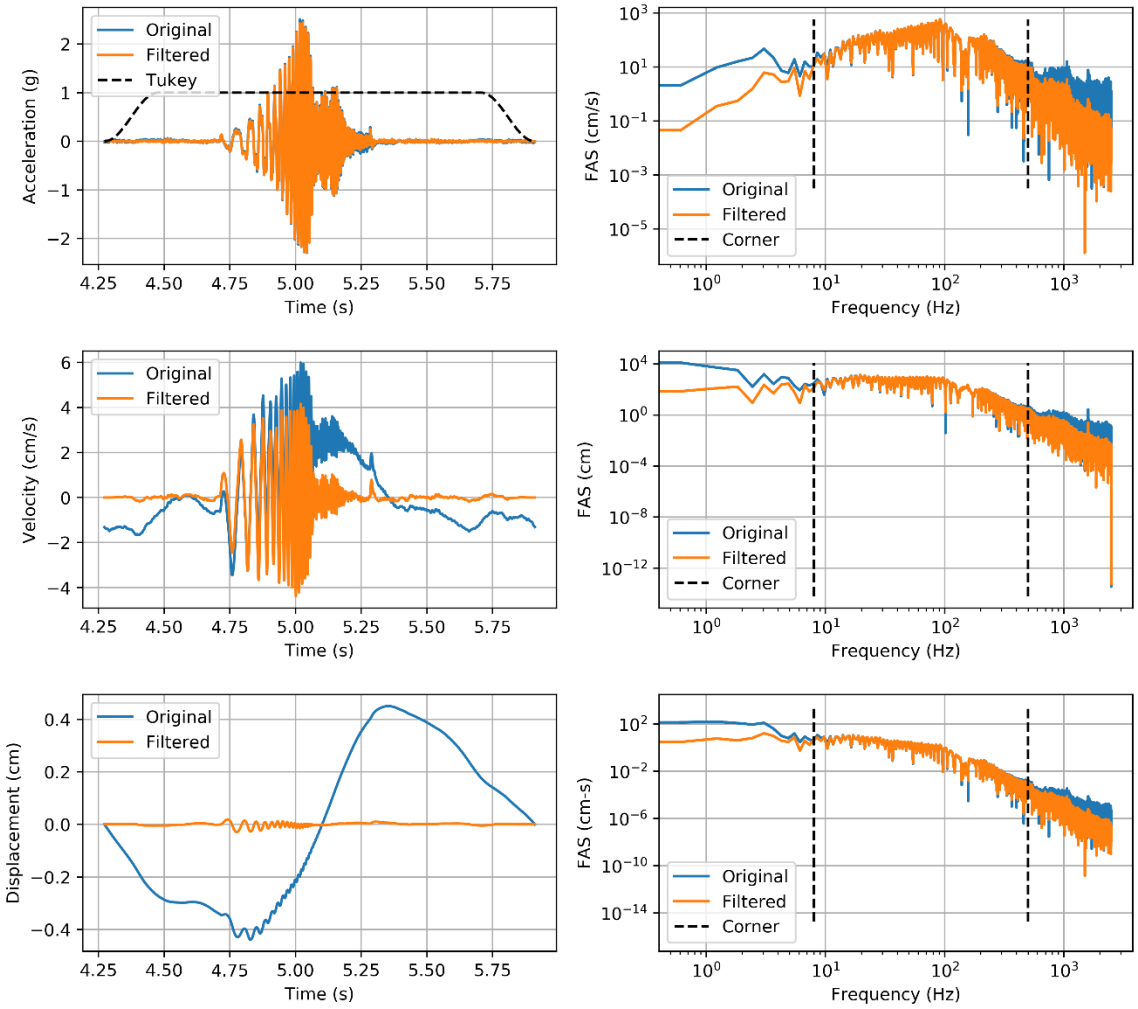

Figure 91: Jupyter Notebook Used to Process Motions with JZB01 Data from SW7-333 [0.2]

8.1.6 Processed Ground Motions

I processed JZB01 and JZB02 ground motions by visually inspecting the plotted records and applying the processing parameters necessary to isolate the predominant ground motion. Because the parameters required to processes accelerometer data were generally similar for ICPs and MEMS accelerometers, respectively, I selected a single

group of parameters for all ICPs and all MEMs for a given data record. Table 11 and Table 12 present the applied data processing parameters I selected for model JZB01 and JZB02 ground motions, respectively.

I output processed motions as ASCII text files for publishing and analysis. Each text file contains ground motion data for all model instrumentation active during testing, including ICP and MEMS accelerometers, strain gages, LPs, and PPTs. Data are published in the data reports for JZB01 and JZB02 on DesignSafe-CI (Buenker et al., 2019; Buenker et al., 2020a). Data published in the data reports include both raw binary data files and processed ASCII files, along with Jupyter notebooks utilized to process the data.

Table 11: JZB01 Applied Data Processing Parameters

Shake No.	*Event Name*	*Scale Factor*	Truncation Start (s)	Number of Data Points	Tukey Period (s)	ICP High Pass Corner (Hz)	ICP Low Pass Corner (Hz)	MEMS High Pass Corner (Hz)	MEMS Low Pass Corner (Hz)
0	Step	2	6.1926	8192	0.5	8	1000	8	500
1	SW7-333	0.2	4.2286	8192	0.5	8	500	8	1000
2	TCU-078	0.2	5.6382	16384	0.5	8	2000	8	2000
3	SW7-333	0.4	3.7856	8192	0.5	8	1000	8	1000
4	TCU-078	0.4	4.8644	16384	0.5	8	2000	8	2000
5	SW7-333	0.2	3.756	8192	0.5	10	2000	12	2000
6	TCU-078	0.6	4.1062	16384	0.5	8	2000	8	2000
7	SW7-333	0.2	5.349	8192	0.5	10	2000	16	2000
8	TCU-078	0.8	4.9904	16384	0.5	8	2000	10	2000
9	SW7-333	0.2	3.815	8192	0.5	10	2000	20	2000
10	TCU-078	1	3.6084	16384	0.5	8	2000	12	2000
11	Kobe-PI(83)	1	3.9846	8192	0.5	8	2000	8	2500
12	SW7-333	0.2	3.9846	8192	0.5	8	2000	8	2000
13	SW7-333	1	4.4058	8192	0.5	10	2000	20	2000

Table 12: JZB02 Applied Data Processing Parameters

Shake No.	*Event Name*	*Scale Factor*	Truncation Start (s)	Number of Data Points	Tukey Period (s)	ICP High Pass Corner (Hz)	ICP Low Pass Corner (Hz)	MEMS High Pass Corner (Hz)	MEMS Low Pass Corner (Hz)
0	Step	2	2.2246	8192	0.4	8	2000	12	500
1	SW7-333	0.2	4.3908	8192	0.5	8	-	12	-
2	TCU-078	0.2	6.1052	16384	0.5	8	-	8	-
3	SW7-333	0.4	5.347	8192	0.5	8	-	8	-
4	TCU-078	0.4	3.4016	16384	0.5	8	-	16	-
5	SW7-333	0.2	4.14	8192	0.5	8	-	12	-
6	TCU-078	0.6	4.645	8192	0.5	8	-	12	-
7	SW7-333	0.2	4.14	8192	0.5	8	-	8	-
8	TCU-078	0.8	4.165	8192	0.5	8	-	16	-
9	SW7-333	0.2	6.1052	8192	0.5	8	-	8	-
10	TCU-078	1	4.037	16384	0.5	8	-	16	-
11	Kobe-PI(83)	1	4.465	8192	0.5	12	-	12	-
12	SW7-333	0.2	4.0514	8192	0.5	8	-	8	-
13	SW7-333	1	6.174	8192	0.5	8	-	8	-

8.2 INPUT MOTIONS

Shaking events applied to centrifuge models JZB01 and JZB02 consisted of five root motions applied over a range of amplitudes. Shaking amplitude generally increased over the sequence of input motions. Figure 92 presents the pseudo-acceleration spectra for these motions in the JZB01 far field (ICP accelerometer A42) and JZB02 far field (ICP accelerometer A52). The number in parenthesis next to the legend entry for a given motion is the applied amplitude for that motion, specific to that model. Most motion response exists in the 0.2- to 0.8-s period range; however, the spikes in amplitude within these periods vary significantly. Sine sweep motions, designated SW7-333, provide an indicator of the natural period of the model soil deposits, as these motions contain a range of frequency contents. The sweep motions indicate the natural period of the model soil deposits range from 0.2 to 0.6 for model JZB01 and 0.2 to 0.4 for model JZB02. Response peaks indicated in the TCU-078 motions indicate similar natural periods of the model soil. Note that the natural period of the model soil deposit is not constant and varies due to high strain and significant model nonlinearities, particularly at high amplitude ground shaking.

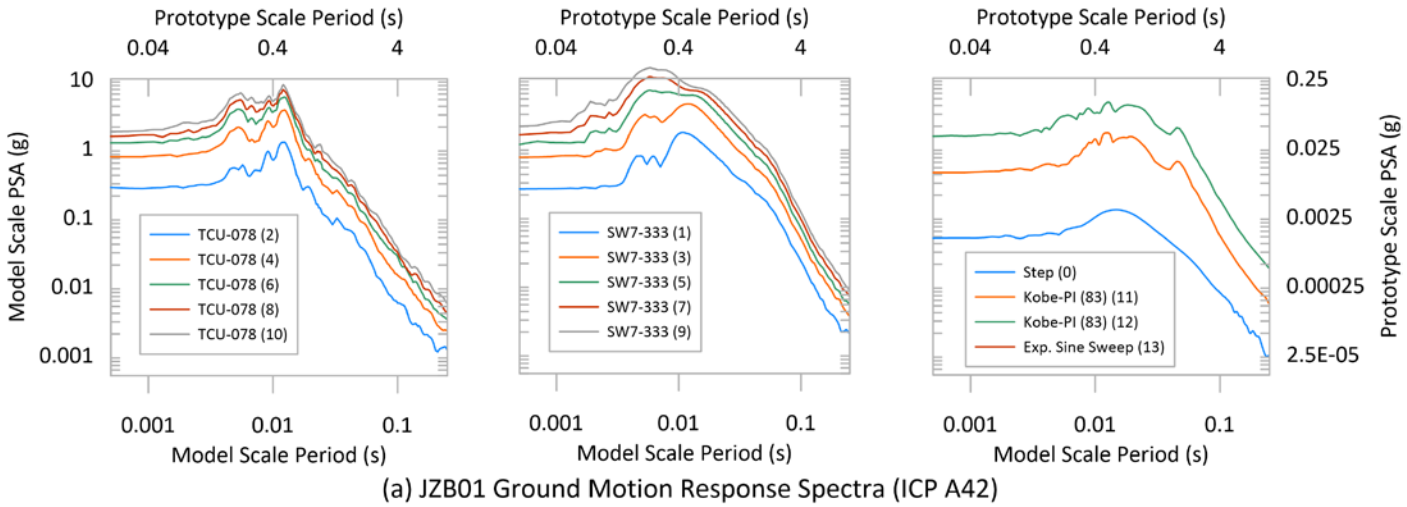

(a) JZB01 Ground Motion Response Spectra (ICP A42)

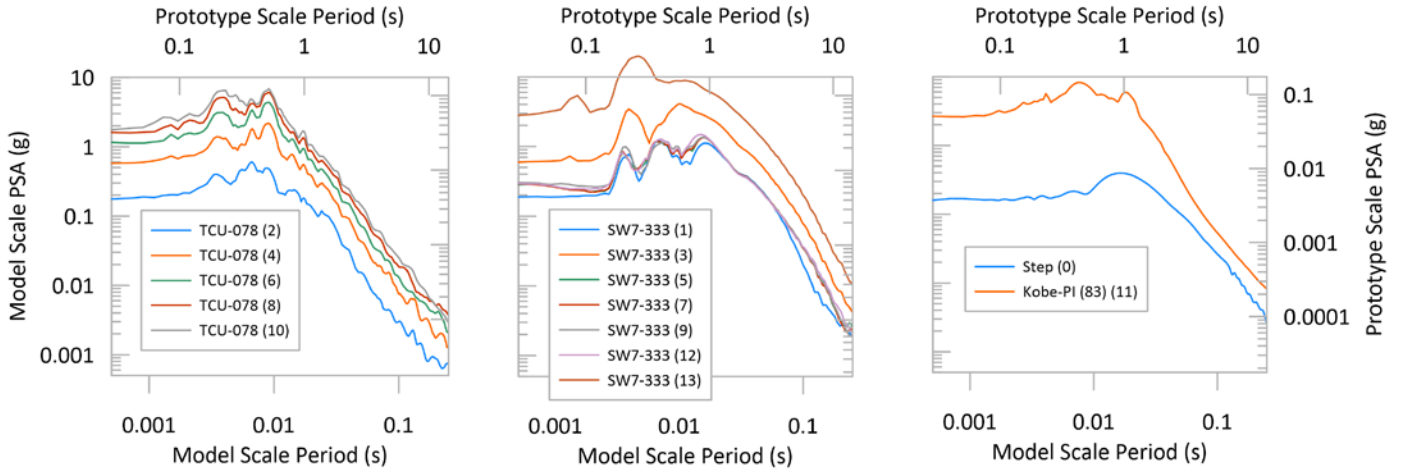

(b) JZB02 Ground Motion Response Spectra (ICP A52)

Figure 92: Base Motion Response Spectra for JZB01 and JZB02

8.3 EMPIRICAL TRENDS

Model structures experienced settlement and rotation during applied shaking events. I monitored structural settlement and rotation using LPs positioned on the top of each structure. Cumulative structural settlement and rotation for model JZB01 and JZB02 are presented in Figure 93 and Figure 94, respectively. Structure 1 experienced bearing capacity failure (e.g. tipped over) during Shake 8 in model JZB01 and during Shake 13 in model JZB02; therefore, settlement and rotations are not presented for the structure for these or subsequent shakes. Each structure experienced settlement that exceeded far field ground settlements. Structures 2 and 3 did not exhibit significant rotations because these structures consist of portal frames and the roof diaphragms provided rotational restraint.

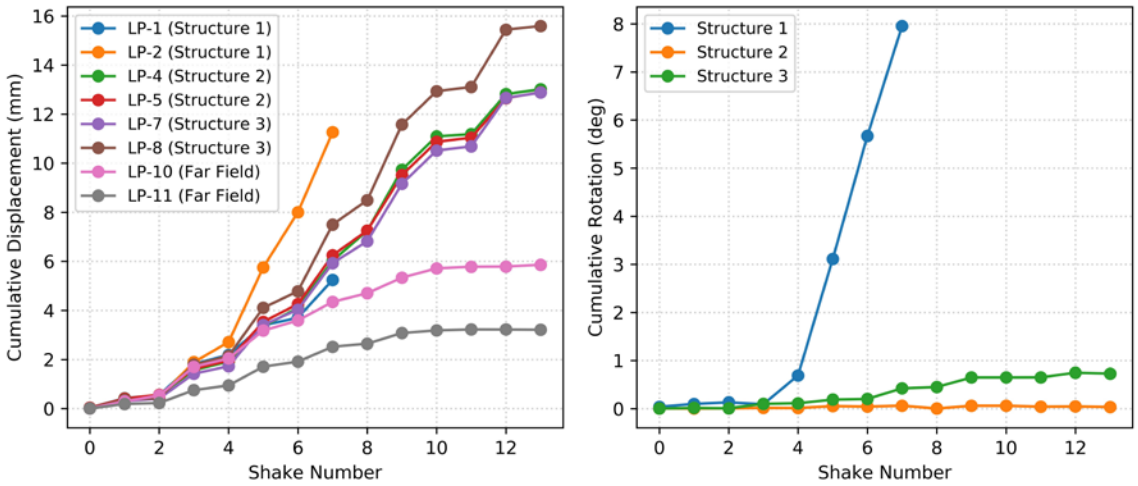

Figure 93: Model JZB01 Cumulative Displacement and Rotation

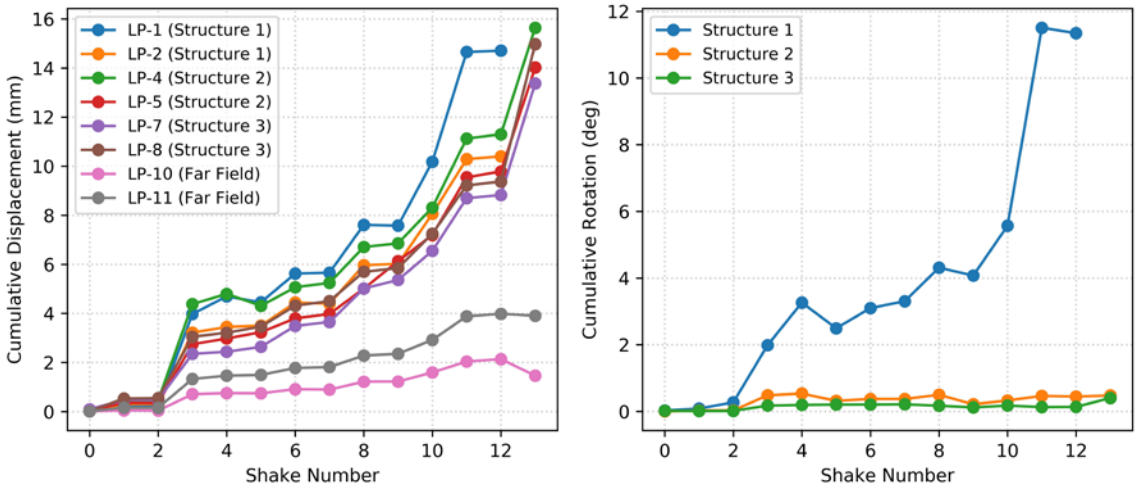

Figure 94: Model JZB02 Cumulative Displacement and Rotation

8.4 MOTION AMPLIFICATION OR DEAMPLIFICATION

Motion may be amplified or de-amplified as it propagates through the model soil. Furthermore, the acceleration at the top of a structure may be smaller or larger than the motion at the foundation level as a function of structure dynamic response. To demonstrate these site and structure effects, peak horizontal accelerations (PHA) at the base of the model, far field surface, and at the roof level for Structures 1, 2, and 3, are plotted in Figure 95. The far field shaking was larger than the base motion for all cases, indicating that the soil profile amplified the input motions. The peak acceleration at the roof of Structure 1 is lower than the far field motion in almost all of the cases, indicting the structure deamplified ground motion. I attribute this to Structure 1 having a low flexible-based natural frequency that was below the peak in the input motion spectrum. As the soil softened, the flexible-base frequency of the structure decreased, resulting in further frequency decreases and increased de-amplification. Structures 2 and 3 tended to amplify low-intensity shaking, and de-amplify high intensity shaking [i.e., after the TCU-078 (6) input motion]. This is a clear indication of nonlinear SSI behavior.

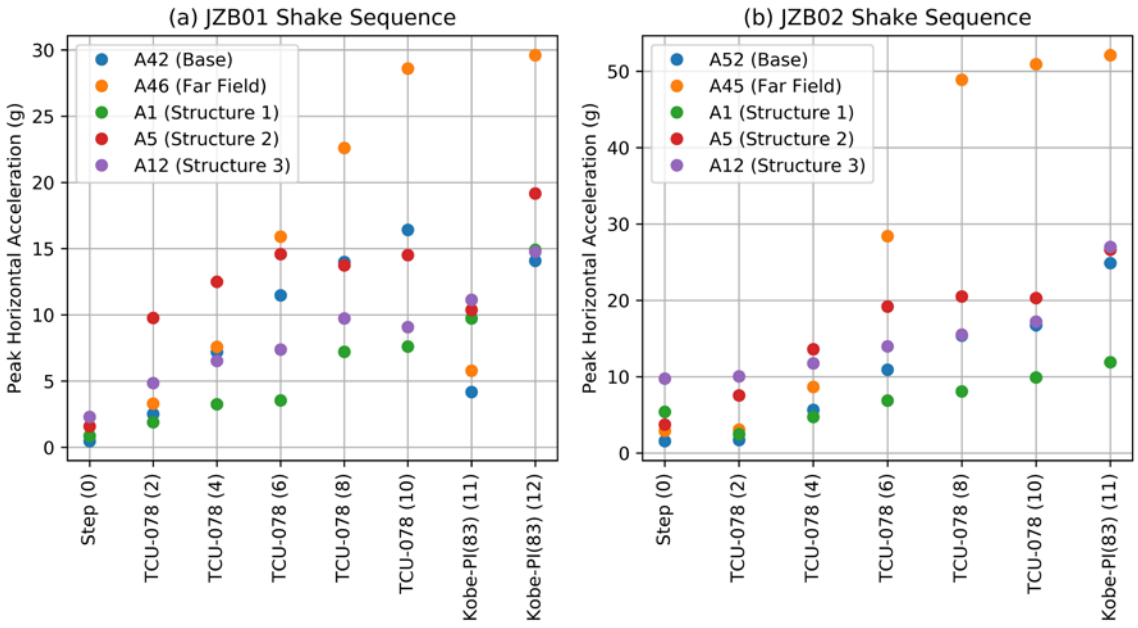

Figure 95: Peak Horizontal Acceleration versus Shaking Event

To further illustrate shaking at different positions within the models, Figure 96 through Figure 98 show acceleration records for JZB01 Shake TCU-078 [4] motion. These records show that the input shaking intensity increased from the base of the container upward through the sand and clay. Furthermore, the footing acceleration for Structure 1 was significantly higher than the roof acceleration, indicating within-structure de-amplification. For Structure 2, the roof acceleration was significantly higher than the footing acceleration, indicating amplification of the motion through the structure. For Structure 3, the roof and footing accelerations have similar amplitudes. These observations are important because the dynamic responses of the structures contribute to the SSI-induced stresses imposed on the soil. The structural models produced a wide range of responses.

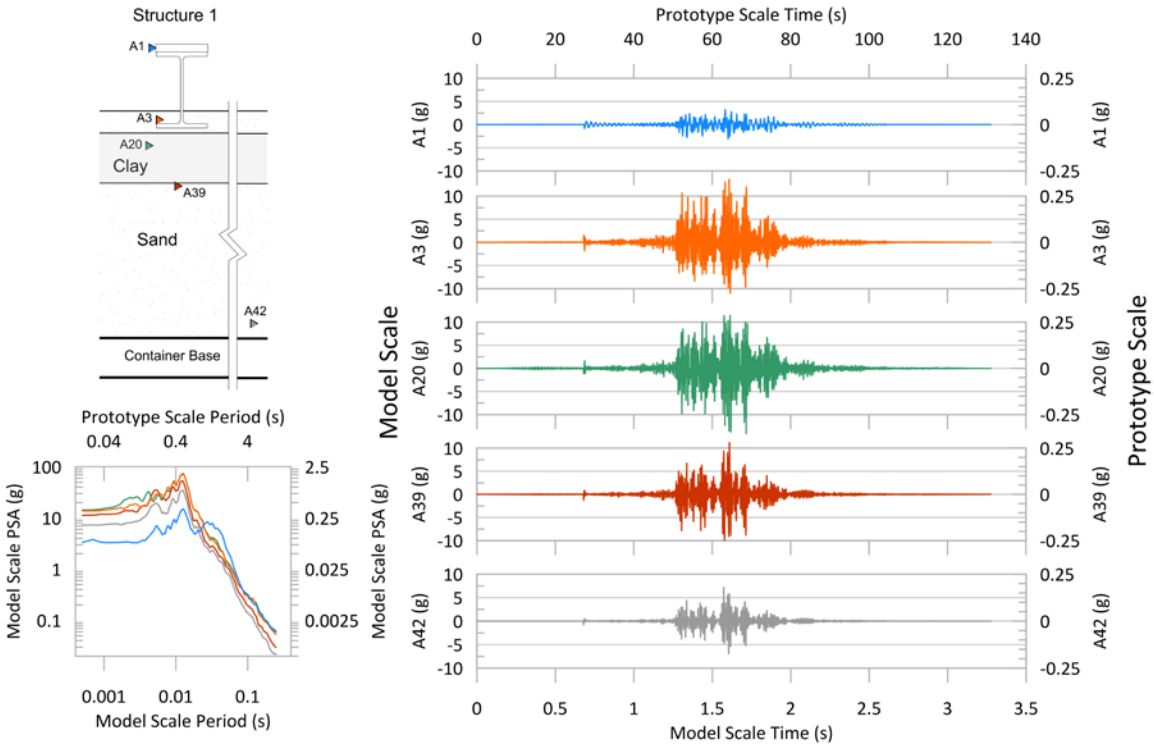

Figure 96: Structure 1 Response Summary during JZB01 Shake TCU-078 [0.4]

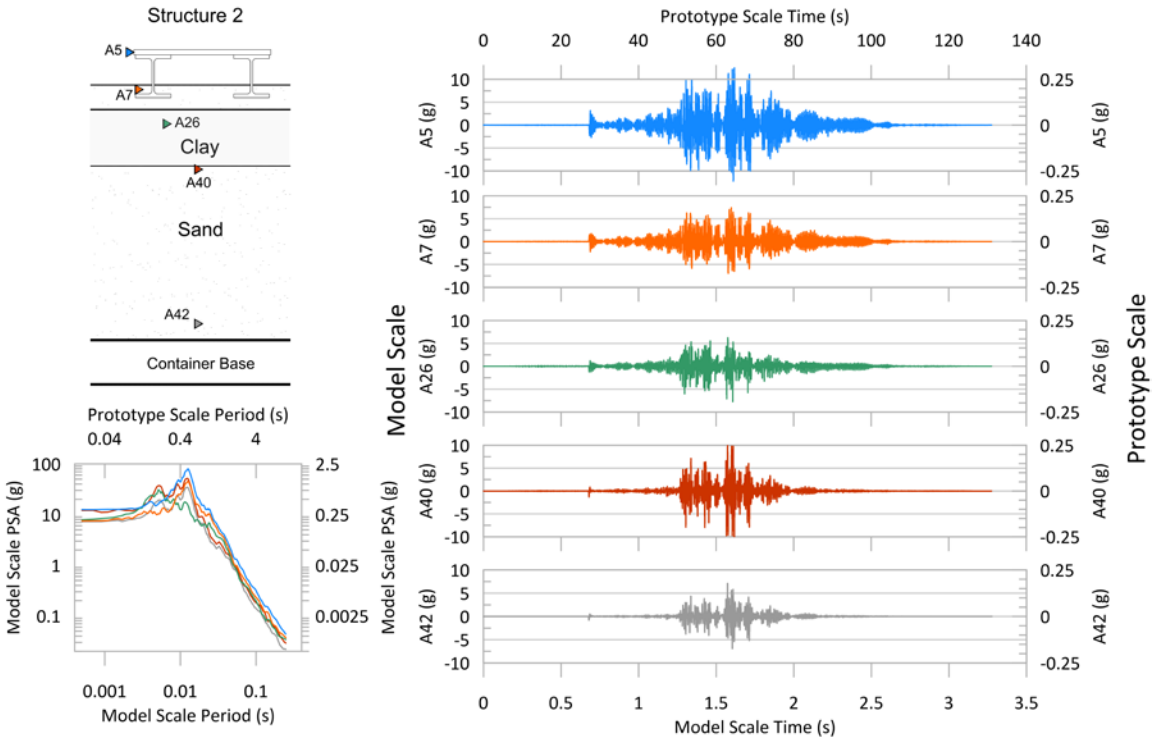

Figure 97: Structure 2 Response Summary during JZB01 Shake TCU-078 [0.4]

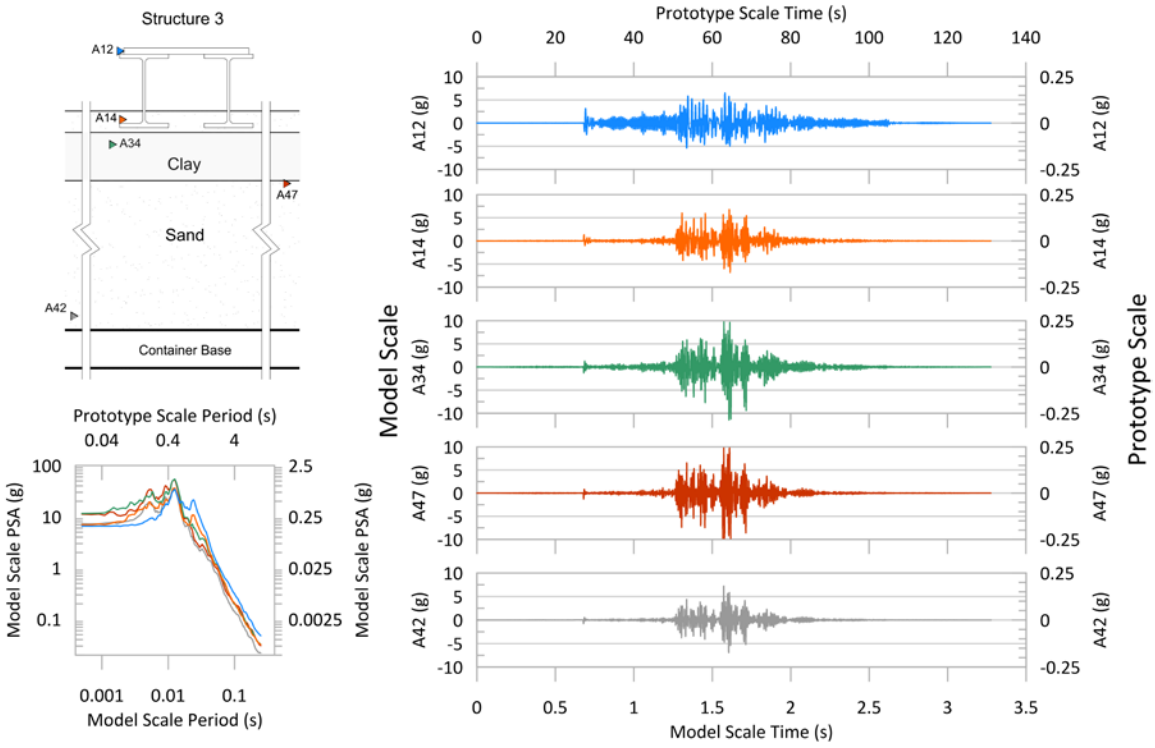

Figure 98: Structure 3 Response Summary during JZB01 Shake TCU-078 [0.4]

8.5 COMBINED GROUND MOTIONS

Model structures experienced settlement and rotation during applied shaking. LPs positioned on the tops of structures were used to monitored structural settlement and rotation. LPs were not rigidly affixed to structure; therefore, the LP displacement recording is subject to systemic error at high frequencies and only usable at low frequencies. Vertically oriented ICPs provide acceleration data that can be integrated to produce displacements usable at high frequencies. This data is correspondingly inappropriate for use at low frequencies due to compounding integration errors that may produce baseline creep in the recording. The two records were combined to produce an aggregate recording of structure settlement valid across the frequency range of interest. The procedure used to produce the aggregate record consisted of applying Tukey windows

and high or low pass Butterworth filters to the data, then combining the data in the frequency domain. The Butterworth corner frequency used on both high and low pass filters was 0.25 Hz. Figure 99 and Figure 100 present settlement and rotation records developed using this procedure for each structure in JZB01 and JZB02, respectively, for a single example ground motion. Note that rotations for each frame structure are small compared to Structure 1, which experienced significant rotation due to shaking.

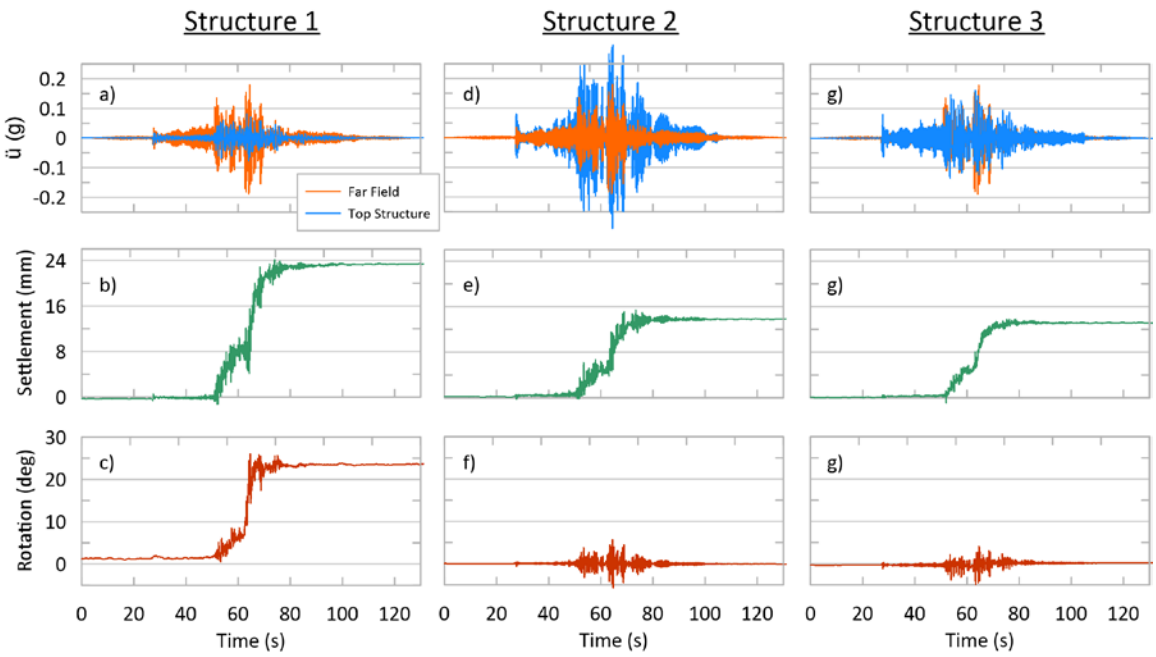

Figure 99: Model JZB01 Data for Shake TCU-078 [0.4]

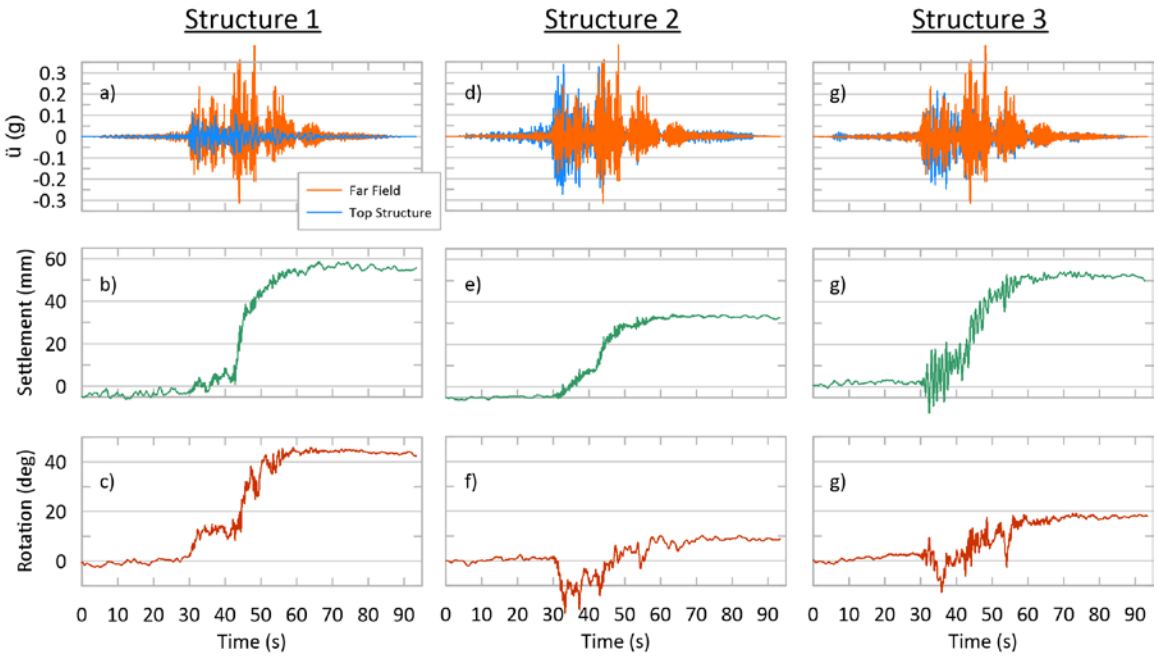

Figure 100: Model JZB02 Data for Shake TCU-078 [0.6]

8.6 GROUND MOTION INTENSITY MEASURES

Ground motion intensity measures are frequently used as a proxy for SSI-induced demand and compared with structure settlement to evaluate performance (Macedo & Bray, 2018; Dashti & Karimi, 2017; Karimi & Dashti, 2017). Although the framework proposed in this dissertation represents a departure from reliance on ground motion intensity measures, I present plots of ground motion intensity parameters versus structure settlement here to review results against the conclusions of other researchers.

Figure 101 and Figure 102 present PGA and PHA a versus settlement for models JZB01 and JZB02. Far field PGA is based on data from ICP accelerometer A46 for JZB01 and A42 for JZB02. Base PGA is from the base of the model container and based on data from ICP accelerometer A42 for JZB01 and A52 for JZB02. The PHA for the bottom of Structures 1, 2, and 3 is based on ICP accelerometers A3, A7, and A14, respectively. The

PHA for the tops of Structures 1, 2, and 3 is based on ICP accelerometers A1, A5, and A12, respectively. Here the bottom and tops of structures denotes an ICP position on the structure footing and roof, respectively. As shown in the figures, base PGA is a decent proxy for performance, which dovetails well with conclusions by Dashti & Karimi (Dashti & Karimi, 2017; Karimi & Dashti, 2017); however, it's unclear whether this trend could be consistently observed in other models with other structures as base PGA cannot account for SSI-effects or site response effects. Bottom structure PHA provides a decent to good proxy for performance, which is intuitive as the structure base should be among the best indicators of SSI-effects, as the ICP position at the foundation level is likely to experience influence from both soil and structure.

Figure 103 and Figure 104 present CAV and Figure 105 and Figure 106 present CAV_{dp} of accelerometer recordings in the far field, model base, structure tops, and structure bottoms. CAV was evaluated in accordance with Equation (2-4) and CAV_{dp} was evaluated in accordance with Equation (2-3). The accelerometers used to evaluate CAV and CAV_{dp} match those used to evaluate PGA and PHA above. CAV calculated at the structure bottom is the most reliable indicator of structural performance among the ground motion intensity measures evaluated here. CAV_{dp} is less reliable, but this indicator is intended as a proxy for structural damage and may not be suited to capture soil performance. CAV_{dp} includes minimum limits that are suited to eliminate non-damaging ground motions that induce response in the structure elastic range. These limits potentially make the measure poorly suited to capture soil response that has a much smaller elastic range than structures. The observation that CAV is a good indicator of performance agrees well with observations by others that CAV-based indicators such as CAV_{dp} (Macedo & Bray, 2018) or CAV_5 (Kramer & Mitchell, 2006) are predictive of soil and structure performance response or evaluation.

Figure 107 and Figure 108 present AI or I_a of accelerometer recordings in the far field, model base, structure tops, and structure bottoms. The figures indicate AI is less predictive than the various CAV-based parameters of performance. However, similar to the CAV-based parameter, AI calculated at the structure bottom is the most reliable indicator of performance, likely due to the position of the ICP accelerometers that facilitates the greatest capture of SSI effects.

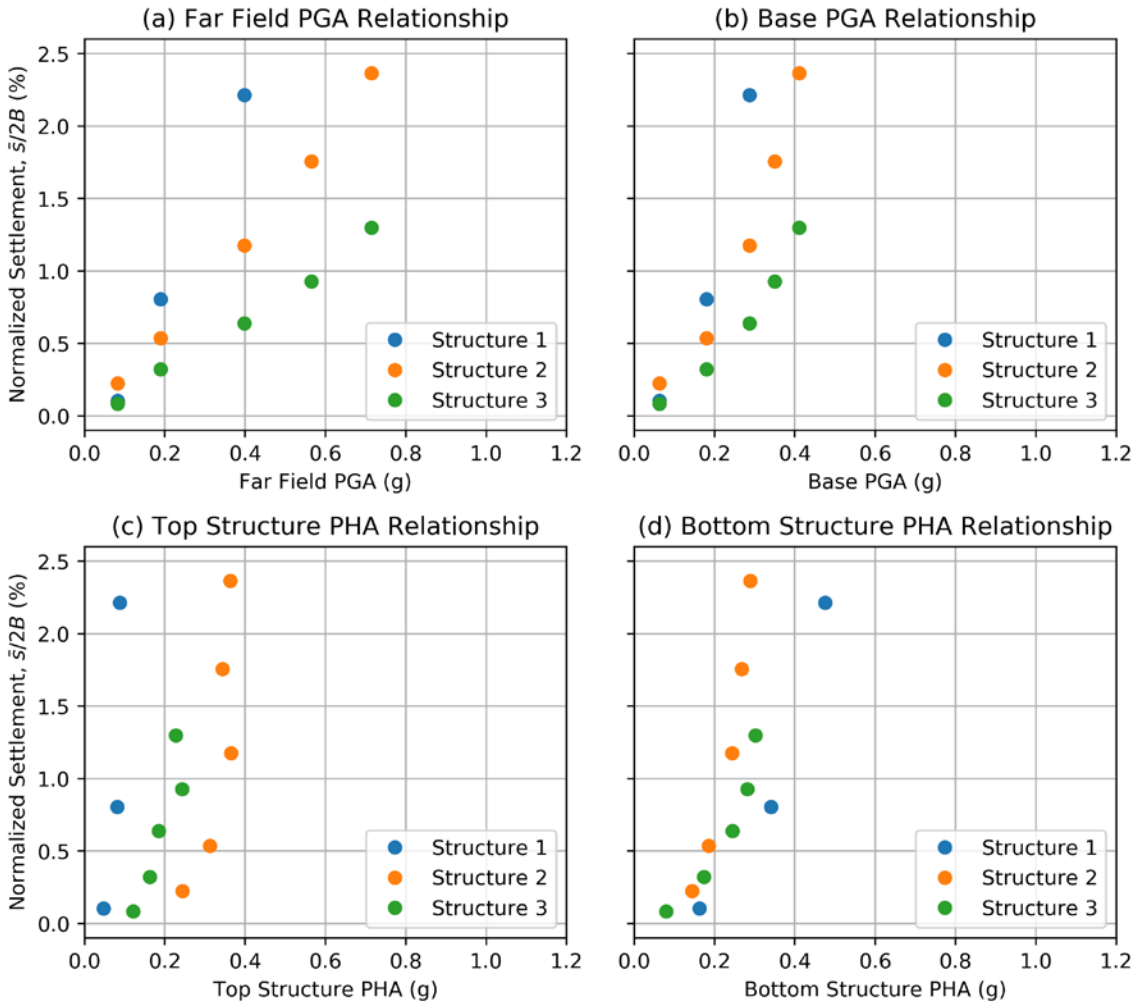

Figure 101: Model JZB01 Acceleration-Based Settlement Relationships

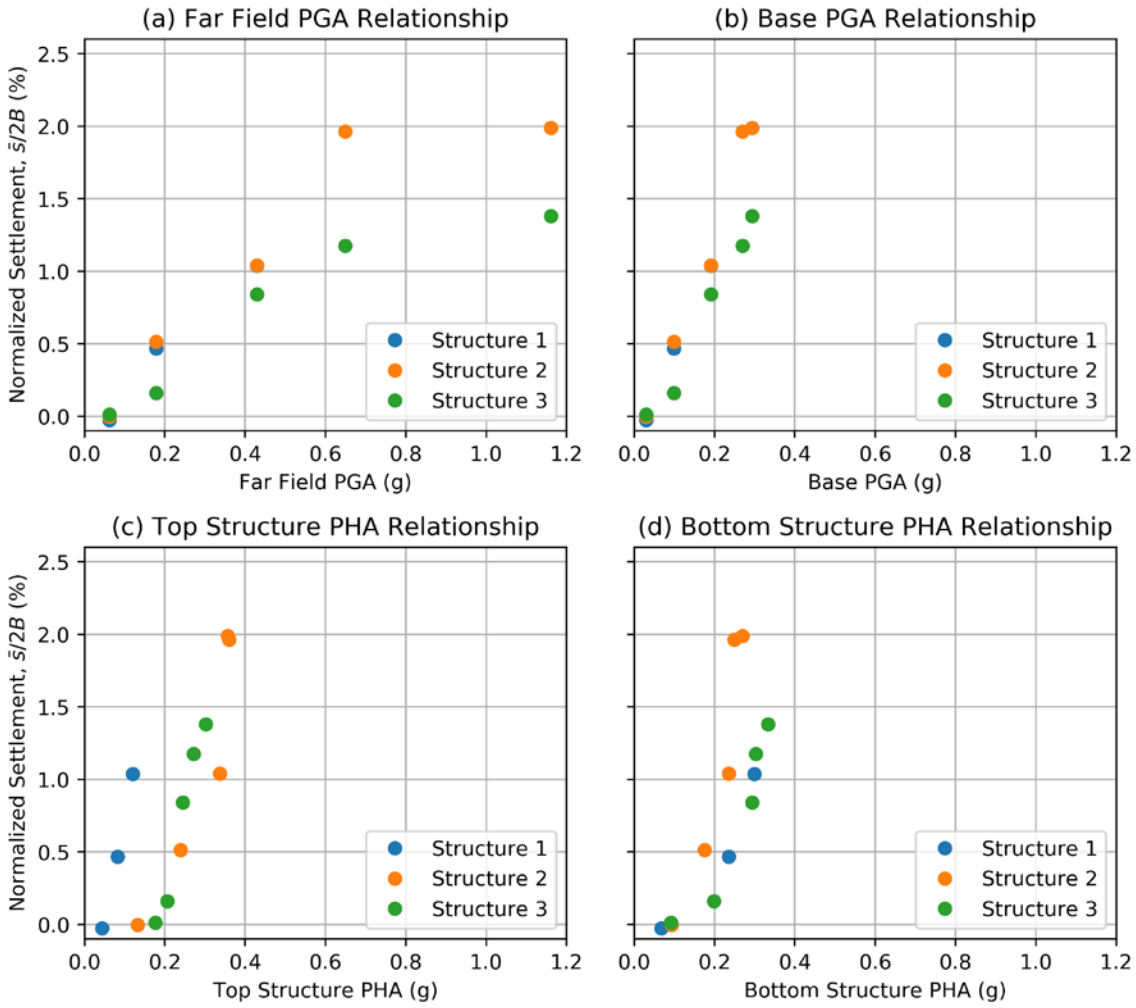

Figure 102: Model JZB02 Acceleration-Based Settlement Relationships

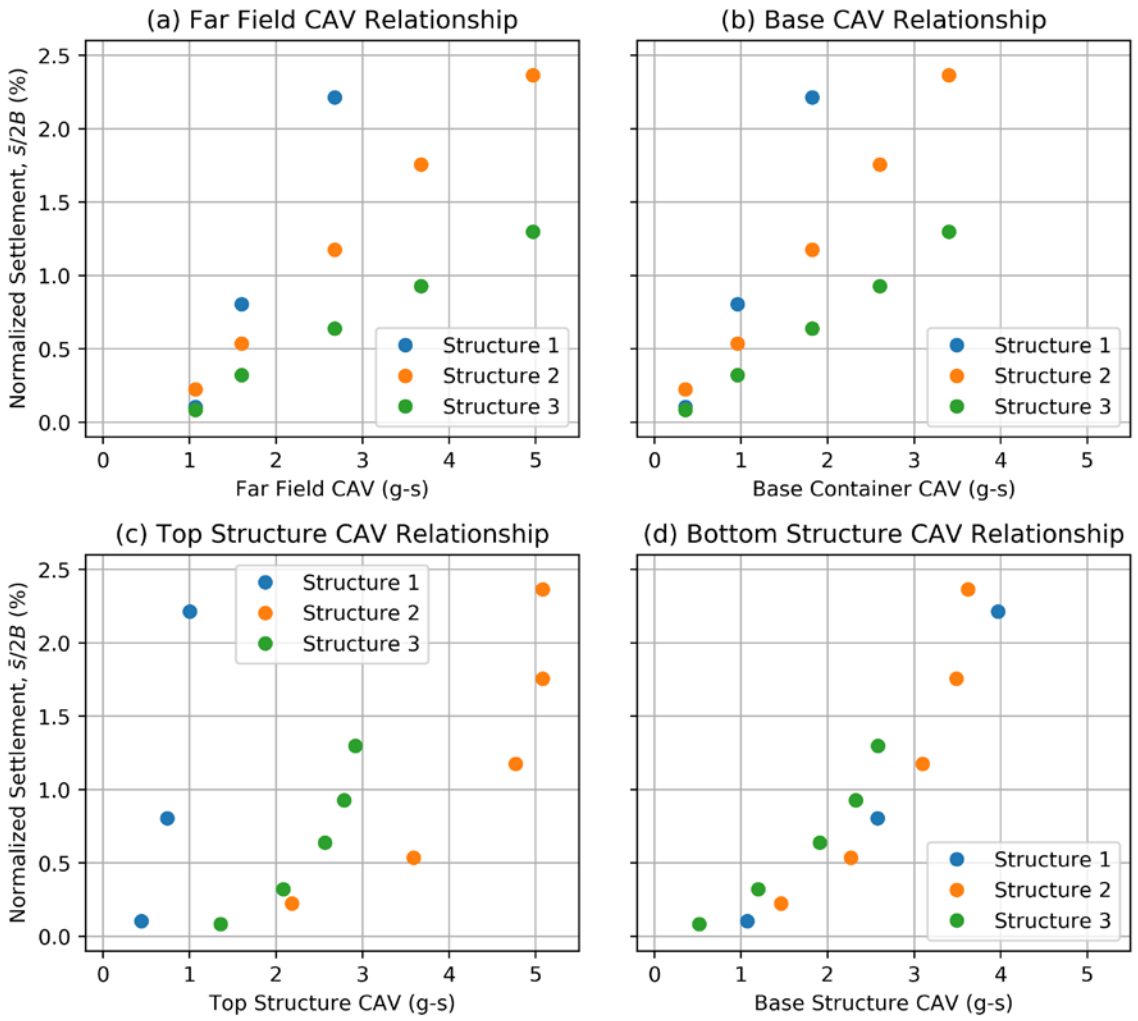

Figure 103: Model JZB01 CAV-Based Settlement Relationships

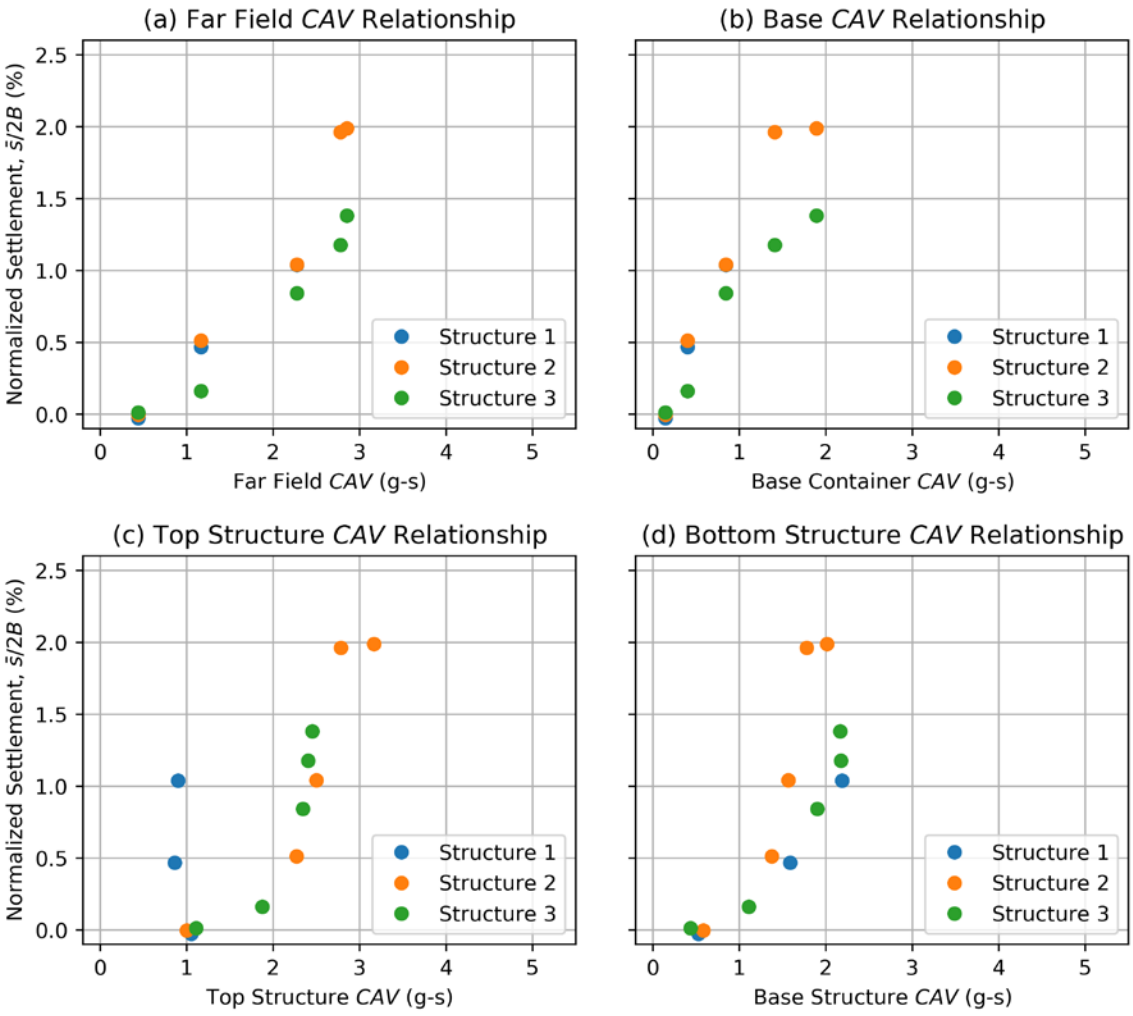

Figure 104: Model JZB02 CAV-based Settlement Relationships

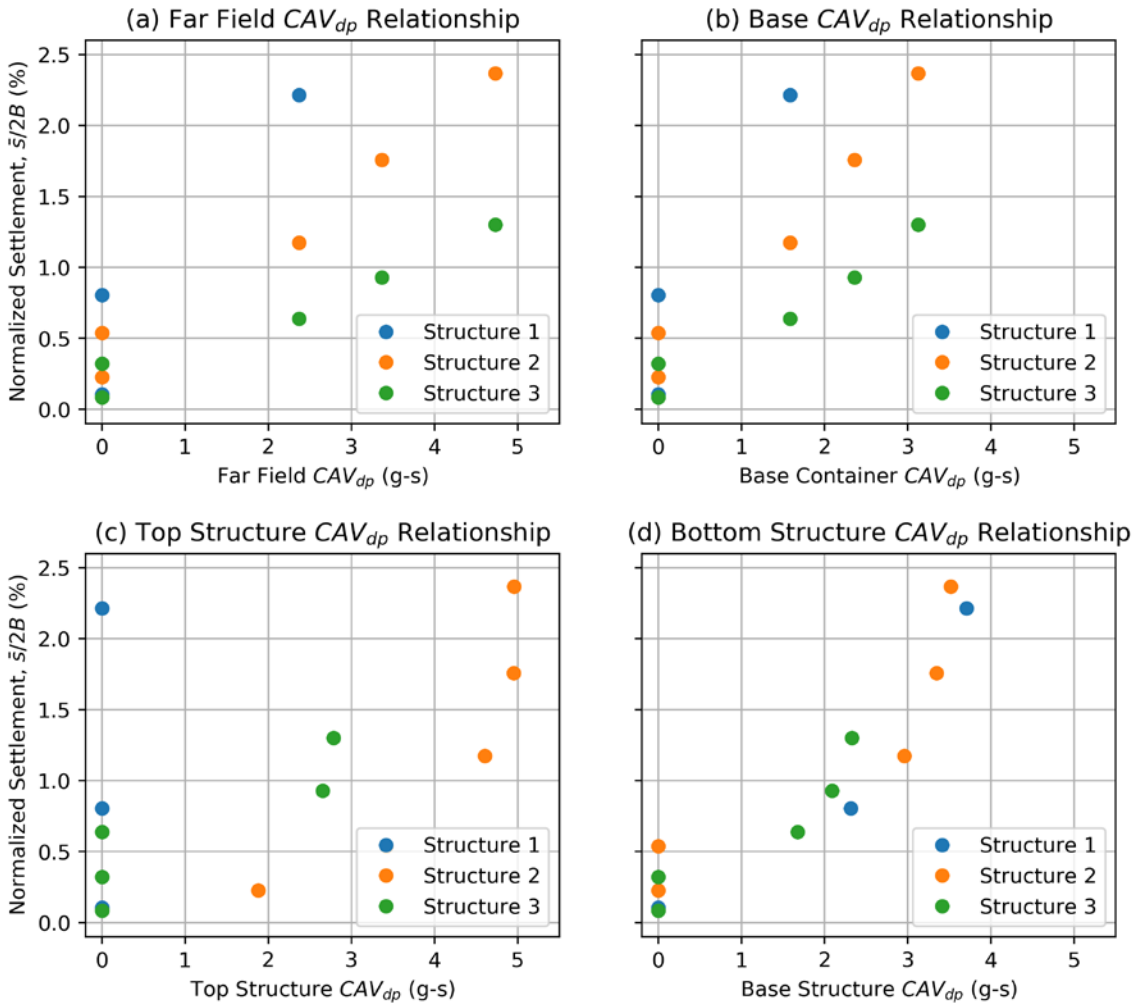

Figure 105: Model JZB01 CAV_{dp}-Based Settlement Relationships

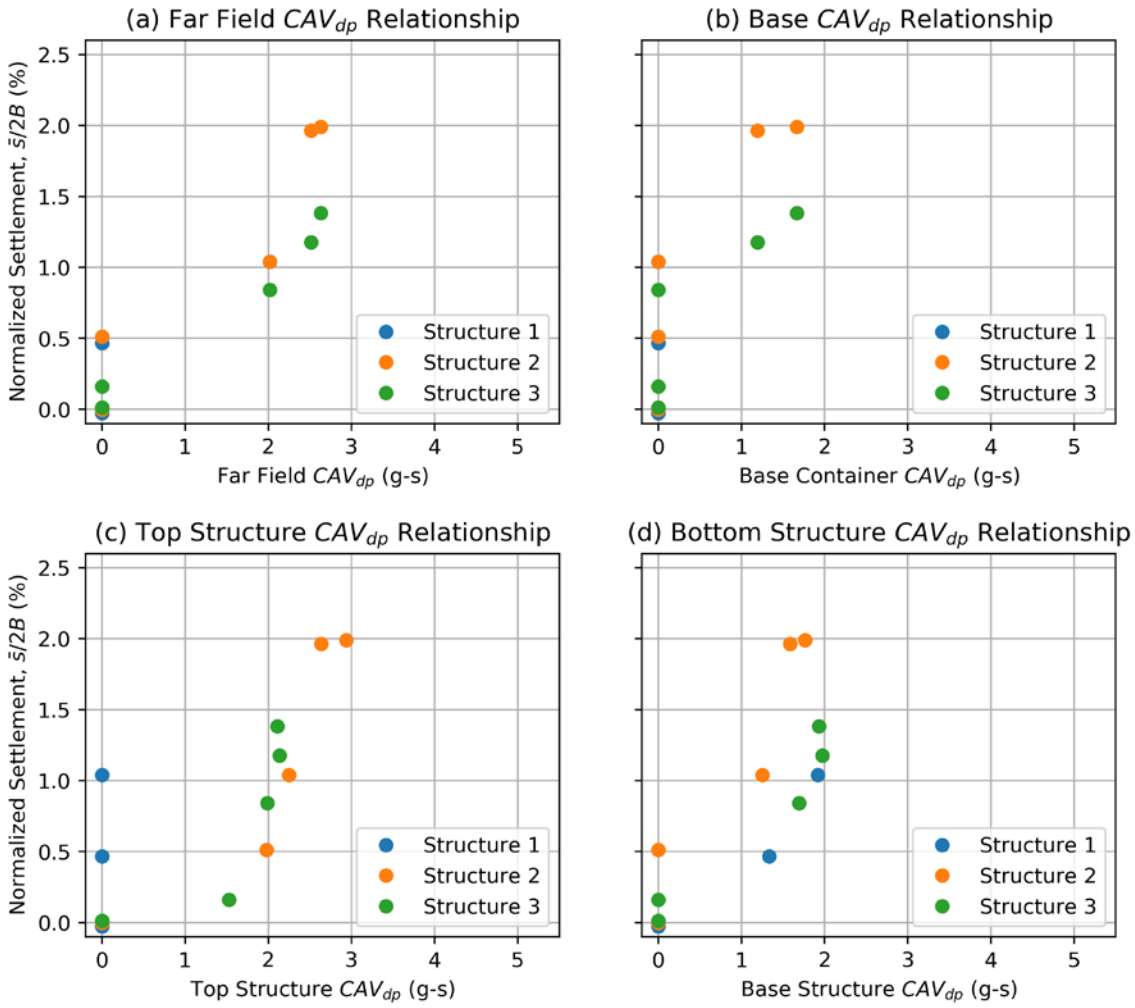

Figure 106: Model JZB02 CAV_{dp}-Based Settlement Relationships

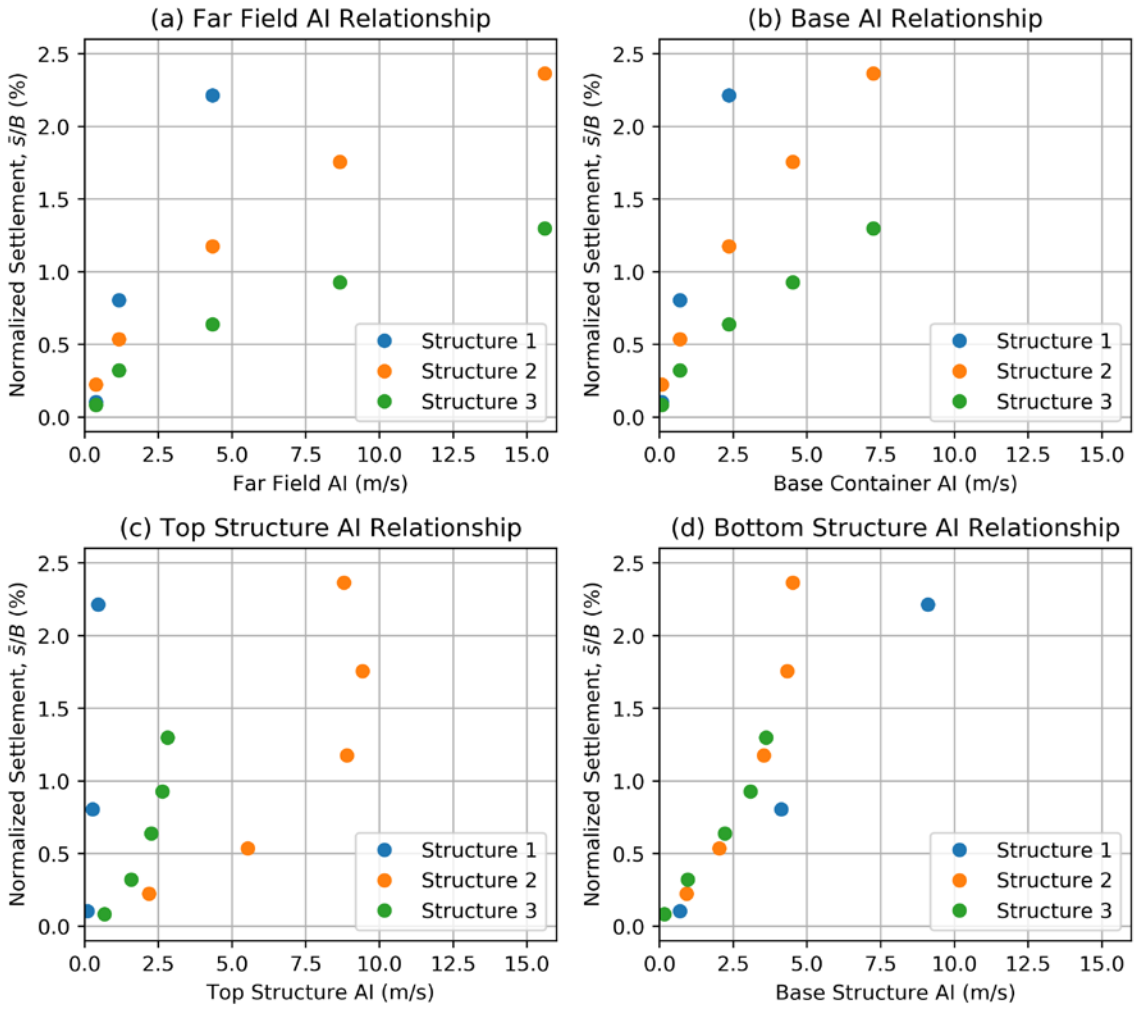

Figure 107: Model JZB01 AI-Based Settlement Relationship

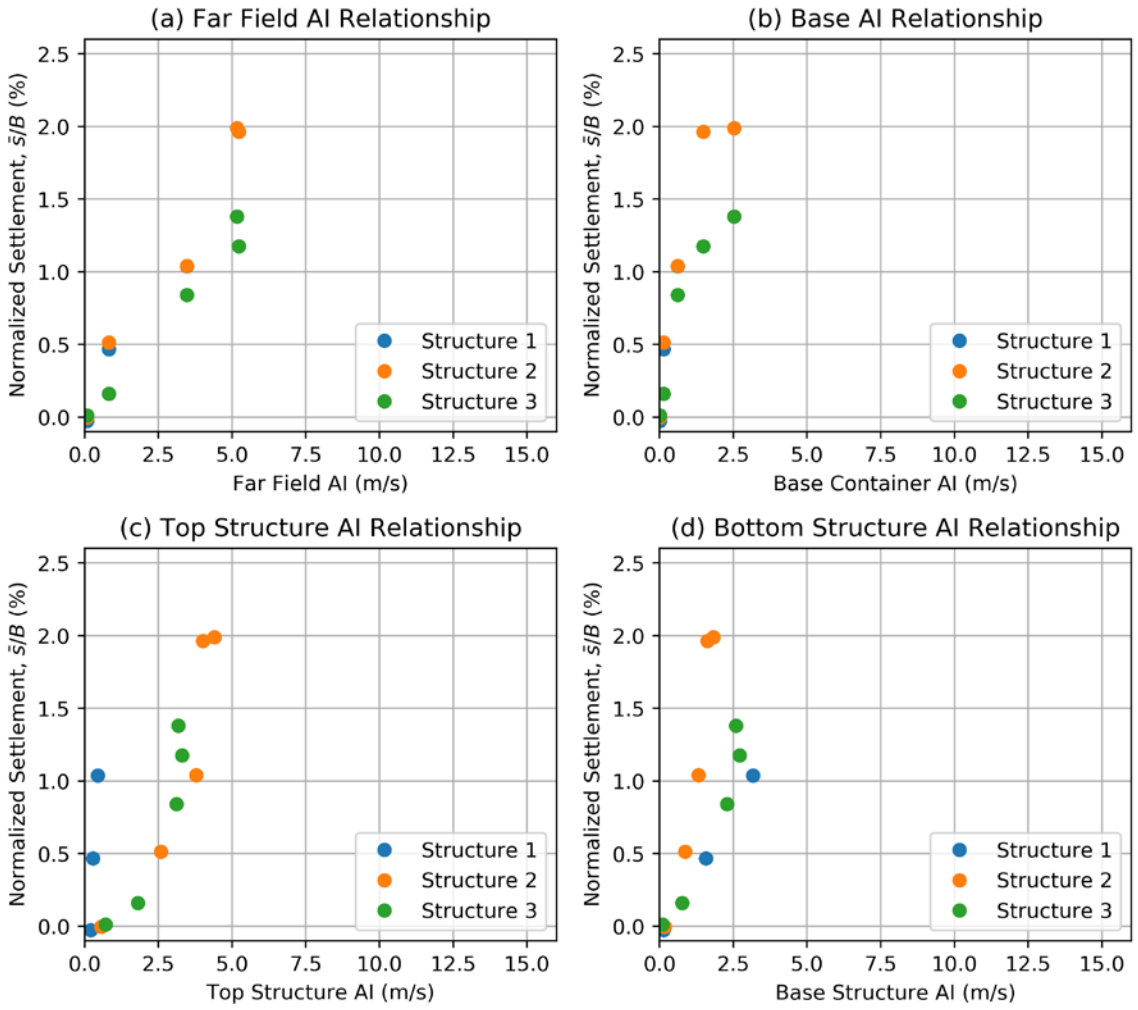

Figure 108: Model JZB02 AI-Based Settlement Relationship

9 IN SITU CLAY STRENGTH AND BEARING CAPACITY OF STRUCTURES

The motivation behind this research is rooted in better understanding soil response to SSI-induced demand during earthquake shaking. A base understanding of existing methodologies and their limitations is therefore critical. Conventional geotechnical practice considers seismic loads on footings in accordance with limit equilibrium bearing capacity theory. I therefore performed limit equilibrium-type bearing capacity analyses to design the structures used in centrifuge models JZB01 and JZB02. Although soil response to SSI-induced demand is unlikely to behave in accordance with limit equilibrium principals, the analyses were intended as a first-order approximation of behavior using routine geotechnical theory and as a basis to understand the limitations of the conventional approach. I later expanded those analyses to incorporate as-built model conditions and structure performance during shaking. I published the analysis for Structure 1 at the 2020 GeoCongress (Buenker et al., 2020b). The Structure 1 analysis and the derivation of in situ clay strength used in the analysis are presented here.

9.1 DESIGN BASIS

Structure design was based on preliminary calculations that computed the factor of safety against bearing capacity failure for static and pseudo-static conditions. Critical design considerations included (i) factor of safety should be adequately high immediately after spin-up, before the clay had time to consolidate under its own self-weight and the structural load, and (ii) factor of safety should be low enough that SSI effects would be anticipated to induce ground failure. Ground motions were modeled as inclined eccentric loads applied as seismically induced base shear, V_b, base moment, M_b, and eccentrically positioned axial loading, P demand, as shown in Figure 109 for Structure 1. Structures 2 and 3 are frames that also include an SSI-induced increase in axial load during shaking, meaning the total axial load would include both static and dynamic components, $P = P_o + P_b$. I evaluated these loads for Structure 1 based on peak horizontal acceleration at the top of the structure (ICP position A-1 for Structure 1).

9.2 BEARING CAPACITY FORMULATION

The ultimate bearing capacity for a strip footing founded on cohesive, frictionless clay is expressed as (Meyerhof, 1951):

$$q_{ult} = 5.14 s_u i_c + q_\sigma \qquad \textbf{(9-1)}$$

where s_u is clay undrained shear strength, i_c is the load inclination correction, and q_σ is the overburden surcharge. Model JZB01 and JZB02 structure footings were lightly embedded ($D_f < B_f$) with groundwater depth at footing level ($z_w \sim D_f$); therefore, depth correction factors accounting for the shearing resistance of overburden material and groundwater were not incorporated.

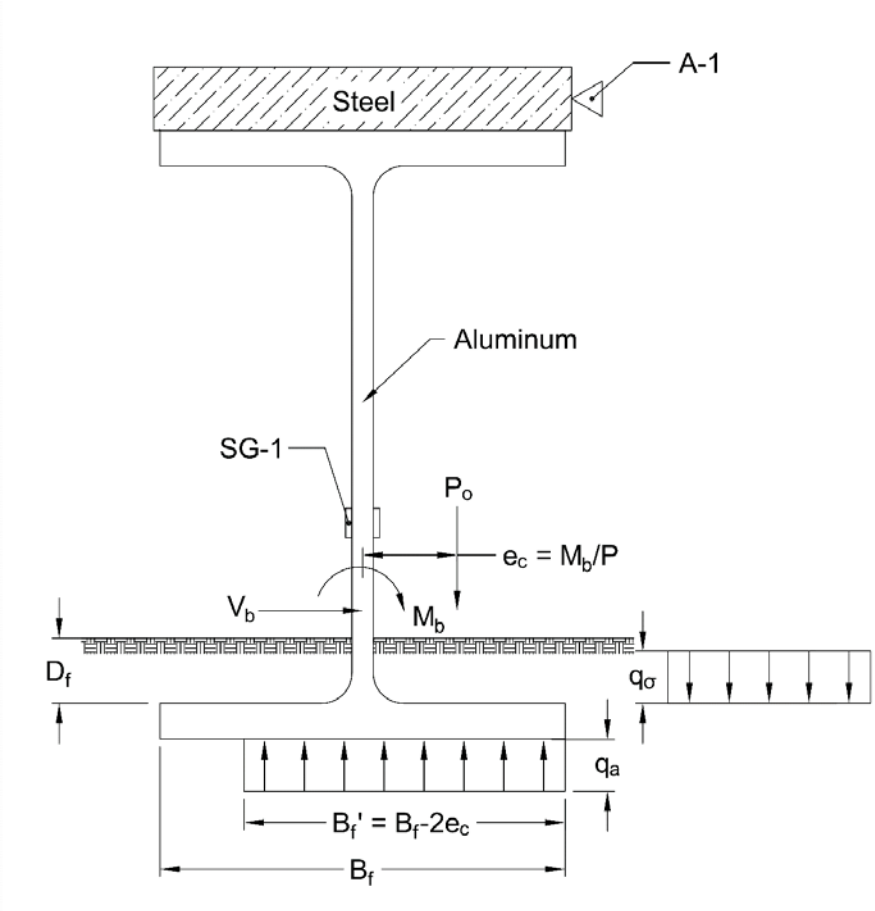

Figure 109: Structure 1 Configuration for Bearing Capacity Evaluation

With i_c evaluated based on V_b (Vesic, 1975), the Equation (9-1) expands to:

$$q_{ult} = \left(5.14 s_u - \frac{2V_b}{B'_f}\right) + q_\sigma \qquad \textbf{(9-2)}$$

In the equation, V_b is expressed in force per out-of-plane unit length. The corresponding factor of safety against bearing capacity failure is:

$$FS = \frac{q_{ult}}{q_a} = \frac{q_{ult} B'_f}{P} \qquad \textbf{(9-3)}$$

In the equation, *P* is expressed in force per out-of-plane unit length.

9.3 CLAY UNDRAINED SHEAR STRENGTH

The key parameter in the evaluation of ultimate bearing pressure from the equations above is clay undrained shear strength. The s_u parameter also factors heavily into the deviatoric-based cyclic softening evaluation framework proposed in Chapter 3. Details regarding the selection of this parameter for each model clay is provided here.

9.3.1 Model JZB01 Clay Strength

The JZB01 model clay was consolidated to a maximum applied pressure of 200 kPa using the CGM's hydraulic press, with PPTs used to confirm dissipation of excess porewater pressures at the midpoint of the clay layer. Original JZB01 structure design therefore incorporated s_u from strength normalization principals by Ladd (1991) consistent with an OCR profile with a maximum past applied consolidation pressure, $\sigma_p = 200kPa$. Later swelling in the clay significantly reduced the OCR and corresponding s_u in the clay, leading to issues with bearing capacity failure in Structure 1 during JZB01 model spin-up. See Chapter 5 for details.

Swelling in the clay reduced OCR by an unknown amount; therefore, evaluating the actual s_u of tested, in situ JZB01 clay involves some ambiguity. I used three approaches to perform the evaluation:

1) Estimate actual σ_p using excess porewater pressure measurements from PPTs collected during spinning. Reevaluate the OCR profile based on actual σ_p. Use strength normalization principals to calculate s_u.
2) Estimate actual σ_p using water content measurements collected following JZB01 Spin 2 and consolidation curves. Reevaluate the OCR profile based on actual σ_p. Use strength normalization principals to calculate s_u.

3) Evaluate s_u from T-Bar testing.

For the first approach, I plotted porewater pressure measurements in the clay using the PPT below Structure 1, designated P1. Figure 110 presents the porewater pressure measurements for JZB01 Spin 5. In the figure, $\sigma_{z,P1}$ is the anticipated vertical total stress at P1 from overburden soil and static Structure 1 load at $N_g = 40$, $u_{o,P1}$ is the anticipated hydrostatic porewater pressure at P1 at $N_g = 40$, and Δu_{P1} is the excess porewater pressure calculated as $\Delta u_{P1} = u_{P1} - u_{o,P1}$. I calculated $\sigma_{z,P1}$ using the elastic solutions presented in Section 3.1. The maximum past consolidation pressure, σ_p, is equal to the vertical effective stress at P1, $\sigma_{z,P1} - u_{o,P1} - \Delta u_{P1}$, which yields σ_p of 37 kPa during Spin 5 at the P1 location near the midpoint of the clay layer. Note the use of the variable u in this section solely denotes porewater pressure and does not denote structure displacement, as used otherwise in this dissertation.

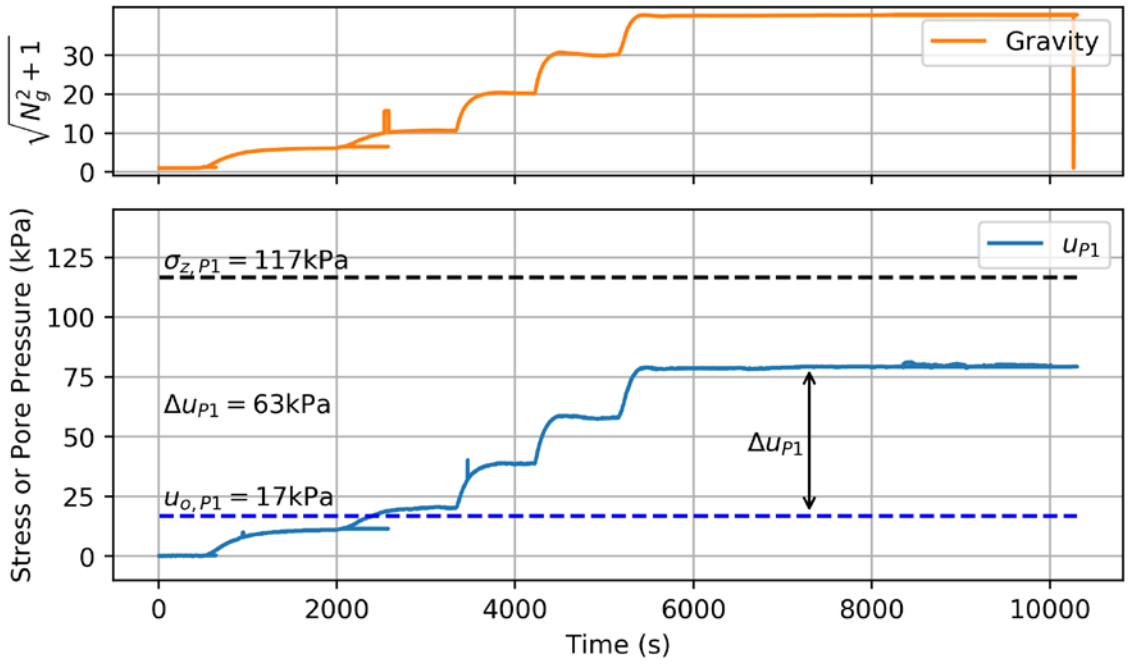

Figure 110: JZB01 Spin 5 Excess Pore Water Pressure below Structure 1

For the second approach, I measured water content of four clay samples collected after JZB01 Spin 2 and used these values to calculate void ratio. I compared measured to expected void ratios using consolidation curves developed from testing on samples of unused JZB01 clay slurry, I determined that the measured void ratios corresponded to σ_p of about 40 to 80 kPa. See Figure 58. The lower bound σ_p is approximately equal to σ_p derived above from PPT data. Note that direct measurement of σ_p could be performed using consolidation testing on the in situ material, but this approach incorporates considerable potential error from sample disturbance. Relatively undisturbed sampling of the JZB01 clay was not performed; samples were instead collected in blocks and the collection process involved considerable disturbance.

I calculated OCR profiles below Structure 1 for each approach using information developed in the preceding paragraphs. I then evaluated clay strength using strength normalization principals. As summarized in Section 4.1, the strength normalization equation applicable to the JZB01 clay is:

$$\frac{s_u}{\sigma'_{vc}} = S \cdot OCR^m \qquad \textbf{(9-4)}$$

$S = 0.213$, $m = 0.718$ for the SBFW blend (Eslami, 2017). For a σ_p range of 40 to 80 kPa OCR is 1 to 2 near the midpoint of the clay layer, which is near PPT P1. These values equate to s_u of 8 to 13 kPa. Note the use of the variable m in this section solely denotes normalized undrained shear strength ratio for a normally consolidated soil and does not denote structure mass, as used otherwise in this dissertation.

For the third approach, I evaluated JZB01 clay strength using in situ T-Bar testing performed during spinning. DeJong et al. (2011) provide a framework to evaluate

undrained shear strength of clay based on the full flow penetrometer behavior of the T-Bar. The framework indicates that s_u may be evaluated in accordance with the equation:

$$s_u = \frac{q_{net}}{N_{T-Bar}} \qquad \textbf{(9-5)}$$

Where q_{net} net pressure resistance at the T-bar tip adjusted for porewater pressure, soil stress, and geometry of the T-bar, and N_{T-Bar} is the T-Bar bearing factor. The value N_{T-Bar} varies with depth and soil type, and typically ranges from 11 to 13. Based on guidance by DeJong et al. (2011), I selected $N_{T-Bar} = 11$.

Figure 111 presents the T-bar test results and the calculated clay s_u. Load values indicated in the figure are measured values from the T-Bar load cell. The calculated strength values are significantly higher than clay strength evaluated from strength normalization procedures.

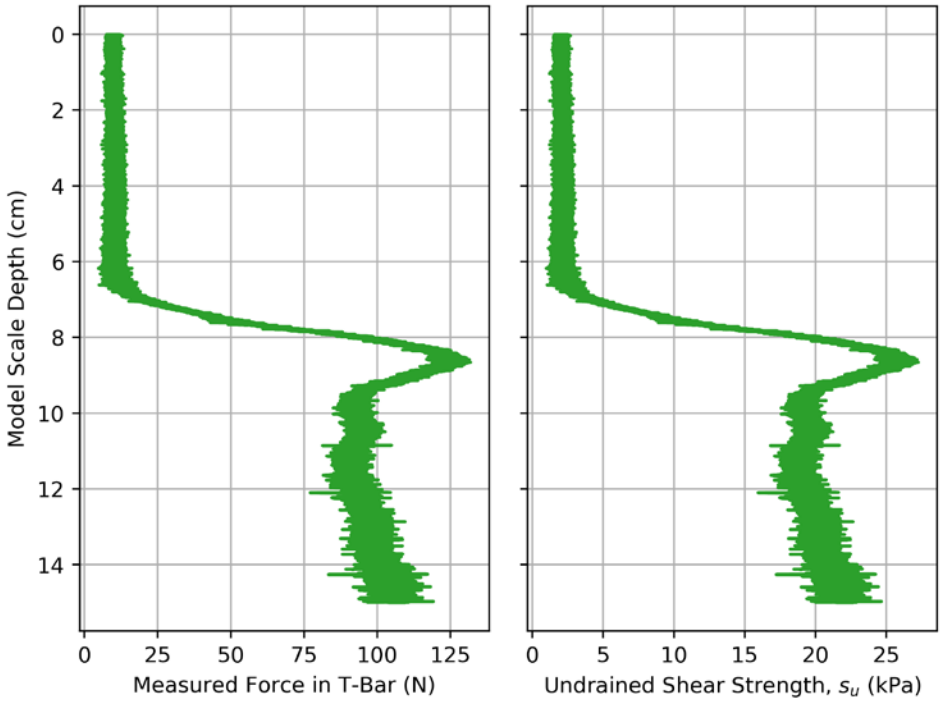

Figure 111: Clay Undrained Shear Strength from T-Bar Testing

The three approaches yield significantly different clay strengths. I used clay strength based on T-Bar testing for the following bearing capacity evaluations and the cyclic softening evaluation detailed later in this dissertation. I selected the T-Bar strength for use because strength normalization procedures may not be appropriate for such large excess porewater pressures and correspondingly low values of effective stress. Further, the low clay strengths from strength normalizations would predict bearing capacity failure of Structure 1, which did not occur during Spin 5 until the application of ground shaking. This implies greater clay strength that is consistent with the T-Bar-based strength. Further, the T-Bar yields a directly measurement of strength, albeit one that requires correction with some ambiguity. The strength normalization parameters are indirect and based on the SBFW blend by Eslami (2017). Some differences exist between the JZB01 clay and the target blend; therefore, a direct measurement of clay strength is preferred.

9.3.2 Model JZB02 Clay Strength

The model JZB02 clay did not exhibit the tendency to swell that complicated the evaluation of JZB01 clay strength. Rather, the JZB02 clay behaved predictably and consistency in-line with behavior of the target Eslami (2017) SKFW blend. JZB02 clay strength can therefore be confidently based on strength normalization coefficients reported for the SKFW blend.

An interesting aspect of the SKFW blend is that behavior was not explicitly clay-like. The Ladd (1991) expression for strength normalization in Equation (9-4) is dependent on clay-like critical state behavior, where the critical state line parallels the normal consolidation line. The SBFW blend supports this behavior, however, the SKFW blend is not fully clay-like. An alternative expression of monotonic undrained shear strength is Equation (9-6):

$$\frac{s_u}{p_a} = S \cdot \left(\frac{\sigma'_{vc}}{p_a}\right)^n \cdot OCR^m \qquad \textbf{(9-6)}$$

The value p_a is atmospheric pressure. Eslami et al. (202X) reported $S = 0.19$, $n = 0.92$, $m = 0.62$ for the SKFW blend.

I used Equation (9-6) to develop distributions of clay strength below the Structure 1 footing. The clay in JZB02 is composed of three clay layers, the upper, middle, and lower clay layers. These layers were consolidated to 140, 180, and 200 kPa, respectively. I developed OCR and s_u profiles below Structure 1 as shown in Figure 112.

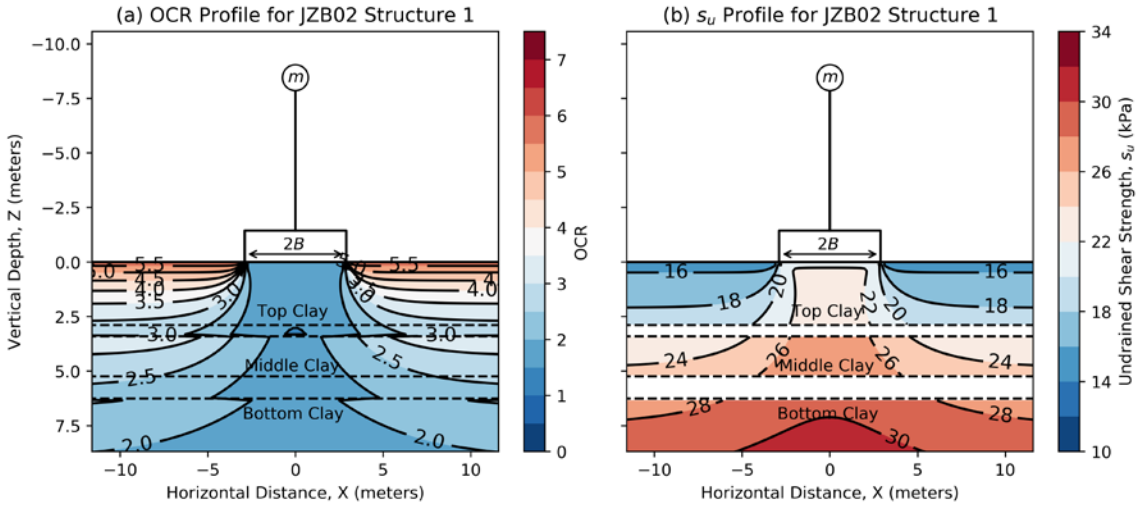

Figure 112: JZB02 Structure 2 OCR and Undrained Shear Strength Profile

Based on the s_u profiles, I selected a representative s_u of 26 kPa for the JZB02 bearing capacity evaluation.

9.4 BEARING CAPACITY EVALUATION

I evaluated bearing capacity for JZB01 and JZB02 Structure 1 using the preceding framework. I evaluated static factor of safety and the peak structural acceleration needed

to generate seismic factor of safety equal to one for Structure 1. Table 1 summarizes results from this analysis procedure.

Table 13: Bearing Capacity Summary

Centrifuge Test	Prototype Scale *B*, (m)	Static q_a, (kPa)	Static q_{ult} (kPa)	Static FS	Acceleration Required to for Seismic FS = 1 (g)
JZB01	4.1	79	127	1.6	0.12
JZB02	5.8	112	172	1.5	0.11

Structure 1 experienced bearing capacity failure during tests JZB01 and JZB02. In each test, the failure occurred progressively, with small vertical residual settlement and tilt following low amplitude ground motions and gradually higher settlement and tilt with increasingly high amplitude motions. Figure 113 indicates the progressive settlement of Structure 1 over the suite of applied ground motions. Figure 114 presents the corresponding peak horizontal accelerations for Structure 1 from each applied ground motions. Settlement is terminated after Shake Number 7 and 11 for JZB01 and JZB02, respectively, because the structure experienced full bearing capacity failure and toppled after these ground motions.

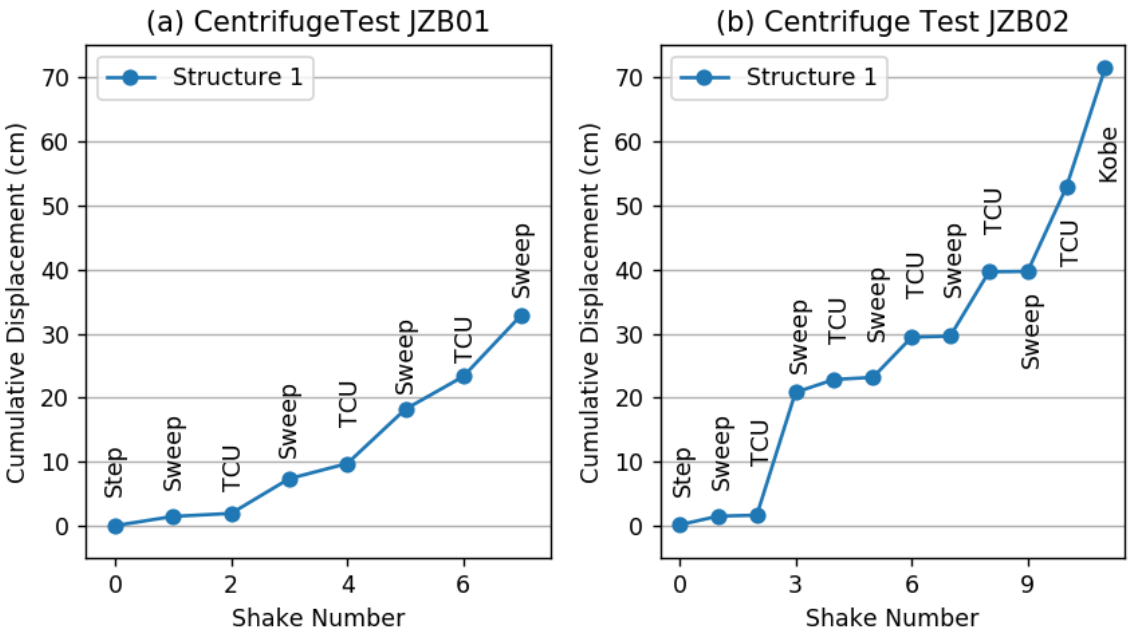

Figure 113: Structure 1 Settlement

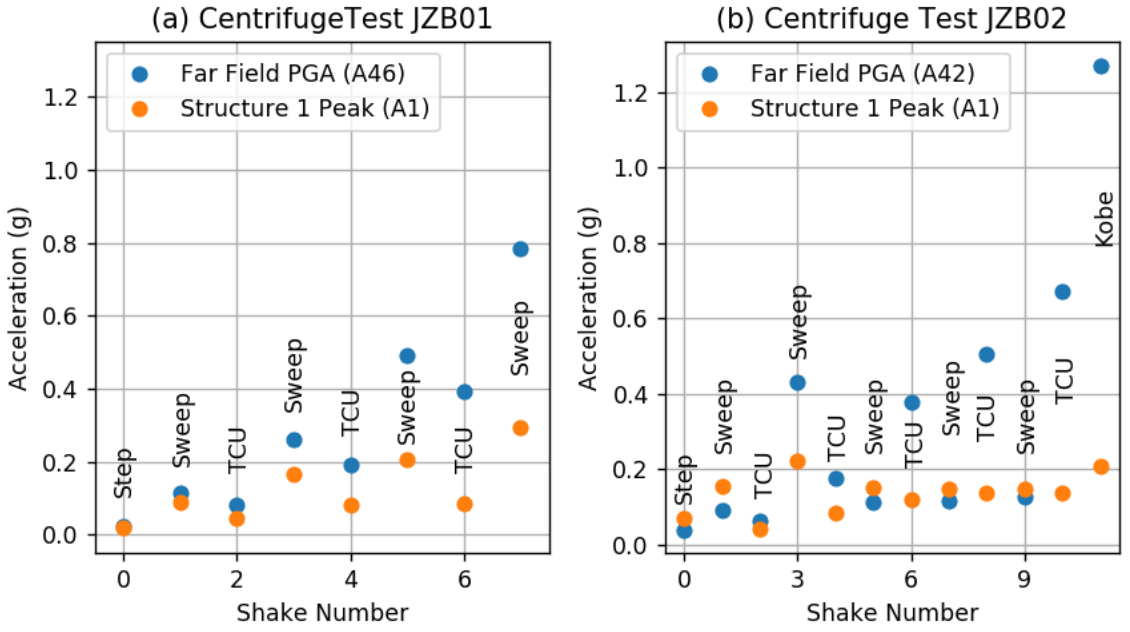

Figure 114: Peak Horizontal Accelerations for Structure 1

I used the limit equilibrium-type bearing capacity framework outlined in the previous section to evaluate structure performance. Figure 115 shows residual settlement versus factor of safety against bearing failure. Settlement tended to increase as FS decreased, and some settlement occurred even for cases with FS > 1.0. This is an indication that the system did not behave in a manner consistent with limit equilibrium concepts. Rather, the failure was strain-based and consisted of the progressive displacement of the foundation until failure occurred. In Figure 115, blue symbols denote cases where far-field ground failure was not predicted based on procedures by Boulanger and Idriss (2007), while orange symbols denote cases where cyclic failure is predicted. Note that the cyclic failure analysis assumes level ground conditions and neglects static and dynamic shear stresses and total stresses exerted by the structure. Cases for which cyclic failure was predicted did have higher settlements than cases for which cyclic softening failure was not predicted.

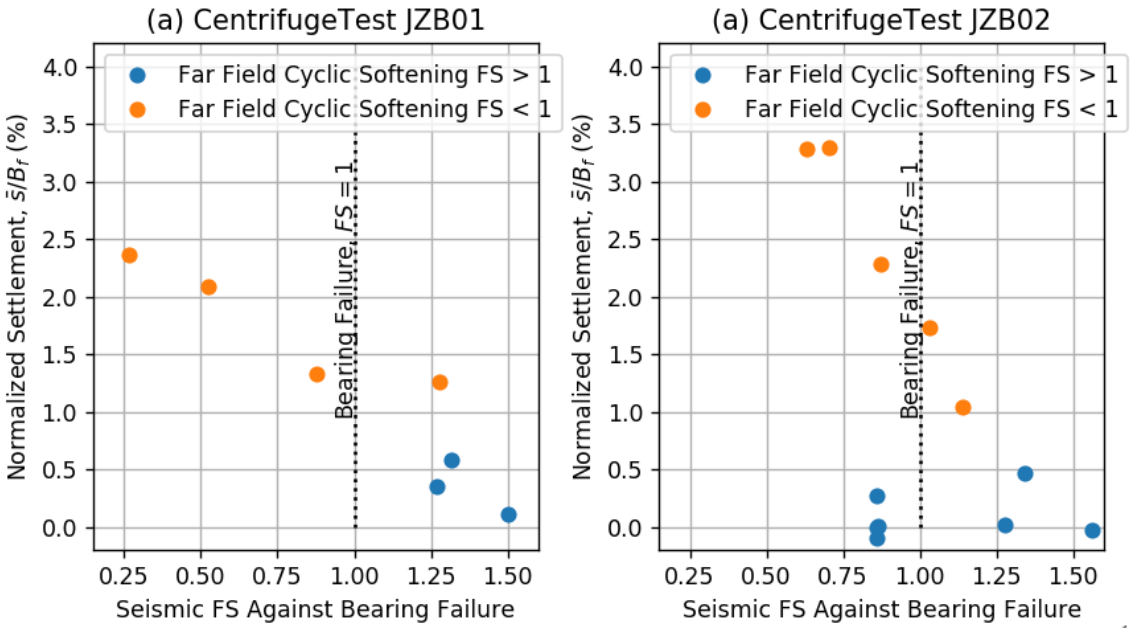

Figure 115: Structure 1 Seismic FS Against Bearing Capacity Failure

9.5 BEARING CAPACITY CONCLUSIONS

The bearing capacity analyses for Structure 1 in models JZB01 and JZB02 yielded mixed results. The bearing capacity analysis indicated that settlement increased as FS decreased, but the trend was not an abrupt increase in settlement when FS crosses the threshold at 1.0. This indicates that the problem is more complicated than implied by limit equilibrium assumptions and challenges the attendant implication that foundations will be suitably stable at FS greater than one. Structural settlement was higher for cases where far-field cyclic softening failure was predicted. The limit equilibrium analyses performed herein account for stresses induced by SSI, whereas the far-field cyclic softening analysis accounts for stresses induced by vertically propagating shear waves. In reality, both mechanisms exert demands on the soil simultaneously. Therefore, an integrated approach is needed that considers demands from vertically propagation waves in addition to those from SSI.

10 CYCLIC SOFTENING EVALUATION

The magnum opus of this dissertation is the evaluation of cyclic softening potential using the deviatoric stress-based framework outlined in Chapter 3 for clay below the structures in centrifuge tests JZB01 and JZB02. I evaluated cyclic softening potential for each TCU-078 earthquake ground motion applied to the models during spinning. The evaluation is intended as both a demonstration and validation of the new framework.

I performed parallel calculations evaluating cyclic softening potential using the framework by Boulanger and Idriss (2007). The parallel calculations are intended to demonstrate differences between conventional procedures that solely incorporate free field stress conditions and the framework here, which considers free field and SSI-induced stresses.

10.1 SOIL BEHAVIOR TYPE

A critical first step in the evaluation of cyclic softening potential is to confirm that the model JZB01 and JZB02 clay soils are indeed “clay-like” and can be characterized as susceptible to cyclic softening. The clays used in the models were based on clay blends developed by Eslami (2017). Fine-grained soil used in model JZB01 was based on Eslami blend

SBFW; fine-grained soil in model JZB02 was based on Eslami blend SKFW. Eslami (2017) made the following observations about the SBFW and SKFW clay during monotonic and cyclic laboratory testing:

1) The maximum equivalent excess porewater pressure ratio, r_u mobilized in the SBFW and SKFW blends during cyclic testing was less than one, with typical values in the range of 0.75 to 0.85.
2) The shape of stress-strain loops was relatively fat
3) The critical state line parallels the normal consolidation line for blend SBFW and nearly parallels the normal consolidation line for blend SKFW.

These observations indicate the SBFW blend used in JZB01 is squarely a “clay-like” material, and that the SKFW blend used in JZB02 can be characterized as “clay-like”, but with some “sand-like” tendencies. These observations agree well with observations regarding strain accumulation previously discussed in Section 4.3.

It is worth noting that the SBFW and SKFW blends are low plasticity fine-grained soils that lay in an interesting region with respect to liquefaction or cyclic softening susceptibility criteria by Bray and Sancio (2006) and Boulanger and Idriss (2006). Bray and Sancio utilize PI and the ratio of natural water content to liquid limit, w_c/LL to assess susceptibility, indicating that a soil is liquefaction susceptible if w_c/LL > 0.85 and PI<12, moderately liquefaction susceptible if 0.8<w_c/LL<0.85 and 12<PI<18, and otherwise is not liquefaction susceptible (or instead susceptible to cyclic softening). By contrast, Boulanger and Idriss (2006) suggest that a fine-grained soil exhibits "sand-like" behavior if PI<4, "clay-like" behavior if PI>7, and transitional behavior in between. Traditional liquefaction triggering procedures are then utilized to assess strength loss potential of sand-like soil, while a different set of cyclic softening procedures are utilized to assess the strength loss potential

of clay-like soil. The model JZB01 and JZB02 clays are presented in Figure 116 relative to the criteria by Boulanger and Idriss and Bray and Sancio.

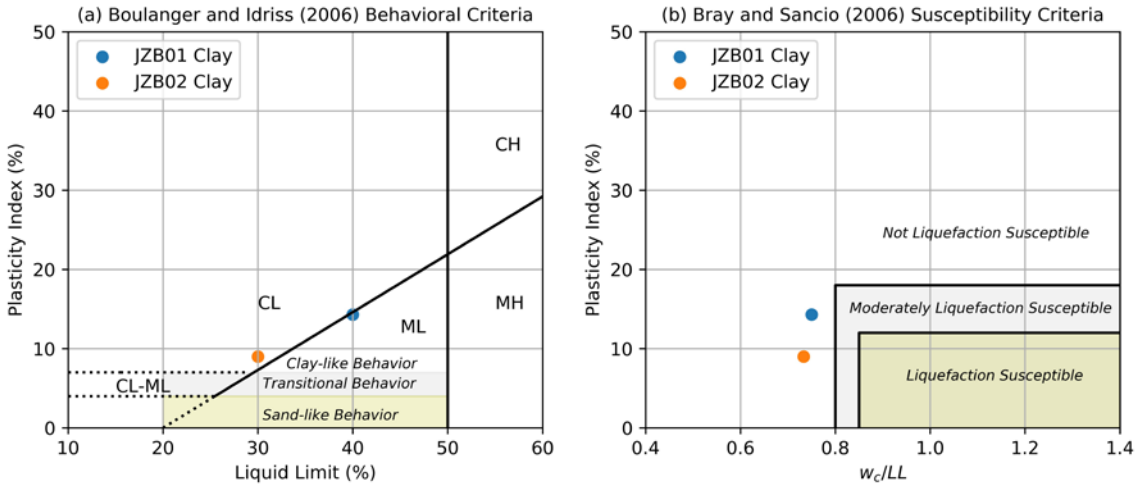

Figure 116: Cyclic Soil Behavior and Susceptibility Criteria

According to the Boulanger and Idriss (2006) procedure, both model JZB01 and JZB02 clays exhibit clay-like behavior and should be evaluated using cyclic softening procedures. Based on susceptibility criteria by Bray and Sancio (2006), both model JZB01 and JZB02 clays are not susceptible to liquefaction. These results agree with observations from clay laboratory testing detailed above. I therefore conclude that a cyclic softening framework is appropriate for the characterization of the clay cyclic behavior.

10.2 Cyclic and Deviatoric Resistance Ratio

The cyclic undrained shear capacity of the clay is characterized using CRR curves in conventional liquefaction or cyclic softening evaluation and DRR curves in the new framework proposed here. CRR and DRR curves can be derived from laboratory cyclic strength testing. Eslami (2017) performed extensive laboratory testing to characterize the strength of these blends, consisting of constant-height monotonic and cyclic DSS testing. I presented applicable portions of the laboratory testing in Chapter 4 and derived deviatoric

resistance ratio, DRR curves for the clays from DSS test data in accordance with the framework detailed in Chapter 3. I derived the DRR curves for multiple strain levels. I also derived corresponding cyclic resistance ratio, CRR curves for multiple strain levels from the Eslami (2017) test data. The curves are presented in Figure 21.

The centrifuge model clays are not identical to the target blends (particularly for JZB01, see Section 5.4.2); although, the clay minerology and base material used to create the clays are the same. Due to schedule limitations, I did not perform strength-based laboratory testing on the centrifuge model clays. However, I anticipate that the cyclic behavior of the clays is likely similar enough to use the Eslami (2017) laboratory data to analyze cyclic ground failure potential here.

10.3 CYCLIC AND DEVIATORIC STRESS RATIO

Cyclic stress demands are represented as DSR for the deviatoric stress framework or CSR for the conventional framework. CSR is a function of the induced cyclic shear stress from the free field ground motion as, $CSR = \tau_{cyc}/\sigma'_{vc}$, or stated in the terms outlined in Chapter 3, $CSR = \Delta\sigma_{xz,ff}/\sigma'_{zzo,ff}$. DSR is a function of free field ground motion and the SSI-induced stresses, including structural base shear, ΔV, base moment, ΔM, and dynamic axial load, ΔP. Equations outlined in Chapter 3 may be used to evaluate vertical normal stress, σ_{zz}, horizontal normal stress, σ_{xx}, out-of-plane normal stress, σ_{yy}, and in-plane shear stress, σ_{xz}, as a function of these loading conditions, which in turn allows evaluation of deviatoric stress and the other DSR terms.

To demonstrate the demand-side evaluation of DSR for the deviatoric stress framework or CSR, I present plots in this section from calculations for JZB01 Structure 1 for the TCU-078 [0.4] ground motion (e.g. the TCU-078 ground motion at an amplitude factor of 0.4). Plots for other structures for other ground motions are omitted for brevity.

10.3.1 Stress Demand

I evaluated stress demand induced in the free field and by Structures 1, 2, and 3 for each TCU-078 earthquake ground motion applied during centrifuge tests JZB01 and JZB02. Stress demands from free field ground motions were evaluated using data from ICP accelerometers positioned in the model far fields (i.e. accelerometer A46 for JZB01 and A42 for JZB02). Structural ΔV, ΔM, and ΔP were evaluated using data from horizontal ICP accelerometers positioned on the tops and bases of each structure (e.g. accelerometers A1 and A3 for Structure 1, A5 and A7/A11 for Structure 2, and A12 and A14/A17 for Structure 3). Those force/moment demands were then used to evaluate cyclic stress demands in foundation soils. Structure 1 is statically determinate; therefore, ΔV and ΔM can be computed directly from measured accelerations without consideration for structural deformation and stiffness. For simplicity, I approximated Structure 1 behavior as a SDOF lumped mass. By contrast, Structures 2 and 3 are portal frames that are statically indeterminate; therefore, structural stiffness and SSI stiffness must be taken into consideration to compute ΔV, ΔM, and ΔP from available measurements. I assumed Structure 2 and 3 model behavior as a rigid top frame over two columns founded on SSI springs. Figure 117 presents the behavioral models for structures. Model mass was taken as the mass contributing to dynamic structure performance, which was typically the portion of the structure mass equal to the top steel plate, top I-beam flanges, and the portion of the web above the neutral axis. I validated the selection of the model mass contributing to dynamic structure performance using bending configuration strain gages mounted on the structure webs (e.g. SG-1 and SG-3 for Structure 1; SG-5 through SG-11 for Structure 2; SG-13 through SG-19 for Structure 3). I did not use the strain gauge data outright for the calculation of base moment due to inconsistencies in the strain data and the tendency for gages to fail at high amplitude ground motions. SSI springs were evaluated using

guidance by the National Institute of Standards and Technology (2012). The SSI spring calculations require input soil properties, which I selected as $\rho = 1850\, kg/m^3$, $\nu = 0.45$, and $V_s = 150\, m/s$. I did not reduce V_s to account for modulus reduction due to soil nonlinearity, because computed ΔV, ΔM, and ΔP were not sensitive to V_s over the range expected from nonlinearity and modulus reduction. The structural properties used for this analysis are consistent with the properties presented in Chapter 7.

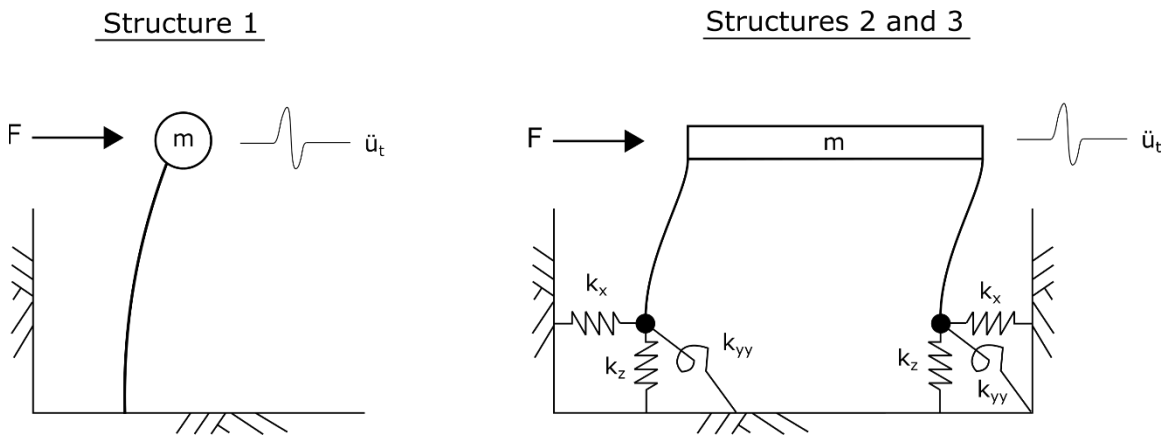

Figure 117: Pseudo-Static Structure Behavioral Models

The soil properties used for SSI springs are also used for as inputs in subsequent calculations. Note that ν is dependent on the loading conditions, where $\nu = 0.5$ corresponds to undrained loading conditions and $\nu < 0.5$ corresponds to progressively more drained loading conditions. I assumed $\nu = 0.3$ for static portions of the elastic solutions and $\nu = 0.45$ for dynamic portions of the elastic solutions for model JZB02, but $\nu = 0.45$ for both static and dynamic portions of model JZB01. As discussed in Chapter 9, the model JZB01 clay likely had positive excess porewater pressures for the duration of centrifuge testing.

To simplify implementation of the procedure for multiple ground motions, I calculated response coefficients for computing ΔV, ΔM, and ΔP. Using the response coefficients,

base shear is expressed $\Delta V = -C_v F$, base moment is expressed $\Delta M = -C_M F$, and dynamic axial load is expressed $\Delta P = C_P F$, where $F = m\ddot{u}_t$. The Structure 1 coefficients are 1, 5.93 meters, and 0, the Structure 2 coefficients are 0.5, 0.17 meters, and 0.61, and the Structure 3 coefficients are 0.50, 0.36 meters, and 1.29 for C_v, C_M, and C_P, respectively.

Demands were expressed as component time histories for ΔV, ΔM, and ΔP for each structure during each ground motion. I then input the time histories into the elastic solutions in Equations (3-4) through (3-16) to produce time-variant stress distributions for σ_{zz}, σ_{xx}, σ_{yy}, and σ_{xz} below each structure. I compiled these stresses into the matrix form in Equation (3-3) and summed the stresses using Equation (3-1). I finally calculated q in accordance with Equation (3-28). The q stress distribution for an example ground motion below Structure 1 is presented in Figure 118 for $t = 0$ (i.e. static in-situ conditions before shaking) and the t corresponding to maximum structure response, $t_{u,max}$. Note the sharp increase in stress below the footing edge due to SSI effects.

The resulting q distributions below the footing correspond to perfectly flexible foundation conditions, whereas real footings exhibit non-zero flexural stiffness. The influence of footing flexibility on q is highest at the point where the corner of the footing contacts the soil (at $X = B, Z = 0$) and becomes smaller as depth increases and as horizontal distance from the corner of the footing increases. An appropriate means of selecting a representative location to evaluate q is critical to the effectiveness of the DSR framework calculations. For the purpose analyzing the factor of safety against cyclic softening, I selected a "representative" location affected by both moment and shear demands, and where SSI-induced stresses are appreciable. For this calculation, I chose to calculate the deviatoric factor of safety at $X = B$, $Z = B$, or one-half footing width below the outside edge of the footing for each structure. Although a somewhat arbitrary selection, demand at this soil position is generally representative of the overall demand below the footing

without excessive influence from footing stiffness or bias towards heavy ΔM or ΔV. Figure 119 presents example demand time histories at $X = B, Z = B$ for Structure 1.

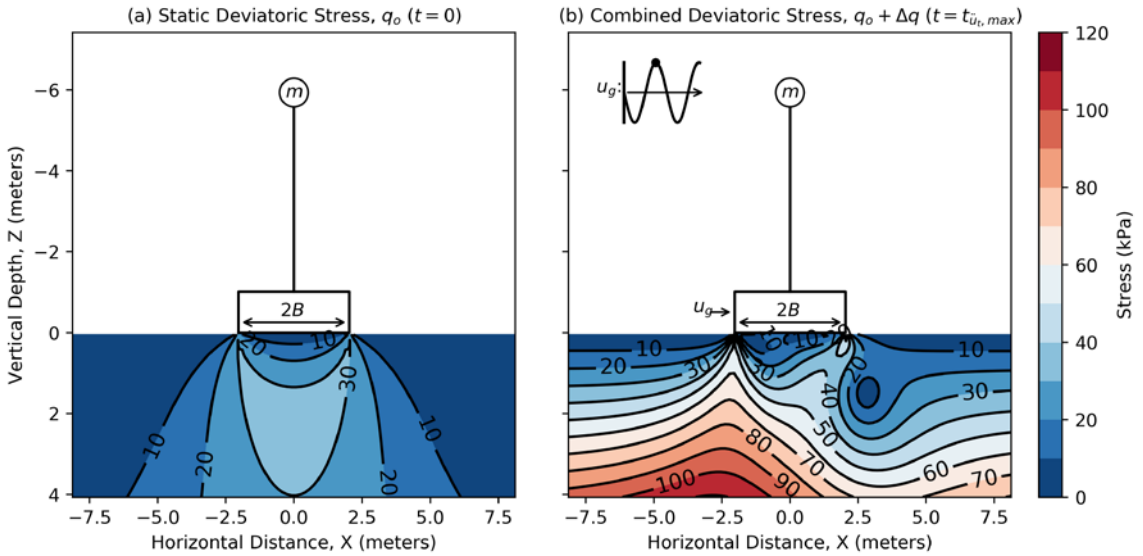

Figure 118: Static Stress and Dynamic Deviatoric Stress at Maximum Structure Response for JZB01 Structure 1 during TCU-078 [0.4]

For compatibility with the DSR framework analysis, I evaluated the CSR demand term $\Delta\sigma_{xz,ff}$ at $Z = B$ in the free field, where B corresponds to the Structure 1 and 3 footings. The depths of far field accelerometer A46 for JZB01 and A42 for JZB02 are approximately $Z = B$, so I calculated $\Delta\sigma_{xz,ff}$ using data from these accelerometers. The CSR analysis results will therefore be more comparable to the DSR framework analysis results for Structures 1 and 3. I didn't not evaluate CSR demand at B corresponding to Structure 2 because data was not available for shallower far field accelerometers A44 and A45 on JZB01 and A39 on JZB02, which failed during centrifuge testing.

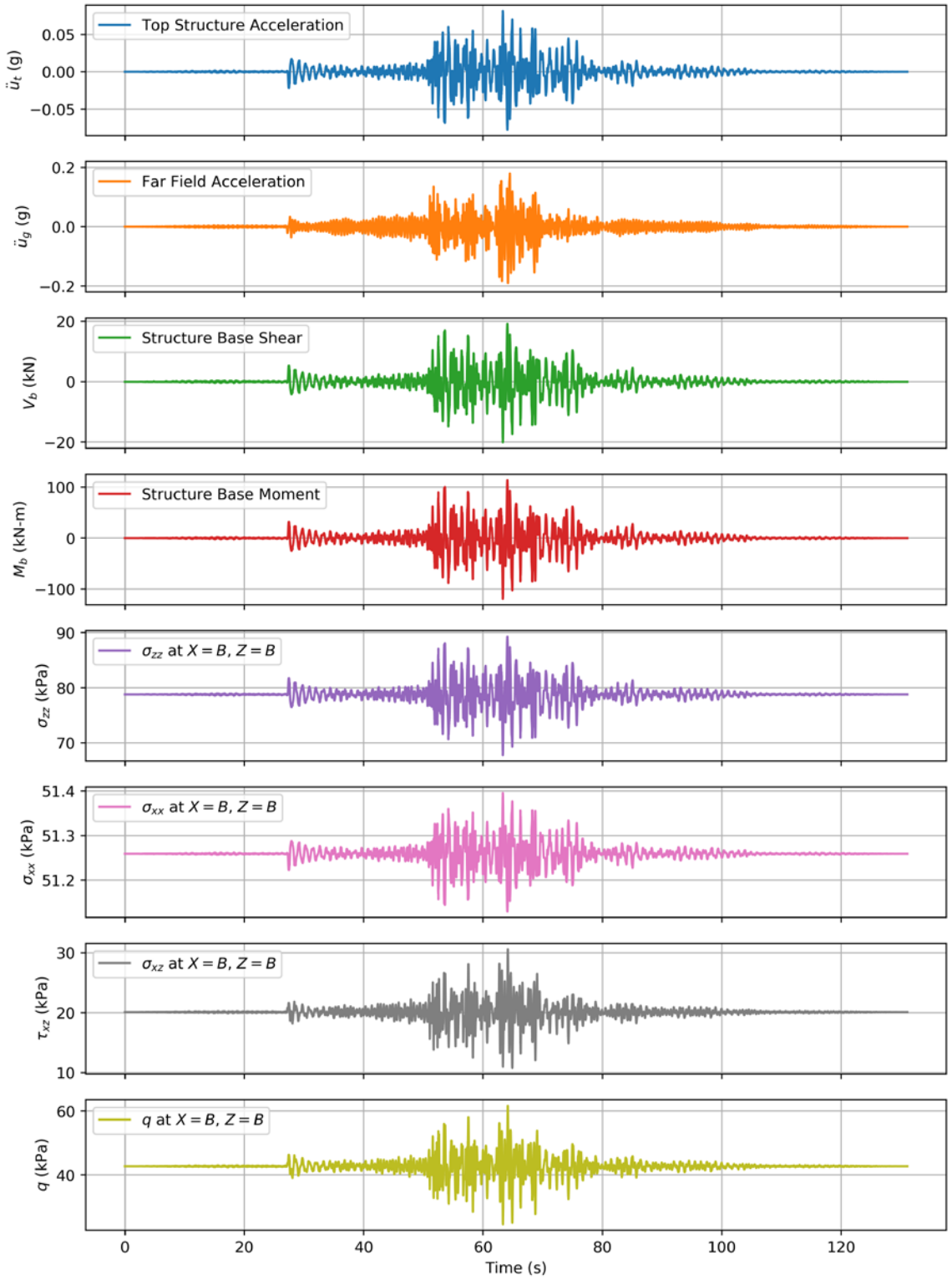

Figure 119: Demand Time Histories for JZB01 Structure 1 during TCU-078 [0.4]

10.3.2 Cycle Counting

I evaluated time histories of the demand measures DSR and CSR using the stress time histories for each ground motion developed in the previous section. I evaluated DSR in accordance with Equation (3-29) and CSR as $CSR = \Delta\sigma_{xz,ff}/\sigma'_{zzo,ff} = \tau_{xz}/\sigma'_{vc}$.

The final input required to evaluate DSR is q_f, which is calculated using the monotonic shear strength, s_u of the foundation soil in accordance with Equation (3-35). I selected s_u values for the model JZB01 and JZB02 clays based on the shear strength evaluation detailed in Chapter 9. Figure 120 presents the calculated DSR time series. Figure 121 presents the CSR time series.

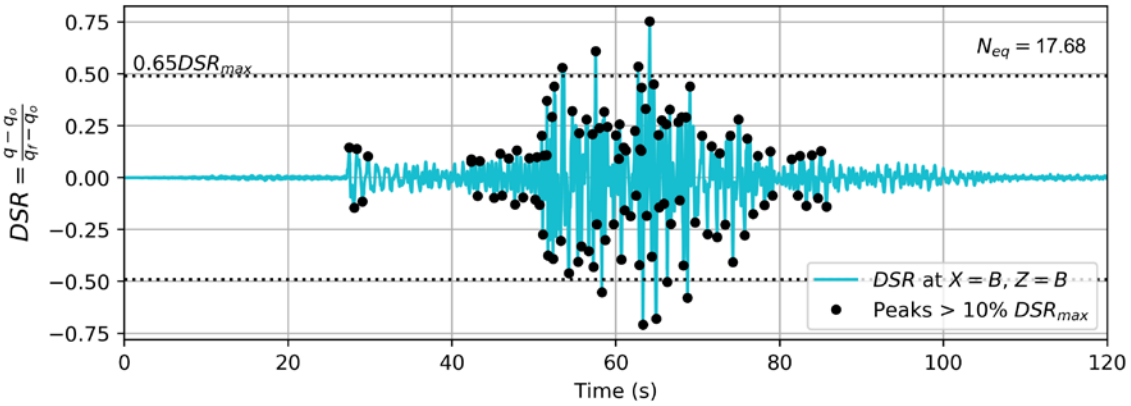

Figure 120: DSR Time series for JZB01 Structure 1 during TCU-078 [0.4]

The DSR time history was converted to a single-amplitude cyclic demand value, DSR_M at an equivalent number of cycles, N_{eq}. I took $DSR_M = 0.65 \cdot DSR_{max}$, in accordance with the procedure in Chapter 3. I performed the conversion by identifying all of the local maxima and minima that cross $\pm 0.1 \cdot DSR_{max}$ and define these values as an array, DSR_{pk}, of length N_{pk}, with each DSR_{pk} value associated with half of a loading cycle. Figure 120 presents the peaks identified to develop DSR_{pk} for the DSR time series. I then computed

the equivalent number of cycles at DSR_M for each value of DSR_{pk}, and summed over the time series based on Equation (3-37).

Similarly, the CSR time history was converted to a single-amplitude cyclic demand value, CSR_M equal to $0.65CSR_{max}$. The conversion considered local maxima and minima that cross $\pm 0.1 \cdot CSR_{max}$, defined as an array, CSR_{pk}, with each peak value associated with half of a loading cycle. Figure 121 presents the peaks identified to develop CSR_{pk} for the CSR time series. I then computed the equivalent number of cycles at CSR_M for each value of CSR_{pk}, and summed over the time series similarly to the deviatoric approach.

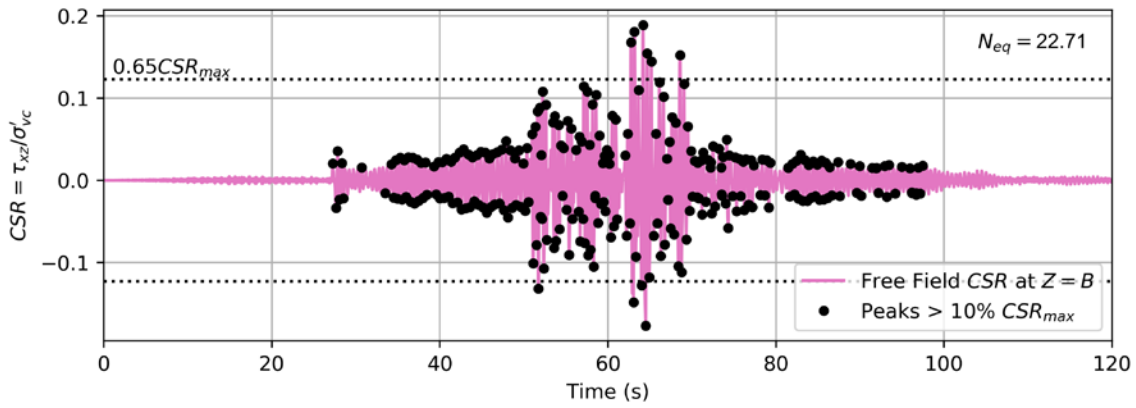

Figure 121: CSR Time Series for JZB01 Structure 1 during TCU-078 [0.4]

10.4 Factor of Safety and Induced Strain

I calculated the factors of safety against cyclic softening ground failure for each ground motion using stress conditions applicable to soil domains beneath structural foundations and in the free-field. The cyclic softening FS for the condition beneath foundations is referred to here as the deviatoric factor of safety, FS_{DSR}, and is computed according to Equation (3-38). The applicable DRR to calculate factor of safety is $DRR_M = DRR(N_{eq})$. The cyclic softening FS for free-field conditions is referred to here as the cyclic based

factor of safety, $FS_{CSR} = CRR_M/CSR_M$, where CRR_M is the value of CRR at the equivalent number of uniform stress cycles corresponding to CSR_M.

The DRR and CRR curves used to evaluate factor of safety are tied to a specific cyclic shear strain, γ_{cyc}. Most simplified procedures evaluating ground failure potential calculate factor of safety for $\gamma_{cyc} = 3\%$. For consistency with these procedures, I computed FS_{DSR} and FS_{CSR} using DRR and CRR curves corresponding to $\gamma_{cyc} = 3\%$. I then compared the computed factors of safety against normalized structure settlement in Figure 122 for FS_{DSR} and in Figure 123 for FS_{CSR}.

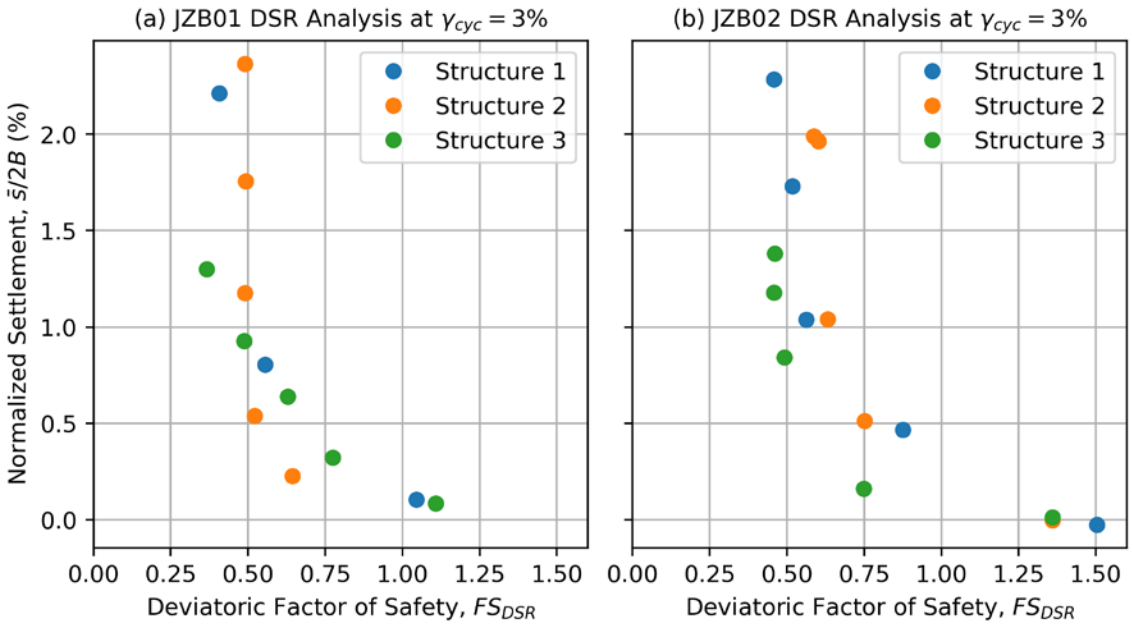

Figure 122: Deviatoric Factor of Safety Against Cyclic Softening

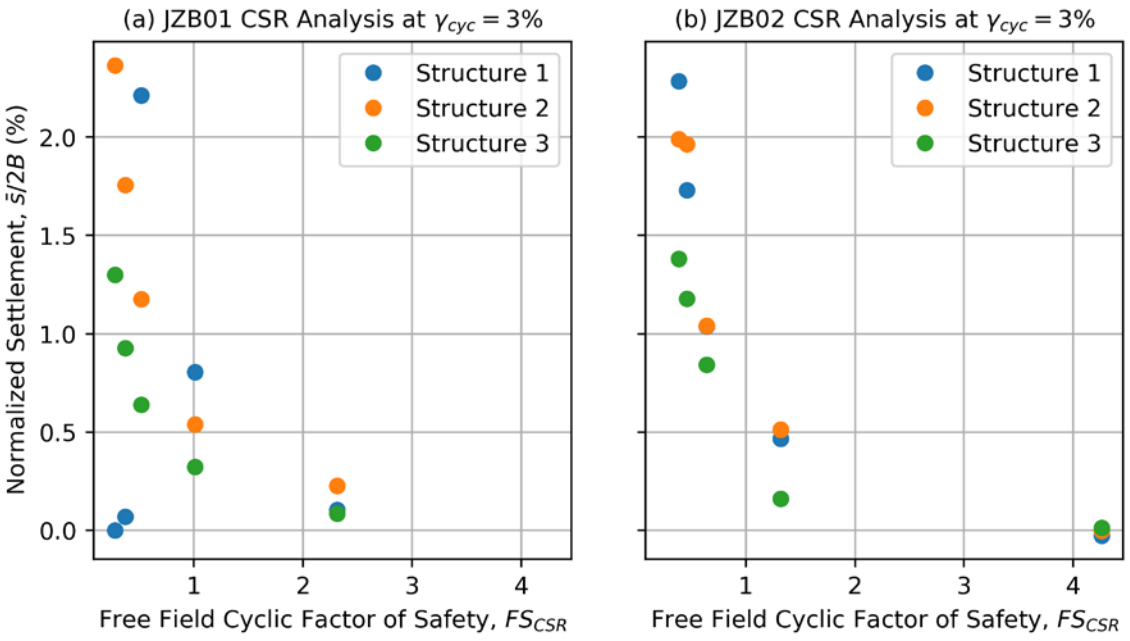

Figure 123: CSR-Based Factor of Safety Against Cyclic Softening

Examining first the far-field condition, Figure 123 shows that 9 shakes in JZB01 and 8 shakes in JZB02 produce a cyclically softened condition, meaning that cyclic degradation is expected to reduce strength and produce large cyclic strains. Despite this, the centrifuge models did not reveal any evidence of permanent ground deformation (lateral movement or settlement) in the far field. This finding of triggering but no consequence in the far (free)-field is typical of past experience with cyclic softening; its impacts are greatest for stability problems involving a large driving static shear stress (e.g., slopes, foundations). For this reason, FS_{CSR} is plotted against structure settlement to gauge the contribution of free field stress conditions to ground failure below structures.

The plots in Figure 122, corresponding to cyclic softening of foundation soils, demonstrate a more direct impact of softening, in this case on foundation settlement. Structure 1 experienced bearing capacity failure (e.g. tipped over) during Shake Numer 8 in model JZB01 and during Shake Number 13 in model JZB02; therefore, settlement and rotations are only presented for the structure before these shakes. Figure 122 indicates a

reasonable trend between DSR and structure settlement. Settlement is generally low or negligible at factors of safety greater than unity, and progressively increases as factors of safety decrease. Note that Structure 2 generally settled more than other structures. This is likely due to increased demand imposed by that structure, because the Structure 2 natural frequency was nearest that of the soil deposit and the structure consistently experienced the highest accelerations among structures. The corresponding trends in Figure 122 between CSR and structure settlement are less robust. At a factor of safety near unity, the structures have already experienced considerable settlement and some settlement even occurs at factors of safety much greater than unity.

In Chapter 4, I developed DRR and CRR curves v. N_{eq} for γ_{cyc} of ½, 1, 3, and 6 percent. To examine the influence of γ_{cyc} on FS_{DSR}, I performed the cyclic softening evaluation for each strain level in the suite of DRR curves. Note that cycle counting procedures used to generate N_{eq} for DSR_M are specific to the c and d coefficients corresponding to the specific DRR curve. This means each DRR curve has a unique value of N_{eq} for a given ground motion, although DSR_M is the same regardless of the DRR curves applied to a given motion. Figure 124 presents the FS_{DSR} for the range of γ_{cyc} used to develop DRR v. N_{eq} curves.

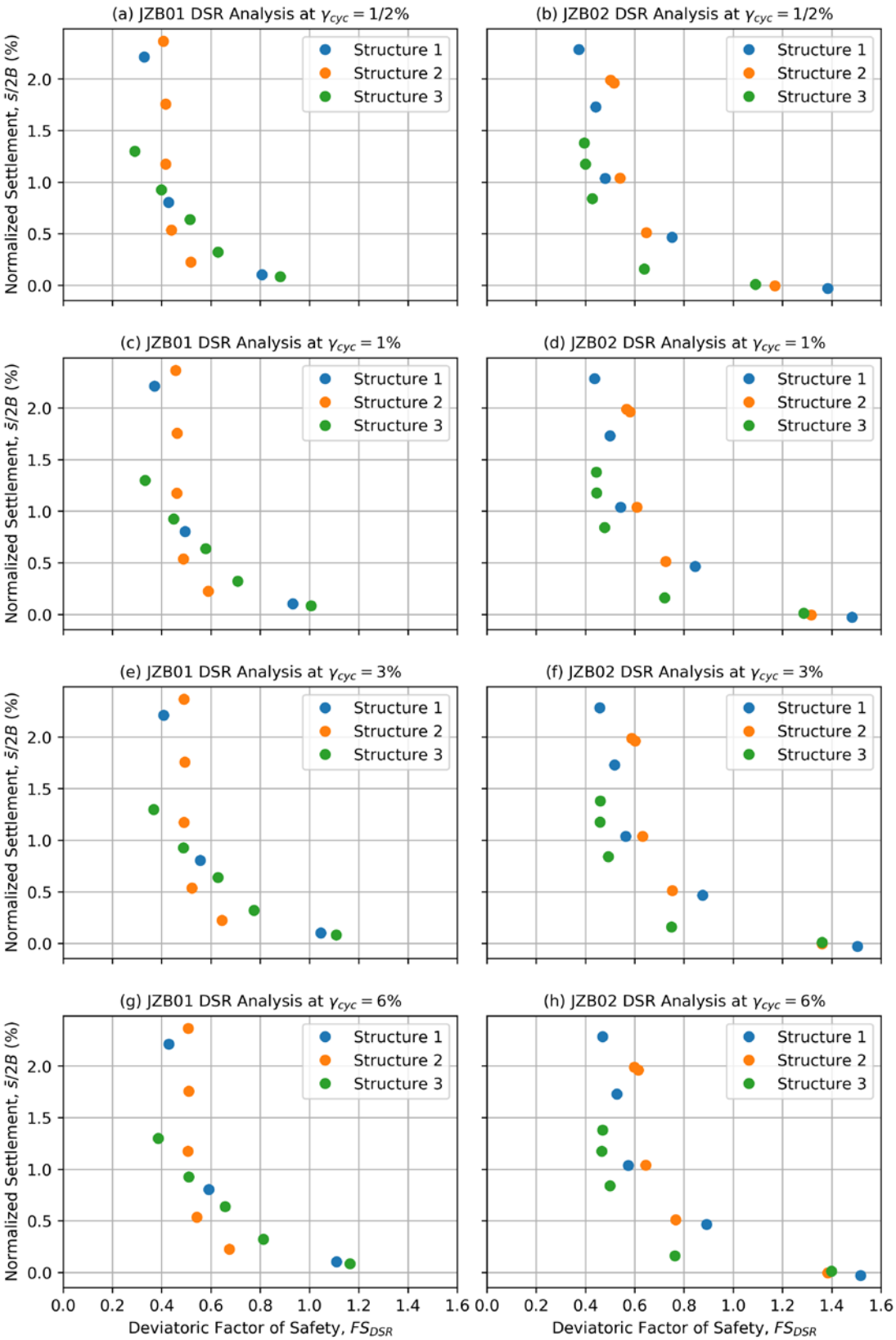

Figure 124: Deviatoric Factor of Safety at Multiple Strain Levels

The results in Figure 124 show that cyclic softening is predicted both in the foundation soils and in the far-field for all of the alternate definitions of cyclic shear strength (i.e., those associated with strain levels other than 3%). As a result, I reach two conclusions: (1) the findings presented here on the onset of cyclic softening are not sensitive to the definition of cyclic strength and (2) large strains, exceeding 6%, are expected in the foundation and far-field soil materials for some of the shakes (because FS < 1 for both cyclic strength definitions).

10.5 STRAIN-BASED DISPLACEMENT INDICES

In the preceding analyses, the FS for cyclic softening was computed using a stress demand evaluated at the single point $X = B,\ Z = B$, with DSR, FS, and γ_{cyc} correspondingly evaluated solely for that point in the subsurface. There are two principle limitations of this analysis: (1) the outcome of the analysis, being expressed as a FS, is not well suited to serve as an index for prediction of foundation deformations, and (2) while demand at the selected soil position is generally representative of demand distribution below the footing, the single-point approach comes with obvious limitations and may be a poor indicator of performance for structures other than those tested for JZB01 and JZB02.

To enhance the preceding analyses and develop a more robust relationship between strain and structure performance, I evaluated strain over a 100 x 100 grid of points below the structure foundations. At each point, I calculated static stress and evaluated time histories for the increase in stress due to the dynamic loading increment. From the stress time histories, I then evaluated DSR and performed cycle counting procedures on each DSR time history to evaluate a single-amplitude cyclic demand value, DSR_M at an equivalent number of cycles, N_{eq} in accordance with the procedure used above. Finally, I used Equations (4-5) and (4-6) to evaluate γ_{cyc} below the foundation. Figure 125

presents an example distribution of γ_{cyc} below the JZB01 Structure 1 footing for the TCU-078 [0.4] ground motion. Note that strain is capped at $\gamma_{cyc} = 10\%$ due to limitations of the DSS test data discussed in Section 4.4. This analysis was performed for each structure in each model for each applied ground motion, resulting in 28 total analyses (analyses were not performed for Structure 1 after it experienced bearing capacity failure). Appendix B presents plots resulting from these analyses.

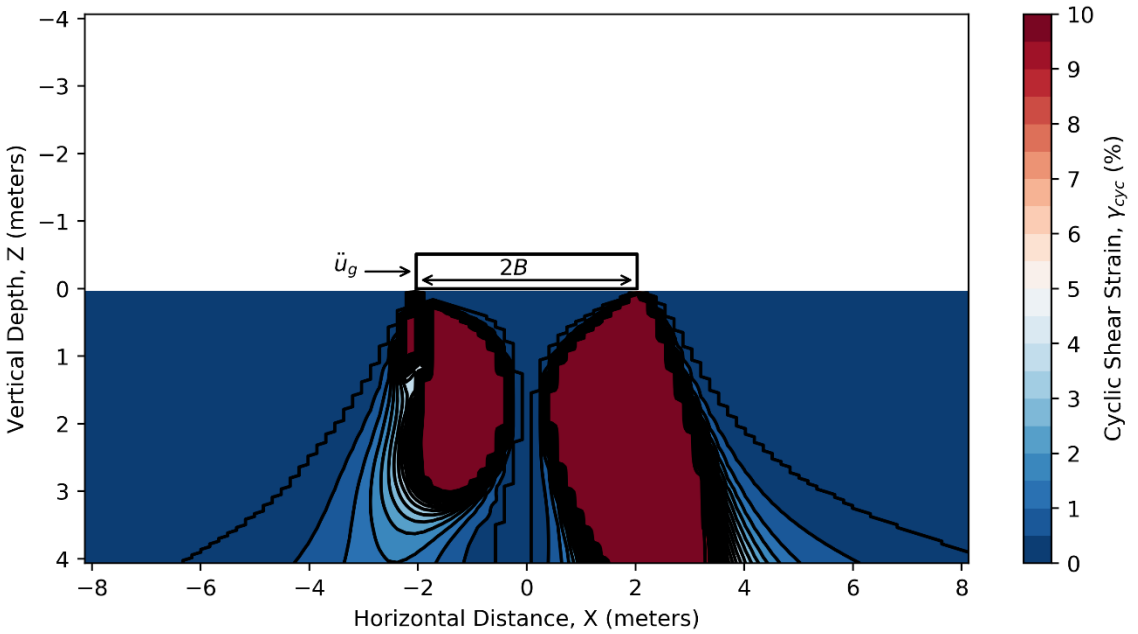

Figure 125: Strain Contours below JZB01 Structure 1 for TCU-078 [0.4]

Cyclic shear strain amplitude below the structure foundations can be integrated to calculate displacement indices that provide a proxy of model performance. I integrated strain in multiple ways to evaluate different indices and plotted the indices against structure settlement. I used the following indices:

- Displacement Index 1 – Vertical integration over a distance equal to one footing width, $2B$ below the footing bottom at a point $B/4$ inside the footing corner, expressed as: $DI_1 = \int_{z=0}^{z=2B} [\gamma_{cyc}/2B]_{x=3B/4} dz$. See Figure 126.

- Displacement Index 2 – Horizontal integration over the footing width, $2B$ at a point one-half footing width, B below the footing bottom, expressed as:

  $DI_2 = \int_{x=-B}^{x=B} \left[\gamma_{cyc}/2B\right]_{z=B} dx$. See Figure 127.

- Displacement Index 3 – Integration over the area extending from the footing bottom to one half footing width, B below the footing bottom, expressed as:

  $DI_3 = \int_{z=0}^{z=B} \int_{x=-B}^{x=B} \left[\gamma_{cyc}/4B^2\right] dxdz$. See Figure 128.

- Displacement Index 4 – Integration over the area extending from the footing bottom to one footing width, $2B$ below the footing bottom, expressed as:

  $DI_4 = \int_{z=0}^{z=2B} \int_{x=-B}^{x=B} \left[\gamma_{cyc}/4B^2\right] dxdz$. See Figure 129.

The index with the best performance is Displacement Index 1, followed by Displacement Index 2. Both of these indices are limited at higher strain levels, as the indices saturate at a value of 10%. Displacement Index 3 saturates at a value of 5% and Displacement Index 4 saturates at a value of 10%. The saturation occurs because the relationship used to evaluate strain is capped at $\gamma_{cyc} = 10\%$, which is the maximum strain due to limitations of the DSS test data discussed in Section 4.4.

Displacement indices are preferred over factors of safety at a point for evaluating structure performance because the displacement indices capture a larger range of the soil response below the foundation. Further, displacement indices suggest a more gradual soil response, as opposed to the limit-equilibrium implications of factors of safety that suggest a rapid change in behavior at unity. The displacement indicates presented here are superior to factors of safety in characterizing structure performance.

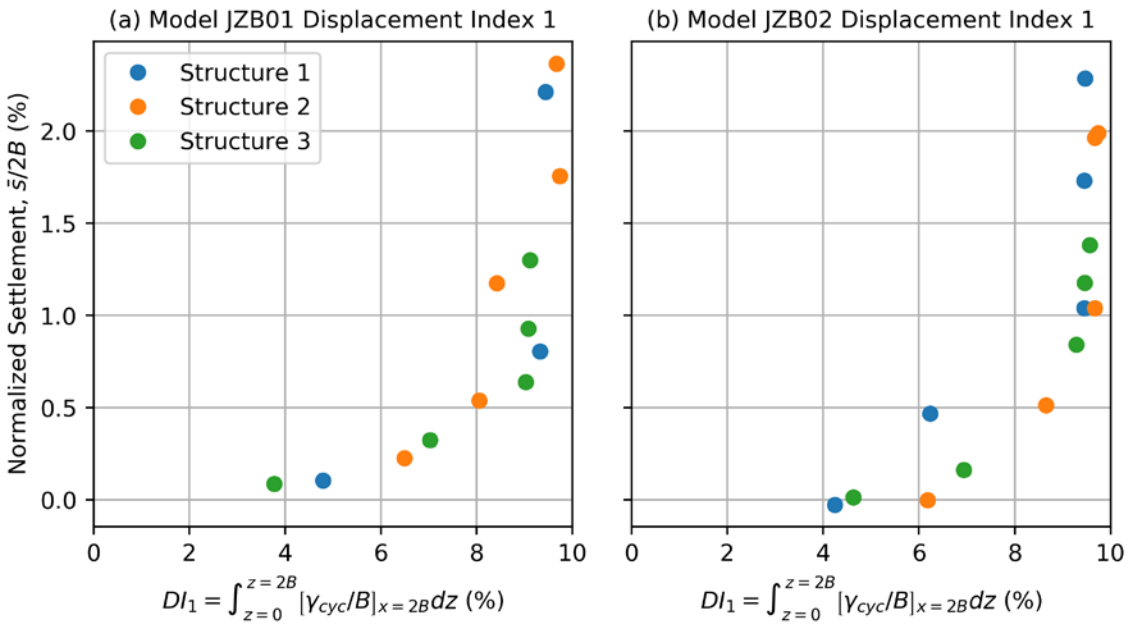

Figure 126: Displacement Index 1 Normalized Relationship

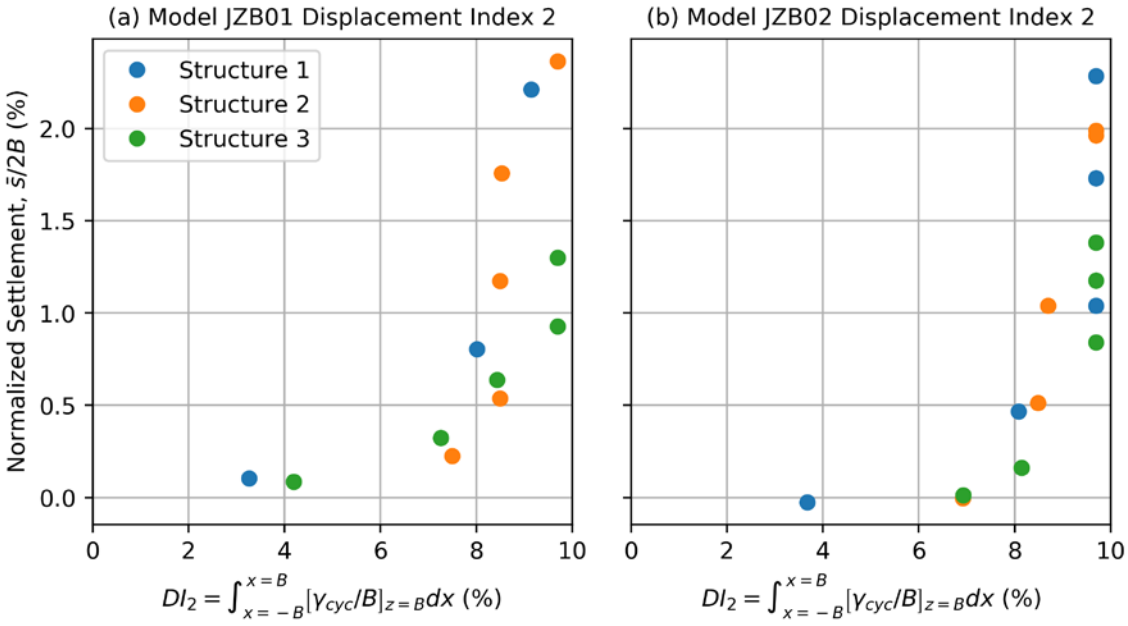

Figure 127: Displacement Index 2 Normalized Relationship

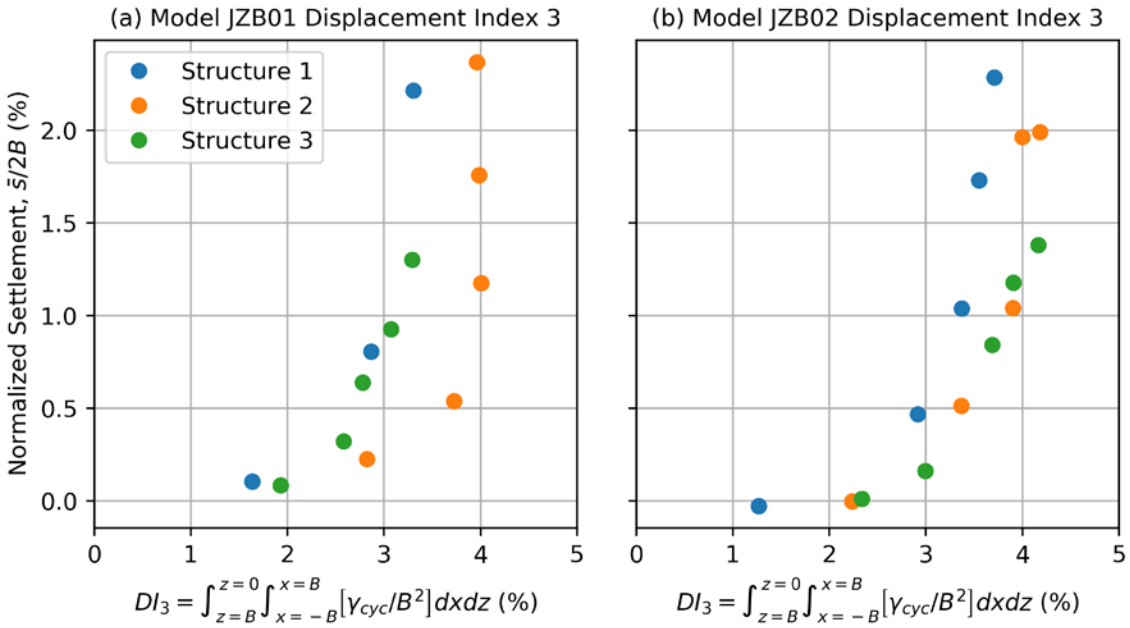

Figure 128: Displacement Index 3 Normalized Relationship

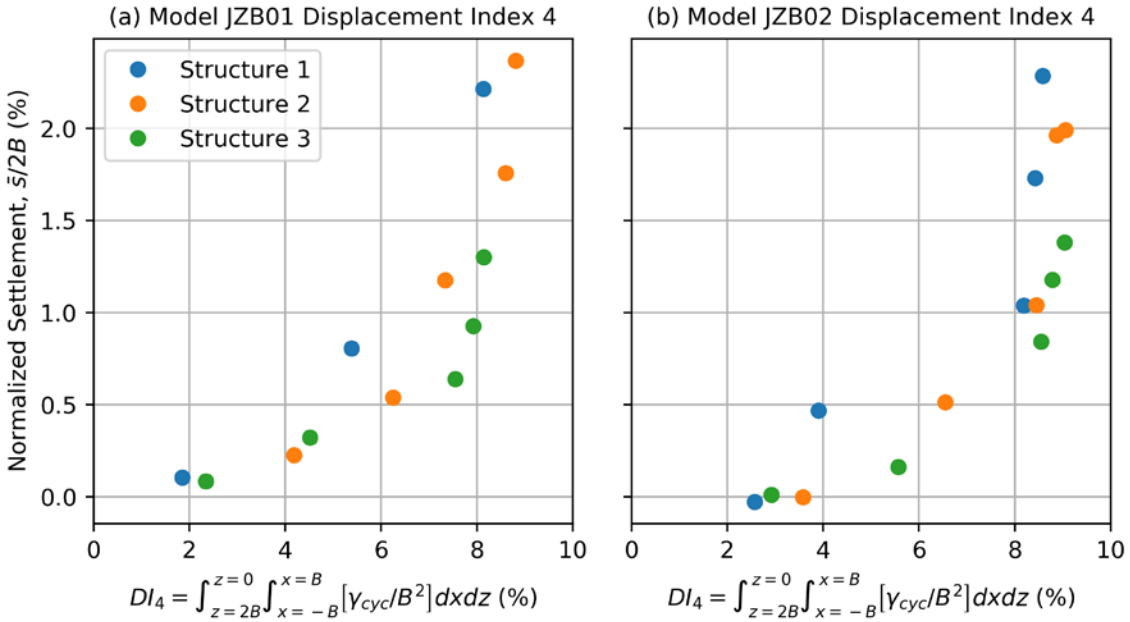

Figure 129: Displacement Index 4 Normalized Relationship

10.6 LIMITATIONS

The proposed deviatoric stress framework and associated cyclic softening and cyclic shear deformation evaluations performed above incorporate simplifications and the

potential for systemic errors exists in the solutions. Some potential limitations are reviewed here.

10.6.1 Wave Propagation Effects

The analysis assumes applied stresses from SSI-based ΔV, ΔM, and ΔP demands are mobilized instantaneously below the foundation as pseudo-static stresses. In reality, some phase lag exists between the application of ΔV, ΔM, and ΔP and the mobilization of soil stresses due to wave propagation effects. The phase lag is small immediately adjacent to the foundation and greater away from the foundation. Further, the SSI-induced stresses are themselves frequency-dependent and dynamic effects play a role in the mobilized SSI stresses below foundations. I used solutions by Heidarzadeh et al. (2015, 2018) to address potential error due to phase lag. Dynamic effects have been neglected for the present analysis.

Heidarzadeh et al. (2015) used the boundary element method to address this problem by developing dynamic solutions for a harmonically oscillating vertical point load, which is the Boussinesq (1885) problem and horizontal point load, which is the Cerruti (1882) problem. Heidarzadeh et al. (2018) developed corresponding dynamic solutions for harmonically oscillating vertical and horizontal line loads, which are the Flamant (1892) problem. I used the Heidarzadeh et al. (2018) to estimate phase lag for the elastic solutions used to evaluate cyclic softening. The phase lag calculation is based on the parameter a_o, where $a_o = \omega R/V_s$. The parameter ω is the frequency of the harmonically oscillating applied vertical and horizontal line loads. The parameter R is the distance from the application point of the vertical or horizontal line load. Because the JZB01 and JZB02 structure foundations are relatively wide, a single representative R parameter is not easily developed for the foundations. For simplicity, I assumed $R = \sqrt{5}B$, which corresponds to conditions where dominant ΔM load is applied to the foundation and the cyclic softening

evaluation is performed at $X = B$ and $Z = B$. These conditions are likely to represent a "worst-case" for wave propagation effects. The parameter V_s is soil shear wave velocity, which was developed in the cyclic softening analysis above.

I calculated the FFT of horizontal motions applied at the tops of the structures to evaluate frequency content of applied SSI-based ΔV, ΔM, and ΔP demands. I then converted the calculated ω to parameter a_o. Figure 130 presents the FFT amplitude versus a_o for Shake No. 4 applied to models JZB01 and JZB02, which was the TCU-078 motion at an amplitude factor of 0.4. The frequency contents are similar for the TCU motion at the other applied amplitude factors.

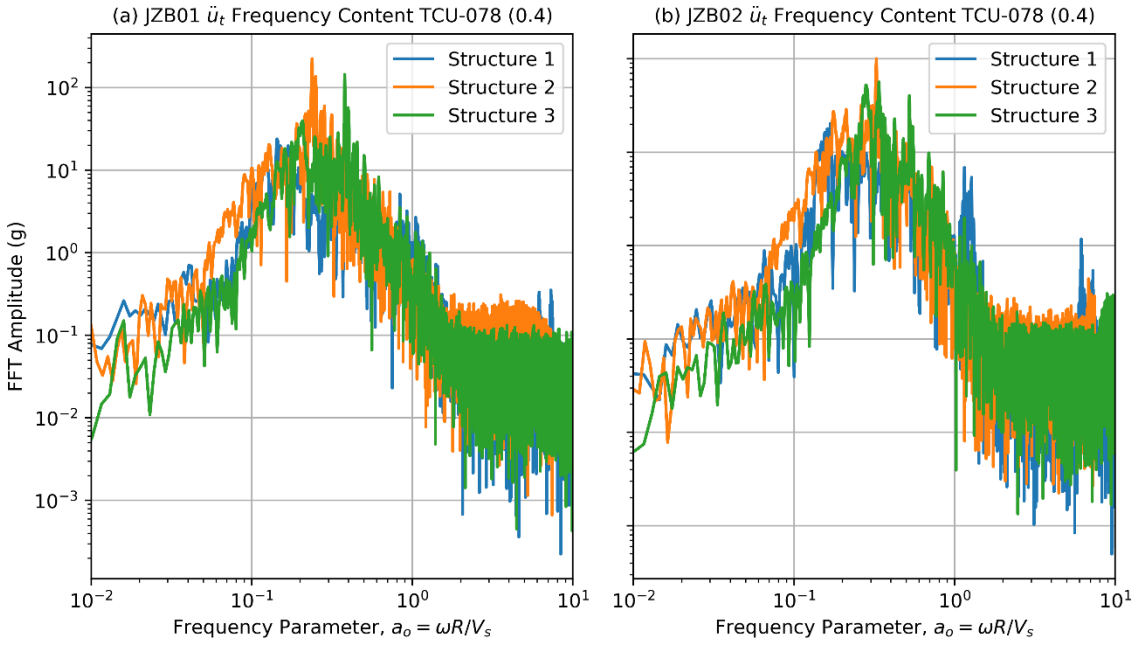

Figure 130: Normalized Frequency Content of Top Structure Horizontal Motions

Nearly all applied motion occurs at a normalized frequency of $a_o < 2$. Based on the Heidarzadeh et al. (2018) solution, the phase lag for an applied vertical line load at $a_o = 2$ is 2.5, 5, and 1.5 degrees for the σ_{zz}, σ_{xx}, and σ_{xz} stress components (0.04, 0.09, and 0.03 radians), respectively. The corresponding phase lag for an applied horizontal line

load at $a_o = 2$ is 1, 1, and 0.5 degrees for the σ_{zz}, σ_{xx}, and σ_{xz} stress components (0.02, 0.02, and 0.01 radians), respectively. The phase lag values are relatively low, indicating time lags ranging from 0.1 to 0.01 seconds for the majority of frequency contents in the motion. This is logical, as dimensionless frequency can be spatially interpreted as the number of wavelengths within a specific spatial interval. Ground motion induced wavelengths tend to be long relative to the distance from the bottom of the footing to the point of interest. Therefore, I anticipate the systemic error introduced by the zero phase assumption for SSI demand waves to be low.

10.6.2 Structural Models

Structure 1 is relatively simple to analyze, because it may be represented as a SDOF system. Structures 2 and 3 are frames and require a greater computational effort to accurately evaluate structural response. To simplify the SSI-demand evaluation procedure, I assumed Structure 2 and 3 model behavior as a rigid top frame over two columns founded on SSI springs. Figure 117 presents the behavioral models for structures. This model configuration is likely imperfect and does not capture important aspects of structural response, including damping, distributed mass, and non-rigid top frames. Correct modeling to more accurately evaluate structural behavior would likely require finite element modeling. However, because predictions of bending moment using behavior models was reasonably compatible with the bending strains measured using strain gages, I anticipate this source of error to be relatively small.

10.6.3 Soil Nonlinearity

The basis for soil stress evaluation in the framework are elastic stress solutions. Nonlinearity obviously exists in soil behavior at even low levels of shaking. The presence of nonlinearity in the actual soil response substantially impacts the soil deformations,

which is accommodated in the present analysis through the linkage of stress demands to deformations. The impact of nonlinearity on the stress demands themselves is minimal (Section 10.3.1), which is typically the case for stress calculations. Hence, the main source of approximation is the representation of the nonlinear deformations with laboratory test results (Section 4.3). While the elastic stress solutions used here introduce small errors to computed stresses, they have the benefit of making the framework accessible to practicing engineers and usable on projects that do not require more advanced modeling. Indeed, the use of numerical modeling on a project renders the framework superfluous, as soil stresses and deformations could instead be evaluated using numerical models that employ constitutive relationships capturing the full range of nonlinear soil behavior. In reality, only large-scale infrastructure projects typically merit numerical modeling by geotechnical engineers. Simpler methods are needed to fill the considerable gap between average geotechnical work and large-scale infrastructure, which is what this framework endeavors to accomplish.

11 CONCLUSIONS

The research summarizes here provides an incremental step forward in the integration of SSI effects with cyclic softening ground failure evaluation. This dissertation summarizes the total output of the research effort, which is centered around the proposed the new framework for evaluation of cyclic ground failure potential in Chapter 3. The framework utilizes elastic solutions to define SSI-based stress demands beneath shallow foundations and proposes a new demand parameter, called the DSR, to quantify incremental stress demands under complex stress paths below footings. The vehicle for validating and demonstrating the proposed new framework was two centrifuge model tests, designated JZB01 and JZB02, and summarized in Chapters 5 through 7. The centrifuge tests incorporated two synthetically blended clays based on work by Eslami (2017). I reviewed clay strength laboratory data by Eslami that I expressed in terms defined using the new framework in Chapter 4. I derived clay strength parameters from the laboratory data for multiple strain levels. Chapter 8 presents data processing and data results from the centrifuge testing program. Chapter 9 presents a pseudo-static bearing capacity evaluation for Structure 1 during each centrifuge model test and derivation of monotonic

clay strength that factors into the deviatoric-based cyclic softening analysis. Chapter 10 presents the deviatoric-based cyclic softening analysis on the centrifuge model structures to demonstrate the new framework. The analysis results are presented as factor of safety plots and strain-based indices that serve as a proxy for normalized structural settlement.

In the final analysis, the proposed cyclic softening framework was proven to be predictive of cyclic softening impacts to structures. Imperfections in the framework and its implementation remain, but framework is solid foundation and the structure of the framework is adaptable to a variety of SSI-based cyclic ground failure problems.

12 FUTURE RESEARCH OPPORTUNITIES

There is always work remaining in any research effort. The research summarized here is no exception. The centrifuge tests alone that were central to this work took over two years to complete. Another nine months were required to process and clean data from the centrifuge program, write data reports, and submit conference/journal papers, before I was in a position to begin the core cyclic softening analysis within the deviatoric framework. In the remaining six months before graduation, I output all work connected to the cyclic softening analysis and weathered many trials and errors before settling on the current approach. With more time, there would certainly be opportunity to output additional research. Consider the following:

- **Develop a Simplified Framework Procedure** – The deviatoric-based cyclic softening evaluation framework proposed here is involved and requires a suite of input parameters that may not be available to practicing geotechnical engineers. Most cyclic ground failure evaluation frameworks in use today by practitioners are simplified procedures in the spirit of the original simplified procedures produced by

Seed and Idriss. A comparable simplified procedure for the deviatoric framework proposed here would be useful.

- **Analyze Centrifuge Models on Liquefaction** – A number of researchers have performed centrifuge modeling of liquefaction ground failure. See Chapter 2. Data from these modeling programs provide the opportunity to test the deviatoric stress framework proposed here against other datasets, particularly in regard to liquefaction.
- **Comparison with Existing Numerical Modeling** – A number of researchers have performed numerical models of SSI-induced liquefaction ground failure. See Chapter 2. Most output from this research is centered around relationships between ground motion demand parameters and structural performance parameters. Review of this work within the deviatoric framework proposed here may provide additional insights on the model results and the relationships observed to date.
- **Numerical Modeling to Capture Nonlinear Soil Behavior** – Numerical modeling could also be performed to evaluate the validity of elastic soil stress solutions employed in the framework. Nonlinearity obviously exists in soil behavior at even low levels of shaking and the elastic stress solutions remain only tenuously valid while the nonlinear behavior does not dominate soil response. Numerical modeling could be used to evaluate the limitations of these elastic solutions and provide recommendations for correction factors based on soil type or behavior.
- **Collaborate with Structural Engineers** – The proposed framework resides at the intersection of SSI effects and cyclically induced ground failure. The modeled SSI demands from structures are simplistic and could likely be enhanced through collaboration with structural engineers. The stress tool introduced here could also be modified to accept input ground motions, rather than harmonic motions. Suites

of ground motions could be input into the tool and parametric studies on the results could be performed to generalize the tool for design-related application.

Additionally, there are many details within this research that could be improved. Code can be made to run faster, and soil or structural parameters could be further refined. The suite of data regarding JZB01 and JZB02 clay consolidation could be a stand-alone PhD and overall model behavior analyzed using numerical methods could be another. There is always a next step. Everything summarized here is the most I could do with the time I had available while at UCLA. I hope the next PhD student will take this work further.

APPENDIX A: CYCLIC DIRECT SIMPLE SHEAR DATA PROCESSING

Cyclic DSS laboratory test data by Eslami (2017) provided the basis for derivation of cyclic clay strength for use in ground failure analysis in this dissertation. DSS testing consisted of constant-height, undrained, stress controlled cyclic tests. Shear load was applied during testing as uniform sinusoidal stress waves at varying CSR. Eslami (2017) presented data from DSS testing in terms of CSR and cyclic shear strain, γ_{cyc}, versus the number of uniform stress cycles, N. He presented strength relationships from the DSS testing as a series of CRR and cyclic strength ratio curves, corresponding to $\gamma_{cyc} = 3\%$. CRR curves can be developed for alternative strain levels by calculating CSR points from the data for the desired strains. I developed the alternative CRR curves from the Eslami (2017) data (i.e. the original data). Then, because of consistency issues with the curves due to variations in the target CSR, I corrected each test dataset to a test-specific CSR that I designated CSR_{base} and rederived the CRR curves from that data (i.e. the CSR-adjusted data). The CSR-adjusted data curves are more consistent with expected behavior.

CURVE FITTING ON ORIGINAL CYCLIC DIRECT SIMPLE SHEAR DATA FROM ESLAMI (2017)

I developed CRR curves for alternative strain levels by first identifying peaks in the CSR versus cyclic shear strain, γ_{cyc} data along with corresponding points in the γ_{cyc} versus N data. I then fit a 6th-order polynomial curve to the γ_{cyc} versus N peaks and a 2nd-order polynomial curve to the CSR versus N peaks using least squared regression. I fit curves to both positive and negative peaks in the form of Equations (A-1) through (A-4).

$$\gamma_{cyc,fit(pos)} = c_1 x^6 + c_2 x^5 + c_3 x^4 + c_4 x^3 + c_5 x^2 + c_6 x + c_7 \quad \textbf{(A-1)}$$

$$\gamma_{cyc,fit(neg)} = c_8 x^6 + c_9 x^5 + c_{10} x^4 + c_{11} x^3 + c_{12} x^2 + c_{13} x + c_{14} \quad \textbf{(A-2)}$$

$$CSR_{fit(pos)} = c_{15} x^2 + c_{16} x + c_{17} \quad \textbf{(A-3)}$$

$$CSR_{fit(neg)} = c_{18} x^2 + c_{19} x + c_{20} \quad \textbf{(A-4)}$$

Table A-1 presents the polynomial curve fitting coefficients for each DSS test on the SBFW and SKFW blends from Eslami (2017). Figures A-1 through A-21 present both the original laboratory data and the fitted curves, as well as datapoints that indicate CSR and N at γ_{cyc} values of ½, 1, 3, and 6 percent. I took the lesser CSR and N yielded by the positive and negative fitted curves. Note that CSR is not constant for the test, particularly at higher strains. Even at lower strains, the CSR is rarely constant, as positive and negative stress loops typically peak at different CSR values. The lack of a consistent CSR is likely due to difficulties associated with the DSS equipment maintaining stress control during testing.

CURVE FITTING ON CYCLIC DIRECT SIMPLE SHEAR DATA FROM ESLAMI (2017) AT ADJUSTED CYCLIC STRESS RATIO

The lack of a consistent CSR will create systemic error in the derivation of CRR curves. To mitigate this error, I corrected the DSS data by adjusted the data to a consistent, test-specific base CSR, CSR_{base} and the equivalent number of uniform cycles, N_{eq}. This data correction process is analogous to the conversion of a broadband ground motion time series into the equivalent number of uniform stress cycles at a constant stress amplitude. The broadband conversion process is detailed in Section 3.2.3 for the deviatoric stress framework proposed in this dissertation. To perform the data correction, I took CSR_{base} as equal to the average CSR amplitude over the first 10 peaks of the CSR versus γ_{cyc} data. I then calculated N_{eq} for each peak in the CSR data, designated CSR_{pk}, using the N value corresponding to that peak, N_{pk}, as shown in Equation (4-3), which is restated here as Equation (A-5):

$$N_{eq} = N_{pk}\left(\frac{CSR_{pk}}{CSR_{base}}\right)^{1/b} \quad \textbf{(A-5)}$$

The corrected data peaks have a constant CSR amplitude equal to CSR_{base}, revised N values equal to N_{eq}, and unchanged γ_{cyc} corresponding to the original data. Equation (A-5) requires an input b parameter. I initially assumed $b = 0.135$ in accordance with Boulanger and Idriss (2007). I then checked the assumption by fitting aN^{-b} curves to the resulting CSR_{base} versus N_{eq} datapoints for the suite of DSS tests. I found that the output b from the fitted power law curves was dependent on both the blend and the strain level; however, output b was not sensitive to the assumed input b. I varied assumed input b over the full range of output b and the output b only changed by +/-0.002. I therefore assumed input $b = 0.135$ for the remainder of the data processing.

Following data correction to a test-specific constant, CSR_{base}, I identified peaks in the CSR_{base} versus cyclic shear strain, γ_{cyc} data along with corresponding points in the γ_{cyc} versus N_{eq} data. I then fit a 6th-order polynomial curve to the γ_{cyc} versus N_{eq} peaks using least squares regression, in accordance with the procedure in the previous section, using the form of Equations (A-1) and (A-2). Note that no regression was necessary for the CSR_{base} versus N_{eq} data, because CSR_{base} is a constant for a given DSS test. Equations are (A-3) and (A-4) are therefore superfluous once the data is adjusted to a test-specific, constant CSR. Table A-2 presents the polynomial curve fitting coefficients for each CSR-adjusted DSS test on the SBFW and SKFW blends from Eslami (2017). Figures A-21 through A-42 present both the original and adjusted laboratory data, the curves fit to the adjusted data, and datapoints that indicate N_{eq} at γ_{cyc} values of ½, 1, 3, and 6 percent. I took N_{eq} as the lesser value yielded by positive and negative polynomial curves.

Additional discussion on the CRR curves resulting from the data processing detailed here is provided in Section 4.3. The section also presents information regarding conversion of data into deviatoric stress terms for use in the ground failure evaluation framework presented in this dissertation.

Table A-1: Fitted Polynomial Curve Coefficients for Original Test Data

Test	c_1	c_2	c_3	c_4	c_5	c_6	c_7	c_8	c_9	c_{10}
SBFW_36_CYC_S	0.1291	0.1531	-0.0087	-0.0024	0.0004	0	0	0.0476	0.1599	-0.0093
SBFW_37_CYC_S	0.0957	0.5741	-0.226	0.0487	-0.0045	0.0002	0	0.0329	0.2976	-0.0493
SBFW_38_CYC_S	0.0191	1.7205	-1.9486	0.9999	-0.2344	0.0272	-0.0013	0.0071	0.1665	1.0399
SBFW_39_CYC_S	0	2.3984	-2.4296	1.2946	-0.3068	0.0345	-0.0015	0	0.7794	0.4904
SBFW_40_CYC_S	0.1248	0.1519	-0.0263	0.0034	-0.0002	0	0	0.038	0.1117	-0.0229
SBFW_44_CYC_S	0.0701	0.1475	-0.0506	0.0082	-0.0006	0	0	0.0439	0.1286	-0.0272
SBFW_45_CYC_S	0.0917	0.0338	-0.0035	0.0002	0	0	0	0.058	0.027	-0.0028
SBFW_46_CYC_S	0.0379	1.101	-1.1582	0.5484	-0.1205	0.0126	-0.0005	0.0031	0.5122	-0.0426
SBFW_56_CYC_S	0.0545	0.0563	-0.006	0.0003	0	0	0	0.0032	0.0941	-0.0097
SBFW_61_CYC_S	0.0506	0.058	-0.0071	0.0004	0	0	0	0.093	0.0533	-0.0048
SBFW_62_CYC_S	0.066	0.1393	-0.0319	0.003	-0.0001	0	0	0.0469	0.1626	-0.0324
SBFW_63_CYC_S	0.1158	0.2841	-0.0953	0.0166	-0.0015	0.0001	0	0.0132	0.4149	-0.2001
SBFW_64_CYC_S	0.0025	0.3669	-0.3173	0.1109	-0.0175	0.0012	0	-0.024	0.4799	-0.3709
SBFW_65_CYC_S	0.1117	-0.0228	0.0158	-0.0021	0.0001	0	0	-0.0619	0.1357	-0.0345
SBFW_66_CYC_S	-0.0328	1.0069	-0.9579	0.3513	-0.0577	0.0043	-0.0001	-0.0235	0.6292	-0.6222
SBFW_67_CYC_S	0	1.2035	-1.2738	0.4884	-0.0265	-0.013	0.0021	0	-0.026	0.744
SBFW_72_CYC_S	0.2391	-0.1565	0.0357	-0.003	0.0001	0	0	0.388	-0.3091	0.0695
SBFW_74_CYC_S	0.0494	0.3238	-0.1391	0.0241	-0.0018	0.0001	0	0.0384	0.064	0.0237
SBFW_75_CYC_S	0.0507	0.3966	-0.2123	0.0465	-0.0045	0.0002	0	0.0258	0.2006	-0.0292
SBFW_76_CYC_S	-0.0048	1.1668	-1.3287	0.5941	-0.1232	0.0118	-0.0004	-0.0201	1.1619	-1.1999
SBFW_78_CYC_S	0	1.7605	-2.7052	1.9428	-0.701	0.1233	-0.008	0	0.8836	-0.6478

Table A-1: Fitted Polynomial Curve Coefficients for Original Test Data

Test	c_{11}	c_{12}	c_{13}	c_{14}	c_{15}	c_{16}	c_{17}	c_{18}	c_{19}	c_{20}
SBFW_36_CYC_S	-0.0016	0.0004	0	0	0.1468	-0.0009	-0.0003	0.1554	0.0006	-0.0006
SBFW_37_CYC_S	0.0051	0.0006	-0.0001	0	0.1671	0.0006	-0.0006	0.1539	0.0008	-0.0004
SBFW_38_CYC_S	-0.8562	0.2969	-0.0429	0.0022	0.1776	0.0008	-0.0012	0.1821	-0.001	-0.0001
SBFW_39_CYC_S	-0.4054	0.1832	-0.0341	0.0022	0.1751	0.0006	-0.0009	0.1976	-0.0008	-0.0001
SBFW_40_CYC_S	0.0024	-0.0001	0	0	0.146	-0.0004	-0.0001	0.1276	0.0014	-0.0021
SBFW_44_CYC_S	0.0033	-0.0002	0	0	0.1296	-0.0032	-0.0006	0.1228	-0.0014	-0.0001
SBFW_45_CYC_S	0.0001	0	0	0	0.103	-0.0035	-0.0014	0.1242	-0.0021	0.0002
SBFW_46_CYC_S	-0.1056	0.0528	-0.0076	0.0004	0.1545	0.001	-0.002	0.1664	-0.0038	0.0003
SBFW_56_CYC_S	0.0004	0	0	0	0.1608	0.0031	-0.0014	0.1831	-0.0004	-0.0002
SBFW_61_CYC_S	0.0002	0	0	0	0.1681	-0.0005	-0.001	0.2108	-0.0015	0
SBFW_62_CYC_S	0.0029	-0.0001	0	0	0.2019	-0.001	-0.0007	0.2074	-0.0016	0.0001
SBFW_63_CYC_S	0.0465	-0.0052	0.0003	0	0.2402	-0.0007	-0.0002	0.2178	-0.0023	0.0001
SBFW_64_CYC_S	0.121	-0.018	0.0012	0	0.1121	-0.0039	-0.0004	0.1238	-0.0039	0.0001
SBFW_65_CYC_S	0.0033	-0.0001	0	0	0.1179	-0.0029	0.0001	0.0818	-0.0159	-0.0013
SBFW_66_CYC_S	0.2422	-0.0429	0.0035	-0.0001	0.1082	-0.0046	0.0002	0.1439	-0.006	-0.0003
SBFW_67_CYC_S	-0.5241	0.0832	0.0235	-0.0047	0.142	-0.0076	0.0005	0.1516	-0.0193	0.0027
SBFW_72_CYC_S	-0.0057	0.0002	0	0	0.1718	-0.007	0.0003	0.1748	-0.0026	0.0001
SBFW_74_CYC_S	-0.0123	0.0019	-0.0001	0	0.2085	-0.0035	0	0.1854	-0.0034	0.0001
SBFW_75_CYC_S	-0.0108	0.0034	-0.0003	0	0.2207	-0.0032	0	0.2164	-0.0043	0.0002
SBFW_76_CYC_S	0.5482	-0.1153	0.0111	-0.0004	0.2335	-0.0061	0.0002	0.2722	-0.0027	0.0001
SBFW_78_CYC_S	0.2174	-0.0094	-0.0066	0.0011	0.2626	-0.0066	0.0004	0.2626	-0.0013	-0.0001

Table A-2: Fitted Polynomial Curve Coefficients for CSR-Adjusted Test Data

Test	c_1	c_2	c_3	c_4	c_5	c_6	c_7	c_8	c_9	c_{10}
SBFW_36_CYC_S	0.1377	0.1166	0.0268	-0.0144	0.0022	-0.0001	0	0.0045	0.3287	-0.1127
SBFW_37_CYC_S	0.0965	0.4075	-0.074	-0.0039	0.0037	-0.0004	0	0.0258	0.3156	-0.0265
SBFW_38_CYC_S	0.0006	1.9359	-2.4104	1.3641	-0.3774	0.0528	-0.0029	0.003	-3.0671	7.3319
SBFW_39_CYC_S	0	0	0.0959	1.3301	-0.7233	0.2102	-0.0165	0	0	0.0243
SBFW_40_CYC_S	0.0993	0.1872	-0.0405	0.0052	-0.0003	0	0	0.0196	0.1854	-0.0608
SBFW_44_CYC_S	0.0603	0.1726	-0.0639	0.0107	-0.0008	0	0	0.1019	-0.106	0.1107
SBFW_45_CYC_S	0.0991	0.0262	-0.0024	0.0001	0	0	0	0.0666	0.0134	-0.0005
SBFW_46_CYC_S	0.0248	1.4758	-1.7315	0.8616	-0.2015	0.0226	-0.001	0.0013	0.1837	0.4346
SBFW_56_CYC_S	0.1861	-0.0387	0.0068	-0.0004	0	0	0	0.3298	-0.1135	0.0173
SBFW_61_CYC_S	0.109	0.0061	0.0007	-0.0001	0	0	0	0.2722	-0.0746	0.0121
SBFW_62_CYC_S	0.0861	0.1088	-0.0238	0.0022	-0.0001	0	0	0.1005	0.0684	-0.0042
SBFW_63_CYC_S	0.0948	0.2896	-0.0893	0.013	-0.0009	0	0	0.027	0.3475	-0.1458
SBFW_64_CYC_S	0.0743	-0.5302	0.741	-0.3316	0.0653	-0.0059	0.0002	0.1291	-2.422	3.0438
SBFW_65_CYC_S	0.2508	-0.1853	0.0386	-0.0028	0.0001	0	0	-0.011	0.0375	-0.0052
SBFW_66_CYC_S	0.1158	-1.0252	1.0569	-0.3601	0.0546	-0.0038	0.0001	0.0095	-0.0813	0.1688
SBFW_67_CYC_S	0	0	0.1427	-0.8326	1.4083	-0.5659	0.0672	0	0	-0.0145
SBFW_72_CYC_S	$-0.1135x^2$	$-0.1031x^2$	$0.0948x^2$	$-0.0269x^2$	$0.0037x^2$	$-0.0003x^2$	$0.0000x^2$	$0.1432x^2$	$-0.3642x^2$	$0.2766x^2$
SBFW_74_CYC_S	0.178	-0.4296	0.3648	-0.0965	0.0111	-0.0006	0	0.1225	-0.3586	0.3149
SBFW_75_CYC_S	0.1826	-0.6154	0.6803	-0.2372	0.0362	-0.0025	0.0001	0.1103	-0.5298	0.6646
SBFW_76_CYC_S	0.0445	0.9262	-0.9628	0.382	-0.0688	0.0056	-0.0002	-0.0105	0.7886	-0.6016
SBFW_78_CYC_S	0	0	0.0985	0.0986	0.4235	-0.2755	0.0463	0	0	0.0203

Table A-2: Fitted Polynomial Curve Coefficients for CSR-Adjusted Test Data

Test	c_{11}	c_{12}	c_{13}	c_{14}
SBFW_36_CYC_S	0.0212	-0.0019	0.0001	0
SBFW_37_CYC_S	-0.0164	0.0057	-0.0005	0
SBFW_38_CYC_S	-5.3392	1.7566	-0.2654	0.0151
SBFW_39_CYC_S	-0.5707	1.2426	-0.3644	0.0377
SBFW_40_CYC_S	0.0094	-0.0007	0	0
SBFW_44_CYC_S	-0.0262	0.0027	-0.0001	0
SBFW_45_CYC_S	0	0	0	0
SBFW_46_CYC_S	-0.379	0.121	-0.0155	0.0007
SBFW_56_CYC_S	-0.0009	0	0	0
SBFW_61_CYC_S	-0.0007	0	0	0
SBFW_62_CYC_S	-0.0003	0	0	0
SBFW_63_CYC_S	0.0301	-0.003	0.0001	0
SBFW_64_CYC_S	-1.2729	0.2353	-0.0198	0.0006
SBFW_65_CYC_S	0.0003	0	0	0
SBFW_66_CYC_S	-0.0674	0.0111	-0.0008	0
SBFW_67_CYC_S	1.7093	-1.5014	0.3971	-0.0288
SBFW_72_CYC_S	$-0.0728x^2$	$0.0095x^2$	$-0.0007x^2$	$0.0000x^2$
SBFW_74_CYC_S	-0.0845	0.0099	-0.0005	0
SBFW_75_CYC_S	-0.2446	0.0387	-0.0028	0.0001
SBFW_76_CYC_S	0.2041	-0.0289	0.0014	0
SBFW_78_CYC_S	-0.0472	0.7296	-0.3817	0.0579

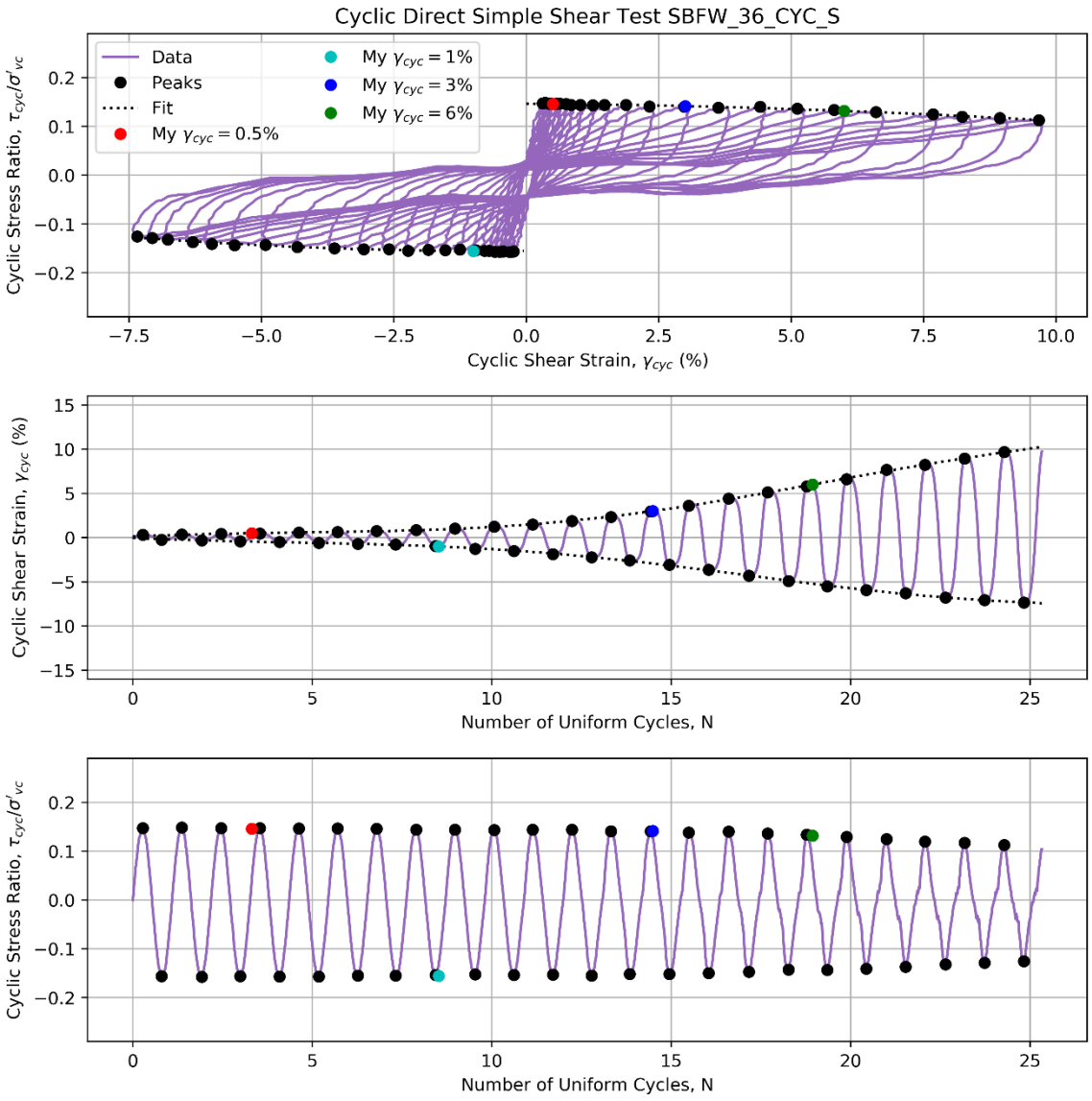

Figure A-1: Fitted Polynomial Curves for SBFW_36_CYC_S Original Test Data

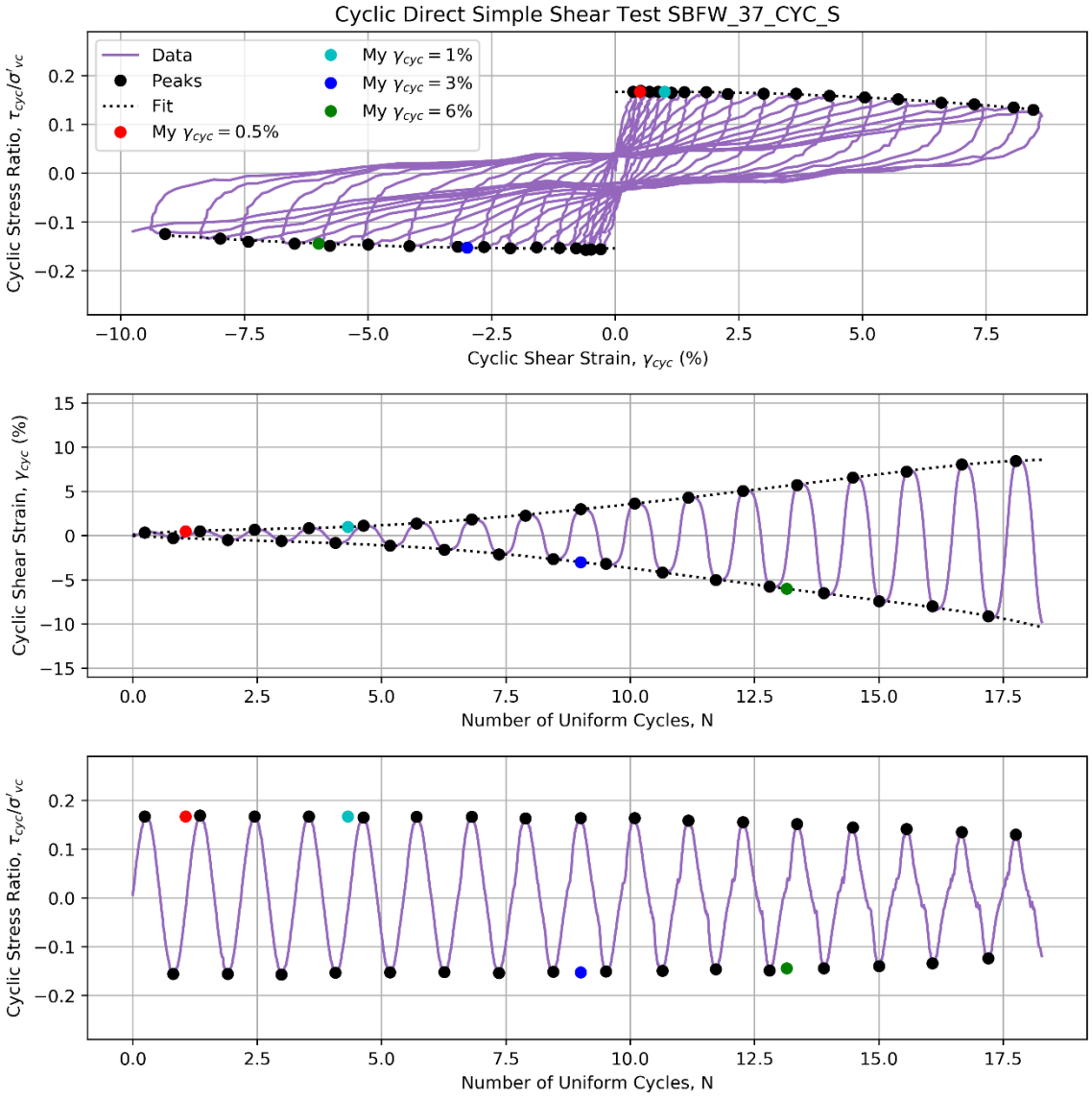

Figure A-2: Fitted Polynomial Curves for SBFW_37_CYC_S Original Test Data

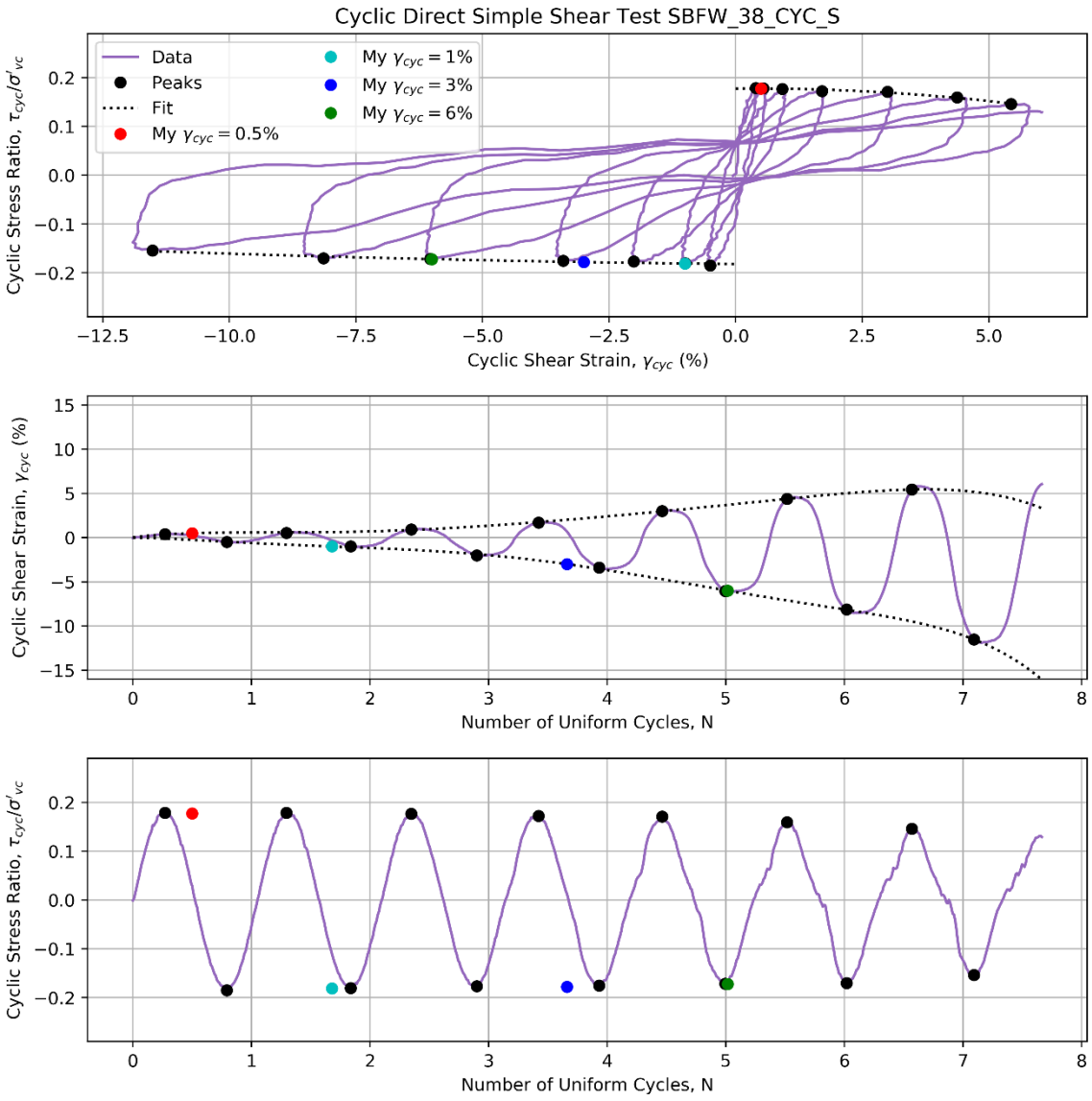

Figure A-3: Fitted Polynomial Curves for SBFW_38_CYC_S Original Test Data

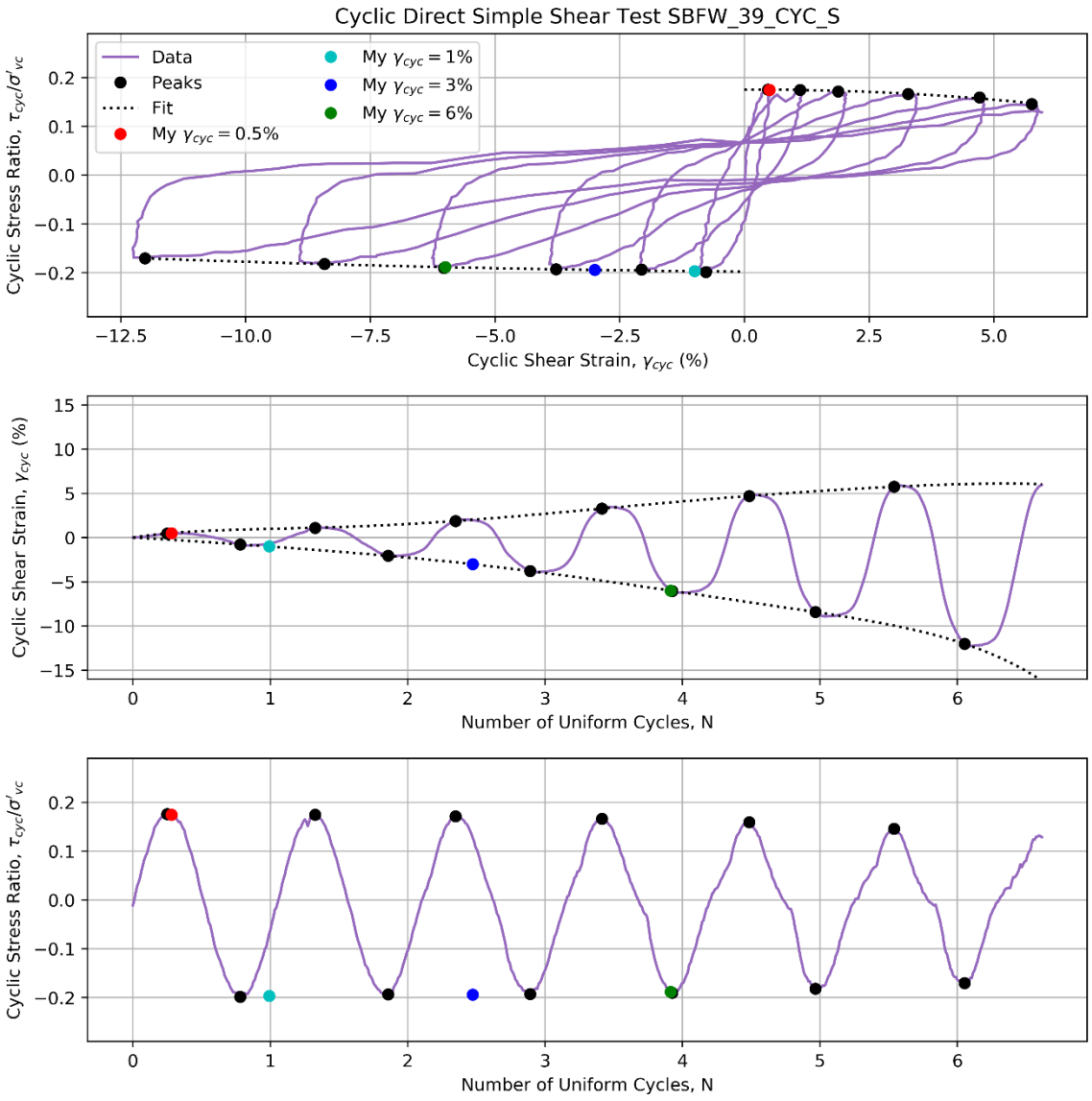

Figure A-4: Fitted Polynomial Curves for SBFW_39_CYC_S Original Test Data

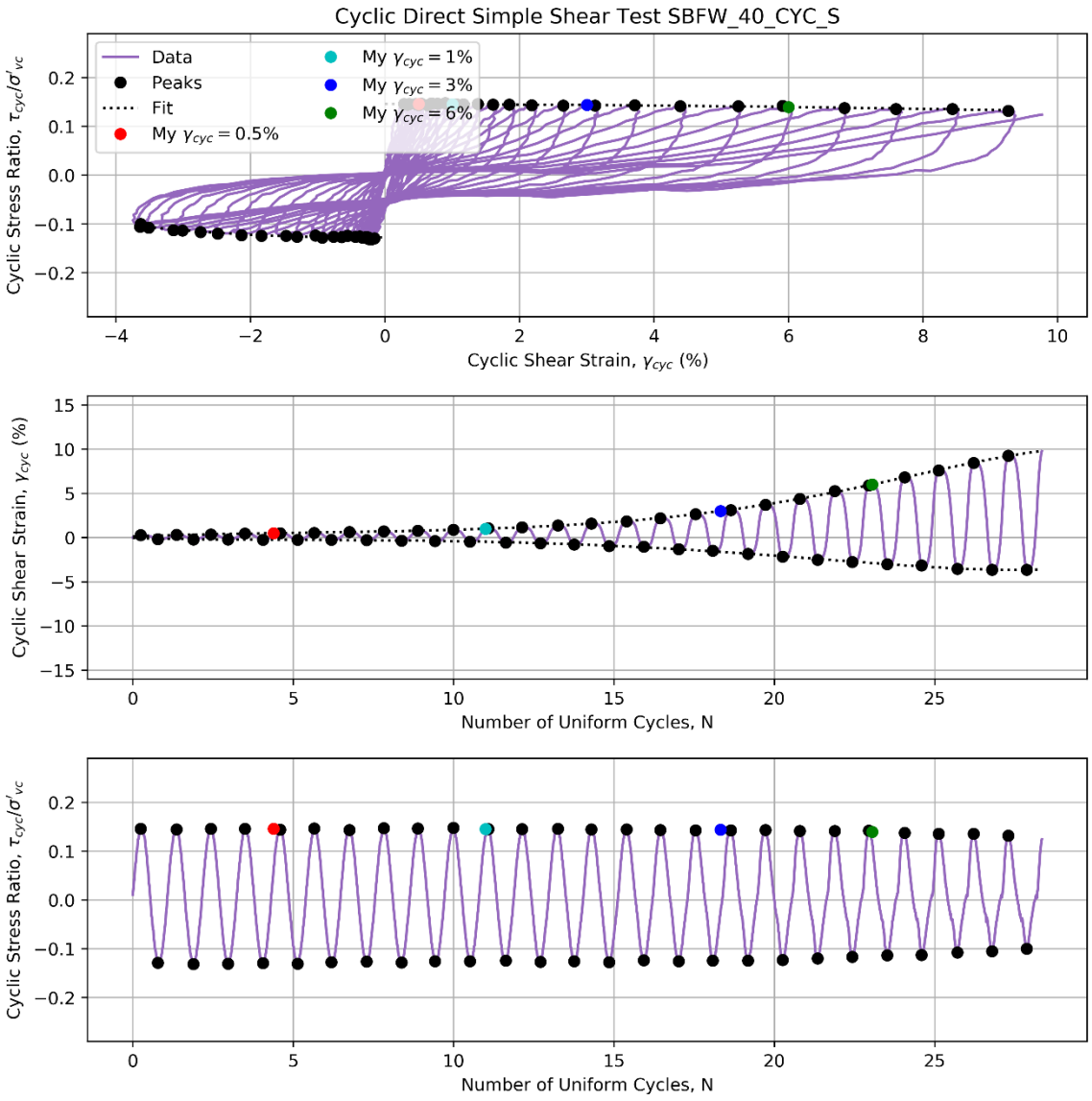

Figure A-5: Fitted Polynomial Curves for SBFW_40_CYC_S Original Test Data

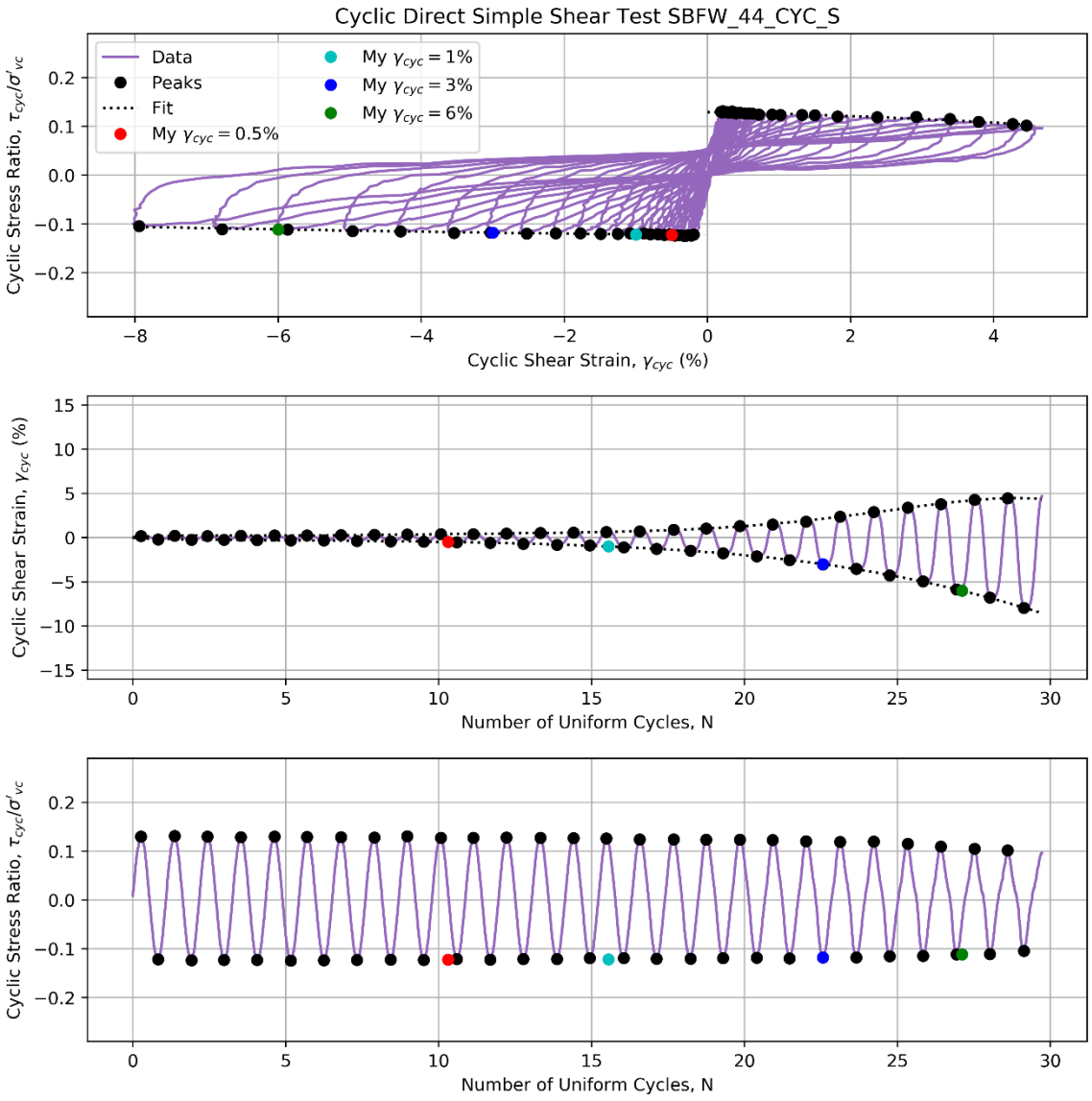

Figure A-6: Fitted Polynomial Curves for SBFW_44_CYC_S Original Test Data

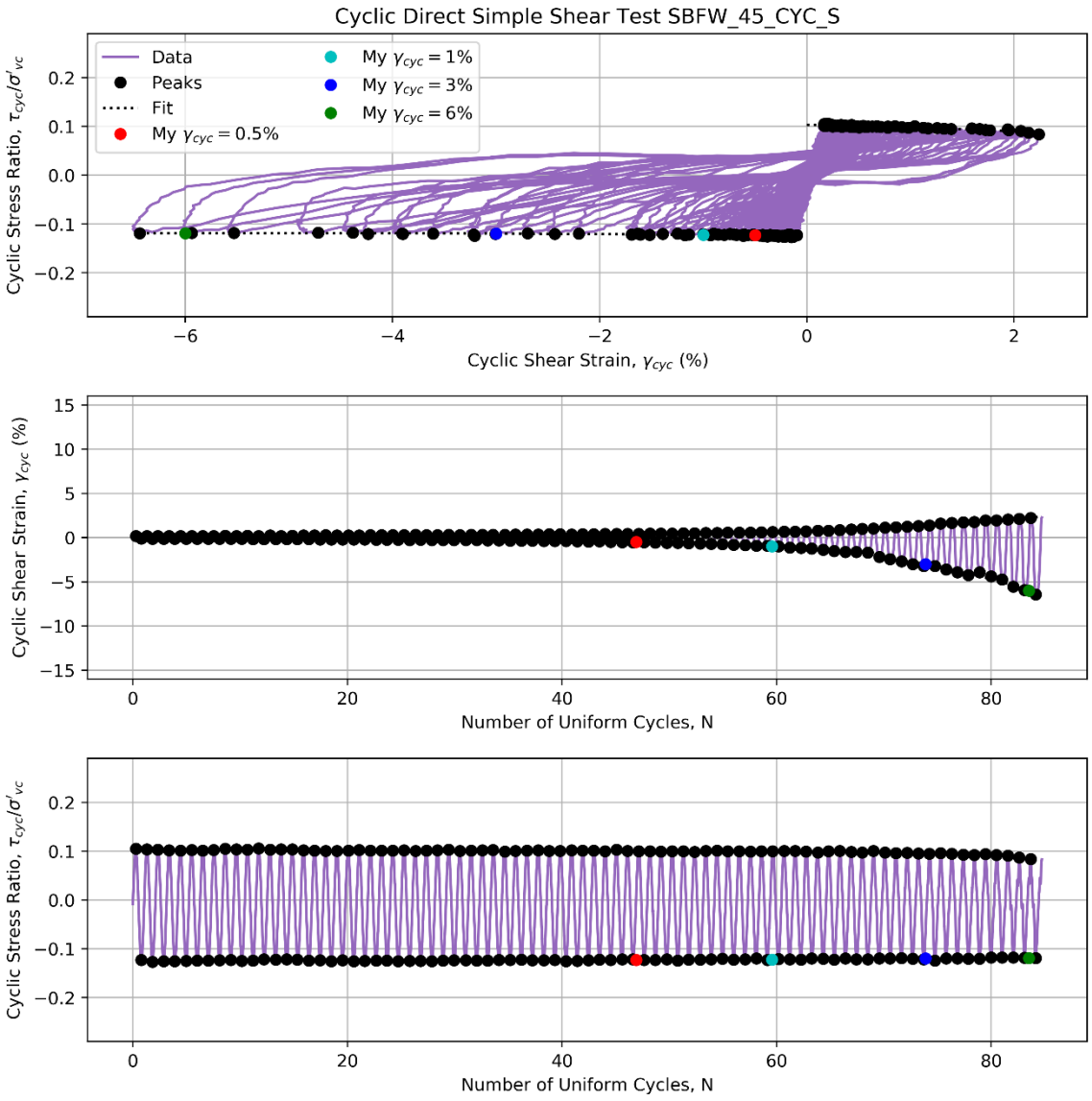

Figure A-7: Fitted Polynomial Curves for SBFW_45_CYC_S Original Test Data

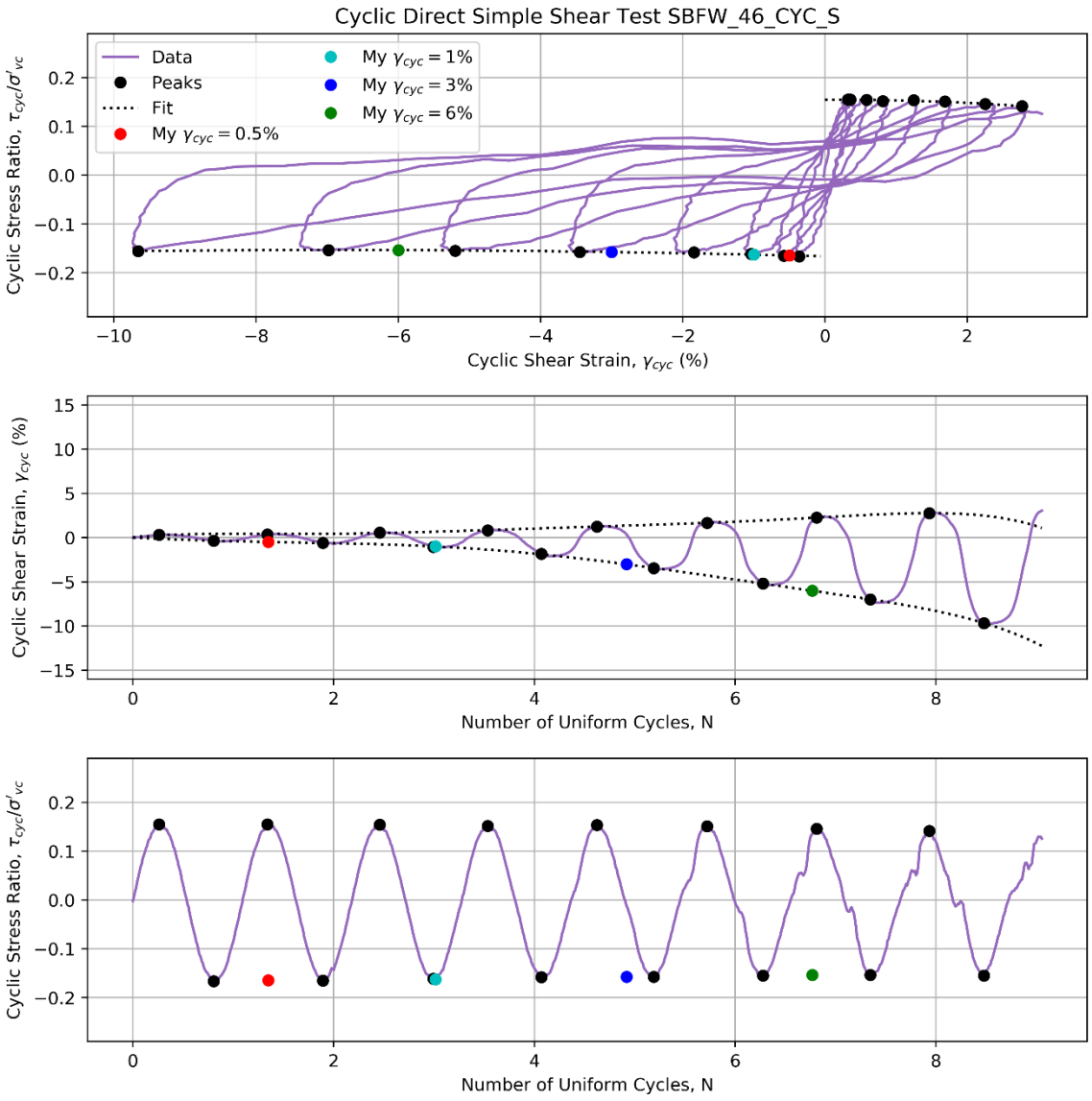

Figure A-8: Fitted Polynomial Curves for SBFW_46_CYC_S Original Test Data

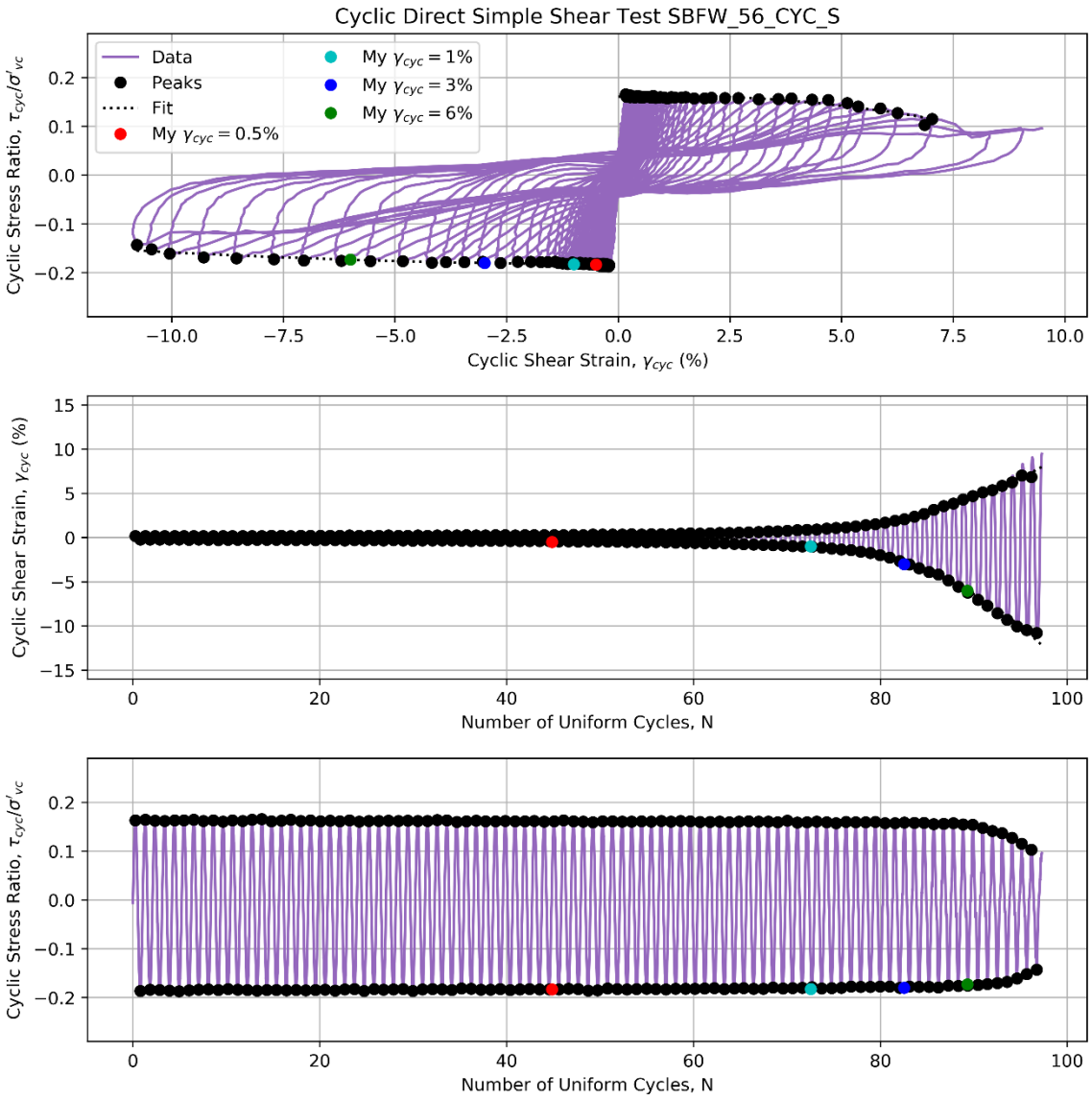

Figure A-9: Fitted Polynomial Curves for SBFW_56_CYC_S Original Test Data

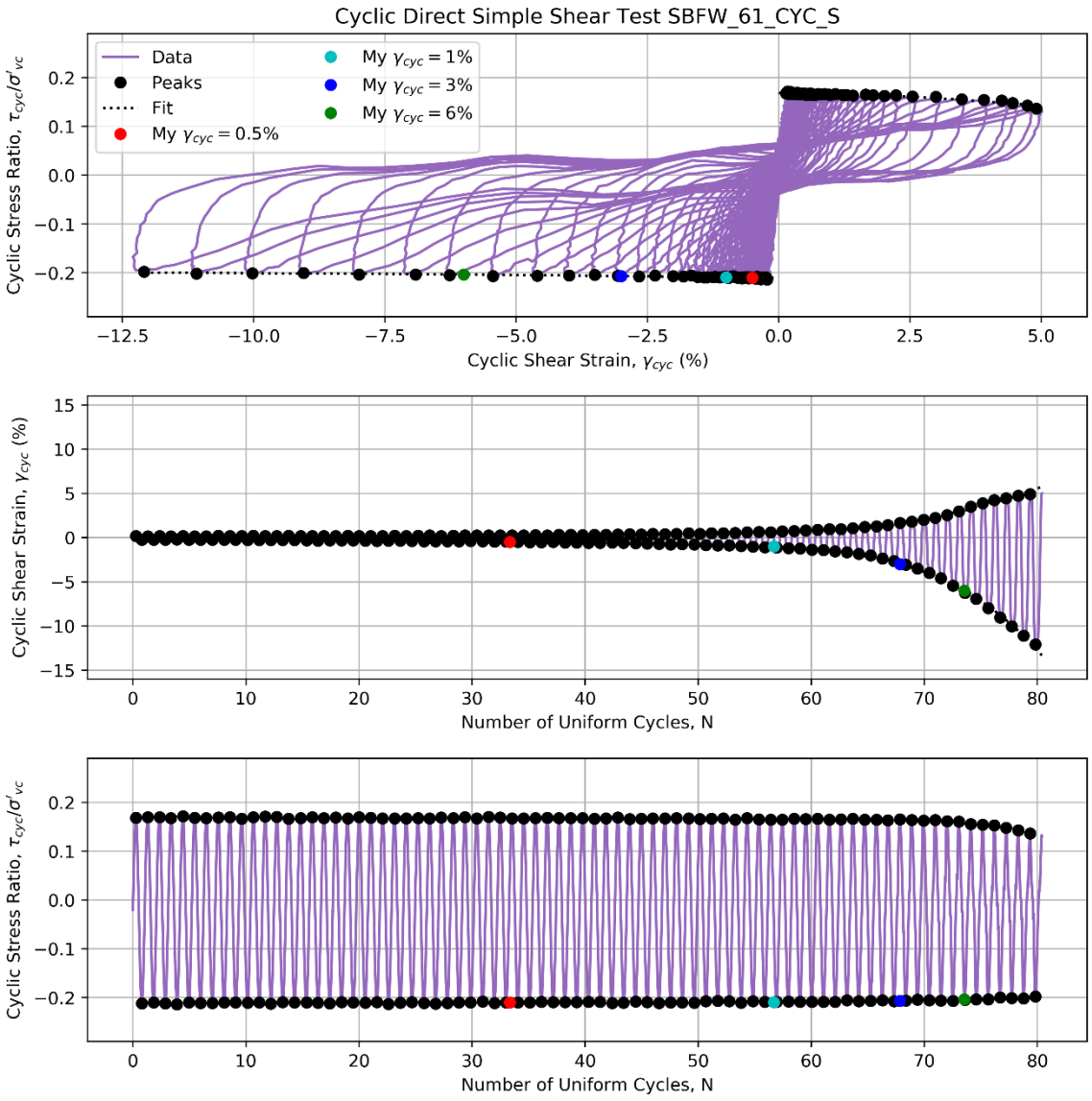

Figure A-10: Fitted Polynomial Curves for SBFW_61_CYC_S Original Test Data

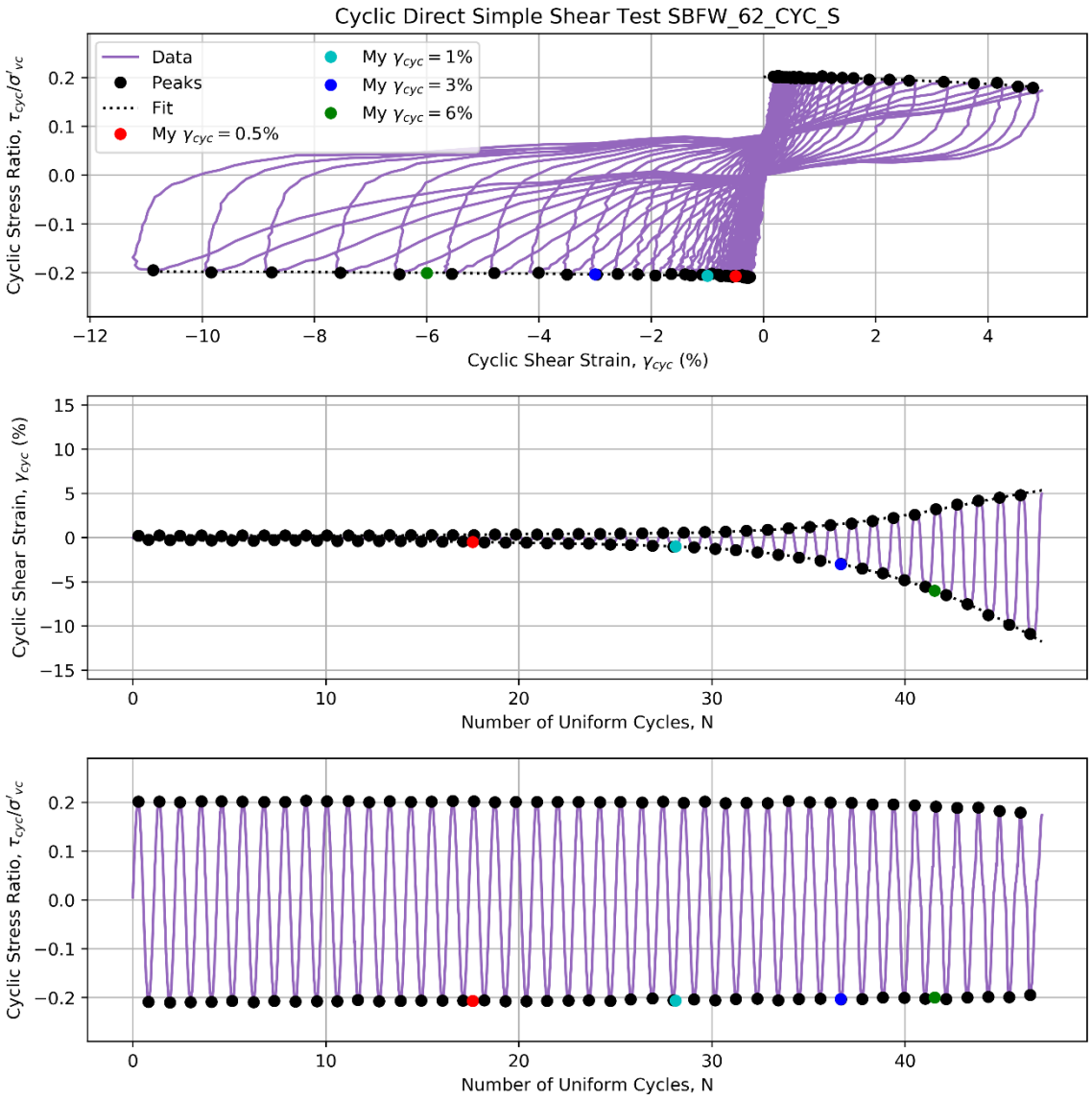

Figure A-11: Fitted Polynomial Curves for SBFW_62_CYC_S Original Test Data

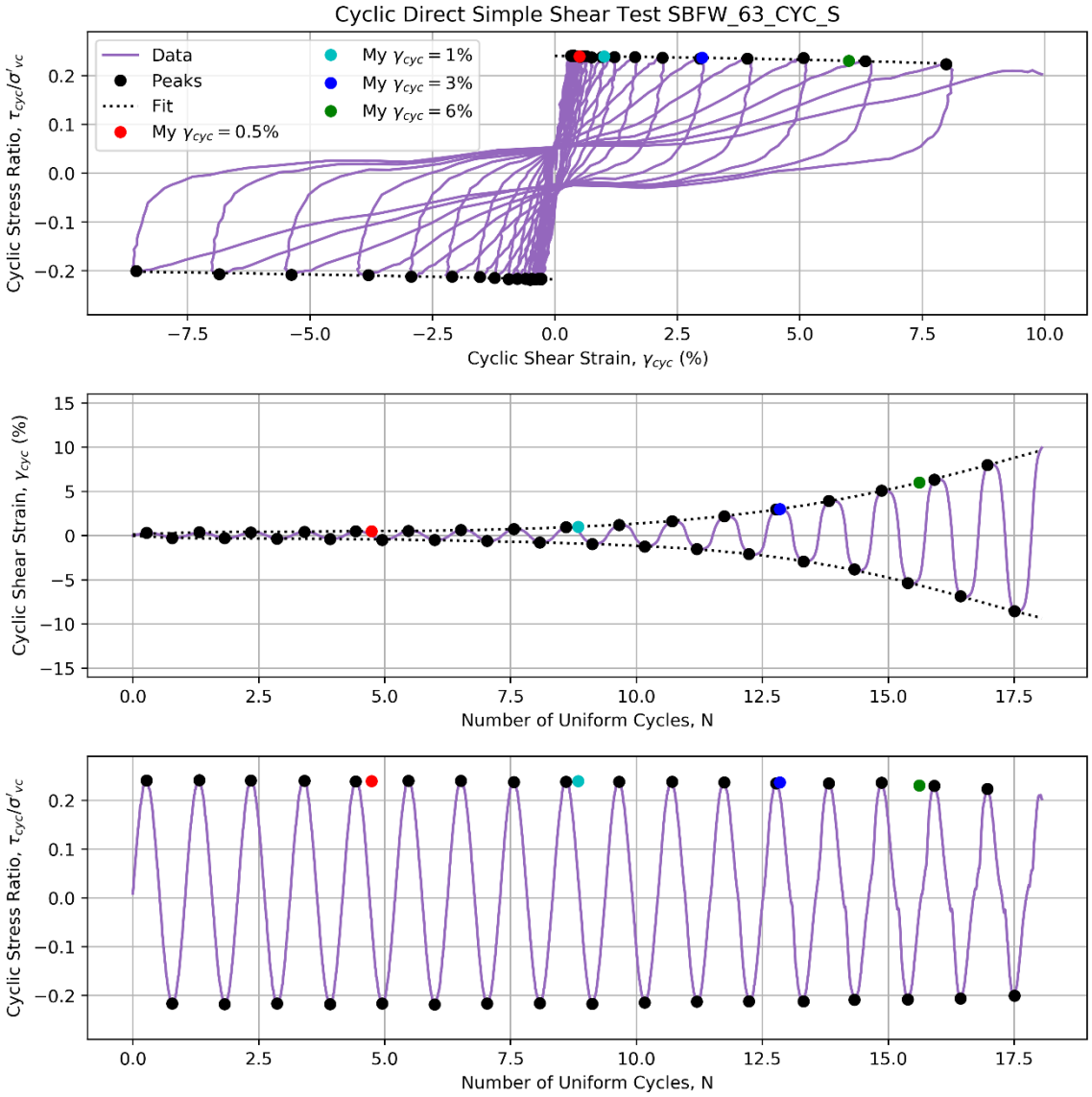

Figure A-12: Fitted Polynomial Curves for SBFW_63_CYC_S Original Test Data

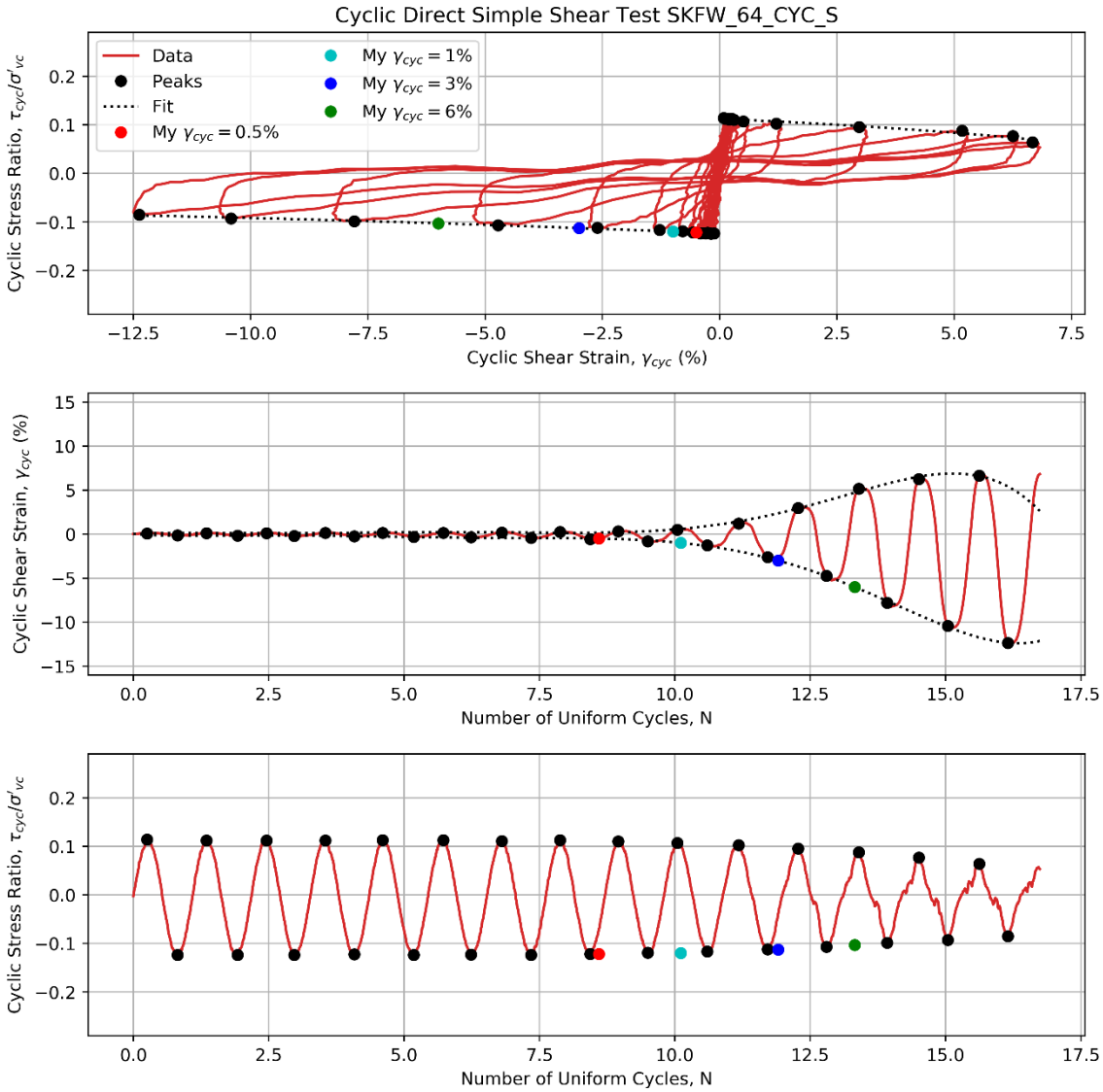

Figure A-13: Fitted Polynomial Curves for SKFW_64_CYC_S Original Test Data

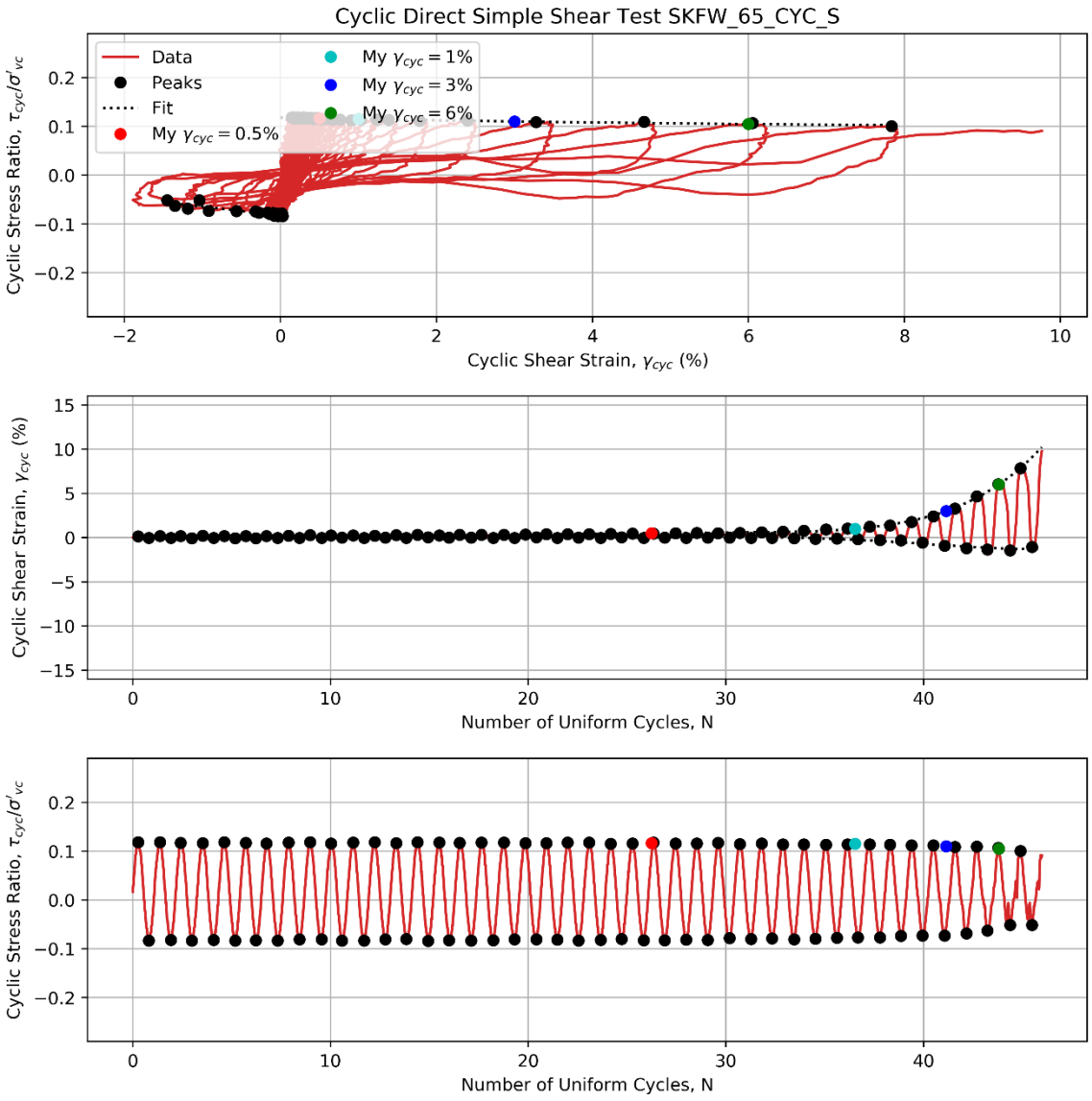

Figure A-14: Fitted Polynomial Curves for SKFW_65_CYC_S Original Test Data

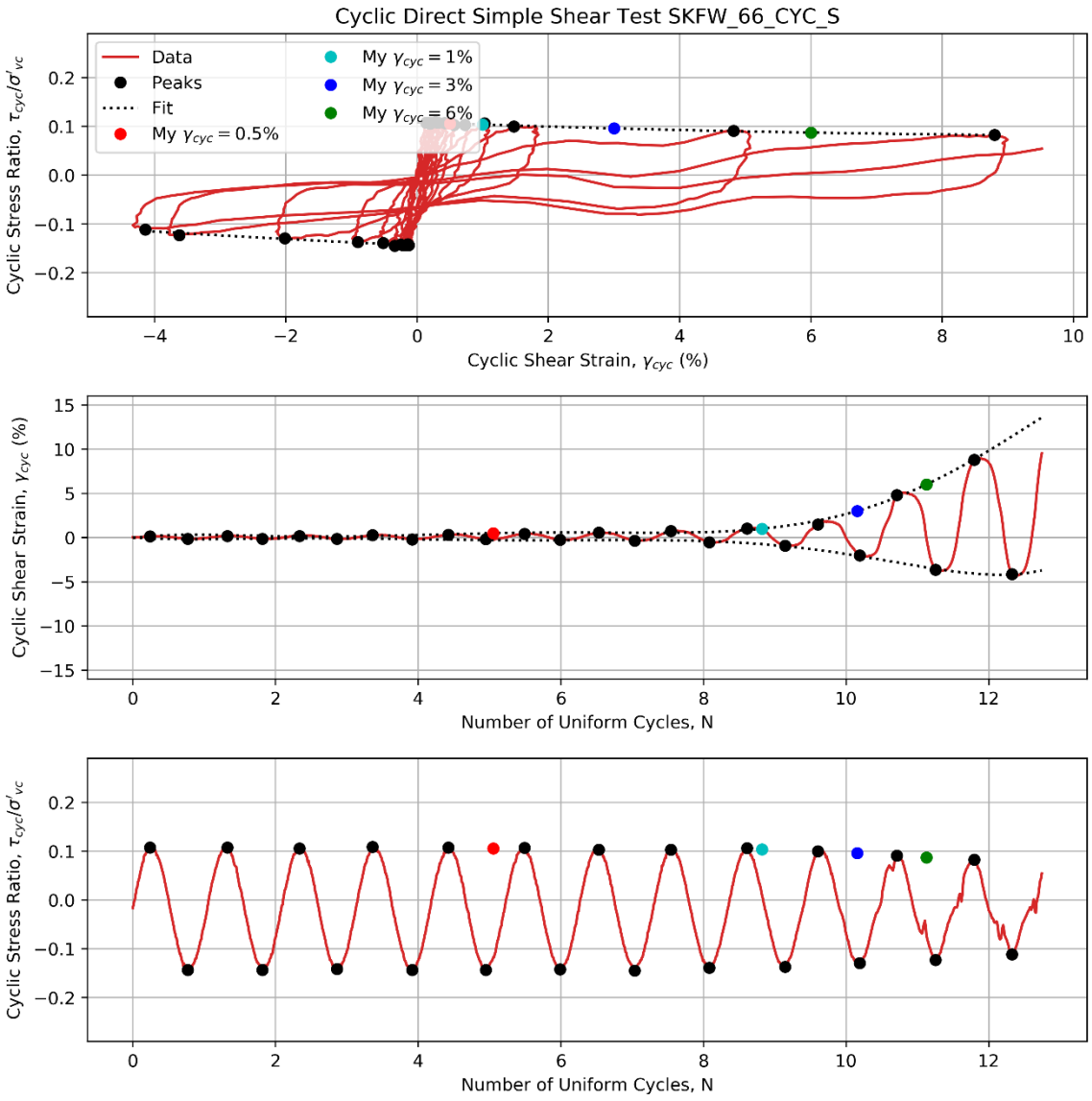

Figure A-15: Fitted Polynomial Curves for SKFW_66_CYC_S Original Test Data

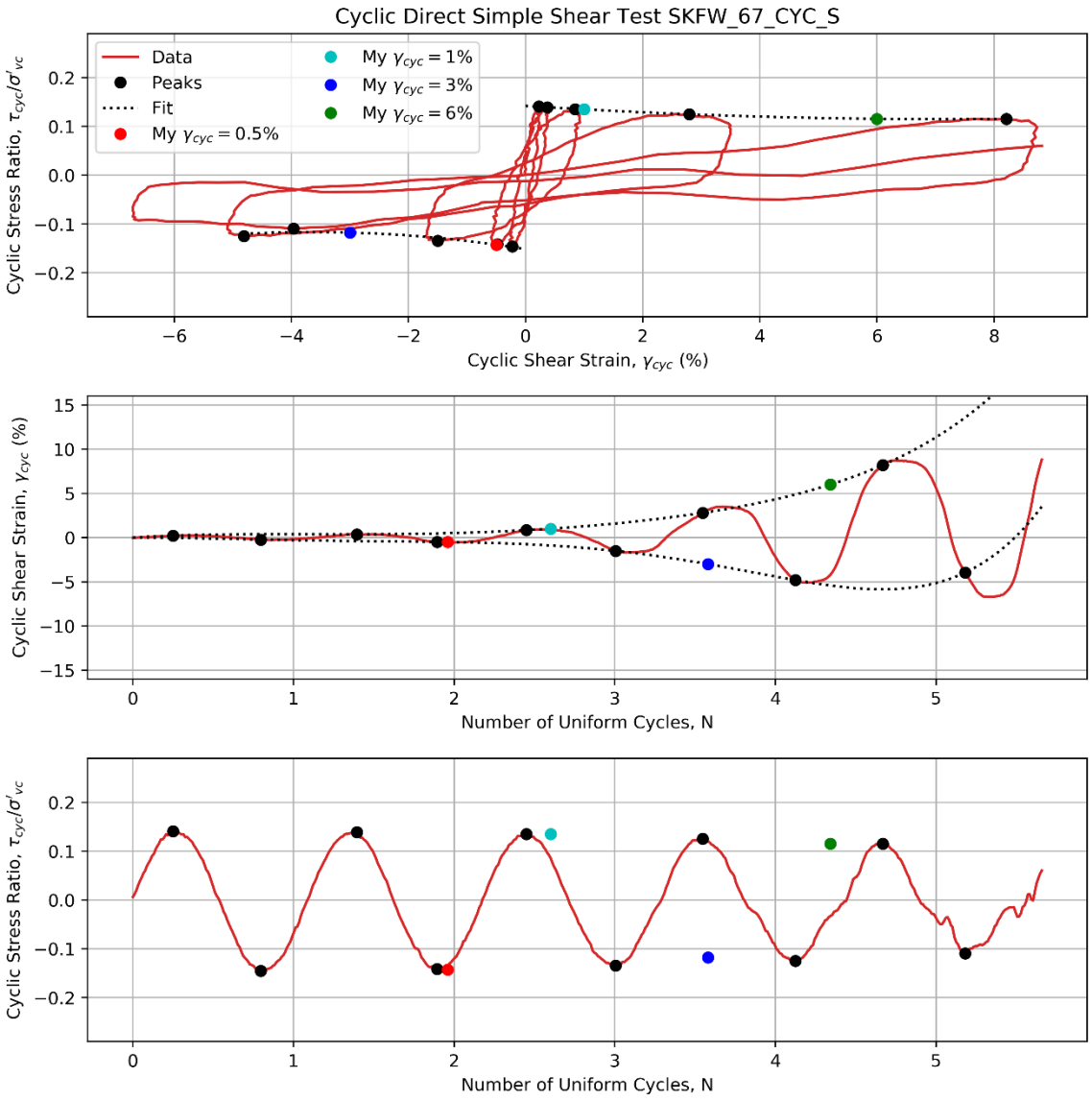

Figure A-16: Fitted Polynomial Curves for SKFW_67_CYC_S Original Test Data

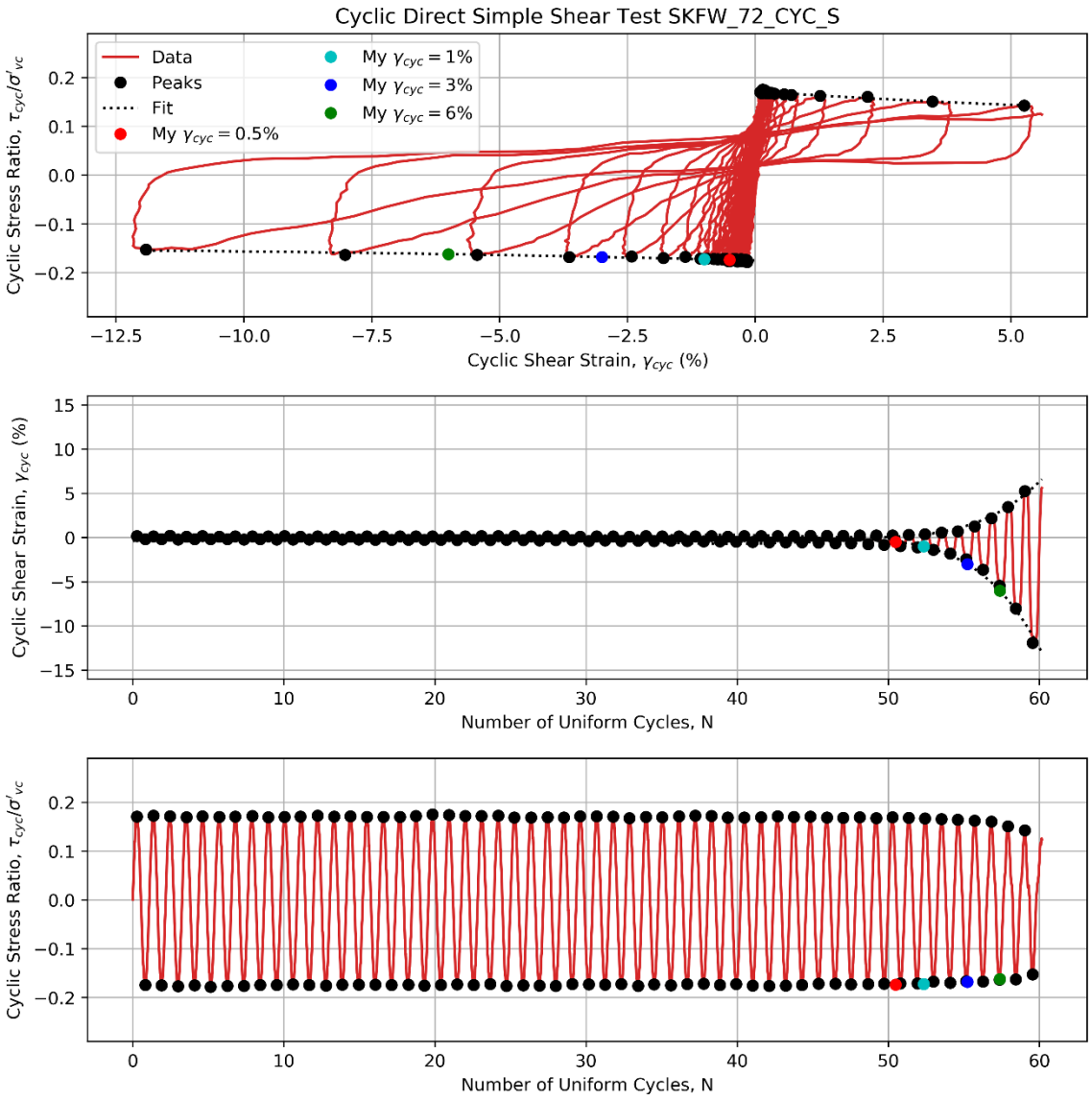

Figure A-17: Fitted Polynomial Curves for SKFW_72_CYC_S Original Test Data

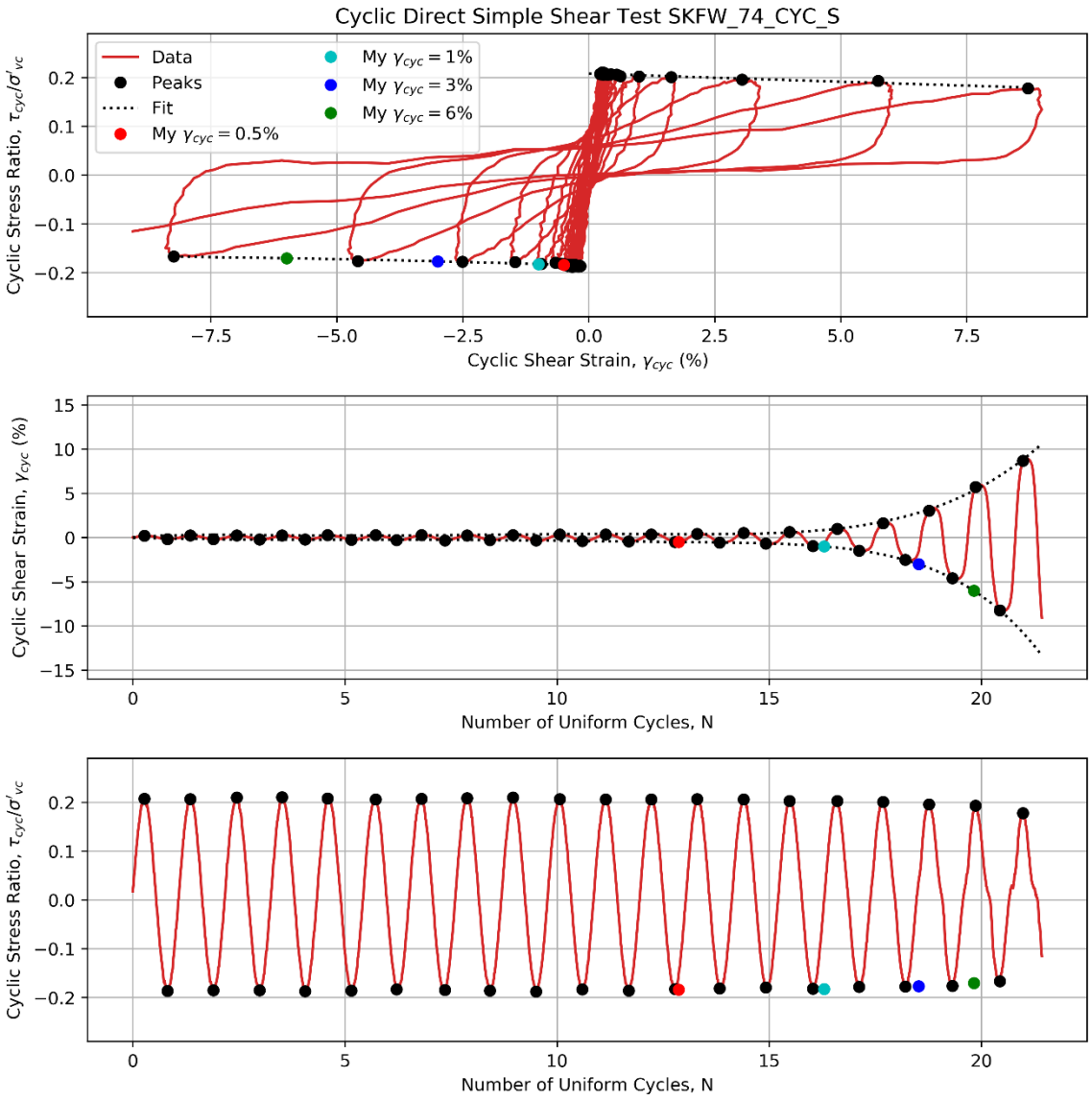

Figure A-18: Fitted Polynomial Curves for SKFW_74_CYC_S Original Test Data

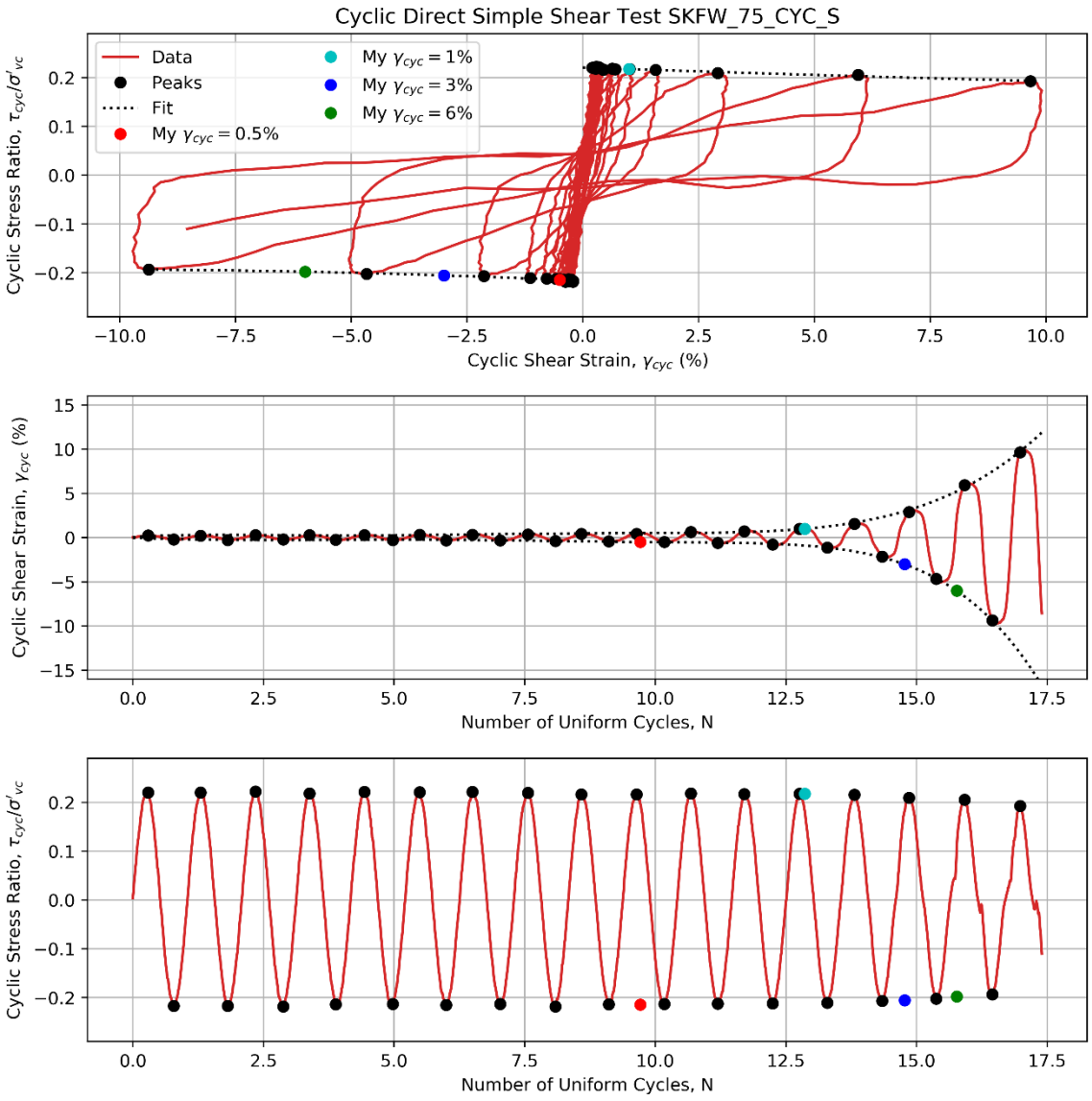

Figure A-19: Fitted Polynomial Curves for SKFW_75_CYC_S Original Test Data

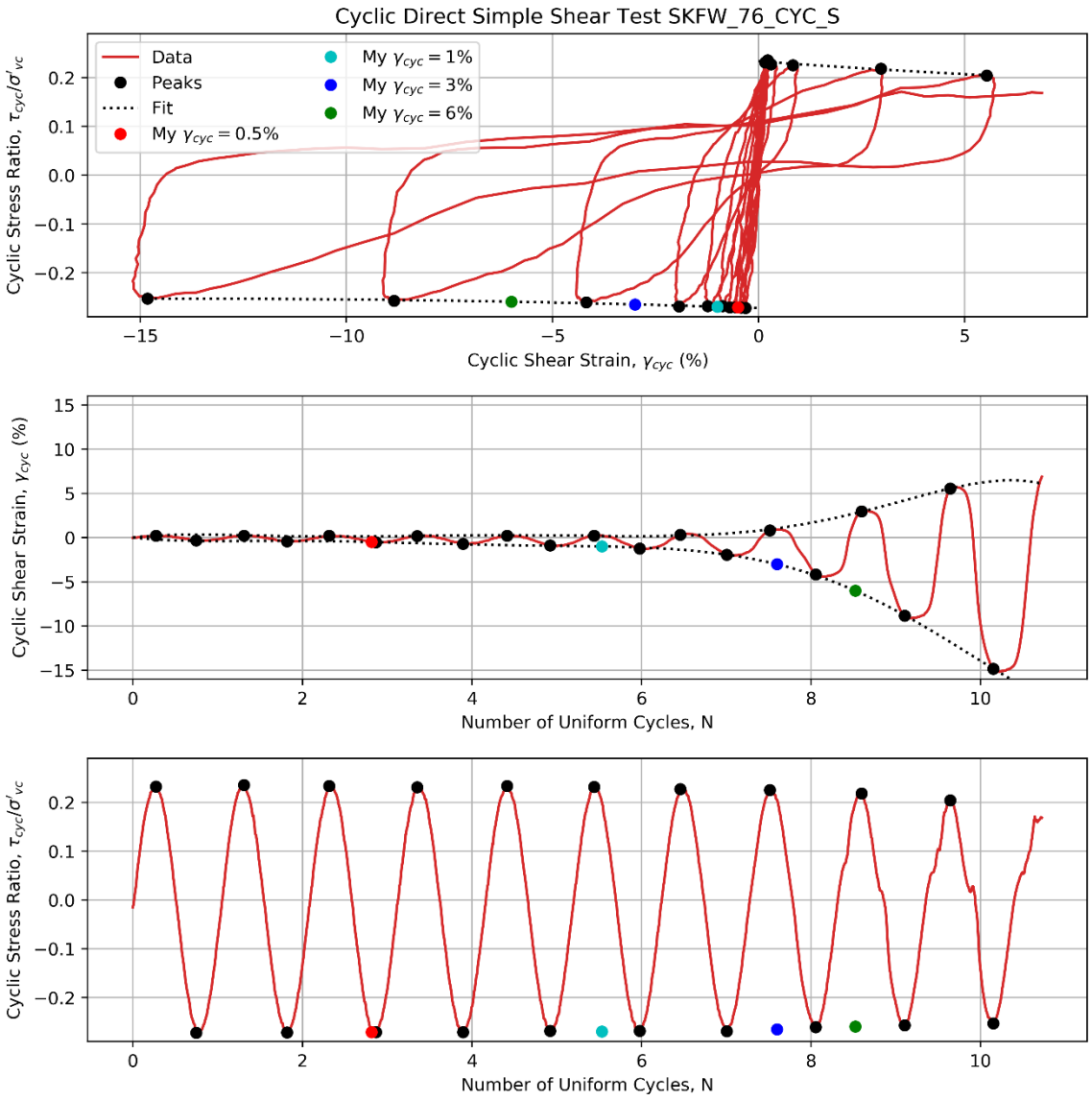

Figure A-20: Fitted Polynomial Curves for SKFW_76_CYC_S Original Test Data

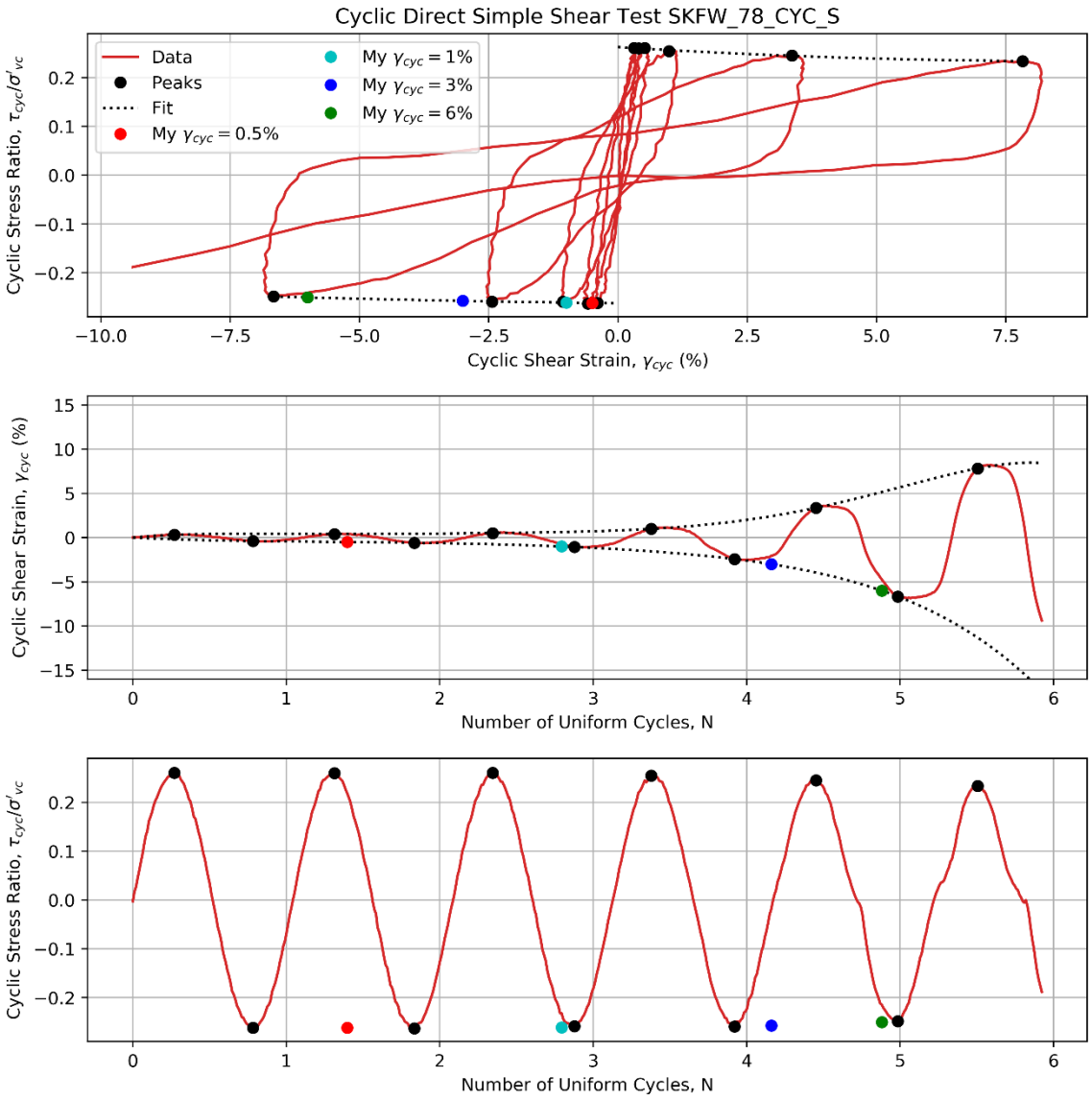

Figure A-21: Fitted Polynomial Curves for SKFW_78_CYC_S Original Test Data

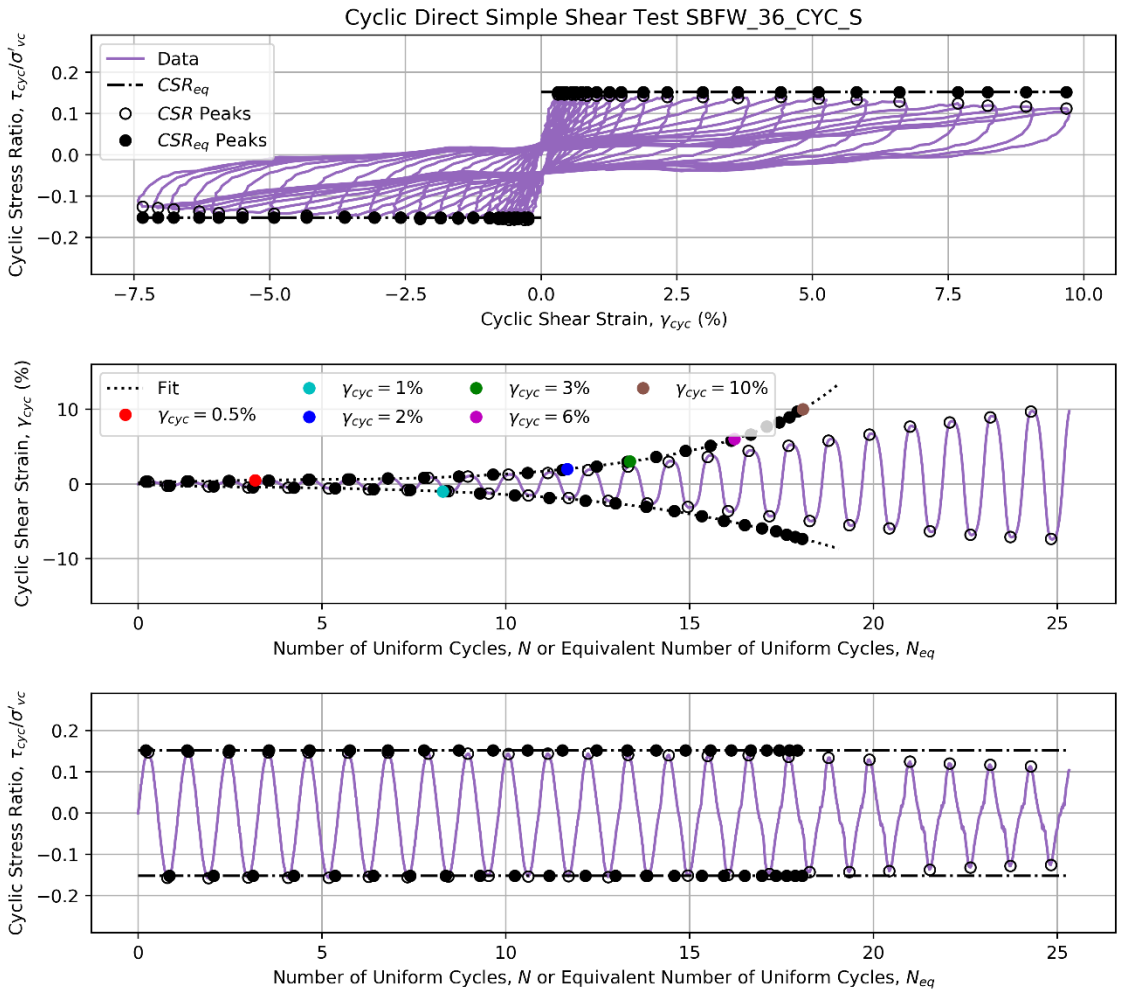

Figure A-22: Fitted Polynomial Curves for CSR-Adjusted SBFW_36_CYC_S Data

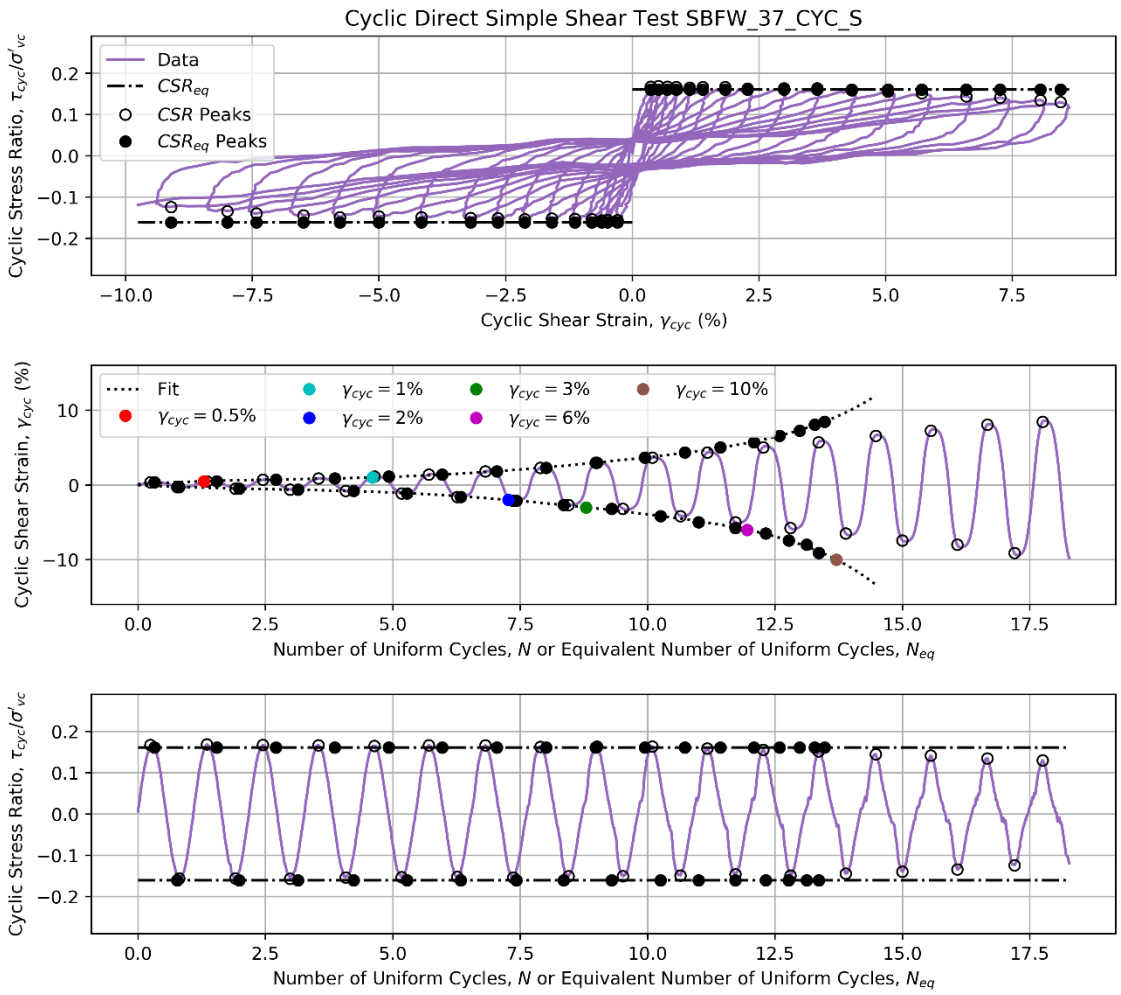

Figure A-23: Fitted Polynomial Curves for CSR-Adjusted SBFW_37_CYC_S Data

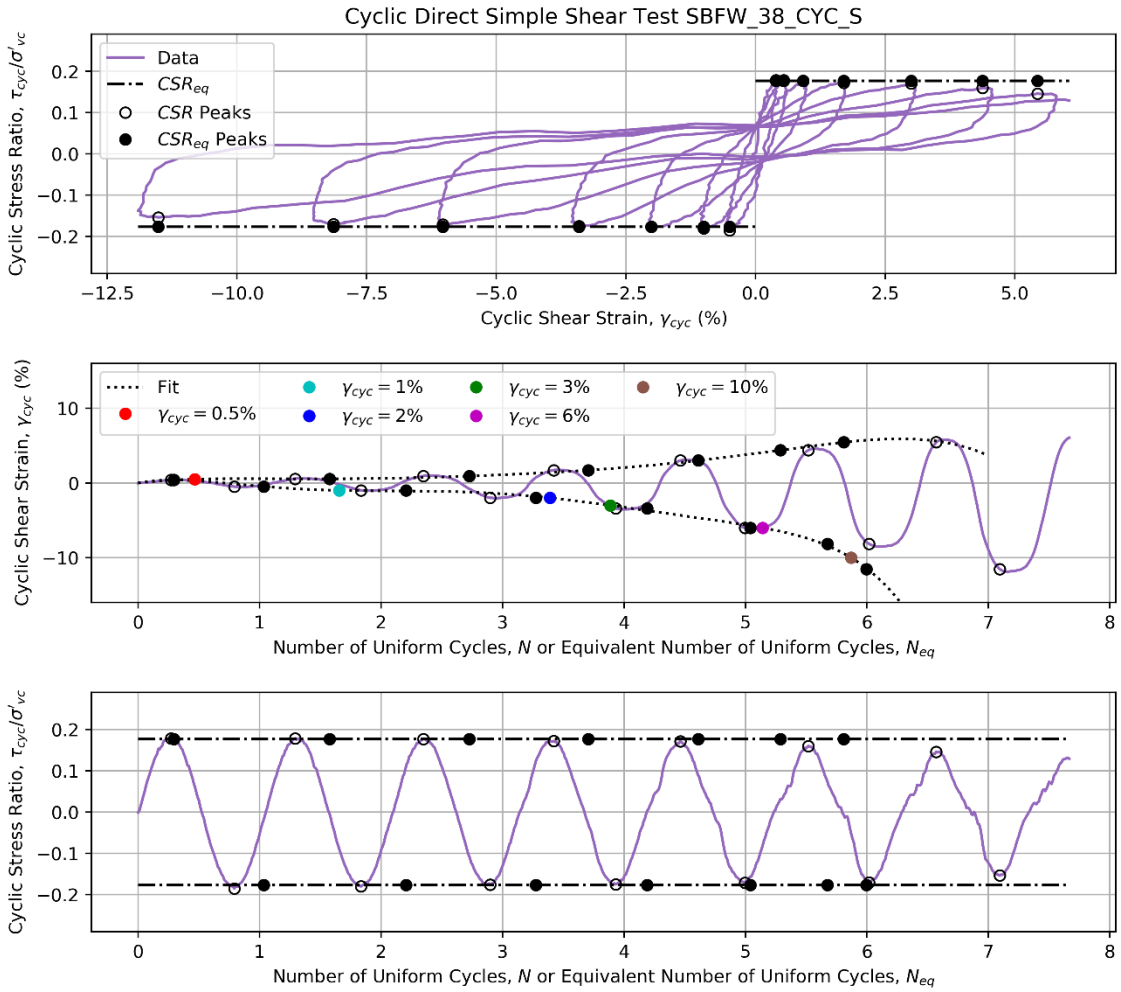

Figure A-24: Fitted Polynomial Curves for CSR-Adjusted SBFW_38_CYC_S Data

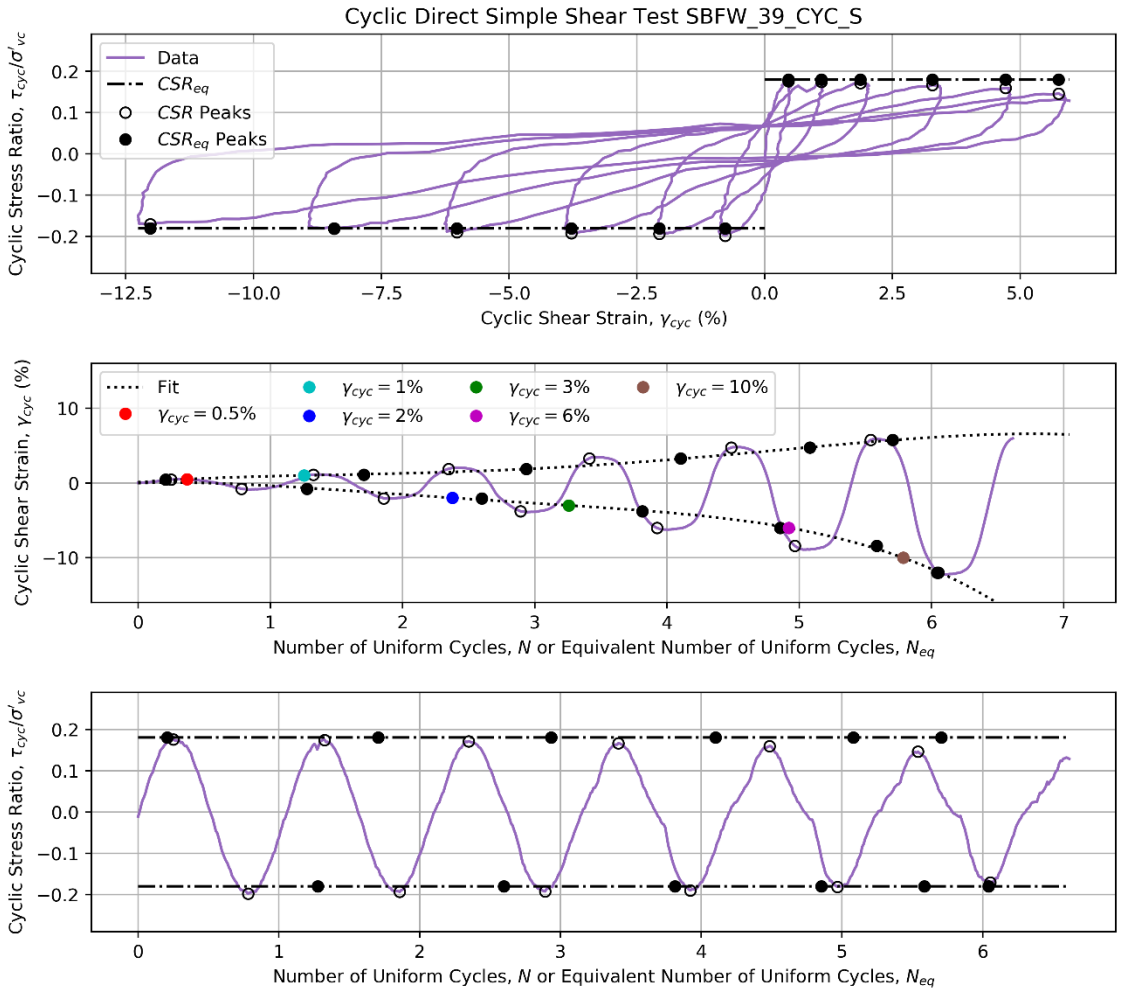

Figure A-25: Fitted Polynomial Curves for CSR-Adjusted SBFW_39_CYC_S Data

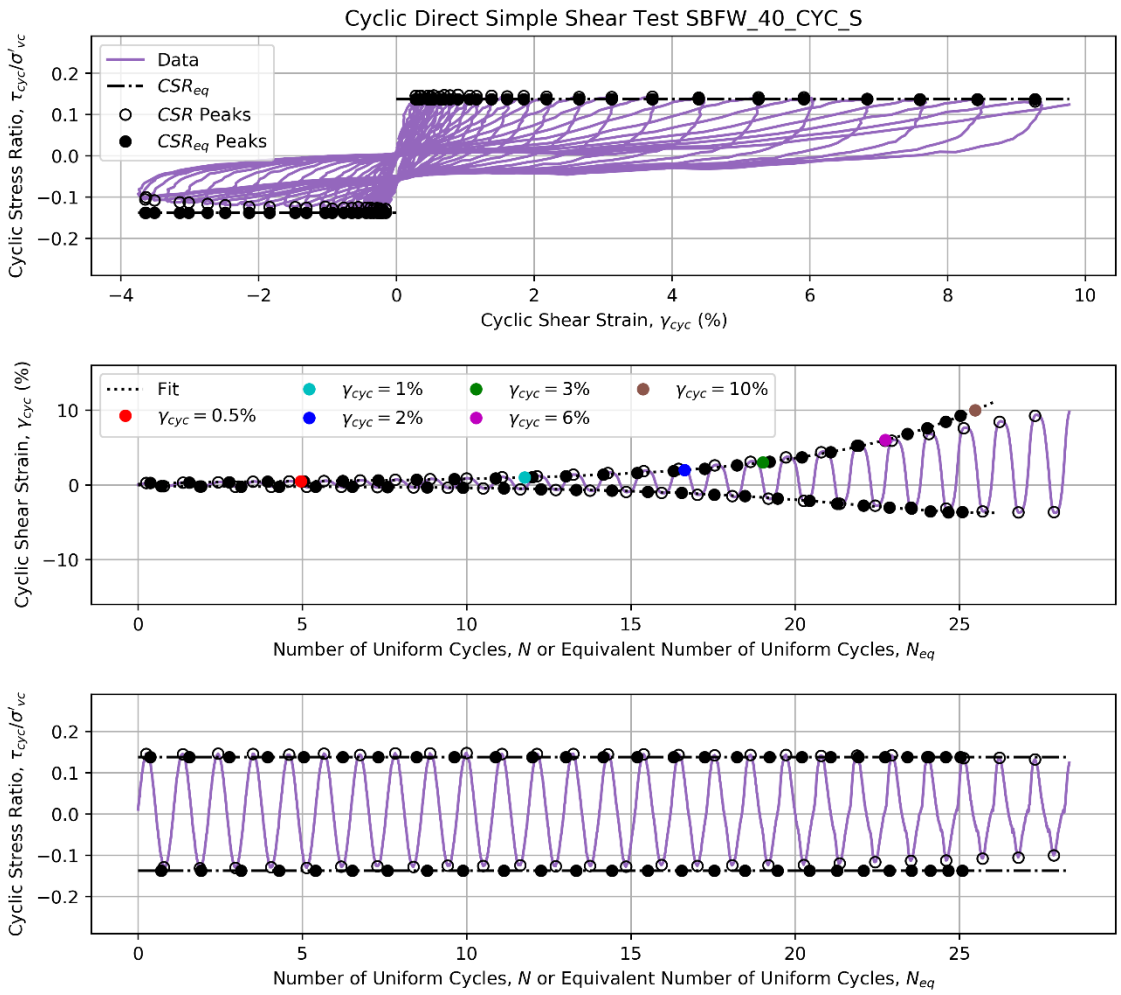

Figure A-26: Fitted Polynomial Curves for CSR-Adjusted SBFW_40_CYC_S Data

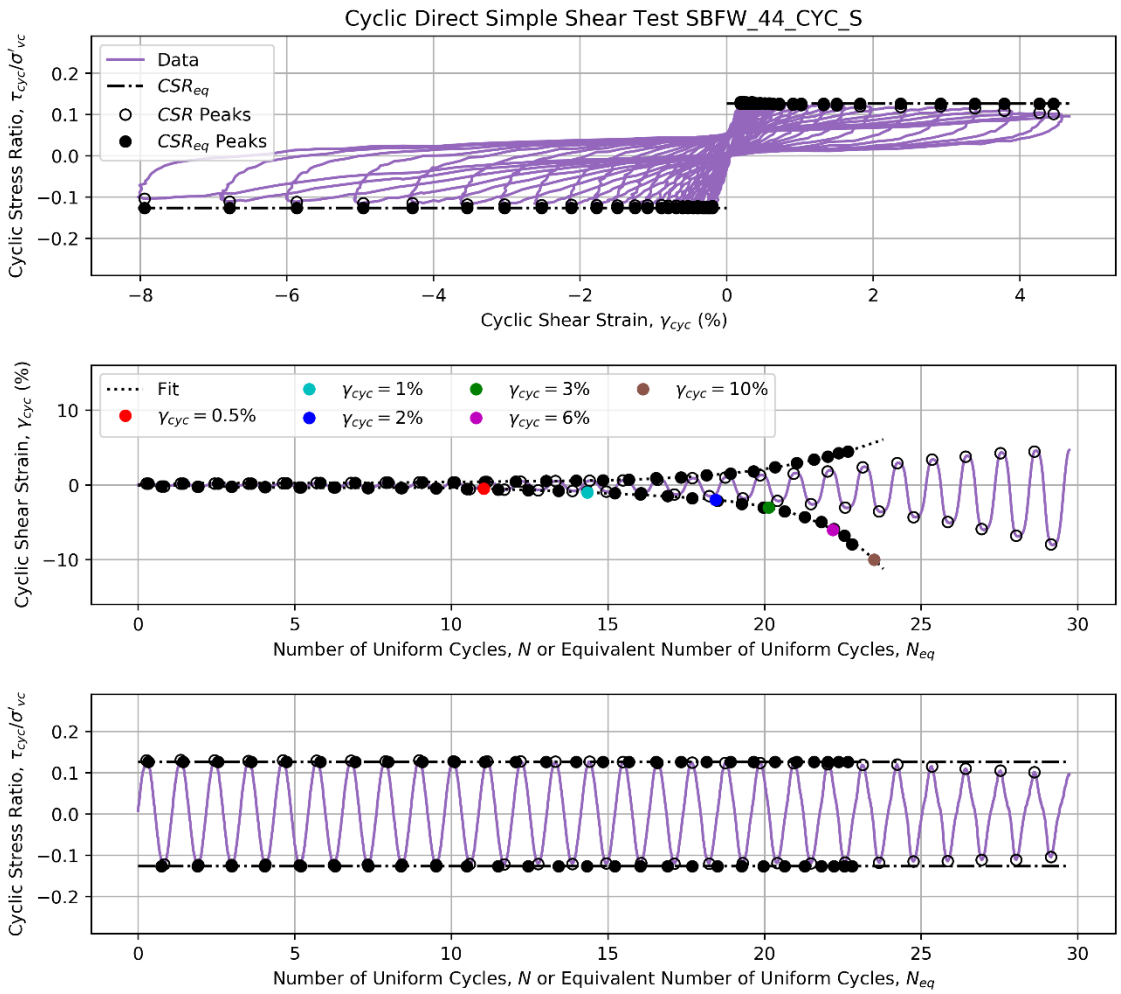

Figure A-27: Fitted Polynomial Curves for CSR-Adjusted SBFW_44_CYC_S Data

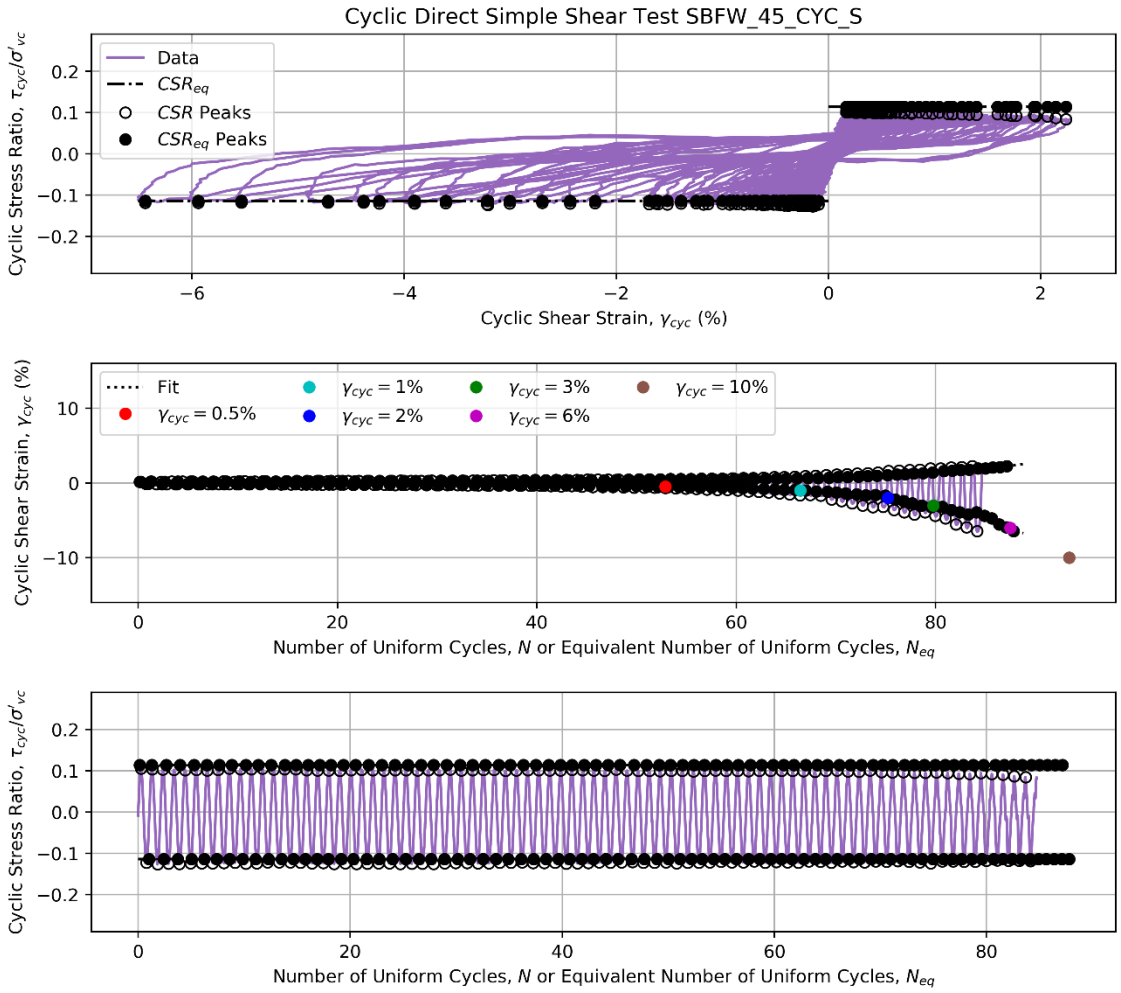

Figure A-28: Fitted Polynomial Curves for CSR-Adjusted SBFW_45_CYC_S Data

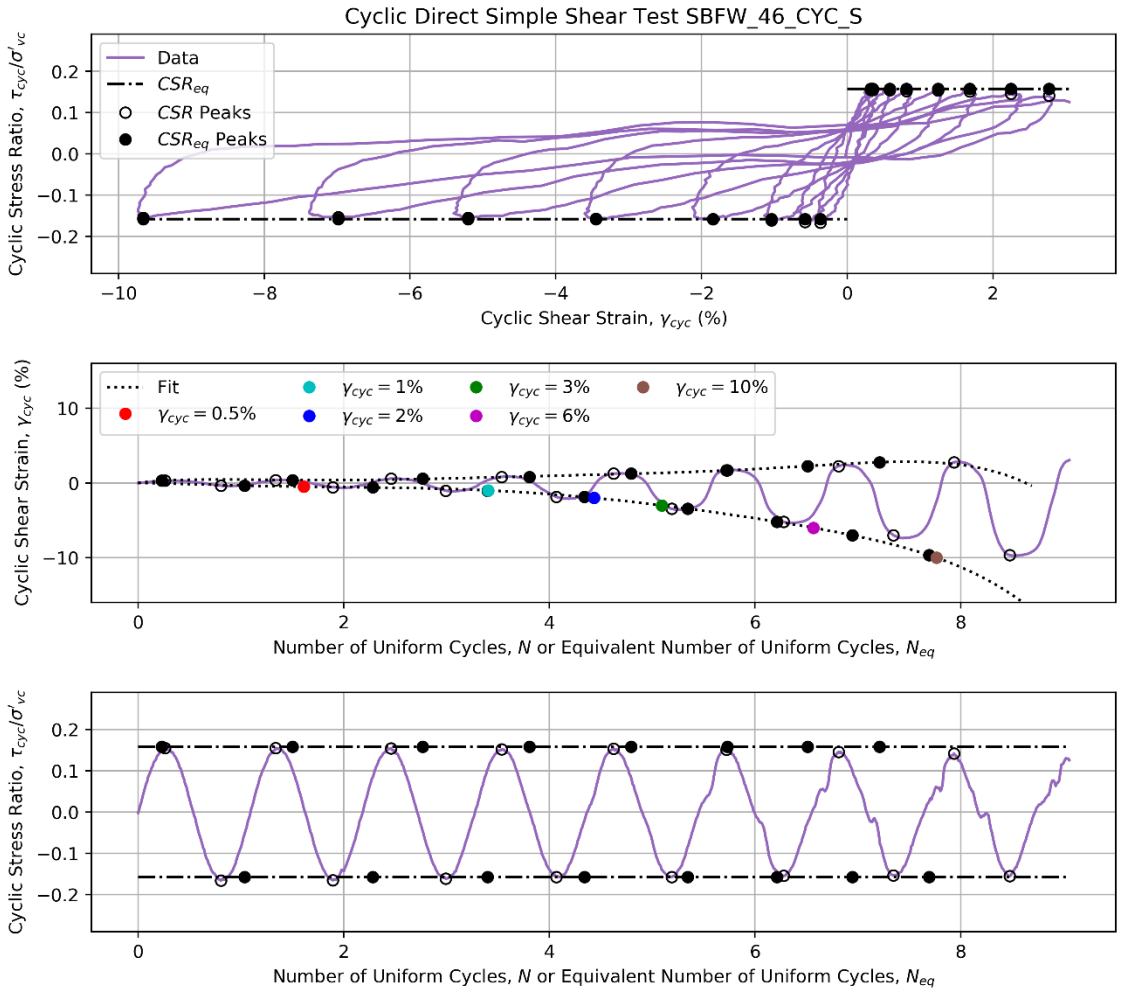

Figure A-29: Fitted Polynomial Curves for CSR-Adjusted SBFW_46_CYC_S Data

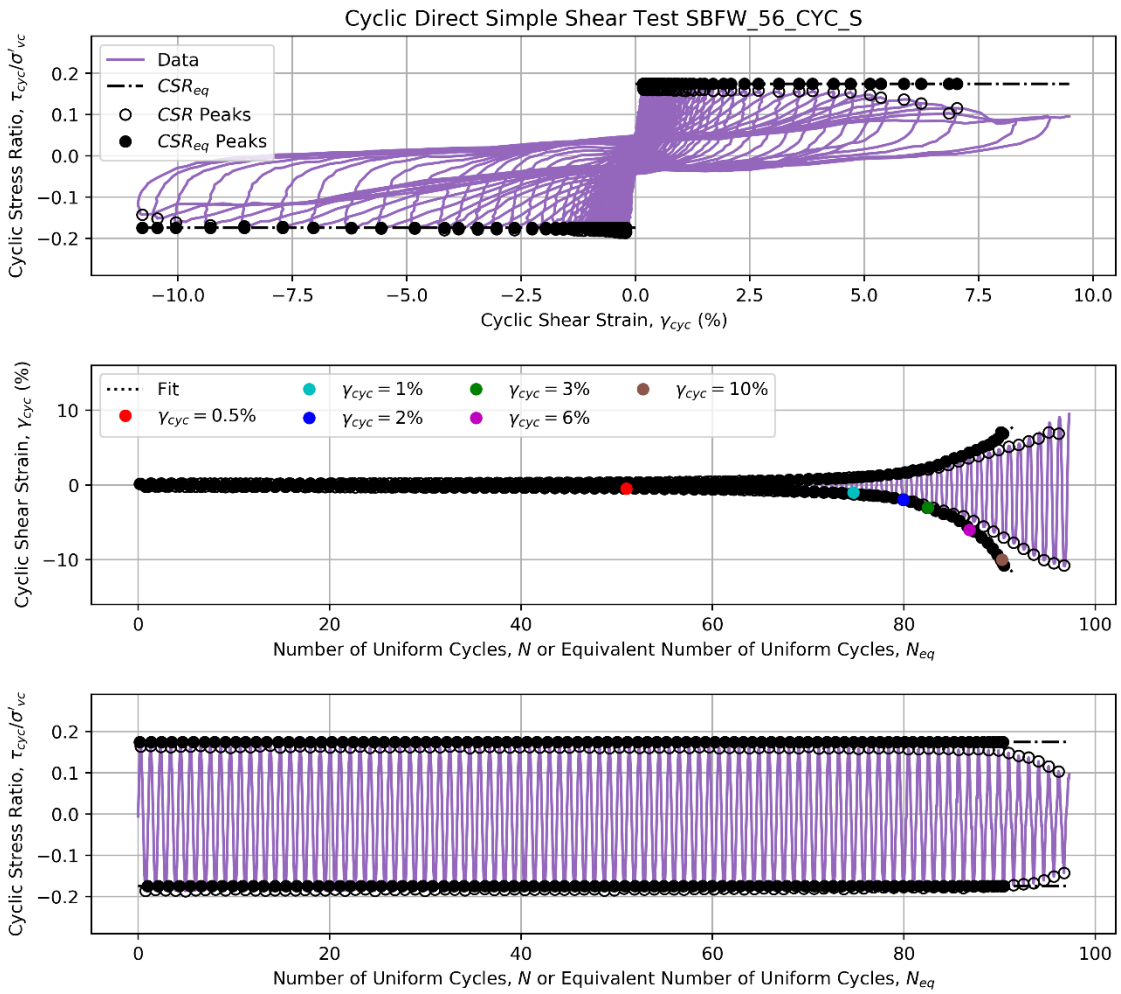

Figure A-30: Fitted Polynomial Curves for CSR-Adjusted SBFW_56_CYC_S Data

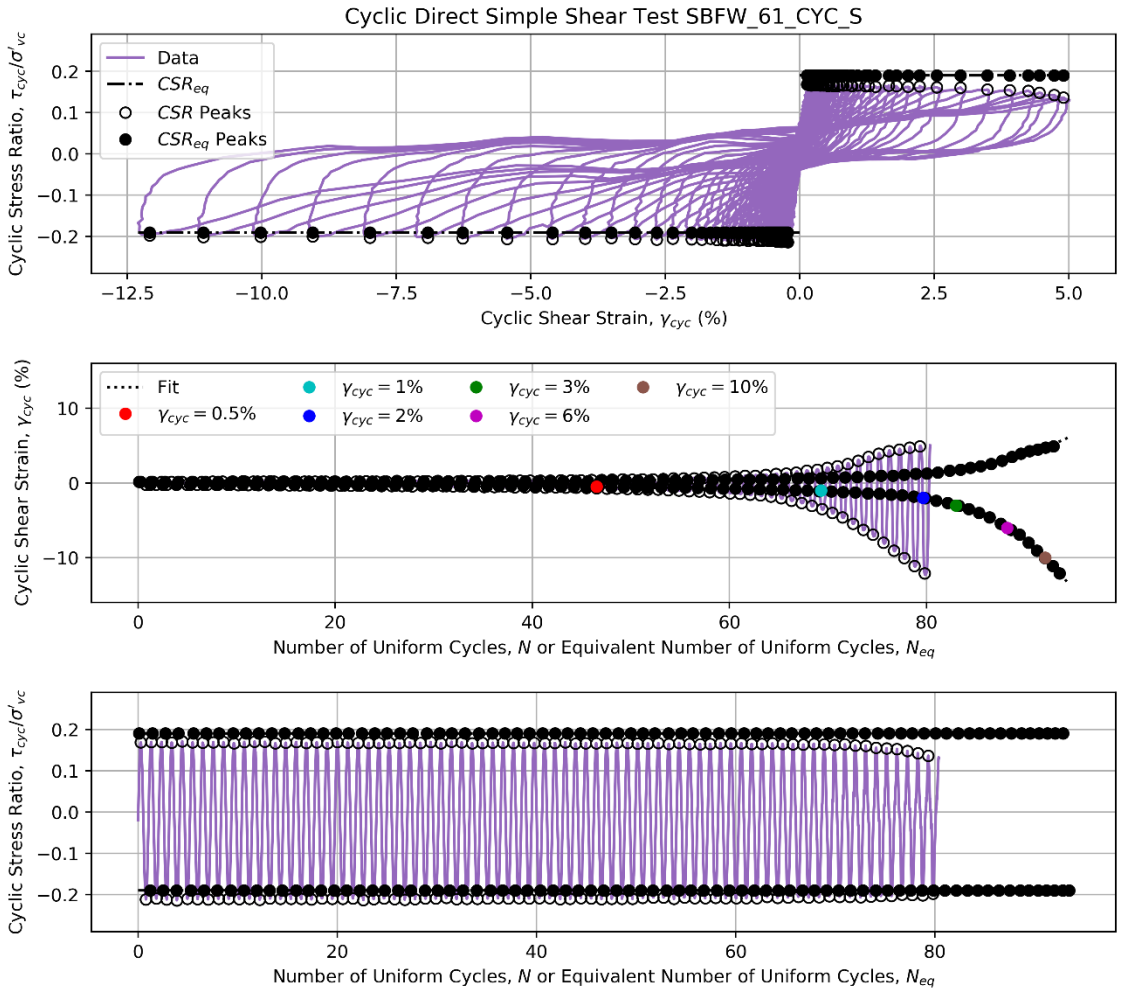

Figure A-31: Fitted Polynomial Curves for CSR-Adjusted SBFW_61_CYC_S Data

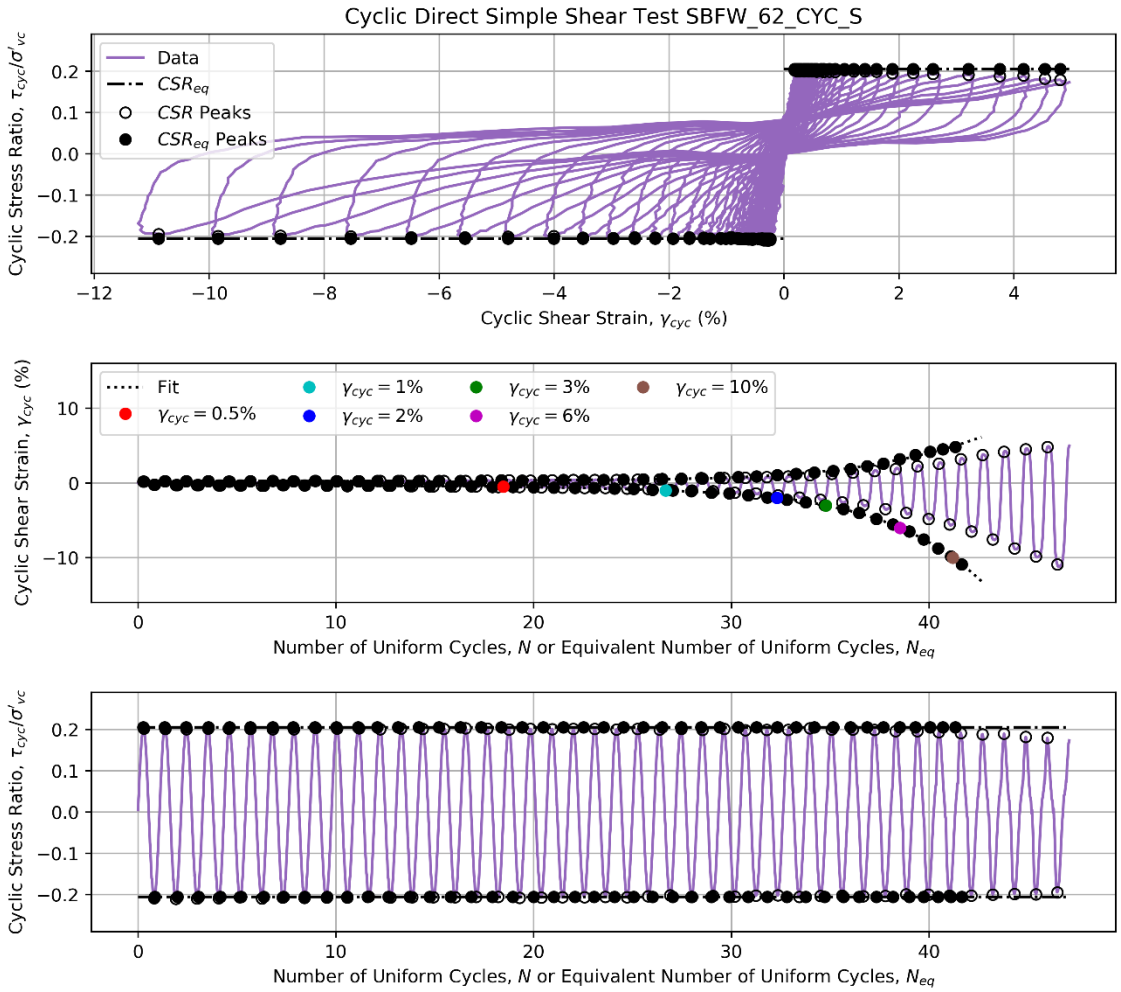

Figure A-32: Fitted Polynomial Curves for CSR-Adjusted SBFW_62_CYC_S Data

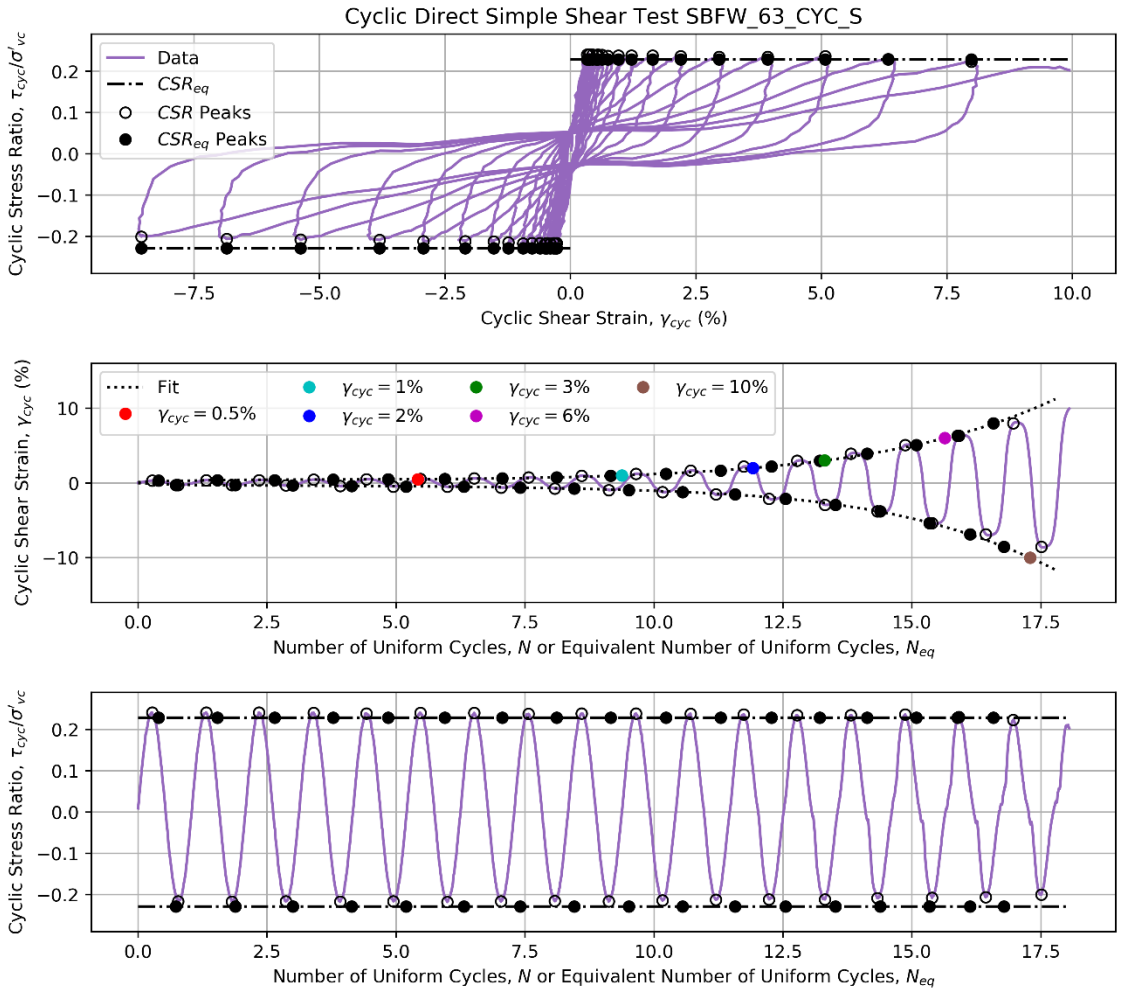

Figure A-33: Fitted Polynomial Curves for CSR-Adjusted SBFW_63_CYC_S Data

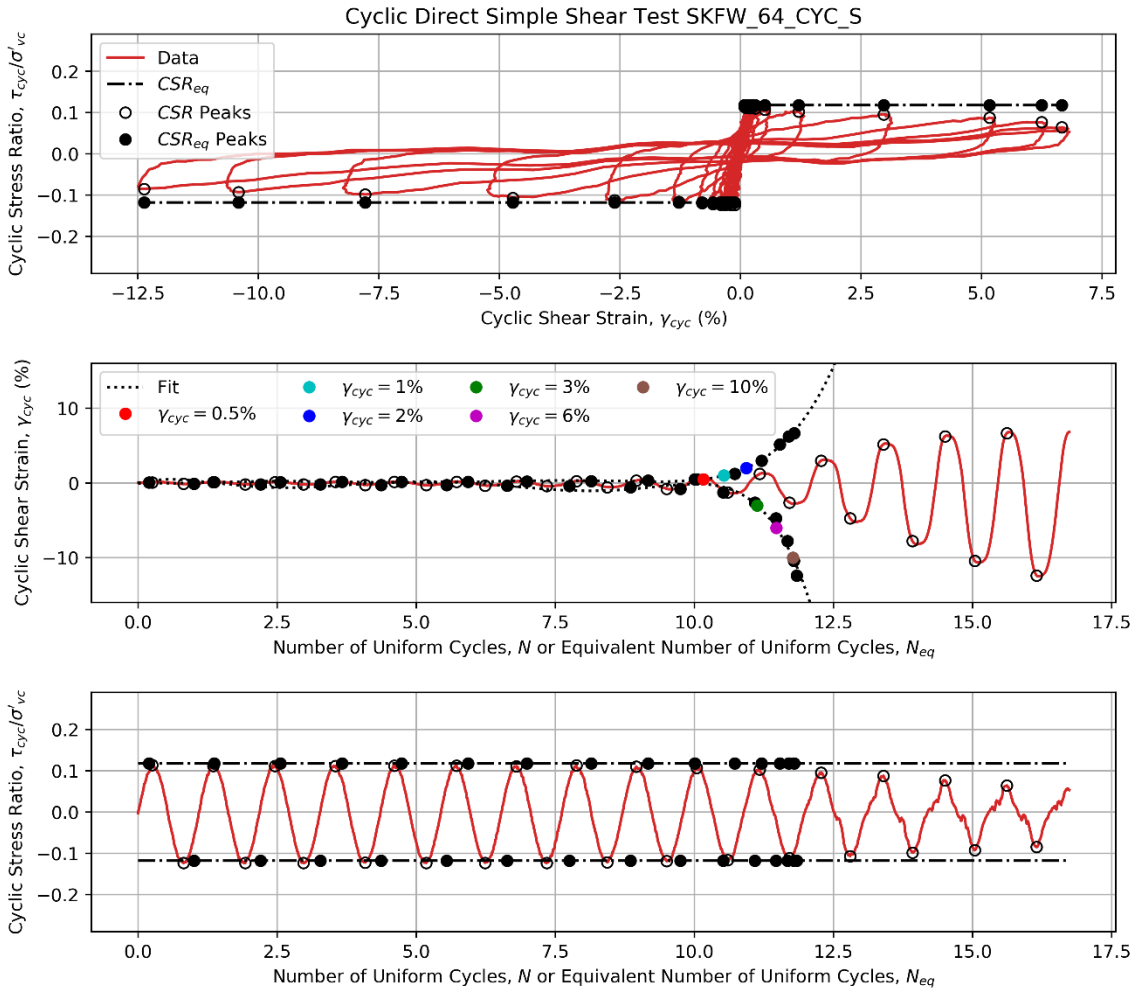

Figure A-34: Fitted Polynomial Curves for CSR-Adjusted SKFW_64_CYC_S Data

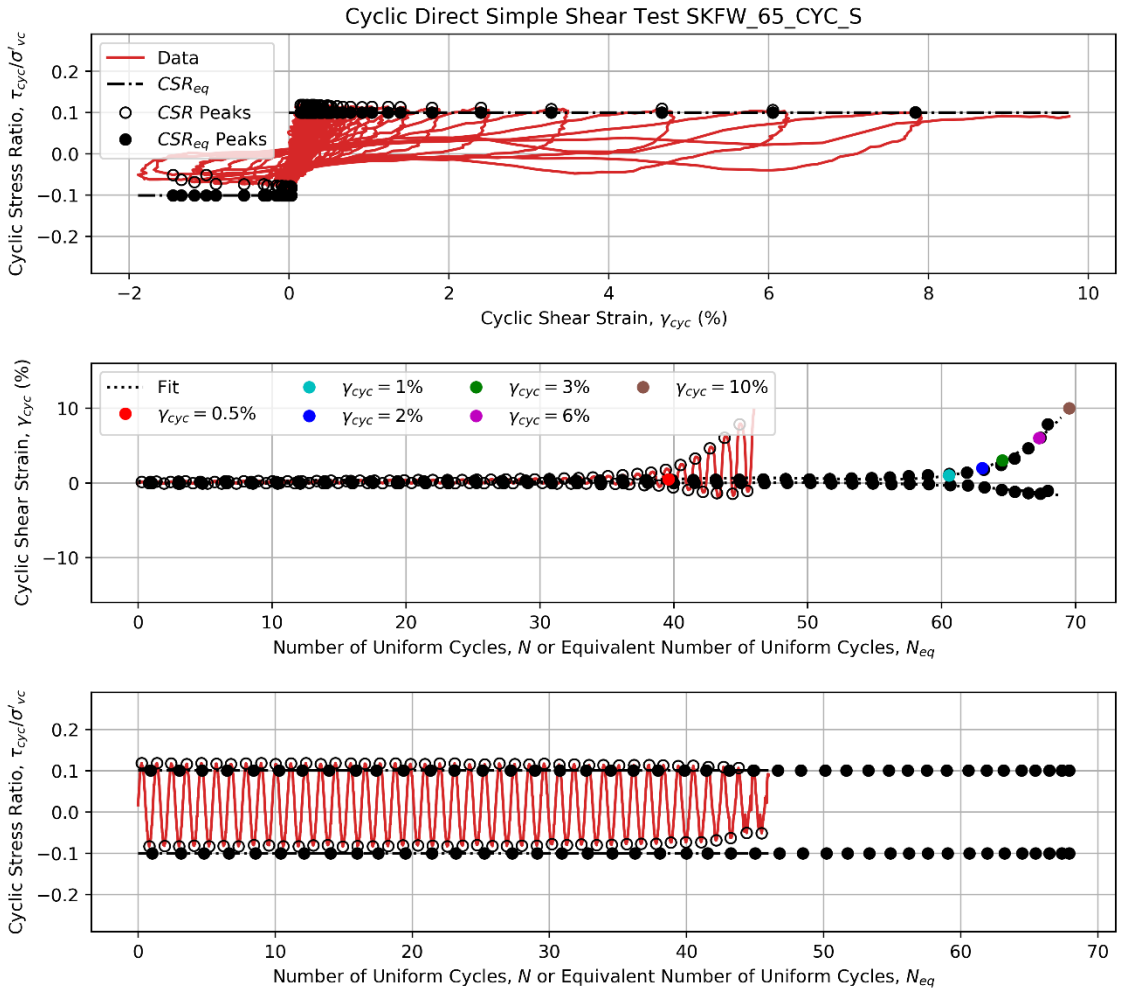

Figure A-35: Fitted Polynomial Curves for CSR-Adjusted SKFW_65_CYC_S Data

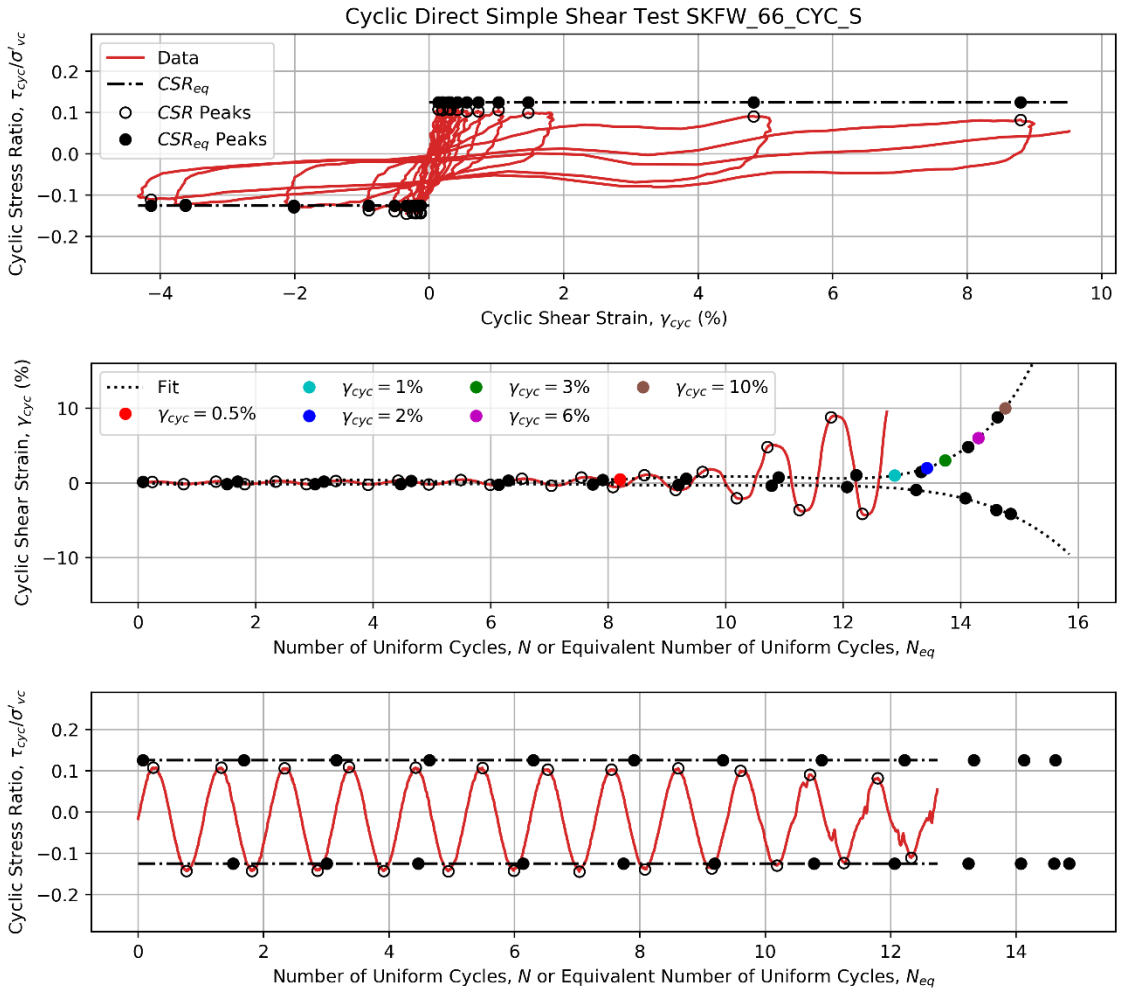

Figure A-36: Fitted Polynomial Curves for CSR-Adjusted SKFW_66_CYC_S Data

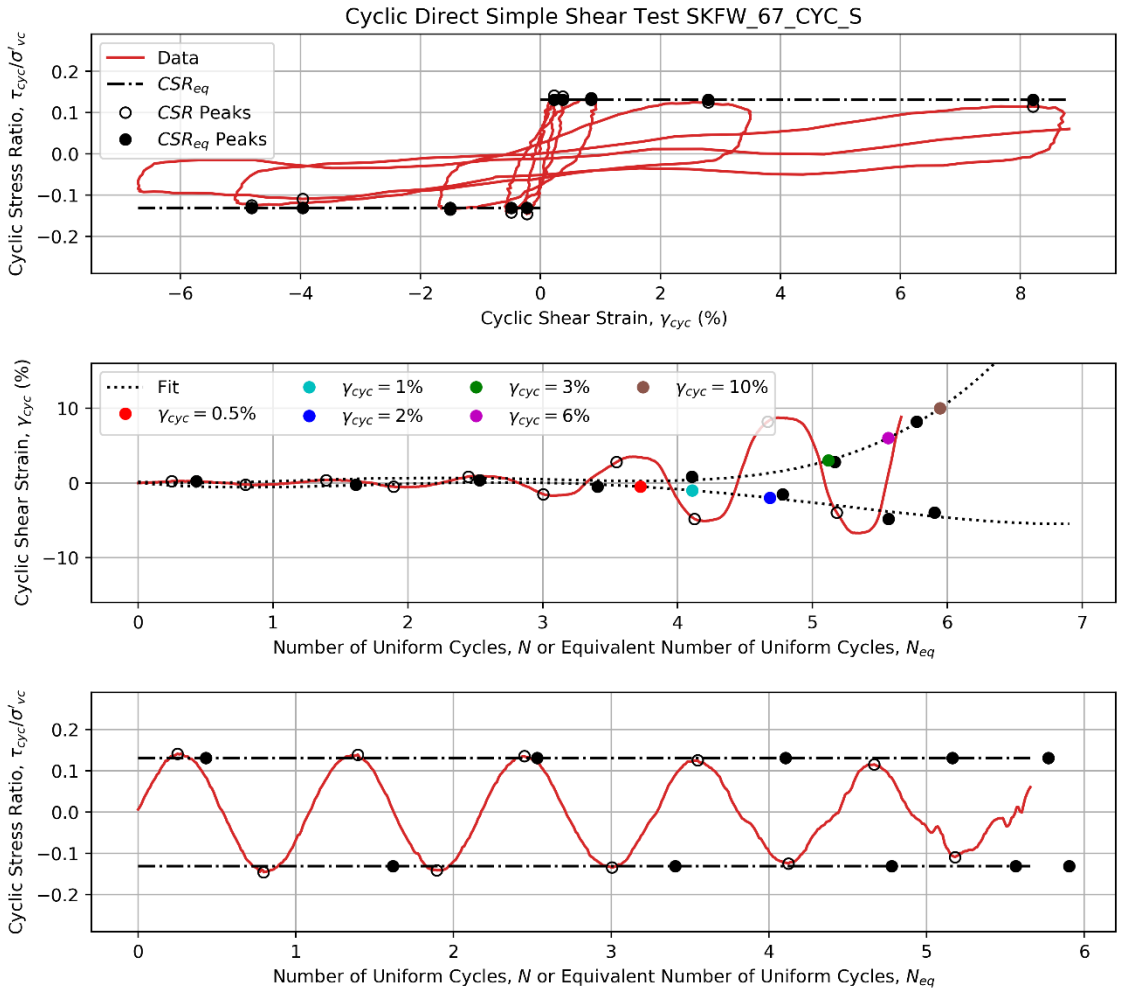

Figure A-37: Fitted Polynomial Curves for CSR-Adjusted SKFW_67_CYC_S Data

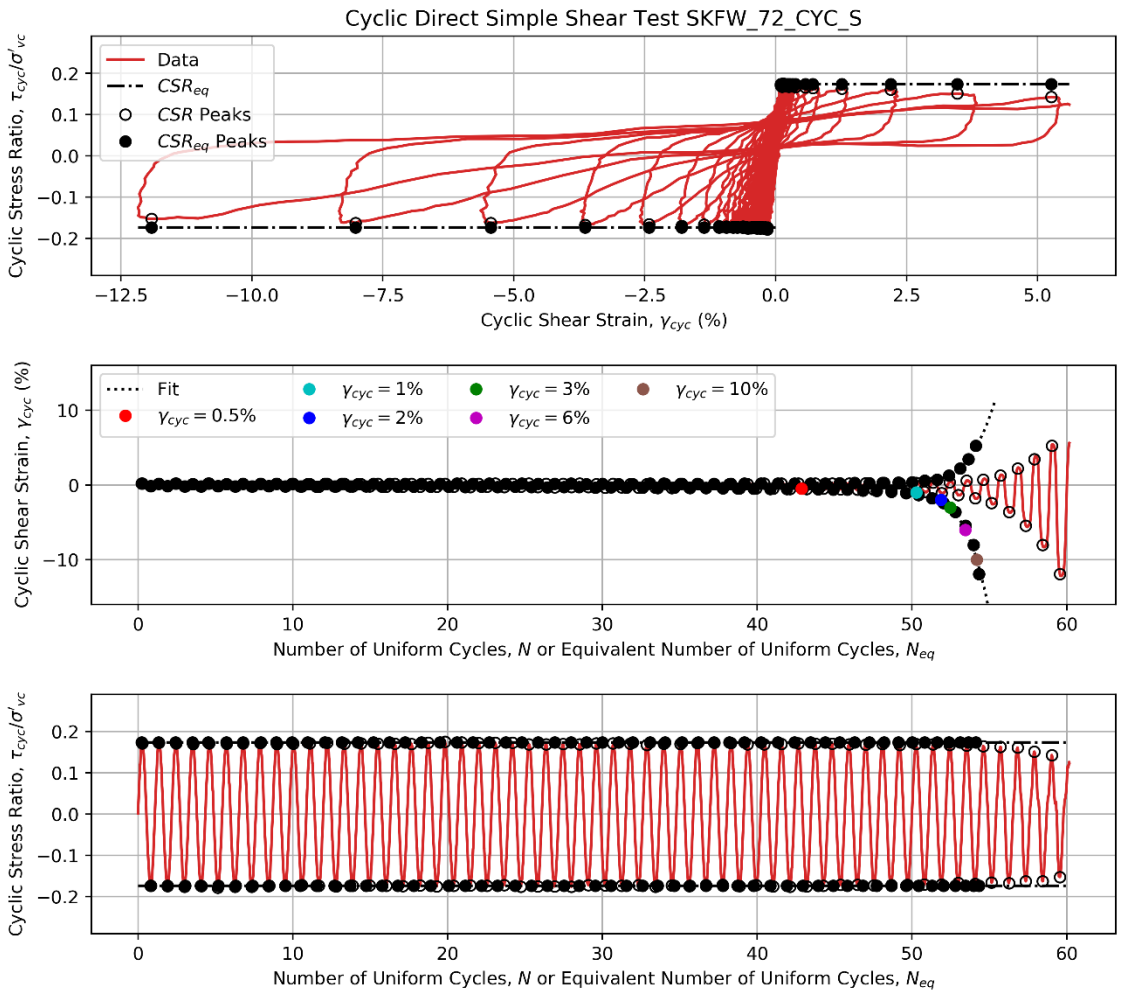

Figure A-38: Fitted Polynomial Curves for CSR-Adjusted SKFW_72_CYC_S Data

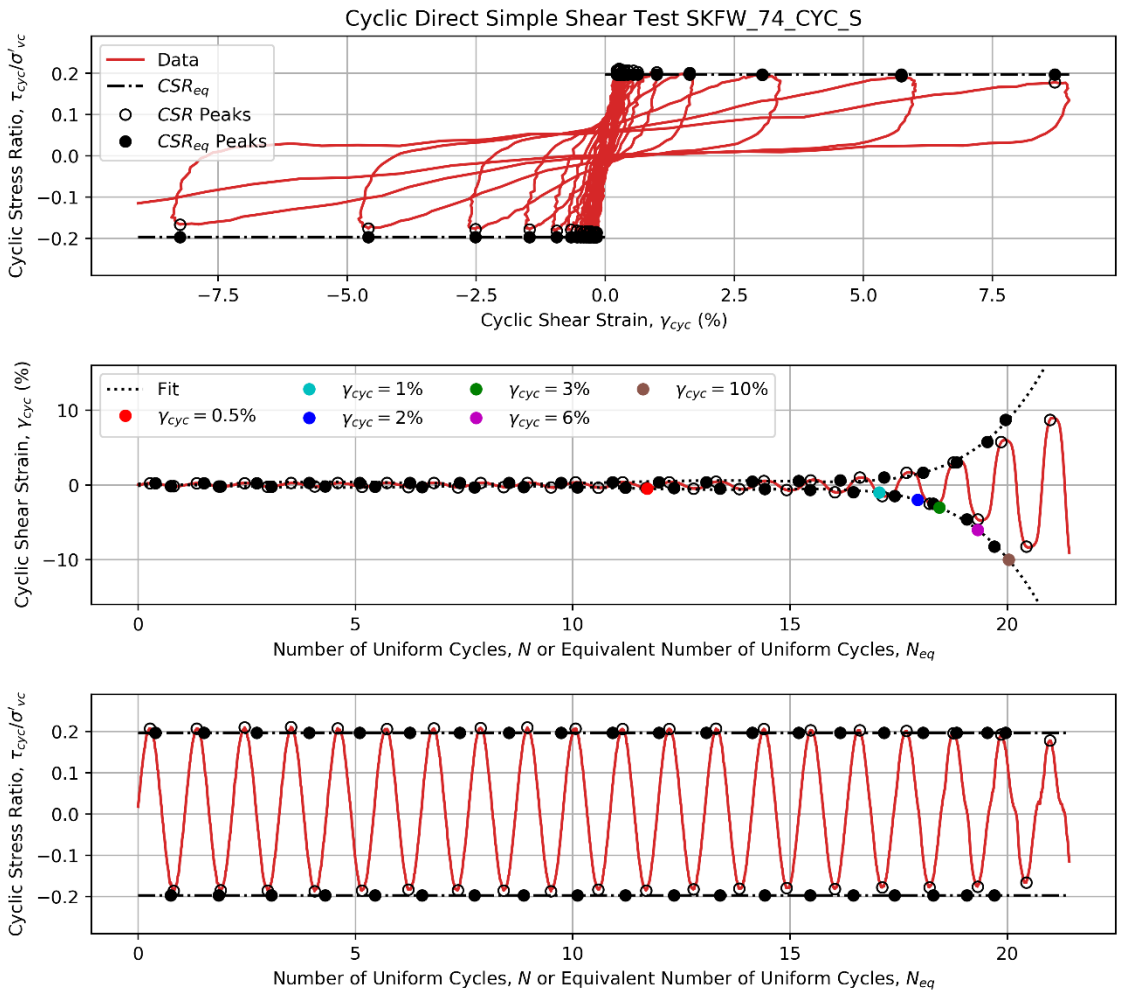

Figure A-39: Fitted Polynomial Curves for CSR-Adjusted SKFW_74_CYC_S Data

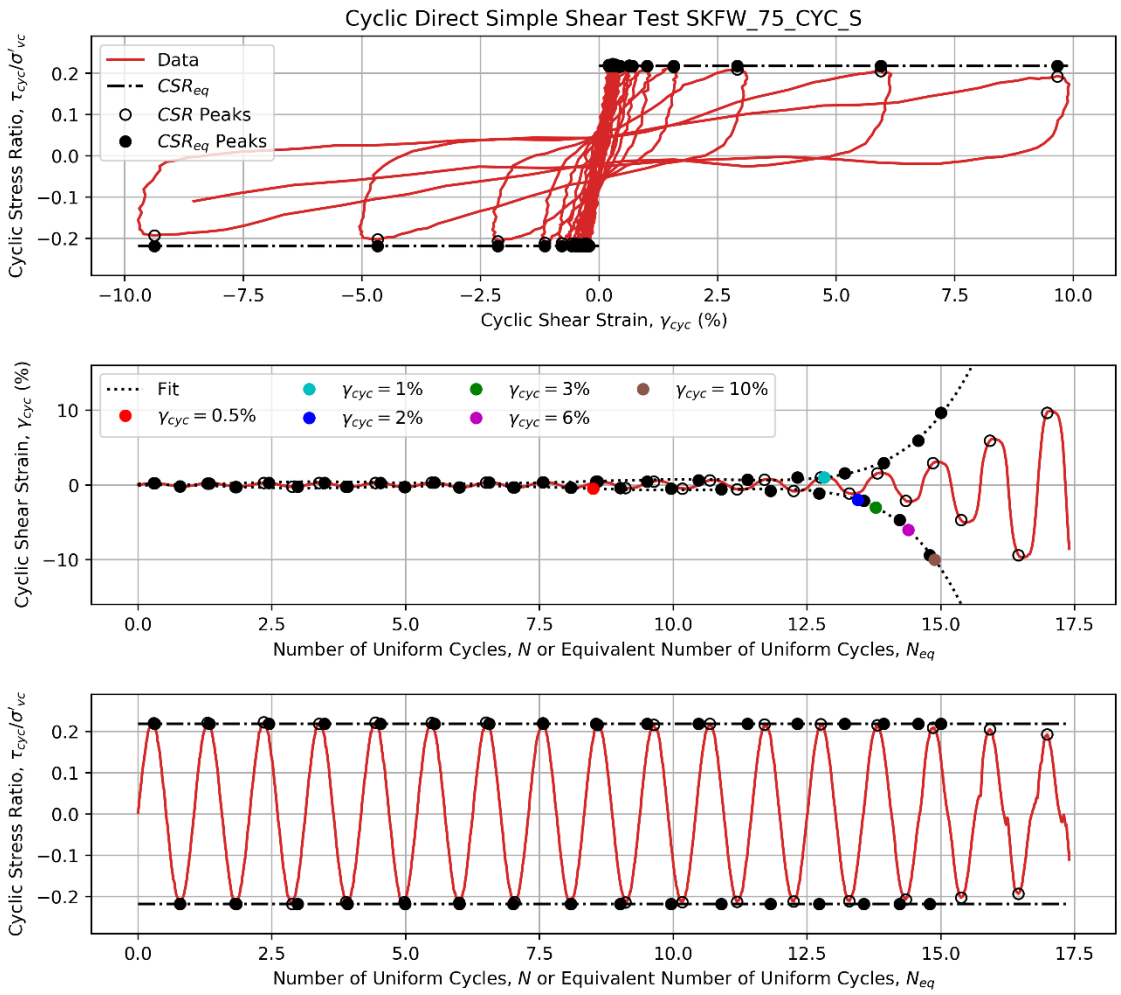

Figure A-40: Fitted Polynomial Curves for CSR-Adjusted SBFW_75_CYC_S Data

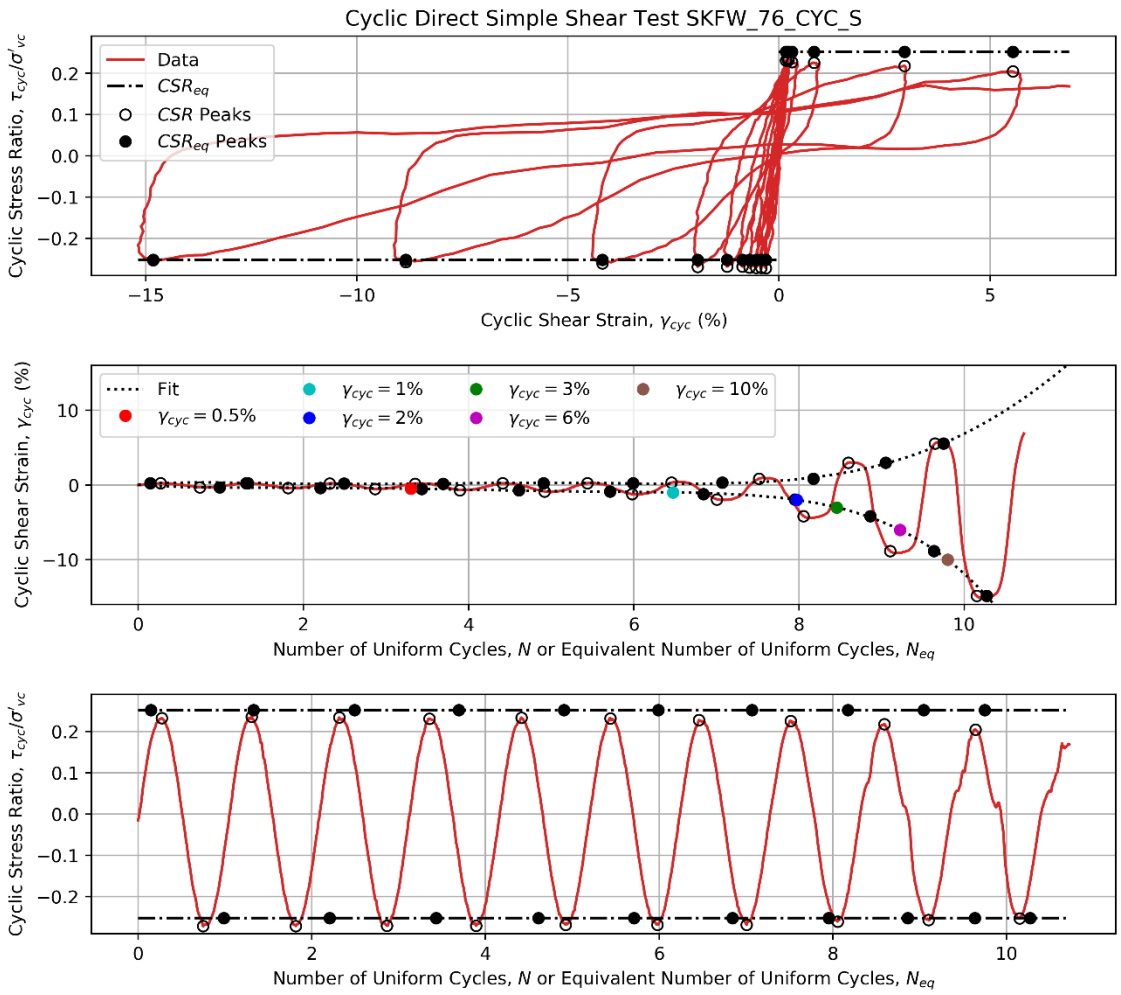

Figure A-41: Fitted Polynomial Curves for CSR-Adjusted SBFW_76_CYC_S Data

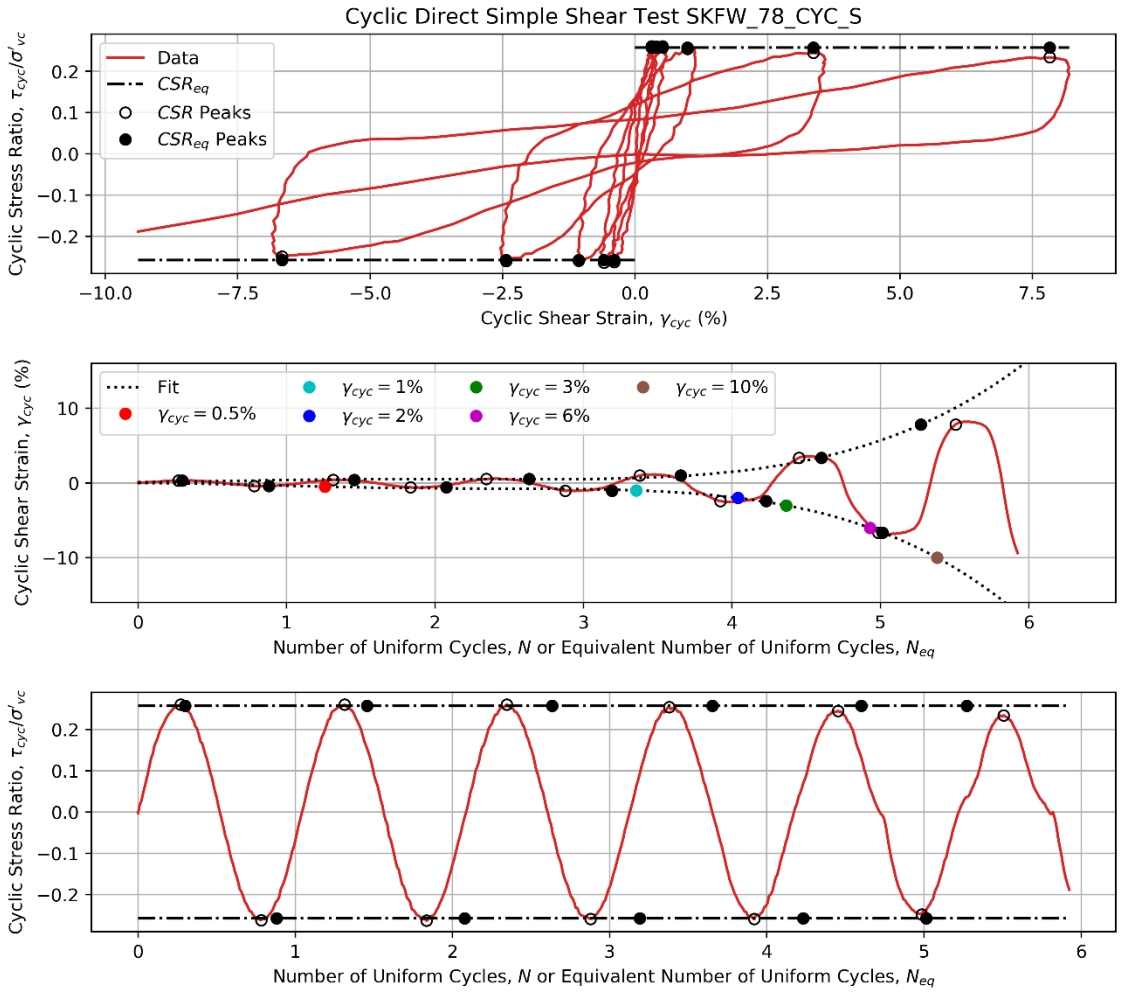

Figure A-42: Fitted Polynomial Curves for CSR-Adjusted SBFW_78_CYC_S Data

APPENDIX B: CYCLIC SHEAR STRAIN BELOW STRUCTURE FOOTINGS

Evaluation of strain below structure footings formed the basis for development of strain indices in Chapter 10 of this dissertation. I evaluated strain over a 100 x 100 grid of points below the structure foundations. At each point, I calculated static stress and evaluated time histories for the increase in stress due to the dynamic loading increment. From the stress time histories, I then evaluated DSR and performed cyclic counting procedures on each DSR time history to evaluate a single-amplitude cyclic demand value, DSR_M at an equivalent number of cycles, N_{eq} in accordance with the procedure used above. Finally, I used Equations (4-5) and (4-6) to evaluate γ_{cyc} below the foundation. The figures below present the results of this analysis for each structure in each model for each applied ground motion, resulting in 28 total analyses (analyses were not performed for Structure 1 after it experienced bearing capacity failure). Strain values are capped at $\gamma_{cyc} = 10\%$ due to limitations of the DSS laboratory data discussed in Chapter 4.

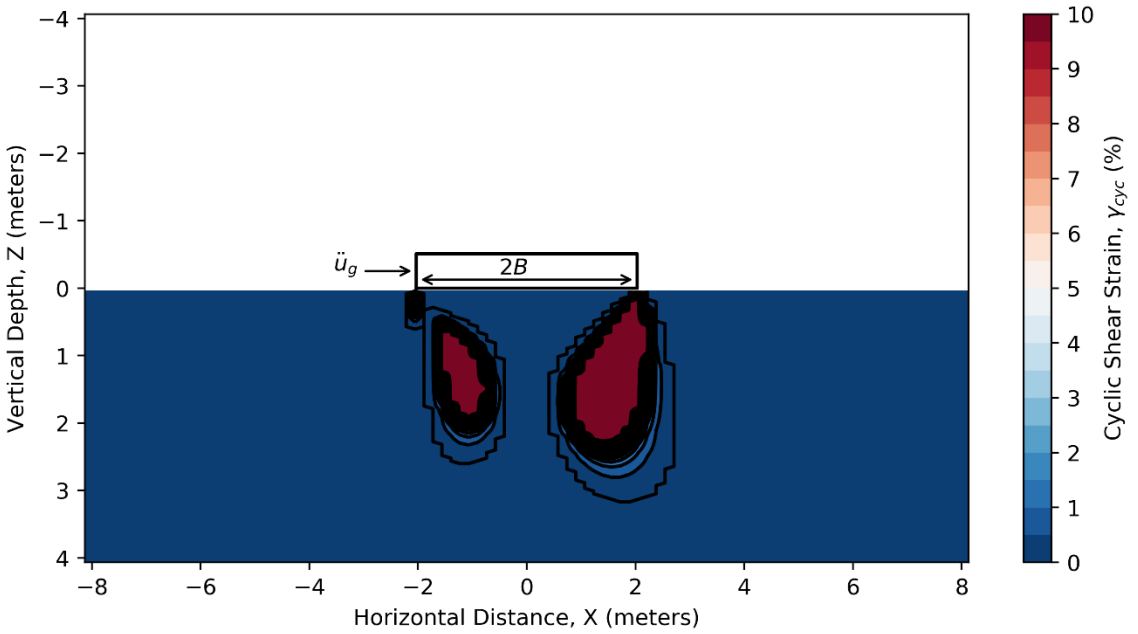

Figure B-1: Cyclic Shear Strain Below JZB01 Structure 1 – TCU-078 [0.2]

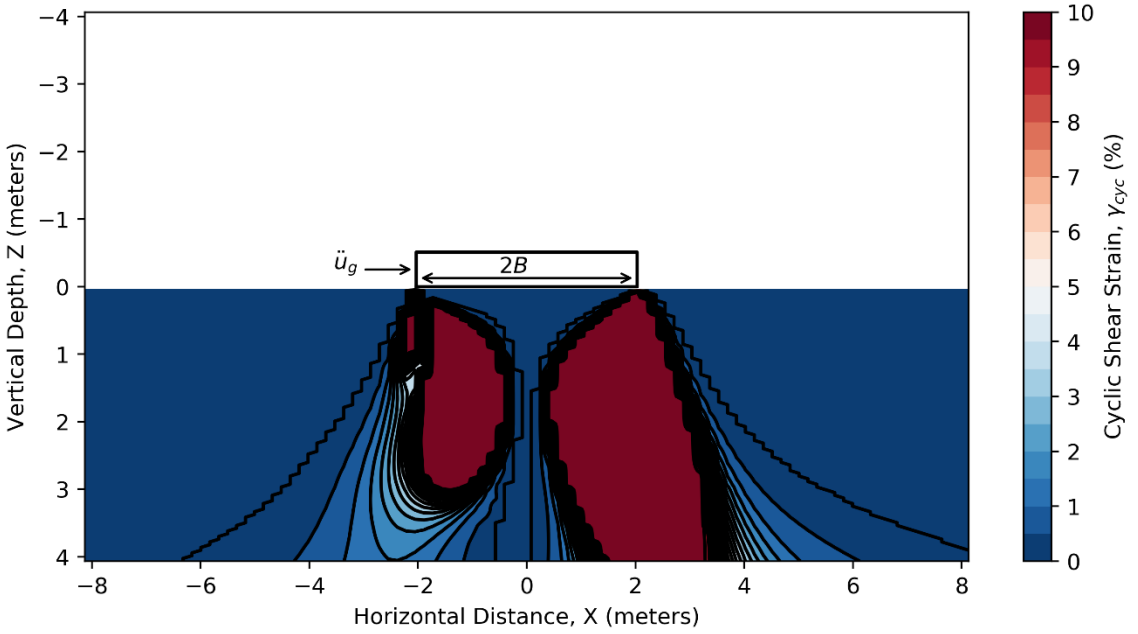

Figure B-2: Cyclic Shear Strain Below JZB01 Structure 1 – TCU-078 [0.4]

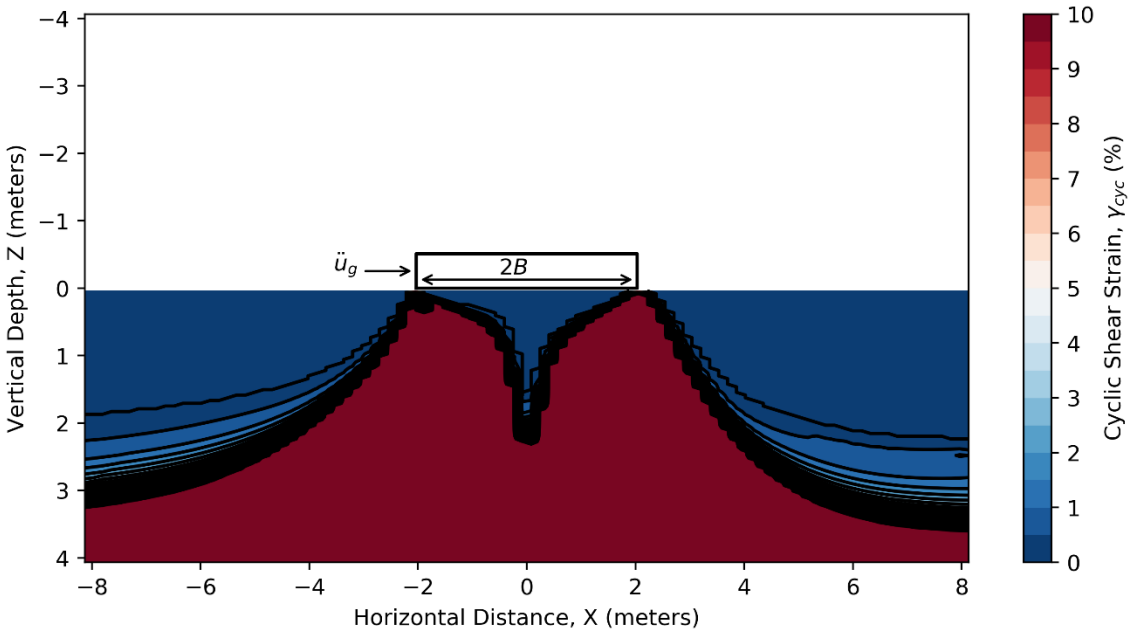

Figure B-3: Cyclic Shear Strain Below JZB01 Structure 1 – TCU-078 [0.6]

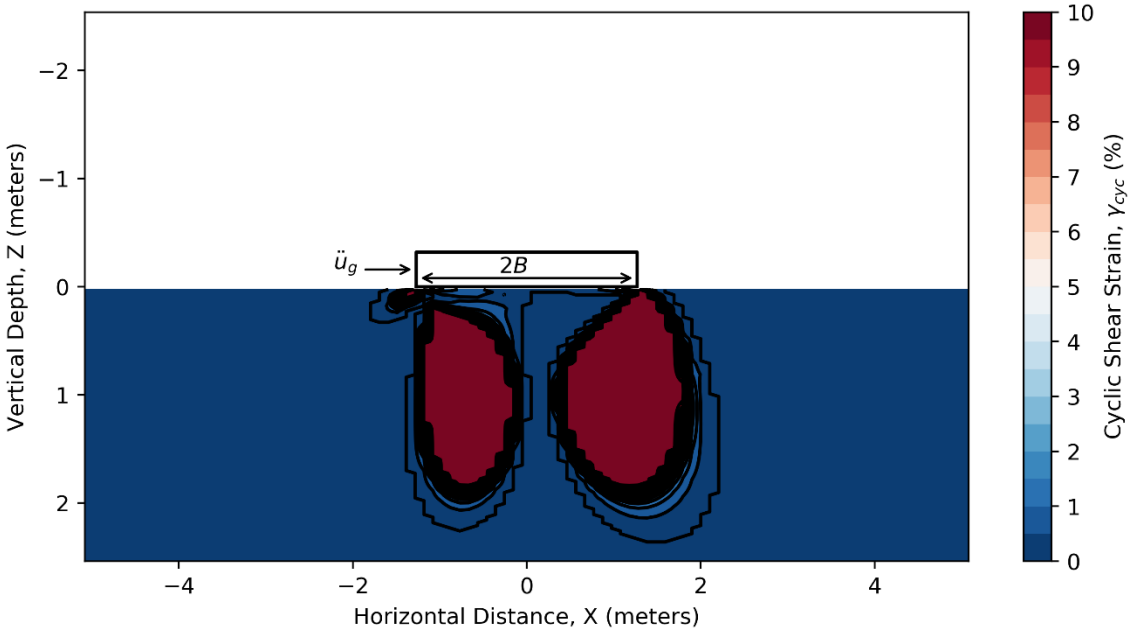

Figure B-4: Cyclic Shear Strain Below JZB01 Structure 2 – TCU-078 [0.2]

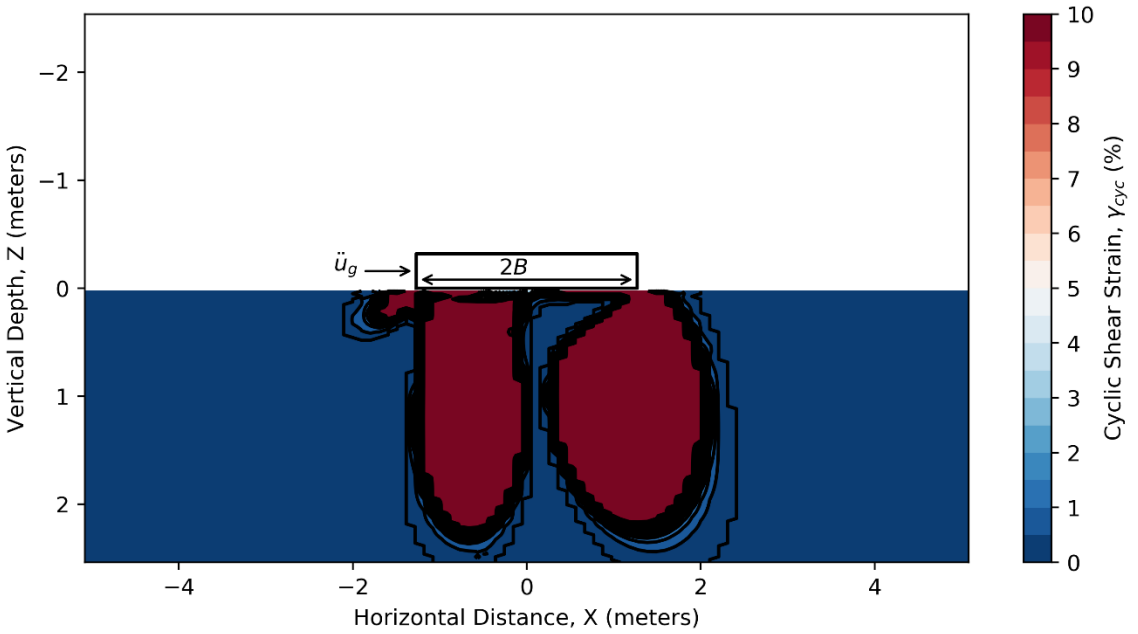

Figure B-5: Cyclic Shear Strain Below JZB01 Structure 2 – TCU-078 [0.4]

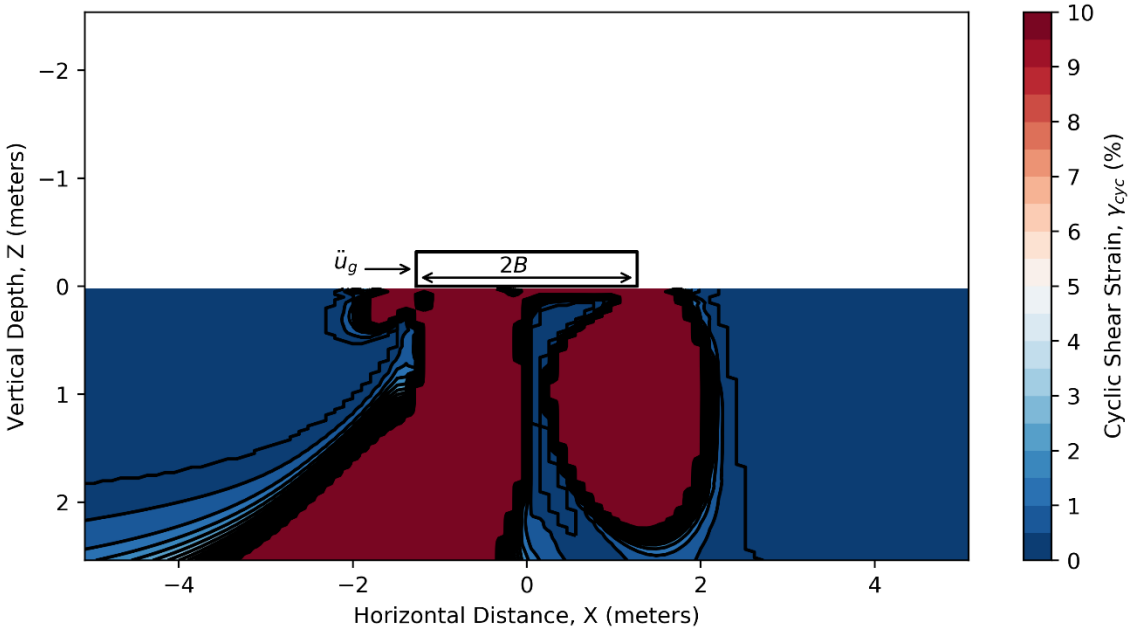

Figure B-6: Cyclic Shear Strain Below JZB01 Structure 2 – TCU-078 [0.6]

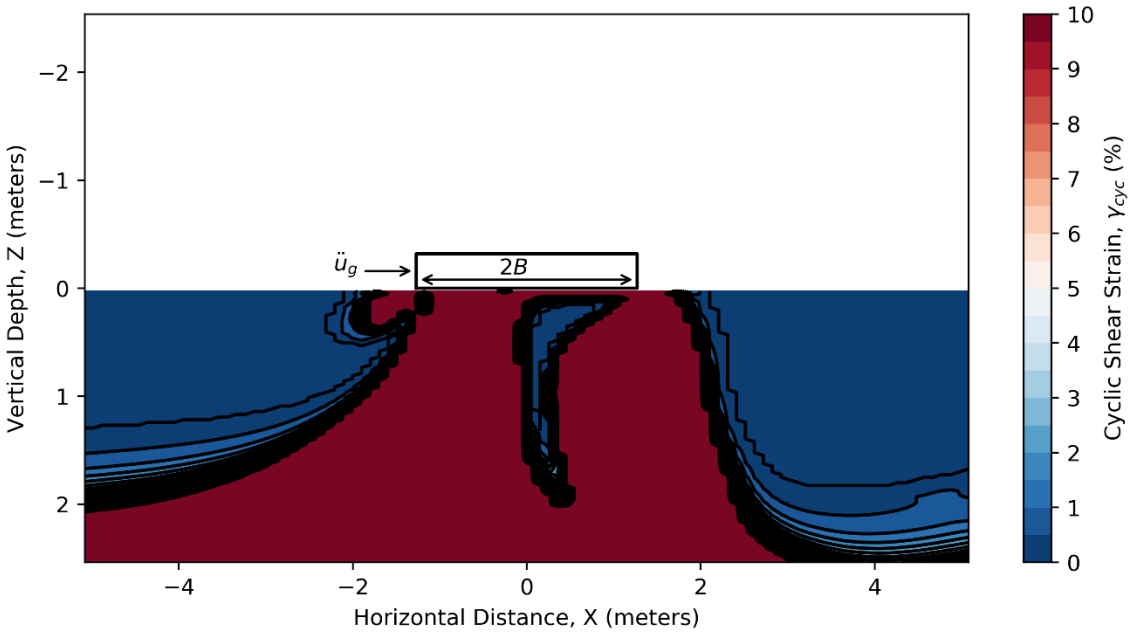

Figure B-7: Cyclic Shear Strain Below JZB01 Structure 2 – TCU-078 [0.8]

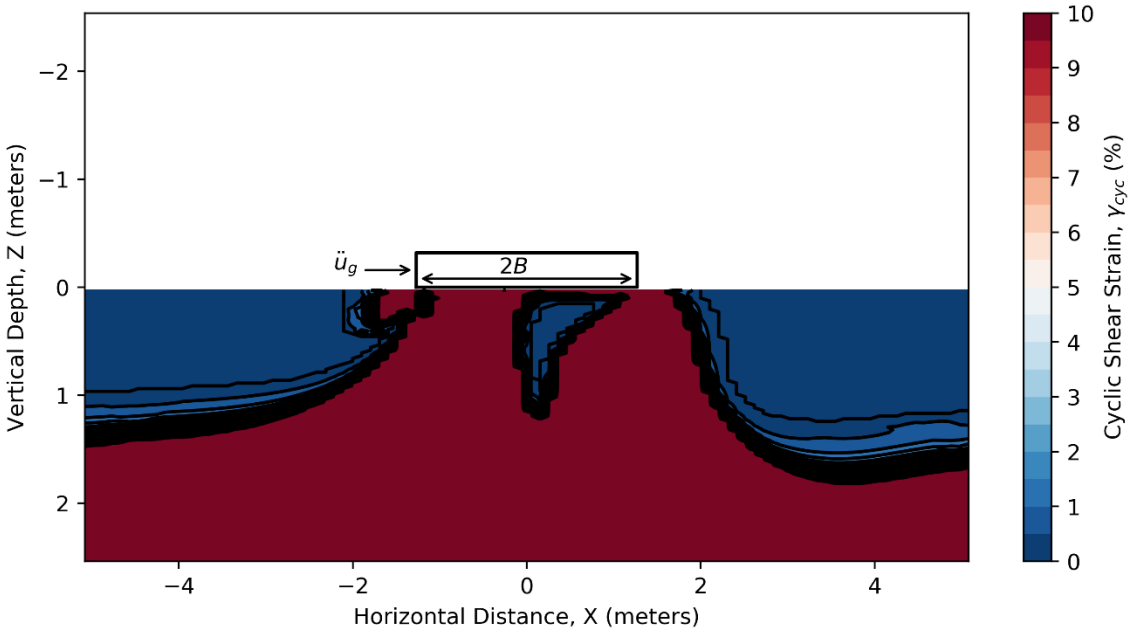

Figure B-8: Cyclic Shear Strain Below JZB01 Structure 2 – TCU-078 [1]

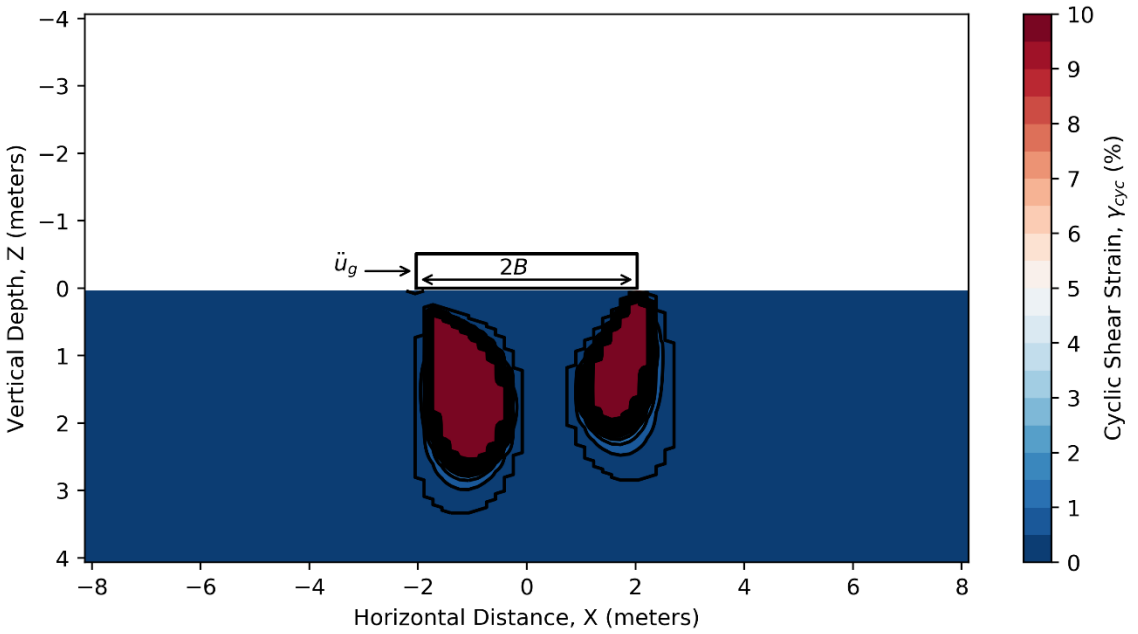

Figure B-9: Cyclic Shear Strain Below JZB01 Structure 3 – TCU-078 [0.2]

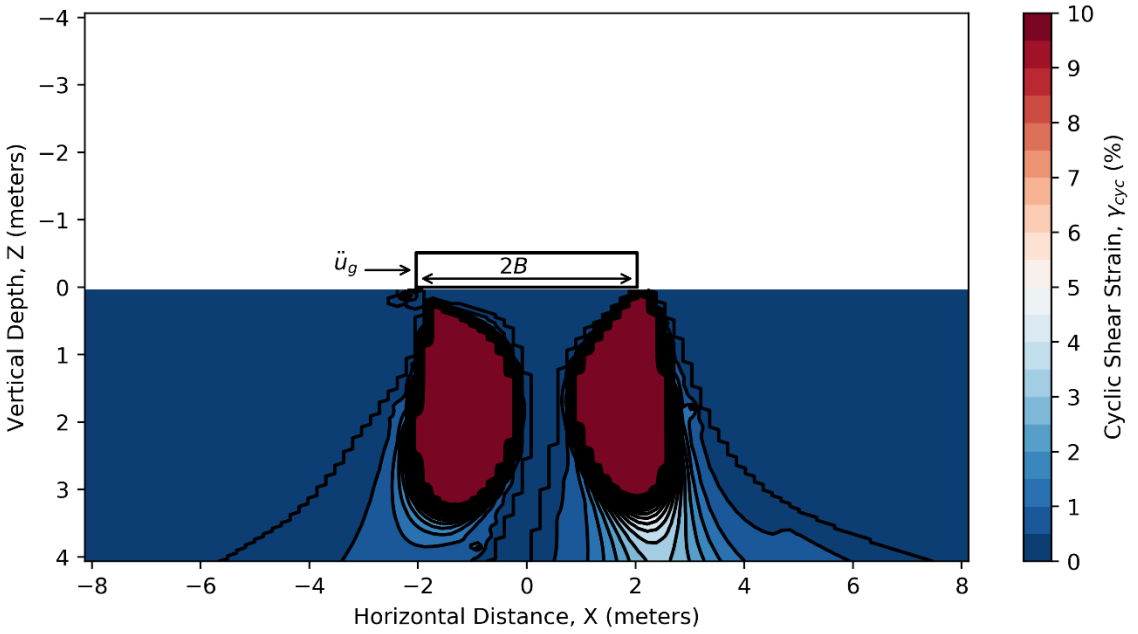

Figure B-10: Cyclic Shear Strain Below JZB01 Structure 3 – TCU-078 [0.4]

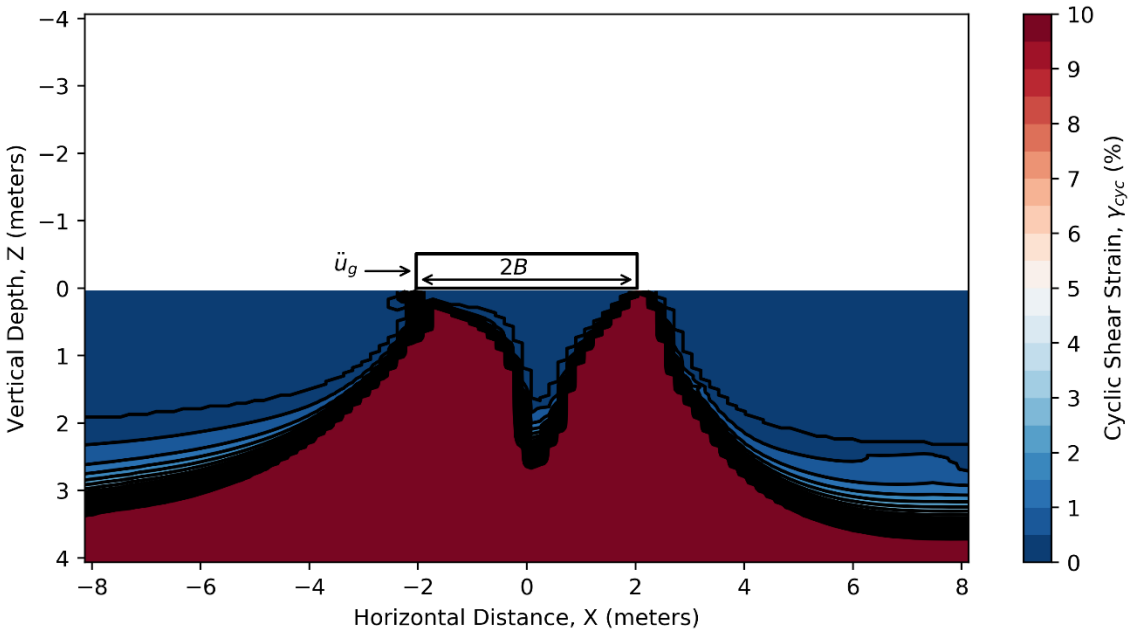

Figure B-11: Cyclic Shear Strain Below JZB01 Structure 3 – TCU-078 [0.6]

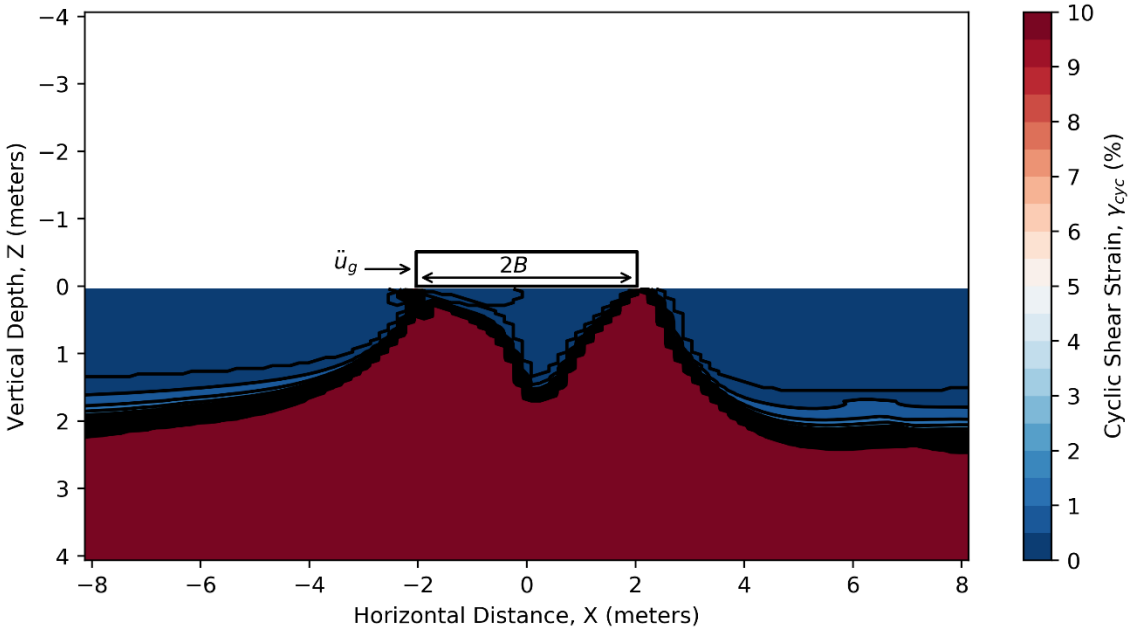

Figure B-12: Cyclic Shear Strain Below JZB01 Structure 3 – TCU-078 [0.8]

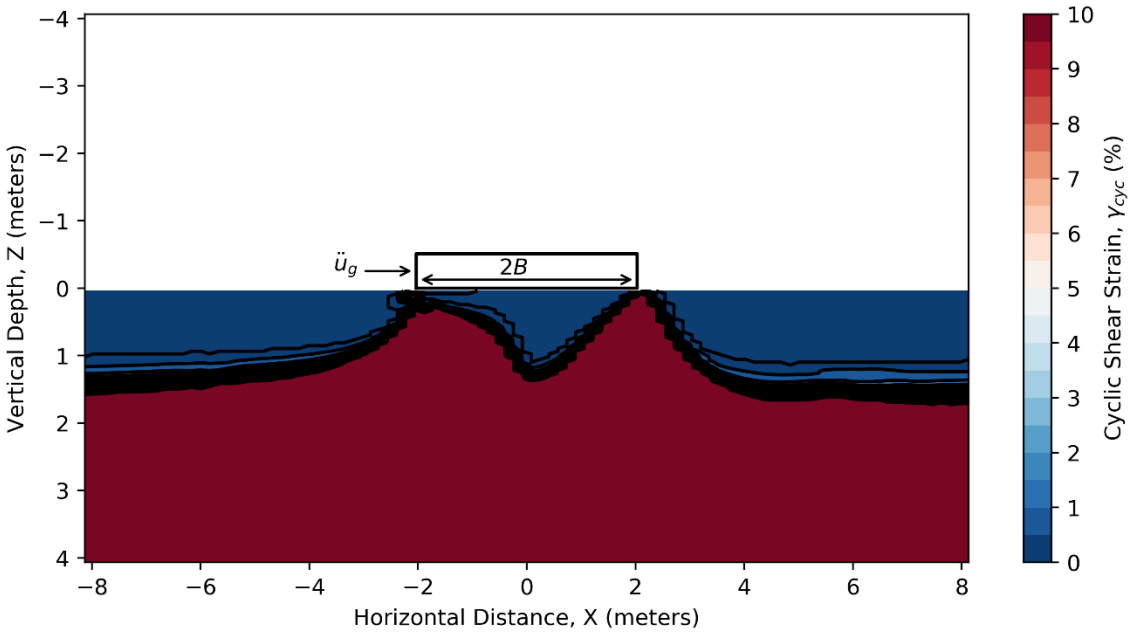

Figure B-13: Cyclic Shear Strain Below JZB01 Structure 3 – TCU-078 [1]

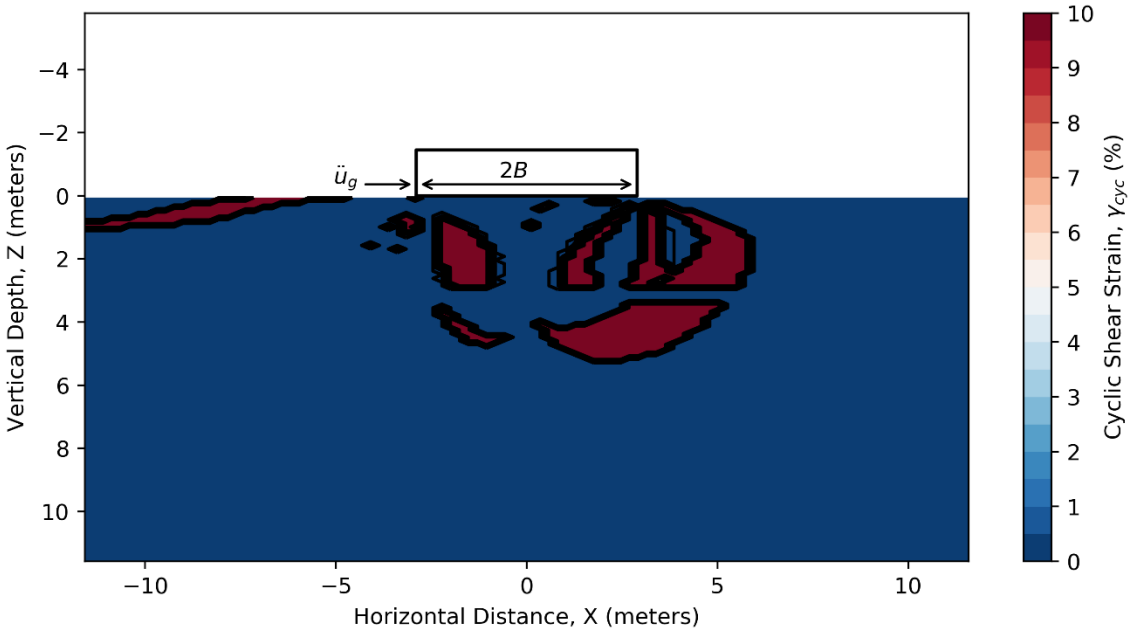

Figure B- 14: Cyclic Shear Strain Below JZB02 Structure 1 – TCU-078 [0.2]

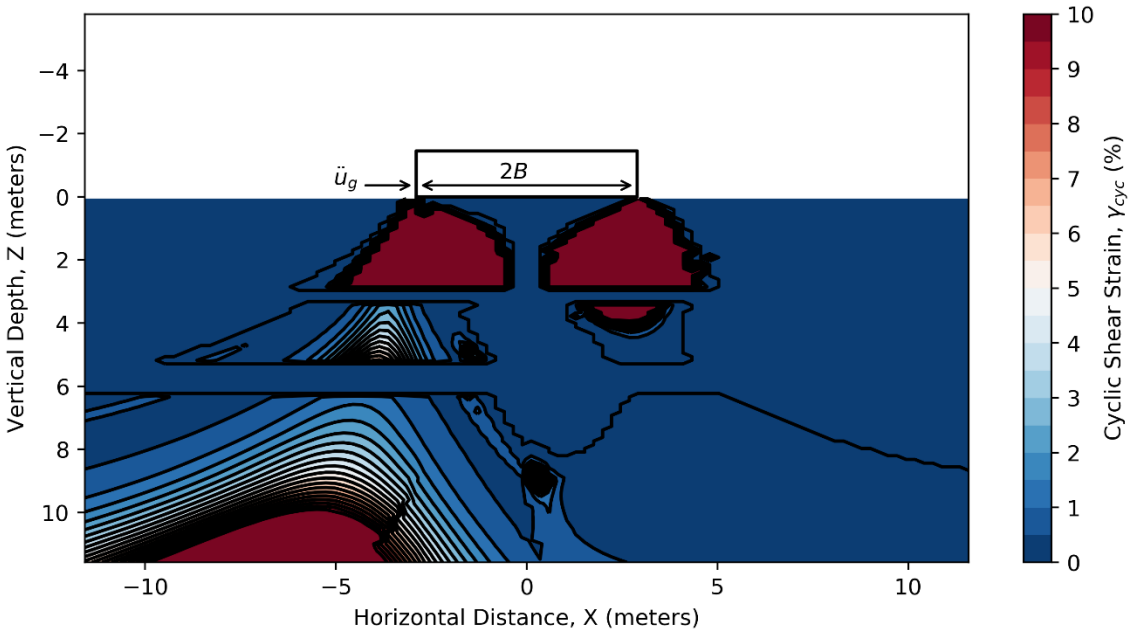

Figure B- 15: Cyclic Shear Strain Below JZB02 Structure 1 – TCU-078 [0.4]

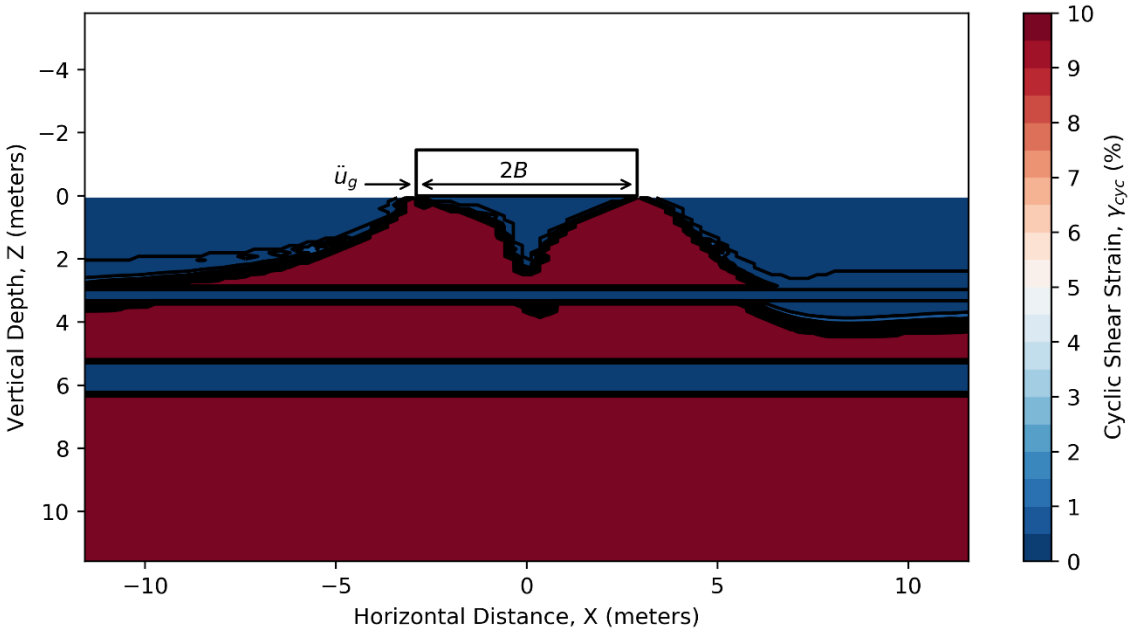

Figure B- 16: Cyclic Shear Strain Below JZB02 Structure 1 – TCU-078 [0.6]

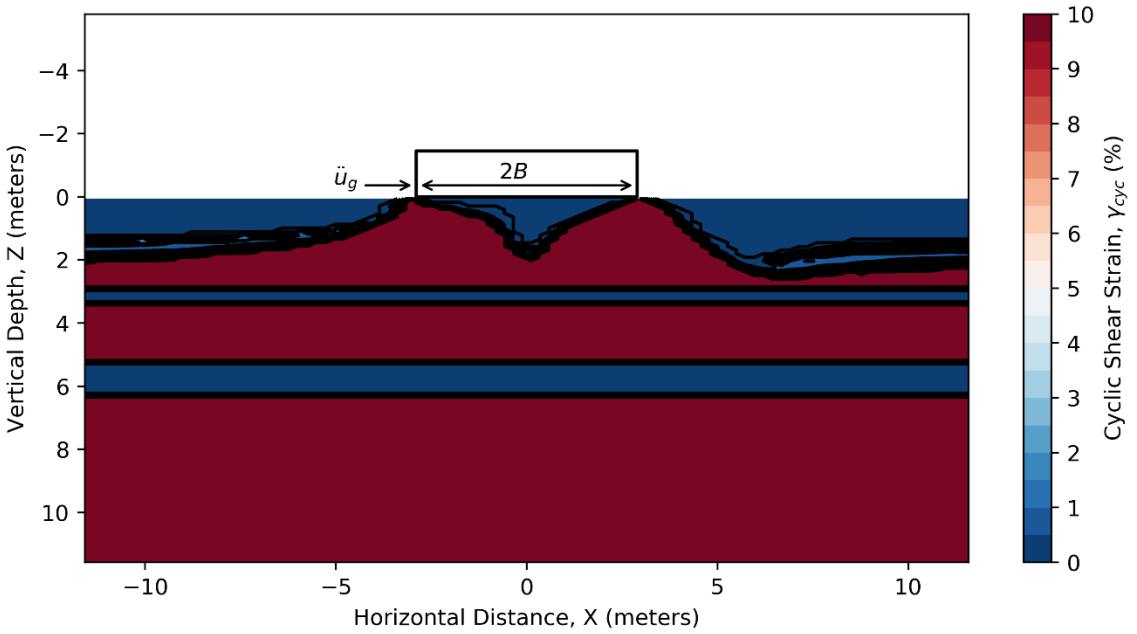

Figure B- 17: Cyclic Shear Strain Below JZB02 Structure 1 – TCU-078 [0.8]

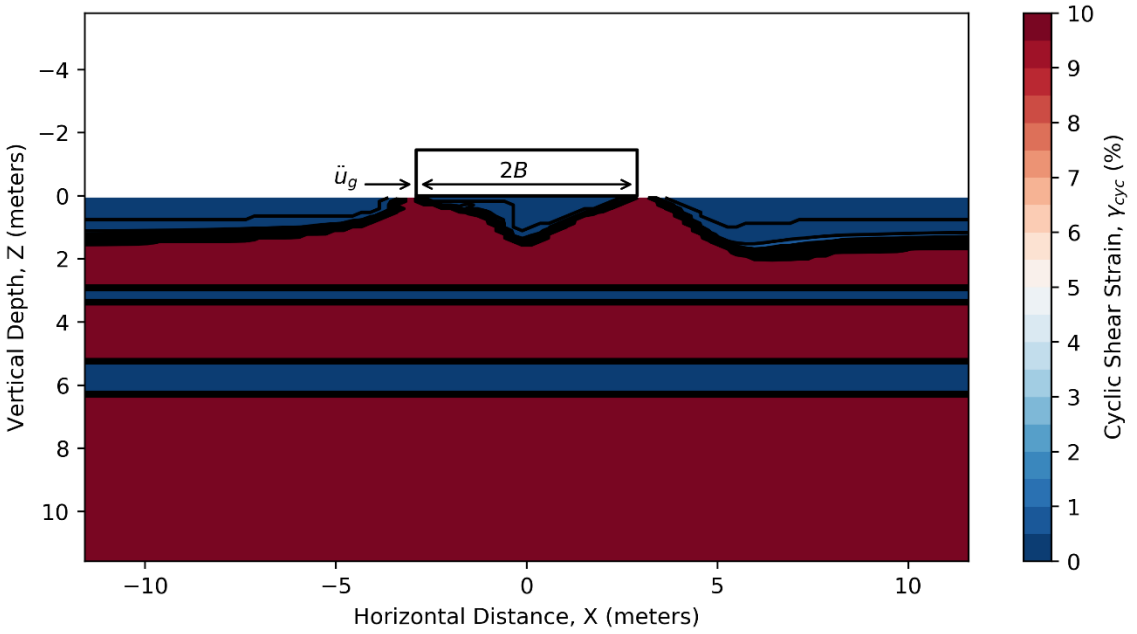

Figure B- 18: Cyclic Shear Strain Below JZB02 Structure 1 – TCU-078 [1]

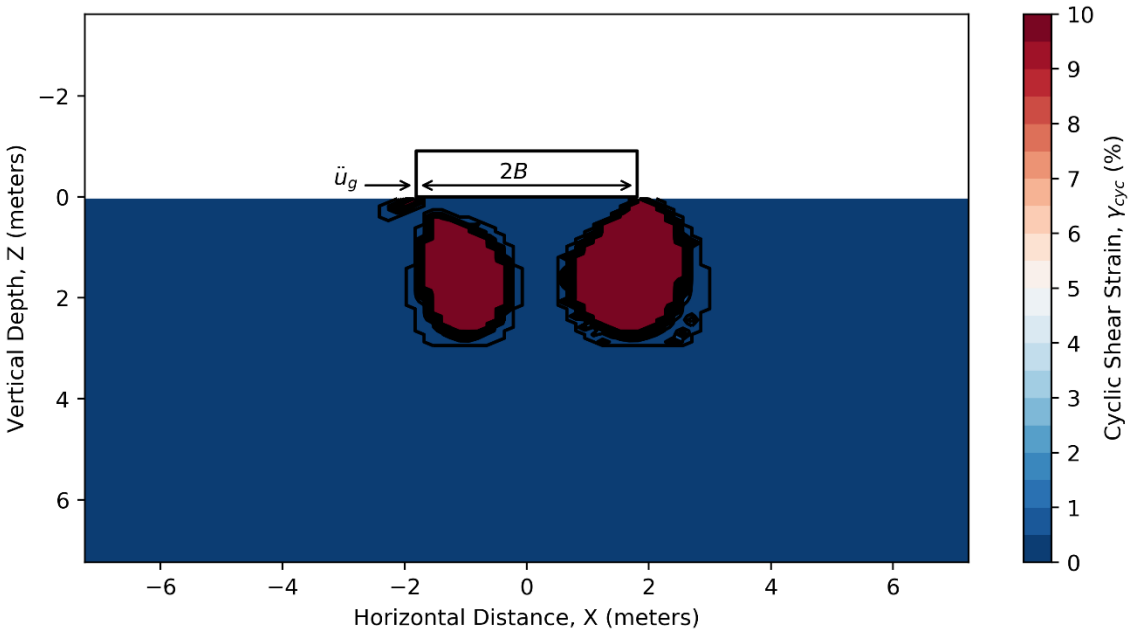

Figure B- 19: Cyclic Shear Strain Below JZB02 Structure 2 – TCU-078 [0.2]

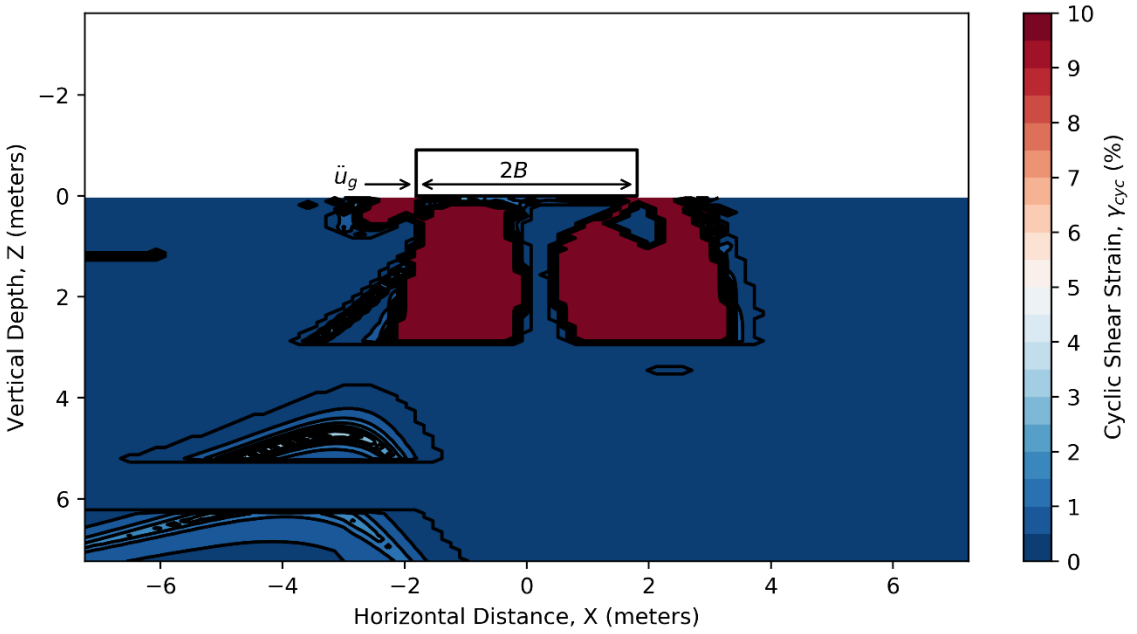

Figure B- 20: Cyclic Shear Strain Below JZB02 Structure 2 – TCU-078 [0.4]

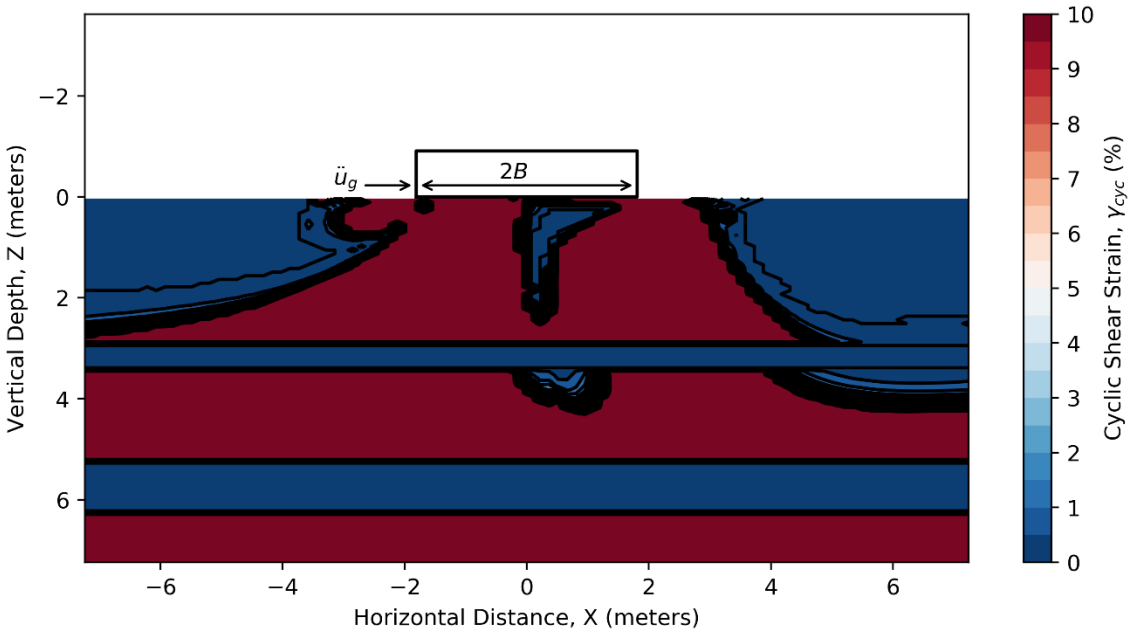

Figure B- 21: Cyclic Shear Strain Below JZB02 Structure 2 – TCU-078 [0.6]

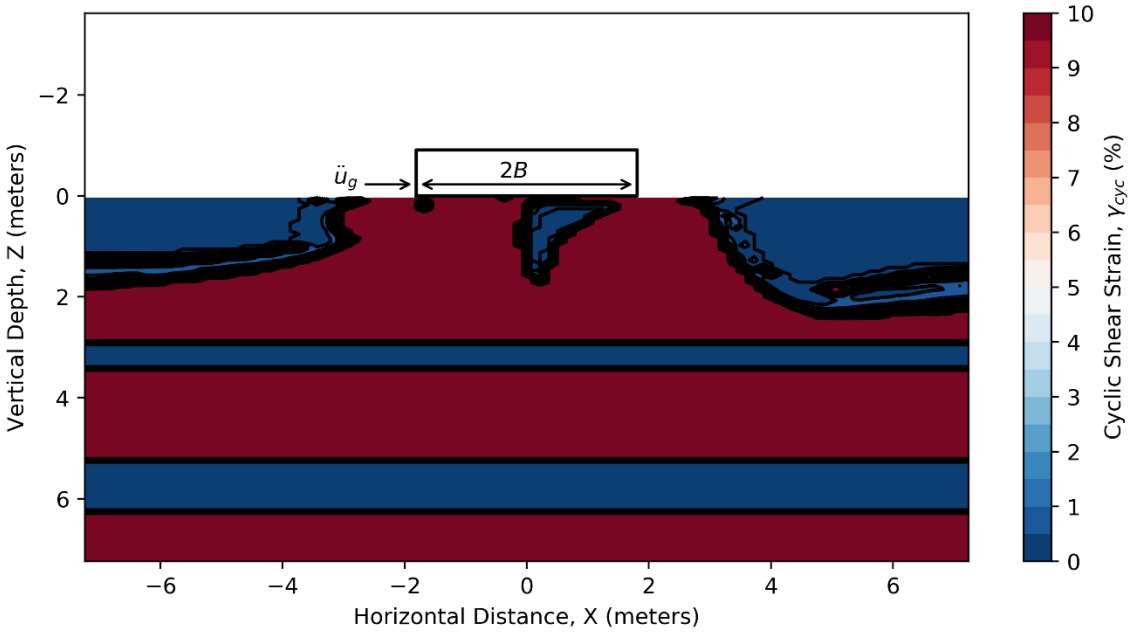

Figure B- 22: Cyclic Shear Strain Below JZB02 Structure 2 – TCU-078 [0.8]

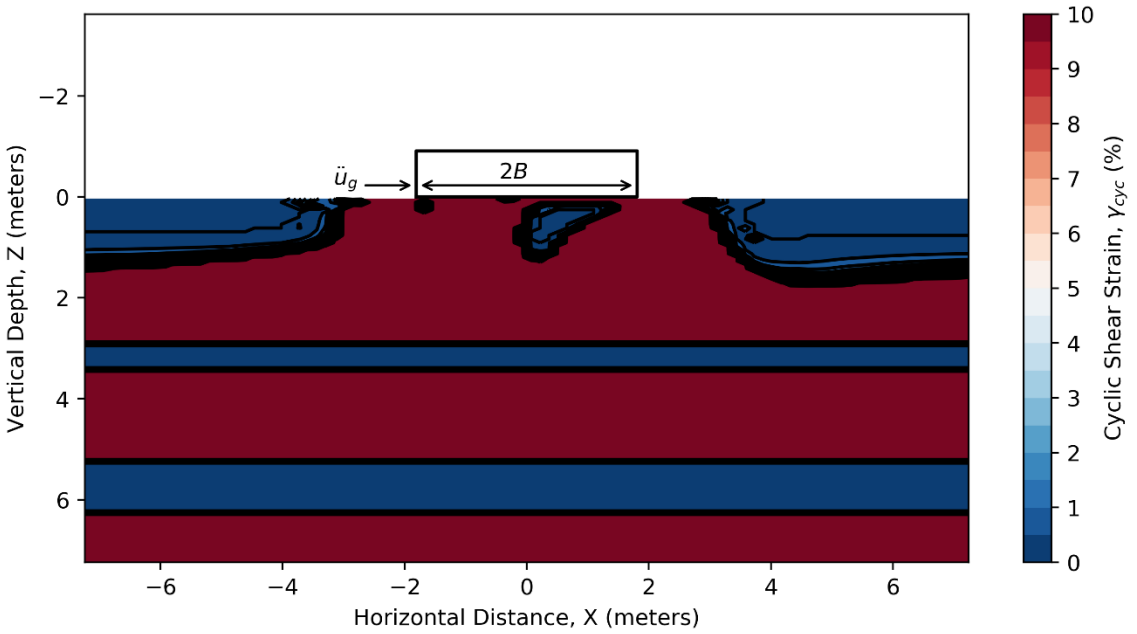

Figure B- 23: Cyclic Shear Strain Below JZB02 Structure 2 – TCU-078 [1]

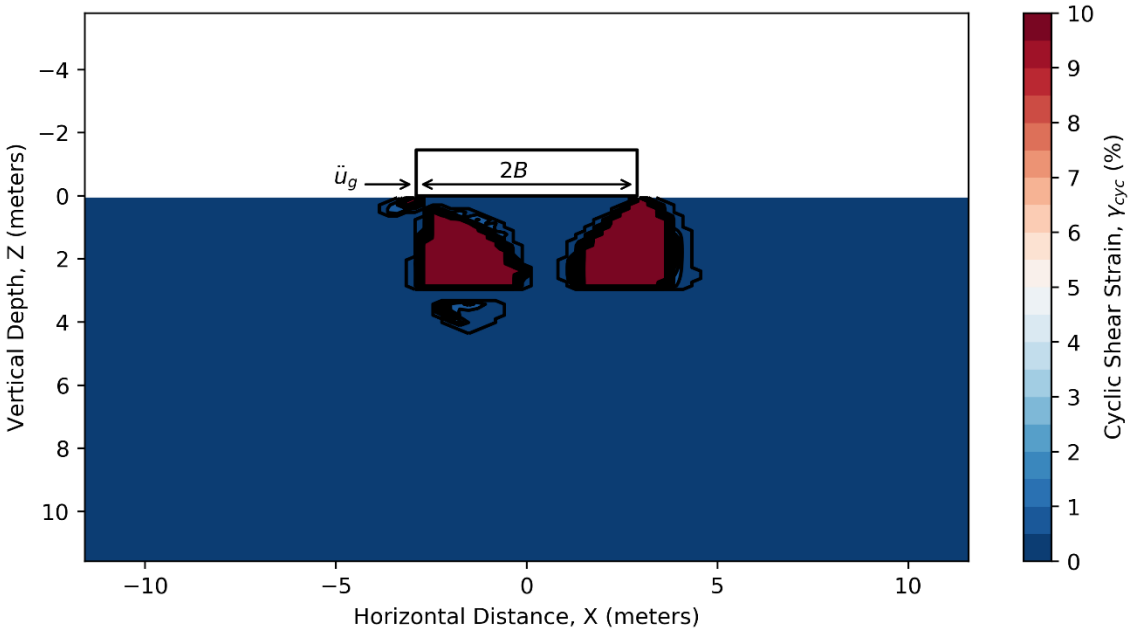

Figure B- 24: Cyclic Shear Strain Below JZB02 Structure 3 – TCU-078 [0.2]

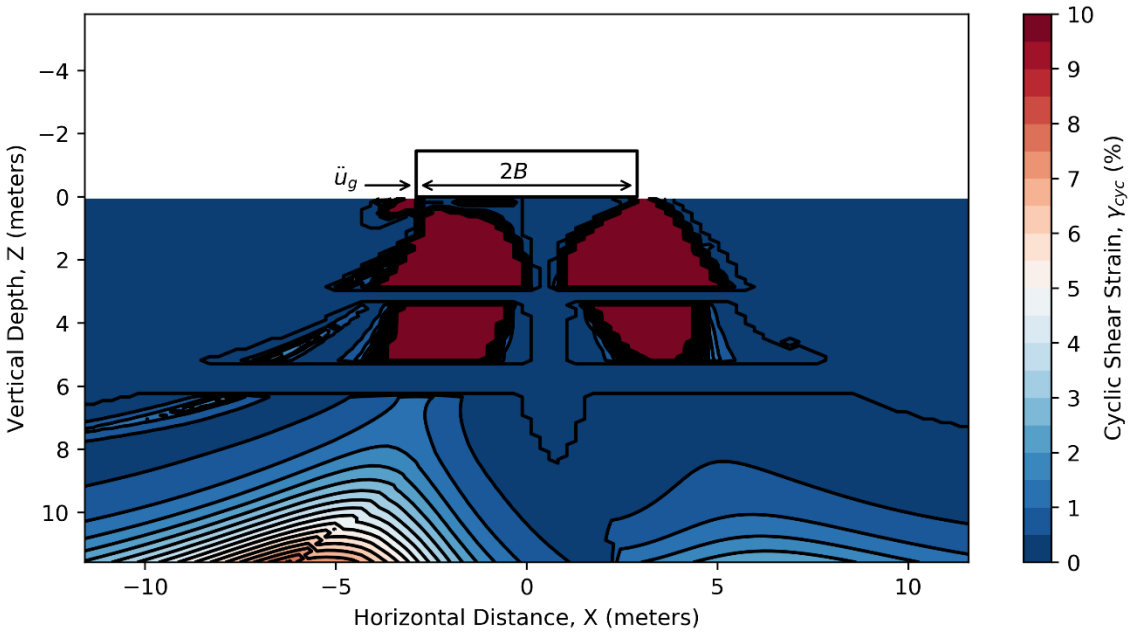

Figure B- 25: Cyclic Shear Strain Below JZB02 Structure 3 – TCU-078 [0.4]

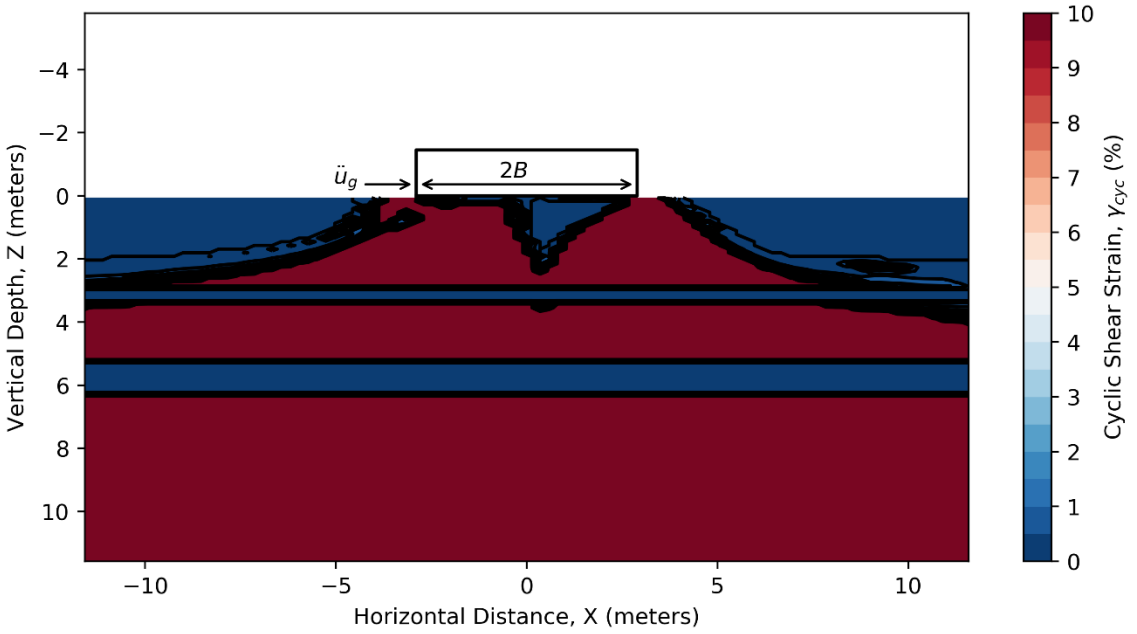

Figure B- 26: Cyclic Shear Strain Below JZB02 Structure 3 – TCU-078 [0.6]

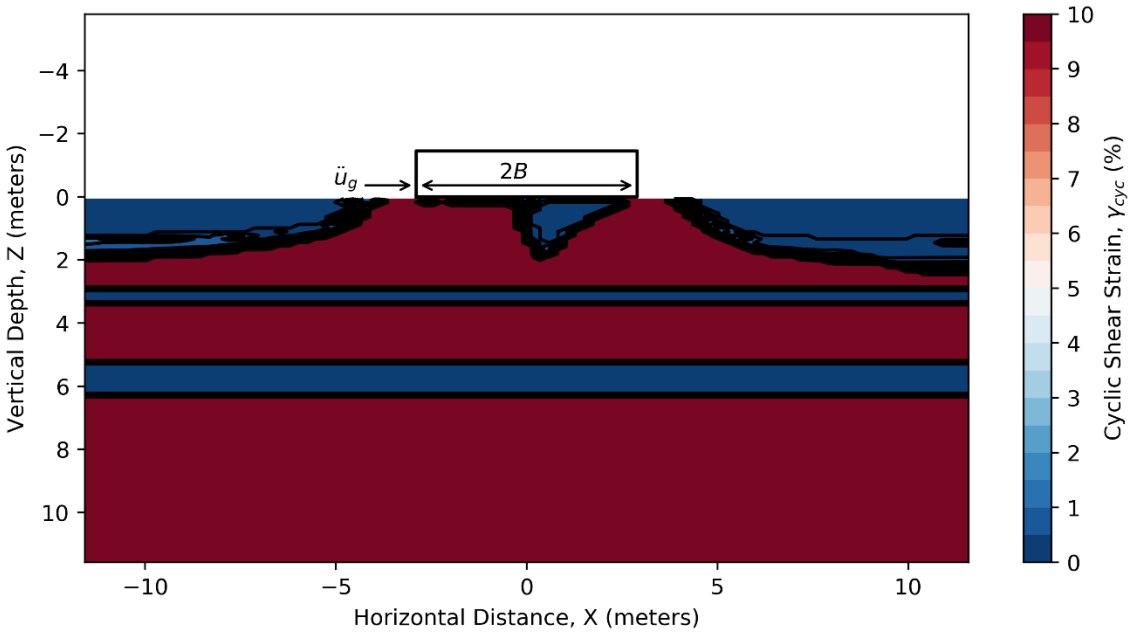

Figure B- 27: Cyclic Shear Strain Below JZB02 Structure 3 – TCU-078 [0.8]

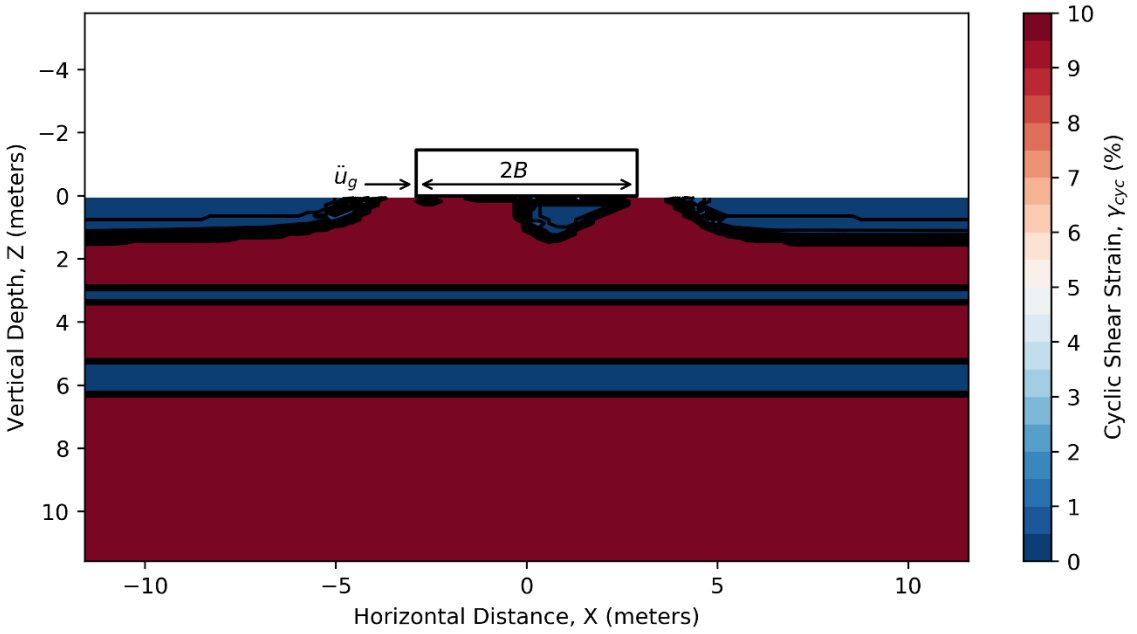

Figure B- 28: Cyclic Shear Strain Below JZB02 Structure 3 – TCU-078 [1]

WORKS CITED

Allmond, J., Kutter, B.L., Bray, J.D. & Hayden, C., 2015. New Database for Foundation and Ground Performance in Liquefaction Experiments. *Earthquake Spectra*, 31(4), pp.2485-509.

Allmond, J. & L., K.B., 2012. Centrifuge Testing of Rocking Foundations on Saturated Sand and Unconnected Piles: The Fluid Response. In *GeoCongress 2012: State of the Art and Practice in Geotechnical Engineering*. Oakland, California, 2012. American Society of Civil Engineers.

Ancheta, T.D. et al., 2013. *PEER NGA-West2 Database*. PEER 2013/03. University of California Berkeley: Pacific Earthquake Engineering Research Center.

Ashford, S.A., Boulanger, R.W., Donahue, J.L. & Stewart, J.P., 2011. *Geotechnical Quick Report on the Kanto Plain Region during the March 11, 2011, Off Pacific Coast of Tohoku Earthquake, Japan*. GEER-025a. Geotechnical Extreme Events Reconnaissance Association.

Bastidas, A.M.P., 2016. *Ottawa F-65 Sand Characterization*. PhD Dissertation. University of California Davis.

Boulanger, R.W. & Idriss, I.M., 2006. Liquefaction Susceptibility Criteria for Silts and Clays. *J. Geotech. Geoenviron. Eng.*, 132(11), pp.1413-26.

Boulanger, R.W. & Idriss, I.M., 2007. Evaluation of Cyclic Softening in Silts and Clays. *J. Geotech. Geoenviron. Eng.*, 133(6), pp.641-52.

Boulanger, R.W. & Idriss, I.M., 2012. Probabilistic Standard Penetration Test-Based Liquefaction-Triggering Procedure. *J. Geotech. Geoenviron. Eng.*, 138(10), pp.1185-95.

Boussinesq, M.J., 1885. *Application des potentiels à l'étude de l'équilibre et du mouvement des solides élastiques*. Paris: Gauthier-Villars.

Bray, J.D. & Sancio, R.B., 2006. Assessment of the Liquefaction Susceptibility of Fine-Grained Soils. *J. Geotech. Geoenviron. Eng.*, 132(9), pp.1165-77.

Bray, J.D. et al., 2004. Subsurface Characterization at Ground Failure Sites in Adapazari, Turkey. *J. Geotech. Geoenviron. Eng.*, 130(7), pp.673-85.

Buenker, J.M. et al., 2019. *Centrifuge Testing on Bentonite Clay - Test UCLA JZB01 in Soil-Foundation-Structure Interaction Effects on the Cyclic Failure Potential of Silts and Clays*. Centrifuge Data Report. DesignSafe-CI.

Buenker, J.M., Brandenberg, S.J. & Stewart, J.P., 2020a. *Centrifuge Testing on Kaolinite Clay - Test UCLA JZB02 in Soil-Foundation-Structure Interaction Effects on the Cyclic Failure Potential of Silts and Clays*. Centrifuge Data Report. DesignSafe-CI.

Buenker, J.M., Brandenberg, S.J. & Stewart, J.P., 2020b. Centrifuge Modeling of Cyclic Softening in Low Plasticity Clays Partially Induced by Seismic Soil-Structure-Interaction. In Hambleton, J.P., Makhnenko, R. & Budge, A.S., eds. *Geo-Congress 2020: Geotechnical Earthquake Engineering and Special Topics (GSP 318)*. Minneapolis, 2020b. American Society of Civil Engineers.

Buenker, J.M., Brandenberg, S.J. & Stewart, J.P., 2020c. Centrifuge Testing of Soil-Foundation-Structure Interaction Effects on Cyclic Failure Potential of Fine-Grained Soil. *Earthquake Spectra*, p.(Publication Pending).

Campbell, K.W. & Bozorgnia, Y., 2011. Predictive equations for the horizontal component of standardized cumulative absolute velocity as adapted for use in the shutdown of U.S. nuclear power plants. *Nucl. Eng. Des.*, 241(7), pp.2558-69.

Cerruti, V., 1882. *Ricerche intorno all'equilibrio dei corpi elastici isotropi*. Vol. 13. Rome: Reale Accademia dei Lincei.

Cetin, K.O. et al., 2004. Standard Penetration Test-Based Probabilistic and Deterministic Assessment of Seismic Soil Liquefaction Potential. *J. Geotech. Geoenviron. Eng.*, 130(12), pp.1314-40.

Chopra, A.K., 2012. *Dynamics of Structures - Theory and Applications to Earthquake Engineering*. Fourth Edition ed. Upper Saddle River, New Jersey: Prentice Hall.

Chu, D.B., Stewart, J.P., Boulanger, R.W. & Lin, P.S., 2008. Cyclic Softening of Low-Plasticity Clay and Its Effect on. *J. Geotech. Geoenviron. Eng.*, 134(11), pp.1595-608.

Chu, D.B. et al., 2004. Documentation of soil conditions at liquefaction and non-liquefaction sites from 1999 Chi-Chi (Taiwan) earthquake. *Soil Dynamics and Earthquake Engineering*, 24, pp.647-57.

Cubrinovski, M. et al., 2011. Geotechnical Aspects of the 22 February 2011 Christchurch Earthquake. *Bulletin of the New Zealand Society for Earthquake Engineering*, 44(4), pp.205-26.

da Silva Marques, A.S.P., de Figueiredo Coelho, P.A.L., Haigh, S. & Madabhushi, G., 2014. Centrifuge modeling of liquefaction effects on shallow foundations. In A. Ilki & M.N. Fardis, eds. *Seismic Evaluation and Rehabilitation of Structures - Geotechnical, Geological, and Earthquake Engineering*. Switzerland: Springer International Publishing. pp.425-40.

Dashti, S. et al., 2010a. Mechanisms of Seismically Induced Settlement of Buildings with Shallow Foundations on Liquefiable Soil. *J. Geotech. Geoenviron. Eng.*, 136(1), pp.151-64.

Dashti, S. et al., 2010b. Centrifuge Testing to Evaluate and Mitigate Liquefaction-Induced Building Settlement Mechanisms. *J. Geotech. Geoenviron. Eng.*, 136(7), pp.918-29.

Dashti, S. & Karimi, Z., 2017. Ground Motion Intensity Measures to Evaluate I: The Liquefaction Hazard in the Vicinity of Shallow-Founded Structures. *Earthquake Spectra*, 33(1), pp.241-76.

DeJong, J.T., Yafrate, N.J. & DeGroot, D.J., 2011. Evaluation of Undrained Shear Strength Using Full-Flow Penetrometers. *J. Geotech. Geoenviron. Eng.*, 137(1), pp.14-26.

Eslami, M., 2017. *Experimental Mapping of Eslatoplastic Surfaces for Sand and Cyclic Failure of Low-Plasticity Fine-Grained Soils*. PhD Dissertation. University of California Los Angeles.

Eslami, M.M., Brandenberg, S.J., Stewart, J.P. & Buenker, J.M., 202X. Cyclic Behavior of Low-Plasticity Fine-Grained Soils with Varying Clay Minerology and Pore Fluid Salinity. *J. Geotech. Geoenviron. Eng.*, (in progress).

Flamant, A., 1892. *Sur la repartition des pressions dans un solide rectangulaire charge transversalement*. 114. Paris: Compte. Rendu. Sci.

Hayden, C.P. et al., 2015. Centrifuge Tests of Adjacent Mat-Supported Buildings Affected by Liquefaction. *J. Geotech. Geoenviron. Eng.*, 141(3), p.04014118.

Heidarzadeh, B., 2016. *Dynamic Stresses in Foundation Soils from Soil-Structure Interaction*. PhD Dissertation. University of California Los Angeles.

Heidarzadeh, B., Mylonakis, G. & Stewart, J.P., 2015. Stresses Beneath Dynamically Applied Vertical Point Loads. In *6th International Conference on Earthquake Geotechnical Engineering*. Christchurch, New Zealand, 2015. International Society for Soil Mechanics and Geotechnical Engineering.

Heidarzadeh, B., Stewart, J.P. & Mylonakis, G., 2018. Dynamic Stresses in Foundation Soils beneath Strip Footings. In Brandenberg, S.J. & Manzari, M.T., eds. *Geotechnical Earthquake Engineering and Soil Dynamics V*. Austin, Texas, 2018. American Society of Civil Engineers.

Idriss, I.M. & Boulanger, R.W., 2006. Semi-empirical procedures for evaluating liquefaction potential during earthquakes. *Soil Dynamics and Earthquake Engineering*, 26(2-4), pp.115-30.

Idriss, I.M. & Boulanger, R.W., 2008. *Soil Liquefaction During Earthquakes*. 12th ed. Oakland, California: Earthquake Engineering Research Institute.

Idriss, I.M. & Boulanger, R.W., 2010. *SPT-based liquefaction triggering procedures*. Rep. CD/CGM-10/02. Dept. of Civil and Environmental Engineering, Univ. of California Davis.

Jurgenson, L., 1934. The Application of Theories of Elasticity and Plasticity to Foundation Problems. *J. of the Boston Society of Civil Eng.*, 21(3).

Karimi, Z. & Dashti, S., 2016. Numerical and Centrifuge Modeling of Seismic Soil-Foundation-Structure Interaction on Liquefiable Ground. *J. Geotech. Geoenviron. Eng.*, 142(1), pp.04015061-1-14.

Karimi, Z. & Dashti, S., 2017. Ground Motion Intensity Measures to Evaluate II: the Performance of Shallow-Founded Structures on Liquefiable Ground. *Earthquake Spectra*, 33(1), pp.277-98.

Kramer, S.L., 1996. *Geotechnical Earthquake Engineering*. Upper Saddle River, New Jersey: Prentice-Hall.

Kramer, S.L. & Mitchell, R.A., 2006. Ground Motion Intensity Measures for Liquefaction Hazard Evaluation. *Eq. Spectra*, 22(2), pp.413-38.

Ladd, C.C., 1991. Stability Evaluation during Staged Construction. *J. Geotech. Geoenviron. Eng.*, 117(4), pp.540-615.

Liu, H. & Qiao, T., 1984. Liquefaction potential of saturated sand deposits underlying foundation of structure. In *8th World Conf. on Earthquake Eng.* San Francisco, California, 1984. International Association for Earthquake Engineering.

Macedo, J. & Bray, J.D., 2018. Key Trends in Liquefaction-Induced Building Settlement. *J. Geotech. Geoenviron. Eng.*, 144(11), p.04018076.

Martin, J.R., Olgun, C.G., Mitchell, J.K. & Durgunoglu, H.T., 2004. High-Modulus Columns for Liquefaction Mitigation. *J. Geotech. Geoenviron. Eng.*, 130(6), pp.561-71.

Meyerhof, G.G., 1951. The Ultimate Bearing Capacity of Foundations. *Geotechnique*, 2, pp.301-32.

National Institute of Standards and Technology, 2012. *Soil Structure Interaction for Building Structures*. NIST GCR 12-917-21. NEHRP Consultants Joint Venture.

National Instruments, 2018. *Measuring Strain with Strain Gages*. [Online] Available at: HYPERLINK "http://www.ni.com/en-us/innovations/white-papers/07/measuring-strain-with-strain-gages.html" http://www.ni.com/en-us/innovations/white-papers/07/measuring-strain-with-strain-gages.html [Accessed November 2018].

Poulos, H.G. & Davis, E.H., 1974. *Elastic Solutions for Soil and Rock Mechanics*. Sydney: Centre for Geotechnical Research, University of Sydney.

Rocscience, Inc., 2018. *RS2 9 Modeler*. V. 9.029 64-bit. Toronto, Canada.

Rollins, K.M. & Seed, H.B., 1990. Influence of Buildings on Potential Liquefaction Damage. *J. Geotech. Geoenviron. Eng.*, 116(2), pp.165-85.

Sancio, R.B. et al., 2002. Correlation between ground failure and soil conditions in Adapazari, Turkey. *Soil Dynamics and Earthquake Engineering*, 22(9-12), pp.1093-102.

Scott, R.F., 1963. *Principles of Soil Mechanics*. Reading, Massachusetts: Addison-Wesley.

Seed, H.B., 1983. Earthquake Resistant Design of Earth Dams. In Howard, T.R., ed. *Proc. Symposium on Seismic Design of Embankments and Caverns*. Philadelphia, Pennsylvania, 1983. American Society of Civil Engineers.

Seylabi, E.E. et al., 2019. Centrifuge Testing o f Circular and Rectangular Embedded Structures with Base Excitations. *Earthquake Spectra*, 35(3), pp.1485-505.

Vesic, A.S., 1975. Bearing Capacity of Shallow Foundations. In H.F. Winterkorn & H.W. Fang, eds. *Foundation Engineering Handbook*. New York: Van Nostrand Reinhold Co. pp.121-45.

Youd, T.L. et al., 2001. Liquefaction Resistance of Soils: Summary Report from the 1996 NCEER and 1998 NCEER/NSR Workshops on Evaluation of Liquefaction Resistance of Soils. *J. Geotech. Geoenviron. Eng.*, 127(10), pp.817-33.

Zupan, J.D. et al., 2013. *Soil-Structure Interaction on the Scale of a City Block - Seismic Performance in Dense Urban Environments (Test-5)*. Centrifuge Data Report. University of California Davis.